High Temperature Electrolysis by Reversing the Function of a Solid Oxide Fuel Cell

by

IRVING BENJAMIN ANNAN

A thesis submitted to the University of Birmingham for the degree of

DOCTOR OF PHILOSOPHY

The Centre for Hydrogen and Fuel Cell Research
Chemical Engineering
University of Birmingham
April 2021

ABSTRACT

The world is increasingly committing to a green energy future. However, to ensure transition of the energy landscape with relatively minimal disruptions, energy storage technologies are required. An energy storage technology of significant promise is the reversible solid oxide cell (rSOC).

A reversible solid oxide cell test apparatus was designed, and tests were performed in both constant solid oxide fuel cell (SOFC) and solid oxide electrolysis (SOE) modes, as well as rSOC cyclic operation. It was observed that cell degradation during SOE operation was generally more than double the degradation during SOFC mode.

Cell performance losses also increased with decreasing temperature and increasing current density. However, performance losses were more strongly correlated with current density increases than with temperature decreases in all operating modes (SOFC, SOE and rSOC).

Like the operating current density, cell degradation also seemed to be strongly correlated with fuel utilisation (which is a function of both current density and reactant flow rates). Cell degradation rate increased with increasing fuel utilisation.

It was also observed that some degradation recovery occurred under the subsequent SOFC mode operation after SOE mode operation during reversible cycling. The magnitude of voltage recoveries was about 40% of the voltage losses during the preceding SOE mode operation.

The effect of switching parameters (and associated transient processes during switching) on cell performance was also studied. It was observed that during rSOC cycling, after SOE mode operation, the cell takes about 30 minutes to recover to the SOFC cell voltage prior to the SOFC mode operation. During rSOC cycling, in order to study the effects of switching time on cell performance, some SOFC mode operations were commenced without waiting for the cell to recover to SOFC OCV. No discernible effect of the switching time on subsequent cell performance was apparent.

ACKNOWLEDGEMENTS

I would like to thank God, my PhD supervisor (Professor Robert Steinberger-Wilckens), my mother and my wife. This could not have been possible without any of them.

CONTENTS

ABSTRACT ii

ACKNOWLEDGEMENTS iii

CONTENTS iv

ABBREVIATIONS AND ACRONYMS ix

FIGURES xiii

1 INTRODUCTION 1

1.1 Background 1

1.1.1 Traditional Energy Landscape 5

1.1.2 Renewable Power, Alternative Fuels and Electrochemistry 5

1.1.3 Electrolysis 7

1.1.4 Basic Electrochemical Principles of Operation for rSOCs 13

1.2 Problem Statement 22

1.3 Research Hypotheses 23

1.4 Project Scope 24

1.5 Project Objectives 25

1.6 Novelty Statement 26

1.7 Thesis Outline 26

2 Overview of the Balance Project 28

2.1 Introduction........ 28

2.2 Project Background and Purpose 28

2.3 Project Participants and Scope 30

2.4 Unit Cell Testing Activities 32

2.4.1 Cell configurations and Test Protocol........ 32

2.4.2 Rationale for Selected Test Periods / Profile 34

2.4.3 Selection of Unit Cell Test Results and Discussion........ 35

2.5 CONCLUSIONS 41

2.5.1 Knowledge Management, Communication and Dissemination 42

3 Literature Review 44

3.1 General........ 44

3.2 Materials and their Degradation 44

3.2.1 Electrolytes........ 45

3.2.2 Air / Oxygen Electrodes........ 48

3.2.3 Fuel/Hydrogen Electrodes........ 57

3.3 Effects of Cell Operating Variables on Performance and Degradation........ 62

3.3.1 Cell Operating Temperature........ 62

3.3.2 Cell Current Density/Mode........ 63

3.3.3 Effects of Reactants (Fuel Electrode) Utilisation 65

3.3.4 Comparative Assessment of rSOC Degradation Rates under SOFC and SOE Operations 66

3.3.5 Effect of other Operation Variables on rSOC Performance and Degradation Rates..................67

3.4 Summary of Conditions Necessary for Symmetrical and Reversible Operation 68

3.5 Conclusions 69

4 Methodology 71

4.1 Materials Tested... 71

4.1.1 Fuel Electrode Material 72

4.1.2 Oxygen electrode material 74

4.1.3 Electrolyte / Oxygen electrode interlayer 77

4.1.4 Electrolyte 80

4.1.5 Current collection materials 82

4.2 Experimental Methods 91

4.2.1 Description of test apparatus 91

4.2.2 Operating variables 97

4.2.3 Test Protocol 101

4.2.4 Electrochemical data acquisition...105

4.2.5 Structural characterisation 113

4.2.6 SEM analysis 115

5 CELL TYPE 1 Reversible Operation 117

5.1 Introduction.. 117

5.2 Test at 0.5 A/cm^2 Current Density (CT1_0.5_750#1)... 120

5.3 Test at 0.5 A/cm^2 Current Density (Cell ID: CT1_0.5_700#1) 137

5.4 Test at 0.5 A/cm^2 Current Density “Upside-down test apparatus configuration” (Cell ID: CT1_0.5_750#2) 143

5.5 Test at 0.5 A/cm^2 Current Density “Upside-down test apparatus configuration” (Cell ID: CT1_0.5_700#2) 149

5.6 Test at 0.7 A/cm^2 Current Density (Cell ID: CT1_0.7_750) 155

5.7 Test at higher SOE Current Density (Cell ID: CT1_1.39_750).. 161

5.8 Test at 1.25 A/cm^2 Current Density (Cell ID: CT1_1.25_750).. 166

5.9 Test at 2.65 A/cm^2 Current Density (Cell ID: CT1_2.65_750) 170

5.10 Summary of Cell Type 1 Results 173

6 CELL TYPE 2 Reversible Operation 175

6.1 Introduction.. 175

6.2 Test with 0.7 A/cm^2 Current Density (Cell ID: CT2_0.7_750).. 177

6.3 Test at 0.5 A/cm^2 Current Density (Cell ID: CT2_0.5_750) 185

6.4 Test at 0.5 A/cm^2 Current Density (Cell ID: CT2_0.5_700) 191

6.5 Summary of Cell Type 2 Results.. 196

7 DISCUSSION 198

7.1 General Observations 198

7.2 Effect of Temperature 200

7.3 Effect of Current Density 207

7.3.1 Comparison of Two different Cell Types Tested at 0.5 A/cm^2 and 0.7 A/cm^2 209

7.3.2 Effect of Silver Paste Contacting on Overall Cell Resistance..215

7.4 Effect of Fuel-Feed Parameters and Overall Fuel Utilisation 221

7.5 Effect of Switching Time 222

8 Summary and Outlook...229

8.1 Technology Relevance 229

8.2 Summary of Work.. 229

8.3 Research Area Outlook 232

9 References..233

Appendix A Supplementary Results 246

A.1 Test at 1.5 A/cm^2 Current Density (Cell ID: CT1_1.5_750#1) 246

A.2 Test at 1.5 (1.05) A/cm^2 Current Density (Cell ID: CT1_1.5_750#2) 249

ABBREVIATIONS AND ACRONYMS

Abbreviation/Acronym	Description
AC	Alternating Current
AE	Alkaline Electrolysis
ASR	Area Specific Resistance
BoP	Balance of Plant
BSCF	Barium Strontium Cobalt Ferrite
CAPEX	Capital Expenditure
CCS	Carbon Capture and Storage
CCV	Close Cell Voltage
CEM	Controlled Evaporator Mixer
CGO	Cerium-Gadolinium Oxide (known alternatively as GDC)
CH_3OH	Methanol
CO	Carbon Monoxide
CO_2	Carbon Dioxide
COP21	Conference of the Parties (21st yearly session)
CPE	Constant Phase Element
CT	Cell Type
CZGY	Cerium Zirconium Gadolinium Yttrite
DC	Direct Current
DG-ENER	Directorate General for Energy
DME	Di Methyl Ether
DRT	Distribution of Relaxation Times

Abbreviation/Acronym	Description
EC	European Commission
ECF	European Climate Foundation
EDX	Energy Dispersive X-Ray
EEC	Equivalent Electrical Circuit
EIS	Electrochemical Impedance Spectroscopy
FCH-JU	Fuel Cell and Hydrogen – Joint Undertaking
G2P	Gas-to-Power
GDC	Gadolinium Doped Ceria
GHG	Green House Gas
H_2	Hydrogen
H_2O	Water
IEA	International Energy Agency
j-V	Current Density - Voltage
LNO	Lanthanum Nickelate
LSC	Strontium-doped Lanthanum Cobaltite
LSCF	Lanthanum Strontium Cobaltite Ferrite
LSCM	Strontium-doped Lanthanum Chromium Manganite
LSCN	Lanthanum Strontium Cobalt Nickelate
LSF	Strontium-doped Lanthanum Ferrite
LSM	Strontium-doped Lanthanum Manganite
LST	Lanthanum Strontium Titanate
LSV	Lanthanum Strontium Vanadate
MeOH	Methanol

Abbreviation/Acronym	Description
MFC	Mass Flow Controller
MIEC	Mixed Ionic Electronic Conductor
Ni	Nickel
Ni-YSZ	Nickel – Yttria Stabilised Zirconia cermet
NNO	Neodymium Nickelate
OCV	Open Cell Voltage
P2G	Power-to-Gas
P2P	Power-to Gas to-Power
PEME	Proton Exchange Membrane Electrolysis
PMI	Positive Material Identification
PNO	Praseodymium Nickelate
PVD	Physical Vapour Deposition
RES	Renewable Energy Source
rSOE	Reversible Solid Oxide Electrolyser
rSOC	Reversible Solid Oxide Cell(s)
RWGS	Reverse Water Gas Shift
ScSZ	Scandia Stabilised Zirconia
SDC	Samarium-doped ceria
SEM	Scanning Electron Microscopy
SET	Strategic Energy Technology
SFN	Strontium Iron Niobia
SiC	Silicon Carbide
SNG	Synthetic Natural Gas

Abbreviation/Acronym	Description
SOE	Solid Oxide Electrolysis / Electrolyser
SOFC(s)	Solid Oxide Fuel Cell(s)
SotA	State of the Art
SRU	Single Repeating Unit
TPB	Triple Phase Boundary
TRL	Technology Readiness Level
WGS	Water Gas Shift
WP	Work Package
YbSZ	Ytterbium Stabilised Zirconia
YSZ	Yttria Stabilised Zirconia

FIGURES

Figure 1-1: Projection of energy sources market shares for 2030 and 2050 against a 2005 benchmark [2]. 2

Figure 1-2: Comparison of typical range of AE, PEME and SOE performances. Reproduced based on [10]. 10

Figure 1-3: Thermodynamic parameters for electrolysis ($H_2O \rightarrow H_2 + {}^1/_2O_2$), 'energy demand' and fuel cell ($H_2 + {}^1/_2O_2 \rightarrow H_2O$), 'energy content' at atmospheric pressure. Reproduced based on [5]. 12

Figure 1-4: Depiction of solid oxide fuel cell electrochemistry (Credit: WikiCommons). 14

Figure 1-5: Depiction of electrolysis using a solid oxide fuel cell showing the electrochemical reversibility (Credit: WikiCommons). 17

Figure 2-1: rSOC concept and its role as a key integrator of the different energy vectors, as investigated in the BALANCE project [3]. 29

Figure 2-2: BALANCE generation 1 (G1), generation 2 (G2) and modified generation 2 (Modified G2) cell configurations. 33

Figure 2-3: Initial j-V curve comparisons of G1 cells tested at three different participating Labs. 36

Figure 2-4: Voltage evolution comparison of BALANCE G1 Cell (Test 1) with commercial cell (Test 2). 36

Figure 2-5: j-V and EIS curves of BALANCE test matrix A1. 37

Figure 2-6: Voltage evolution of G1 cell tested under test matrix A5. 38

Figure 2-7: Comparison of G1 and G2 cells' initial performance. 39

Figure 2-8: Comparison of voltage evolution of G1 and G2 cells. 40

Figure 2-9: Comparison of voltage evolution of G2 and Modified G2 cells. 41

Figure 4-1: Energy-dispersive X-ray spectrograph of fuel electrode material. 73

Figure 4-2: Scanning electron micrograph of the virgin fuel electrode material. 73

Figure 4-3: Energy-dispersive X-ray spectrograph of oxygen electrode material. 75

Figure 4-4: Scanning electron micrograph of oxygen electrode material for cell type 1 (also see *Figure 4-8*). 75

Figure 4-5: Cross-section of cell type 2 showing LSC infiltrated backbone oxygen electrode between pure GDC interlayer LSC contact layer. a) complete cell cross-section, b) to h) EDX scan showing elemental distribution across the SOC cross-section. 77

Figure 4-6: Energy-dispersive X-ray spectrograph of electrolyte / oxygen electrode interlayer material. 78

Figure 4-7: Scanning electron micrograph of the GDC interlayer (surface image of the exposed GDC interlayer at the rim of the oxygen electrode, see Figure 4-10 b)). 79

Figure 4-8: Cross-section of cell type 1 showing GDC layer between electrolyte and oxygen electrode. 79

Figure 4-9: YSZ electrolyte material for both cell types 1 and 2. 81

Figure 4-10: Silver-based current collection system attached to a) fuel electrode and b) oxygen electrode. 82

Figure 4-11: SOFC mode OCV at 750 °C. 83

Figure 4-12: Current - voltage characteristics in SOFC mode at 750 °C. 84

Figure 4-13: j-V characteristics under a ramp rate of 0.05 Amps/cm^2/min prior to operation in SOFC under constant current at 750 °C. 84

Figure 4-14: Operation in SOFC mode under constant current at 750 °C. 85

Figure 4-15: SOFC mode Nyquist plot. 86

Figure 4-16: SOFC mode Bode plot. 86

Figure 4-17: SOE mode OCV at 750 °C. 87

Figure 4-18: Current - voltage characteristics in SOE mode at 750 °C. 88

Figure 4-19: SOE mode Nyquist plot (significant scatter in the mass transfer region). 88

Figure 4-20: SOE mode Bode plot. 89

Figure 4-21: Degradation of the silver-based current collectors under test conditions. 90

Figure 4-22: Gold and nickel mesh/wires current collection system 91

Figure 4-23: Schematic of rSOC experimental test apparatus. 92

Figure 4-24: rSOC experimental test apparatus with the CEM for delivery of the reactants to the fuel electrode located at the top {a), and CEM for delivery of the reactants to the fuel electrode located at the bottom {b}. 93

Figure 4-25: An illustration of the alumina tube-in-tube reactor in accordance with test apparatus configuration {a}. 95

Figure 4-26: Lack of gas tightness / adequate sealing at the alumina tube edge around the unit cell. . 96

Figure 4-27: Male and female end closure connectors designed to improve leak-tightness. 97

Figure 4-28: SOE efficiencies for different cathode water utilisation and input temperature [138]. .. 103

Figure 4-29: Flow chart for the typical test regime used in the work (i.e., power-to-gas-to-power application specific test programme). Switching time between SOFC and SOE modes was approximately 30 minutes. 104

Figure 4-30: Typical profile for the overall test protocol (j = ±0.5 A·cm^{-2} during reversible operation). 105

Figure 4-31: Galvanostatic stair-step used for recording SOC j-V characteristics {a} shows voltage drop per step whilst {b} shows current density increase per step. 106

Figure 4-32: Fuel cell and electrolysis example j-V curve. 107

Figure 4-33: Raw impedance spectra and EEC model fit spectra 109

Figure 4-34: Employed EEC model [80], [140], [141]. 111

Figure 5-1: Configuration of cell type 1 117

Figure 5-2: Voltage evolution characteristics of CT1_0.5_750#1 tested at 750°C and ±0.5 A/cm^2 current density. 121

Figure 5-3: Cell voltage recovery under SOFC cycles during rSOC operation. 123

Figure 5-4: Cell voltage evolution during SOE cycles during rSOC operation. 124

Figure 5-5: Difference in magnitude between voltage losses during SOE and voltage recovery during SOFC. 125

Figure 5-6: Comparison of j-V characteristic of CT1_0.5_750#1 before and after SOFC, SOE and rSOC operation testing (captured under SOFC (a) and SOE (b) conditions). 128

Figure 5-7: Change in cell ASR with mode of operation, as captured under SOFC and SOE environments for CT1_0.5_750#1 130

Figure 5-8: Nyquist and Bode impedance plots of CT1_0.5_750#1 before and after SOFC, SOE and rSOC operation testing (captured under SOFC conditions). 131

Figure 5-9: Nyquist and Bode impedance plots of CT1_0.5_750#1 before and after SOFC, SOE and rSOC operation testing (captured under SOE conditions). 133

Figure 5-10:Virgin (a, b and c) and post-test (d to l) SEM images of the tested CT1_0.5_750#1 cell. . 136

Figure 5-11: Cell elements distribution/identification. 137

Figure 5-12: Voltage evolution characteristics of CT1_0.5_700#1 tested at 700°C and ±0.5 A/cm^2 current density. 139

Figure 5-13: Comparison of j-V characteristics of CT1_0.5_700#1 before and after SOFC and SOE operation testing (captured under **(a)** SOFC and **(b)** SOE conditions). 140

Figure 5-14: Nyquist and Bode impedance plots of CT1_0.5_700#1 before and after SOFC, SOE and rSOC operation testing (captured under SOFC conditions). 141

Figure 5-15: Nyquist and Bode impedance plots of CT1_0.5_700#1 before and after SOFC, SOE and rSOC operation testing (captured under SOE conditions). 142

Figure 5-16: Voltage evolution characteristics of CT1_0.5_750#2 tested at 750°C and ±0.5 A/cm^2 current density (upside-down test apparatus configuration, see Figure 4-2 (b)). 145

Figure 5-17: Comparison of j-V characteristics of CT1_0.5_750#2 before and after SOFC, SOE and rSOC operation testing (captured under **(a)** SOFC and **(b)** SOE conditions). 146

Figure 5-18: Nyquist and Bode impedance plots of CT1_0.5_750#2 before and after SOFC, SOE and rSOC operation testing (captured under SOFC conditions). 148

Figure 5-19: Nyquist and Bode impedance plots of CT1_0.5_750#2 before and after SOFC, SOE and rSOC operation testing (captured under SOE conditions). 149

Figure 5-20: Voltage evolution characteristics of CT1_0.5_700#2 tested at 700°C and ±0.5 A/cm^2 current density (upside-down test apparatus configuration). 150

Figure 5-21: Comparison of j-V characteristics of CT1_0.5_700#2 before and after SOFC, SOE and rSOC operation testing (captured under **(a)** SOFC and **(b)** SOE conditions). 152

Figure 5-22: Nyquist and Bode impedance plots of CT1_0.5_700#2 before and after SOFC, SOE and rSOC operation testing (captured under SOFC conditions). 153

Figure 5-23: Nyquist and Bode impedance plots of CT1_0.5_700#2 before and after SOFC, SOE and rSOC operation testing (captured under SOE conditions). 154

Figure 5-24: Voltage evolution characteristics of CT1_0.7_750 tested at 750°C and ±0.7 A/cm^2 current density. 156

Figure 5-25: Comparison of j-V characteristics of CT1_0.7_750 before and after SOFC and SOE operation testing (captured under SOFC and SOE conditions). 158

Figure 5-26: Change in cell ASR with mode of operation, as captured under SOFC and SOE environments for CT1_0.7_750. 159

Figure 5-27: Nyquist and Bode impedance plots of CT1_0.7_750 before and after SOFC and SOE operation testing (captured under SOFC conditions). 160

Figure 5-28: Nyquist and Bode impedance plots of CT1_0.7_750 before and after SOFC and SOE operation testing (captured under SOE conditions). 161

Figure 5-29: Voltage evolution characteristics of CT1_1.39_750 tested at 750°C and at +1.39 A/cm^2 under SOFC conditions and -2.65 A/cm^2 current density under SOE conditions. 163

Figure 5-30: Comparison of j-V characteristics of CT1_1.39_750 before and after SOFC operation testing (captured under (a) SOFC and (b) SOE conditions). 164

Figure 5-31:Nyquist and Bode impedance plots of CT1_1.39_750 before and after SOFC operation testing (captured under SOFC conditions). 165

Figure 5-32: Nyquist and Bode impedance plots of CT1_1.39_750 before and after SOFC operation testing (captured under SOE conditions). 166

Figure 5-33: Voltage evolution characteristics of CT1_1.25_750 tested at 750°C and ±1.25 A/cm^2 current density. 168

Figure 5-34: Initial j-V characteristics. 169

Figure 5-35: Voltage evolution characteristics of CT1_2.65_750 tested at 750°C and ±2.65 A/cm^2 current density. 170

Figure 5-36: Initial j-V characteristic of CT1_2.65_750 tested at 2.65 A/cm^2 current density............ 171

Figure 5-37: Initial Nyquist and Bode plots of CT1_2.65_750 tested at 2.65 A/cm^2........................... 173

Figure 5-38: Virgin SEM image.. 173

Figure 5-39: Initial j-V characteristics of CT1_1.5_750#1. 173

Figure 5-40: Virgin CT1_1.5_750#1 SEM image showing crack-like features. 173

Figure 5-41: j-V characteristics of virgin CT1_1.5_750#2. 173

Figure 5-42: Virgin CT1_1.5_750#2 SEM images showing crack-like features in cathode possibly linked to the observed poor performance.. 173

Figure 6-1: Configuration of cell type 2 175

Figure 6-2: Voltage evolution characteristics of test CT2_0.7_750 (750°C and ±0.7 A/cm^2 current density). 178

Figure 6-3: Comparison of j-V characteristic of CT2_0.7_750 before and after SOFC and SOE operation testing (captured under (a) SOFC and (b) SOE conditions)... 181

Figure 6-4: Nyquist and Bode impedance plots of CT2_0.7_750 before and after SOFC, SOE and rSOC operation testing (captured under SOFC conditions).. 182

Figure 6-5: Nyquist and Bode impedance plots of CT2_0.7_750 before and after SOFC, SOE and rSOC operation testing (captured under SOE conditions).. 183

Figure 6-6: Post-test SEM images of CT2_0.7_750. 184

Figure 6-7: Voltage evolution characteristics of CT2_0.5_750 tested at 750°C and ±0.5 A/cm^2 current density. 186

Figure 6-8: Comparison of j-V characteristic of CT2_0.5_750 before and after SOFC and SOE operation testing (captured under SOFC (a) and SOE (b) conditions)... 188

Figure 6-9: Nyquist and Bode impedance plots of CT2_0.5_750 before and after SOFC and SOE operation testing (captured under SOFC conditions). 189

Figure 6-10: Nyquist and Bode impedance plots of CT2_0.5_750 before and after SOFC and SOE operation testing (captured under SOE conditions). 191

Figure 6-11: Voltage evolution characteristics of CT2_0.5_700 tested at 700°C and ±0.5 A/cm^2 current density. 193

Figure 6-12: Comparison of j-V characteristic of CT2_0.5_700 before and after SOFC operation testing (captured under SOFC and SOE conditions). 194

Figure 6-13: Nyquist and Bode impedance plots of CT2_0.5_700 before and after SOFC and SOE operation testing (captured under SOFC conditions). 195

Figure 6-14: Nyquist and Bode impedance plots of CT2_0.5_700 before and after SOFC and SOE operation testing (captured under SOE conditions). 196

Figure 7-1: Characteristic changes in open circuit voltage and voltage under polarisation, relative to rSOC cycle number. 198

Figure 7-2: j-V Comparison of cell types 1 and 2 at temperatures of 750°C and 700°C (captured under SOFC conditions). 202

Figure 7-3: j-V Comparison of cell types 1 and 2 at temperatures of 750°C and 700°C (captured under SOE conditions). 202

Figure 7-4: ASR comparison of cell types 1 and 2 at 700°C and 750°C (captured under SOFC and SOE conditions) 203

Figure 7-5:Nyquist comparison of cell types 1 and 2 at temperatures of 750°C and 700°C (captured under SOFC conditions). 205

Figure 7-6: Bode comparison of cell types 1 and 2 at temperatures of 750°C and 700°C (captured under SOFC conditions). 206

Figure 7-7: Nyquist comparison of cell types 1 and 2 at temperatures of 750°C and 700°C (captured under SOE conditions). 206

Figure 7-8: Bode comparison of cell types 1 and 2 at temperatures of 750°C and 700°C (captured under SOE conditions). 207

Figure 7-9: j-V comparison of cell types 1 and 2 at current densities of 0.5 A/cm^2 and 0.7 A/cm^2 (captured under SOFC conditions) 210

Figure 7-10: j-V Comparison of cell types 1 and 2 at current densities of 0.5 A/cm^2 and 0.7 A/cm^2 (captured under SOE conditions) 210

Figure 7-11: ASR comparison of cell types 1 and 2 at 0.5 A/cm^2 and 0.7 A/cm^2 (captured under SOFC and SOE conditions) 212

Figure 7-12: Nyquist comparison of cell types 1 and 2 at current densities of 0.5 A/cm2 and 0.7 A/cm2 (captured under SOFC conditions) 213

Figure 7-13: Bode comparison of cell types 1 and 2 at current densities of 0.5 A/cm^2 and 0.7 A/cm^2 (captured under SOFC conditions) 213

Figure 7-14: Nyquist comparison of cell types 1 and 2 at current densities of 0.5 A/cm2 and 0.7 A/cm2 (captured under SOE conditions) 214

Figure 7-15: Bode comparison of cell types 1 and 2 at current densities of 0.5 A/cm^2 and 0.7 A/cm^2 (captured under SOE conditions) 214

Figure 7-16: j-V comparison of cell type 1 at different current densities (captured under SOFC conditions) 215

Figure 7-17: j-V comparison of cell type 1 at different current densities (captured under SOE conditions) 216

Figure 7-18: ASR comparison of cell types 1 and 2 at 750^{o}C and 700^{o}C (captured under SOFC and SOE conditions) 217

Figure 7-19: Nyquist comparison of cell type 1 at different current densities (captured under SOFC conditions) 219

Figure 7-20: Bode comparison of cell type 1 at different current densities (captured under SOFC conditions) 219

Figure 7-21: Nyquist comparison of cell type 1 at different current densities (captured under SOE conditions) 220

Figure 7-22: Bode comparison of cell type 1 at different current densities (captured under SOE conditions) 220

Figure 7-23: Time to establish steady state SOFC OCV after SOE operation 223

Figure 7-24: Time to establish steady state SOE OCV after SOFC operation 223

Figure 7-25: Effect of switching time from SOE operation to SOFC operation on SOFC voltages..... 224

Figure 7-26: No discernible effect of switching time on voltage drop and voltage recovery during SOFC operation..... 227

1 INTRODUCTION

1.1 Background

Over the last few decades, environmental concerns have led to a groundswell of popular opposition to the widespread use of fossil fuels as energy sources. The European Commission (EC), in 2009, set the goal of reducing Green-House Gas (GHG) emissions by 80-95% relative to 1990 emissions by 2050 [1]. To provide a fact-base for the EU emission targets, the European Climate Foundation (ECF) launched the 'Energy Roadmap 2050' project [2] to chart the pathways to a prosperous, low-carbon Europe. The final report discussed the feasibility and challenges of achieving a GHG reduction of at least 80% for the whole of Europe, "while maintaining or improving *present* levels of electricity supply reliability, energy security, economic growth and prosperity". Specifically, the Energy Roadmap 2050 final report, as a minimum, mandates the increased penetration of renewables into the European energy mix if an 80% GHG reduction objective is to be realised (*Figure 1-1*). It requires a 97% share for renewables in the electricity market, and at least a 75% share for renewables in the gross final energy supply by 2050. According to this energy policy recommendation, as seen in *Figure 1-1*, by 2050, the proportion of liquid fossil fuels (in particular) in the energy mix needs to decrease significantly. Liquid fossil fuels will then account for approximately only 15%, compared to the 2005 benchmark of approximately 40%. This is hugely ambitious since the transportation industry presently relies almost exclusively on liquid fossil fuels. A technology is therefore required, which could, as a minimum; economically convert any excess electricity generated by some of the renewable energy sources into transport fuel, i.e., a fuel shift from fossils (oil and gas) to power. The EU's goals for such a technology can be categorised broadly as follows [3]:

1. Integrate the different energy grids and infrastructures (electrical, natural gas, transport fuel) by converting electricity to gas and/or liquid fuels and vice versa;
2. Decarbonise power generation and transportation fuels by reducing reliance on fossil fuels;
3. Efficiently store electrical energy from renewable sources.

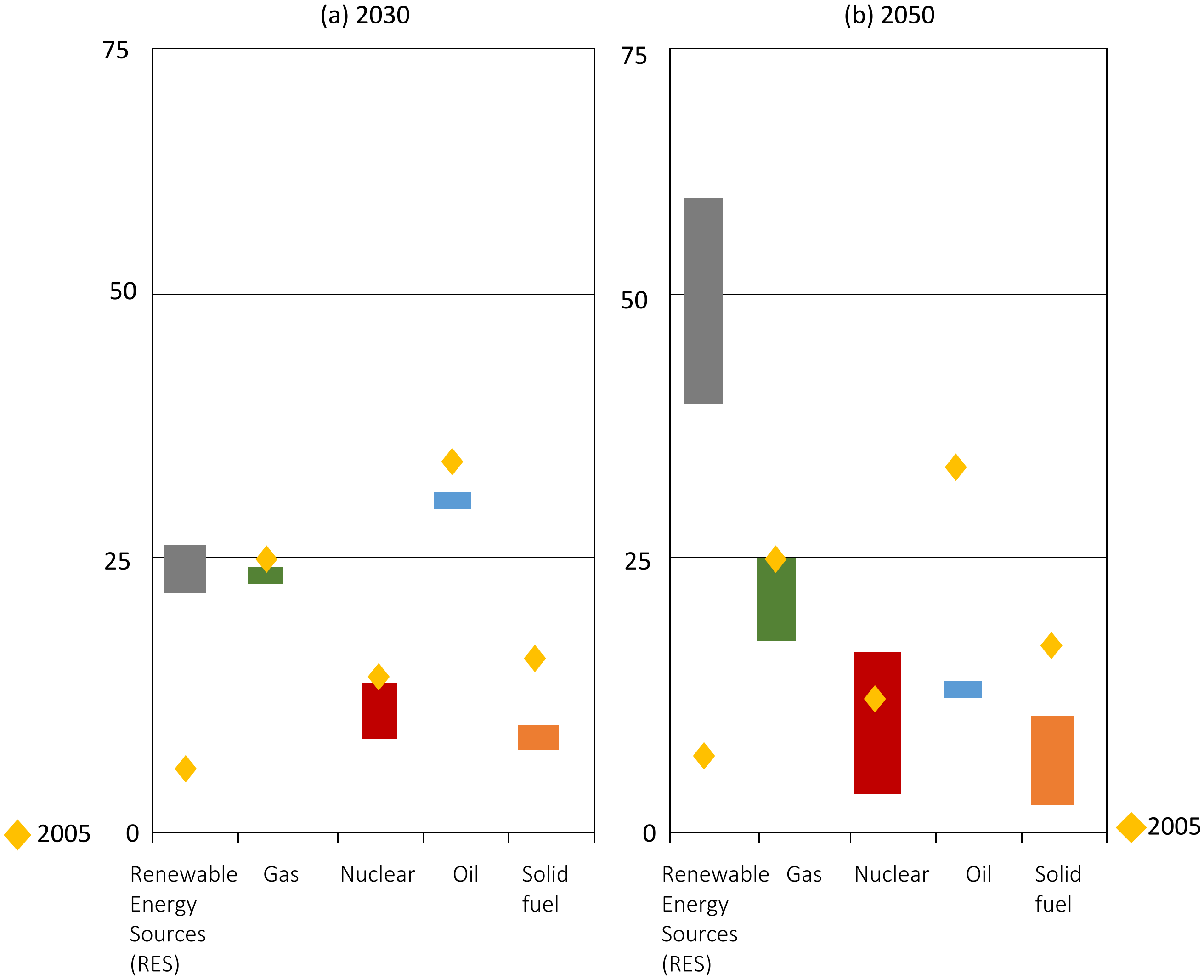

Figure 1-1: Projection of energy sources market shares for 2030 and 2050 against a 2005 benchmark *[2]*.

On the world stage, in December 2015 world leaders signed the COP21 Paris Agreement [4] aimed at limiting perceived climate change by phasing out, and in some cases immediately eliminating, greenhouse gas producers from the energy landscape. Phasing out, and ultimately eliminating, GHG emitting energy sources requires their replacement with low- to no-GHG energy technologies as illustrated by the EU Energy Roadmap 2050 initiative [2]. The Paris agreement thus promulgates a commitment on the part of world governments to prioritise and tackle issues related to low-carbon energy technologies. Significant political-will is thus on the side of green energy sources with the attendant increased focus on solving the teething problems which made industrial scale production of renewable fuel/power uneconomic and uncompetitive relative to fossil fuels.

To this effect, and in response to the EU's goals as detailed in the Energy Roadmap 2050 [2] initiative as well as the EU's commitments under the COP21 agreement [4], the European Commission Directorate-General for Energy (DG-ENER), under the auspices of the EU H2020 programme, launched the BALANCE project [3] in December 2016. The stated aim of the BALANCE project was "increasing [*the broad]* penetration of renewable power [*and]* alternative fuels, [*as well as improving]* grid flexibility by [*harnessing]* cross-vector electrochemical processes". The participants in the BALANCE project were VTT (Finland), CEA (France), DTU (Denmark), ENEA (Italy), TU Delft (The Netherlands), EPFL (Switzerland), IEn (Poland), and University of Birmingham (UK). Each of these participants is a leading research centre in an aspect of SOFC and/or hydrogen technology. The project therefore brings them together to collaborate and thus accelerate the development of a highly promising green energy technology. The vision for this effort is that synergies would be created, and significant breakthroughs realised by pooling together the resources of these leaders in SOFC and hydrogen technologies, to focus on developing this highly promising technology.

The BALANCE project specifically focused on accelerating the development of a presently low-TRL European rSOC technology into a sufficiently mature technology (~TRL 6). rSOC is a high temperature electrolysis-based technology [5] that is characterised by very high efficiencies relative to other competing electrolyser technologies. The BALANCE project would develop the next generation of rSOC cells, optimise cell-integration into stack assemblies, and investigate constraints on reversible operation at system level and upon integration with the energy grid. The reversibility concept is addressed in Section 1.1.4 of this thesis. The cost of the technology would be addressed by investigating the use of readily available, inexpensive materials whilst improving manufacturability.

Representative computer models and simulations would support all the experimental work conducted under the auspices of the BALANCE project. Techno-economic analyses of varied integration strategies of the rSOC technology in various industrial applications would also be performed to provide industry and other stakeholders with clear cost-benefit bases for adopting and/or promoting the technology.

A more detailed overview of the BALANCE project, including the project achievements, is presented in Chapter 2.

1.1.1 Traditional Energy Landscape

Fossil fuels dominate the existing European energy mix (and more broadly, the world's energy system). Hydrocarbons from fossil sources such as crude oil, coal and natural gas traditionally comprise more than 95% of European energy supply [1], [2]. This significant reliance on energy sources deemed harmful to the environment is clearly unsustainable, especially in an age of acute environmental concerns and increasing awareness. Europe's electrical grids, energy for heating, and transport fuels must be significantly decarbonised if Europe is to meet its climate change commitments and energy policy goals. In addition, Europe depends quite heavily on fuel imports from other regions. Aside from the economic vulnerabilities that come with the dependence on imported fuels, there are also questions regarding security. Not the least of these security concerns is with 'security of supply' since most of the world's fossilised hydrocarbon deposits also happen to be in the world's most politically unstable regions [6].

1.1.2 Renewable Power, Alternative Fuels and Electrochemistry

Broad penetration of renewable power and alternative fuels into the European energy matrix is required if Europe is to meet its COP21 commitments and energy policy goals. The European Commission (Directorate-General for Energy, DG Ener) has detailed several research themes [1] that would enable the cost-effective and broad penetration of renewable power and alternative fuels into the energy system. These themes relate to energy storage, grid integration/balancing, and decarbonisation.

Undoubtedly, a lot of work has been done and more is being done to diversify our energy sources, power generators and the energy flexibility/facility of our end-use appliances. This growing diversity of energy technologies however makes the integration of the energy system increasingly challenging. Nevertheless, integration of the diversifying energy system is required in order to significantly decarbonise the energy system, promote efficiency, and maintain a safe and reliable infrastructure [1]. Integration of the energy system will affect primary energy use, grid flexibility, equity, free trade and circulation, land use and ultimately the environment [2]. The challenges inherent in energy integration are even more pronounced in Europe due to the density of localised populations, high living standards, diverse cultures, ingrained habits and geographically biased/based traditional infrastructure [2]. Therefore, as a minimum, the integrating technology(ies) must be clean, efficient, reliable and negligibly disruptive so as not to impair the social habitat or the end-user's standard of living.

In effect, cost-effective technologies are required which can:

1. efficiently store excess electrical energy from renewable power sources;
2. serve as a link to integrate and/or promote cross-vectoring of the electrical and (natural) gas (for heating) energy grids, with transport fuel infrastructure, as well as balance the electricity grid;
3. decarbonise the power sector, heat and mobility / transportation fuels.

Technological innovations that would wholly address the above three challenges, and which are cost-competitive should naturally have precedence relative to competing technologies that would address only one or even two of these challenges.

The technology presented in this thesis addresses all three challenges. The subject technology of this thesis, rSOC, uses electrochemistry to integrate the electricity and gas grids, and commodity energy markets by transforming them into value-adding cross-vectors. This is because, as explained in Section 1.1.4, the technology is also able to utilise CO_2, a waste product of various ‘polluting industries’ such as hydrocarbon oil and gas refining, fossil fuel power generation, etc, but also a component of biogas or a product of biomass combustion, as a commodity to produce syngas, a valuable intermediate resource as detailed in Section 1.1.3.

A significant number of very important industrial processes are already based on electrochemistry [7], [8]. Industrial processes such as production and purification of metals, production of inorganic compounds (chlorine, sodium hydroxide, fluorine, etc.), electroplating, electrocoating and electroforming are all fundamentally driven by electrochemistry. Reversible solid oxide cells are unique in that the same device operates back and forth, as explained in Section 1.1.4, to electrochemically convert power to fuel and fuel to power, as required. This makes the concept extremely flexible: having significant potential not only to serve as an agent to integrate the energy system but also very useful as a power buffer or a grid balancing system. rSOCs offer the possibility to store excess renewable power in highly flexible commodities such as hydrogen, syngas (H_2+CO), and/or even methane. In a future energy system with a high proportion of fluctuating electricity generators (wind, solar, etc.), rSOC will complementarily support the growth of the renewable energy market.

1.1.3 Electrolysis

Electrolysis is an electrochemical process whereby electrical current is used to drive a chemical splitting reaction. Different types of electrolysis exist, and some are utilised industrially, ranging from the production of sodium hydroxide and chlorine in the chloralkali process to the production of aluminium [7]. This thesis focuses primarily on the electrolysis of water.

Electrolysis has lent itself as one way of synthesising and storing renewable energy in the form of a fuel gas (e.g. it is essential in the production of high purity hydrogen). However, the process is not very efficient, losing about 30 to 40% of the energy in the process, and is thus not economically competitive at present, when compared with pyrolysis or even reforming of hydrocarbons. Nevertheless, high temperature electrolysis promises higher efficiencies due to the endothermic nature of the reactions at the temperatures of interest. As an example, although 'electrolysis' at approximately 2500^oC is presently impractical mainly as a result of material limitations; at such temperatures, electrical input is unnecessary since water breaks down into oxygen and hydrogen by thermolysis. The temperature range of interest in this study will be 700^oC to 850^oC, as this is also the conventional operating temperature range of solid oxide fuel cells. Theoretically, the rSOC device allows the electrochemical conversion of electrical energy into fuel gas (electrolysis mode, SOE) and the reversible conversion of fuel gas into electrical energy (fuel cell mode, SOFC). Similar device architecture may be employed in the co-electrolysis of H_2O + CO_2 mixtures. Successful co-electrolysis, at the SOFC temperature range, is expected to produce syngas ($CO+H_2$), a valuable intermediate resource for producing several chemicals, e.g., CH_3OH, plastics, synthetic natural gas (CH_4), or synthetic petroleum, amongst others.

1.1.3.1 Competing Electrolysis Techniques

The two main electrolysis techniques competing with the rSOC technique are Alkaline Electrolysis (AE) and Proton Exchange Membrane Electrolysis (PEME). Both competitors are low temperature (~90^oC) technologies, are relatively well established, significantly optimised, and are employed on an industrial scale. These competing technologies however present various drawbacks, which the rSOC technology potentially eliminates. Examples of such drawbacks of AE and PEME processes are:

1. relatively high voltages (high over-voltages) are required to produce hydrogen due to the low operating temperatures (and thus requiring higher electrical input to meet activation energy demand) of both AE and PEME - resulting in lower efficiencies (see *Figure 1-2*);
2. they mainly require expensive metal catalysts (high CAPEX) in order to increase exchange currents (also as a result of the low operating temperature); and
3. they are not inherently reversible cells since they require different catalysts in fuel cell and electrolyser modes. For instance, in the case of PEM fuel cells platinum (Pt) is used on both electrodes, whilst in the case of PEM water electrolysis Pt is used as the fuel catalyst and Iridium (Ir), Iridium/Ruthenium (Ir/Ru) or their oxides are the materials of choice on the air side. Note: although reversible PEM concepts have been proposed and designed, overcoming the difficulties presented due to operation in fuel cell and electrolyser modes is much more complex resulting in typically low energy storage cycle efficiencies. This largely limits their research exclusively to niche sectors such as for military and space applications [9].

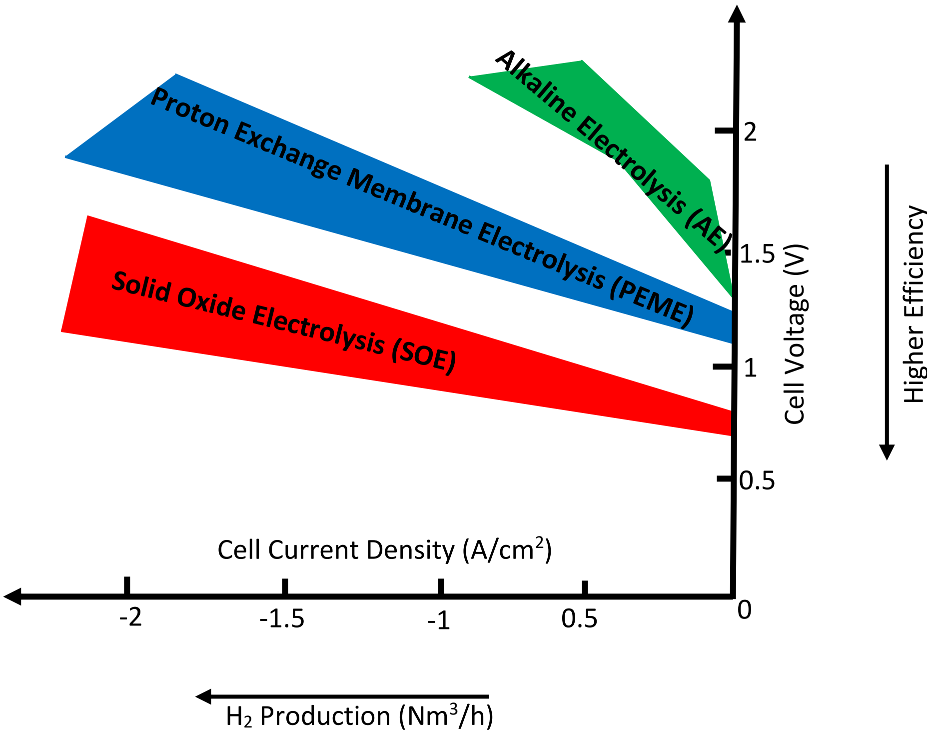

Figure 1-2: Comparison of typical range of AE, PEME and SOE performances. Reproduced based on *[10]*.

1.1.3.2 High Temperature Electrolysis

High-temperature electrolysis, specifically via rSOCs, is of great interest as a key enabling technology in a sustainable renewable energy economy because of:

1. relative simplicity in system design;
2. leveraging of the significant research into SOFCs;
3. potentially high energy conversion efficiency due to decreased resistances across the cell as a result of higher reaction kinetics (also see *Figure 1-3*);
4. potential to generate significant quantities of clean hydrogen at lower current densities relative to low temperature electrolysis;

5. facility to utilise potentially available waste heat from other sources such as from power stations or nuclear energy facilities to further boost efficiency;
6. facility to also split CO_2 into CO and O_2; and as mentioned before,
7. potential facility to integrate renewable electricity into the future energy landscape.

The theoretically high efficiency of high temperature electrolysis mainly stems from two contributory factors. The increased electrode catalytic activity at high temperatures (i.e. high electrode reaction kinetics leading to low activation over-potentials) and the thermodynamics of water decomposition. The overall enthalpy change (ΔH) of water decomposition remains relatively constant with increasing temperature, showing only a slight increase, *Figure 1-3*. However, the entropy changes significantly with increasing temperature in line with the second and third laws of thermodynamics. Therefore, in accordance with Equation 1-1, the Gibbs free energy change, ΔG, decreases with increasing temperature, *Figure 1-3*). This change in Gibbs free energy implies that the magnitude of any external energy (electric energy in the case of electrolysis) required to carry out a defined amount of work also decreases. Thus, the efficiency of high temperature electrolysis can theoretically be more than 100% if waste heat (from solar concentrators or generation IV nuclear reactors) is used.

$$\boldsymbol{\Delta G = \Delta H - T\Delta S} \qquad \boldsymbol{Equation\ 1-1}$$

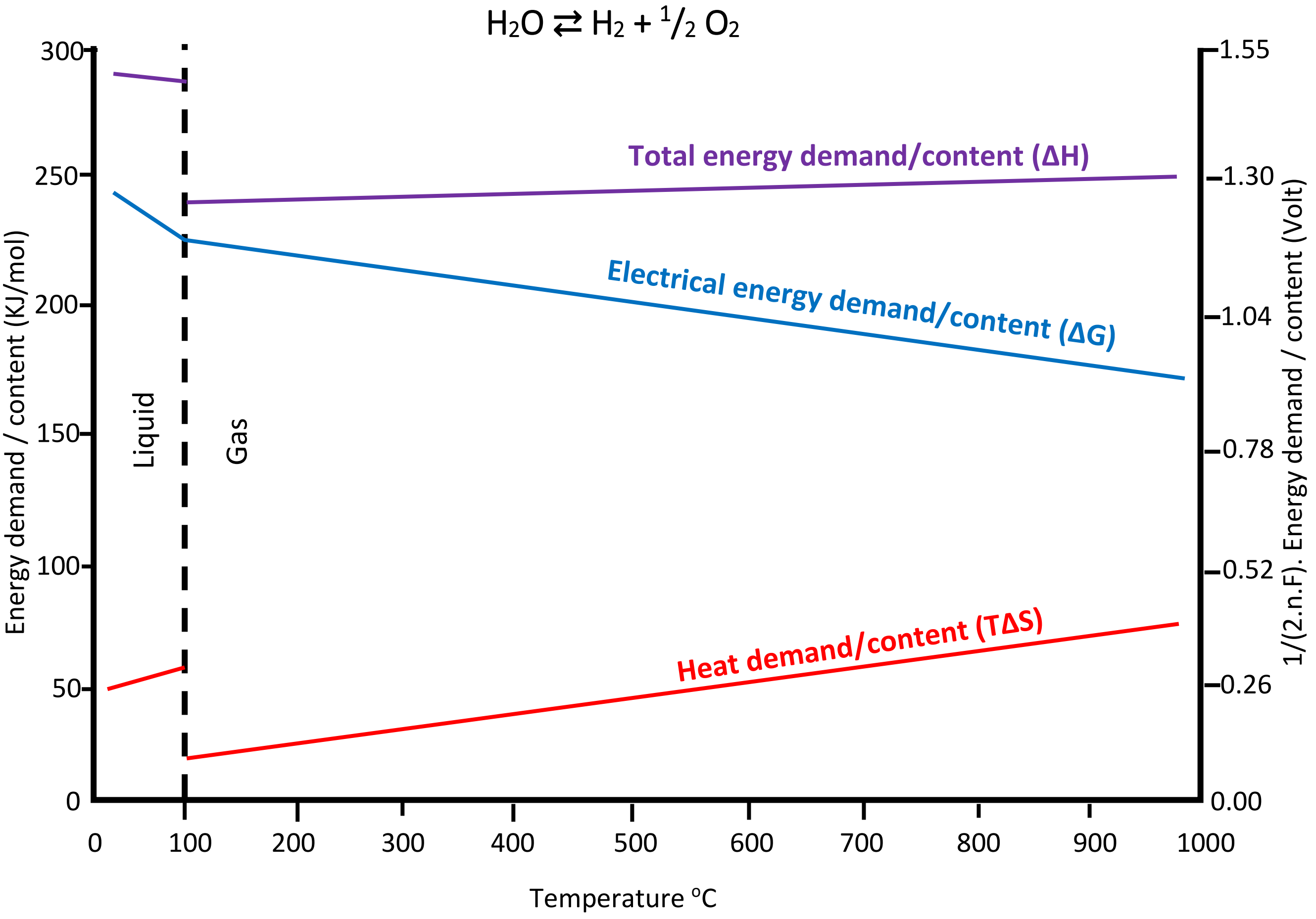

Figure 1-3: Thermodynamic parameters for electrolysis ($H_2O \rightarrow H_2 + {}^1/_2O_2$), 'energy demand' and fuel cell ($H_2 + {}^1/_2O_2 \rightarrow H_2O$), 'energy content' at atmospheric pressure. Reproduced based on *[5]*.

In accordance with Figure 1-3, a high temperature electrolysis system may be operated under three distinct thermodynamic regimes: endothermal, exothermal, and thermoneutral. The endothermal operating mode, with the supply of 'waste heat' to the system as explained above, results in an electricity-to-hydrogen conversion efficiency above 100% [10] [11]. In this mode, the heat contribution, TΔS, required for water splitting is greater than the enthalpy of reaction and therefore external heat must be supplied to maintain the temperature, resulting in a cell voltage less than that required for thermal equilibrium. This mode thus requires the least electric energy input. On the other hand, in exothermal operation, the electric energy input, ΔG, for water splitting exceeds the enthalpy of reaction and the electricity-to-hydrogen conversion efficiency is less than 100%. In this mode, the cell voltage is above that required for thermal equilibrium. When the electric energy input is equal to the enthalpy of reaction, the system operates at its thermal equilibrium, i.e. thermoneutral mode. In this mode, the temperature of the products is equal to that of the reactants since the heat contribution, $T\Delta S$, required for splitting the reactants is equal to the heat generated by the loss reactions in the cell, and 100% electricity-to-hydrogen conversion efficiency is attained [10].

Although different types of cell configurations have been proposed and designed, planar cells presently offer the highest efficiencies. Therefore, even though design concepts combining planar and tubular features may offer better efficiencies in the future [12], [13], planar cells will be used in this project.

1.1.4 Basic Electrochemical Principles of Operation for rSOCs

1.1.4.1 Outline

This subsection introduces rSOC key themes and describes the technology. The objective is to give a basis for an understanding of the subjects presented in the following chapters of this thesis. It begins with a brief description of the electrochemical principles of SOFC and SOE, and then focuses on the requirements and state of the art of rSOCs.

1.1.4.2 Solid Oxide Fuel Cells

Fuel cells efficiently convert chemical energy directly to electrical energy with minimal production of pollutants. This is because combustion of the reactants does not occur, and the process is solely electrochemical. SOFCs utilise a solid oxide ionic conductor operating at relatively high temperatures (500°C – 900°C) for this chemical to electrical energy conversion.

SOFCs have three main components: an electrolyte and two electrodes (an anode or fuel electrode, and a cathode or air electrode), as shown in *Figure 1-4* .

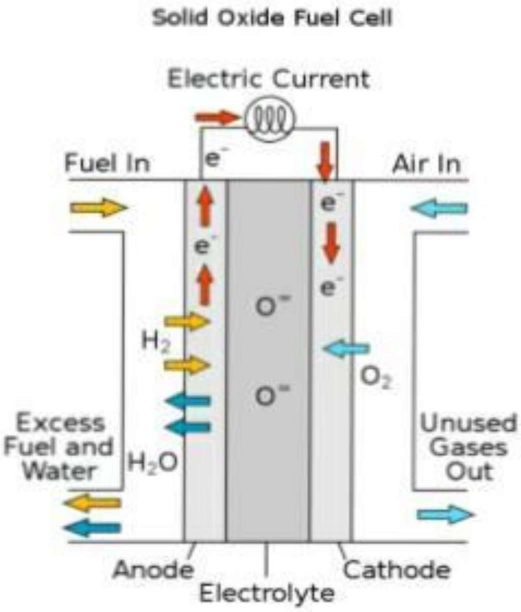

Figure 1-4: Depiction of solid oxide fuel cell electrochemistry (Credit: WikiCommons).

The electrolyte is a solid oxide, hence the technology or device's name. The solid oxide electrolyte is traditionally an oxygen ion conductor that is electronically insulating and gas tight. The cathode and anode, also known as the air electrode and fuel electrode, respectively, are electronically conductive and porous to gas. The designation of cathode and anode is dependent on whether electrons are entering or leaving the electrode. The electrodes perform the reverse function in electrolytic cells, i.e. an electrolysis cell anode is a fuel cell cathode as the electrons are moving in the opposite direction. A cathode may thus be defined as the electrode where electrons enter the cell and reduction occurs, and an anode as the electrode where electrons leave the cell and oxidation occurs. To avoid confusion in the rest of this thesis since it deals with aspects of both fuel cells and electrolyser cells, the electrodes will be identified as hydrogen/fuel electrodes and oxygen/air electrodes.

The fuel (hydrogen, light hydrocarbons such as methane or externally reformed heavy hydrocarbons), enters the fuel cell at the fuel electrode, where it is oxidised by oxygen ions from the air electrode [Equation 1-2]. The oxygen ions are produced by the reduction of oxygen (from air) [Equation 1-3] at the air electrode and travel through the solid electrolyte to the fuel electrode. The fuel oxidation at the fuel electrode produces two (2) electrons (for each molecule of fuel reacted), as well as H_2O [Equations 1-2 and 1-4] and heat. The electrons, which are the primary electric charge carriers, travel around the external circuit where they can do work. The process then repeats as the electrons continue to the air electrode for the reduction of oxygen [Equation 1-3], etc.

Hydrogen electrode half–cell reaction:

$$\boldsymbol{H_2 + O^{2-} \rightarrow H_2O + 2e^-} \qquad \boldsymbol{Equation\ 1-2}$$

Oxygen electrode half–cell reaction:

$$\boldsymbol{\frac{1}{2}O_2 + 2e^- \rightarrow O^{2-}} \qquad \boldsymbol{Equation\ 1-3}$$

Full cell reaction:

$$\boldsymbol{H_2 + \frac{1}{2}O_2 \rightarrow H_2O} \qquad \boldsymbol{Equation\ 1-4}$$

Commercial-scale SOFC stacks are available, such as the Japanese “Ene-Farm” home-use fuel cell [14], and the technology is fairly established. Current SOFC technical research is mainly focused on component and/or system design optimisation to improve lifetime durability, and manufacturability to further improve the efficiency, and render the technology cost-effective and more economical relative to competing technologies.

1.1.4.3 Solid Oxide Electrolysis

Solid oxide electrolysis is the electrochemical reverse of solid oxide fuel cells, *Figure 1-5*. It converts electrical energy into chemical energy by splitting the polarised molecules of H_2O into their constituent ions. The chemical energy is stored in the form of hydrogen (in the case of water electrolysis), or syngas (H_2+CO) / light hydrocarbon compounds such as methane (in the case of H_2O+CO_2 co-electrolysis). SOE seeks to utilise the high-temperature operation of SOFCs running in reverse mode to achieve this synthesis of chemical energy. Since the electrochemical principles of solid oxide electrolysis are typically solid oxide fuel cells operating in reverse mode, the electrons must be forced to the negative electrode, i.e. the hydrogen electrode, by the application of an external voltage. In electrolysis mode, the "fuel" (water), contacts the electrons on the hydrogen electrode, where it dissociates into hydrogen and oxygen ions [Equation 1-6]. The oxygen ions travel through the electrolyte to the oxygen electrode where they combine to form a molecule of oxygen with the release of two electrons [Equation 1-5]. The electrons travel around the external circuit to the hydrogen electrode where they combine with two hydrogen ions to form a molecule of hydrogen [Equation 1-6], which is the desired chemical energy product. The full cell reaction is given by [Equation 1-7]. The pure oxygen produced at the air electrode may also be harvested for various uses, such as in catalytic partial oxidation reactors, for the gasification of biomass or in the medical industry.

Oxygen electrode half–cell reaction:

$$\boldsymbol{O^{2-} \rightarrow {}^{1}/_{2}\, O_2 + 2e^-} \qquad \boldsymbol{Equation\ 1-5}$$

Hydrogen electrode half–cell reaction:

$$H_2O + 2e^- \rightarrow O^{2-} + H_2 \qquad Equation\ 1-6$$

Full cell reaction:

$$H_2O \rightarrow H_2 + {}^1/_2\, O_2 \qquad Equation\ 1-7$$

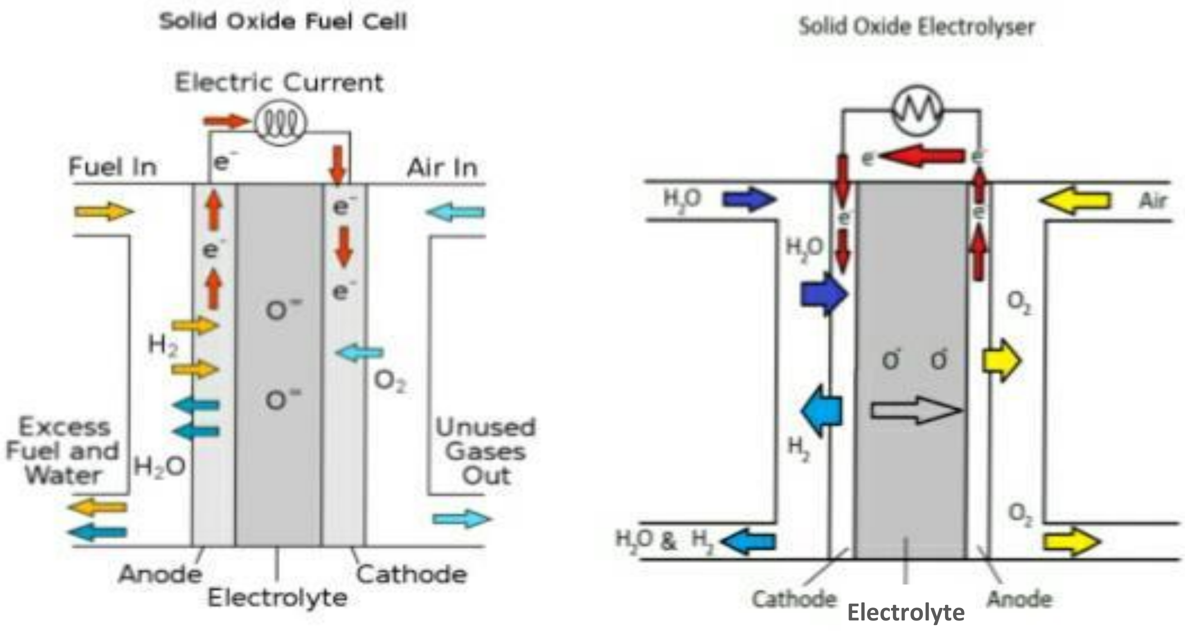

Figure 1-5: Depiction of electrolysis using a solid oxide fuel cell showing the electrochemical reversibility (Credit: WikiCommons).

This reverse operation of SOFC technology to synthesise and store chemical energy using electrical energy is very attractive primarily due to the peak-and-trough or cyclical nature of electricity output from most renewable sources. As an example, solar panels only operate during the day. At night, power generation drops to nil. It is therefore very attractive to store any excess electricity generated during the day for use at night or during downtimes. Solid oxide electrolysis would thus be used to convert (and store) any excess electrical energy from renewable sources into (and in the form of) chemical energy, to be converted back to electrical energy via even the same device when required. This chemical energy product also lends itself for use as a transport fuel, energy for heating, or as a commodity in various industrial processes [15].

Single cell and multi-cell stack SOEs have been operated to produce hydrogen or syngas from the electrolysis of H_2O or H_2O+CO_2, respectively, under laboratory conditions. It has been acknowledged that significant research is required to demonstrate the industrial feasibility of the technology [16].

Similar SOE stacks have been subjected to long-term electrolysis and co-electrolysis conditions at similar current densities with total unit resistances (i.e. ASR) after electrolysis of ≤1 $Ohm.cm^2$. It was suggested that Ohmic resistance and mass transport losses contribute the most to performance degradation [18]. Details of these challenges are discussed in Section 1.5.4 and in Chapter 2.

Like SOFCs, where efforts are being directed towards using alternative fuels, in addition to the traditional hydrogen; the production of alternative fuels - especially liquid fuels - in addition to the traditional hydrogen, using electrolysis is receiving increased attention. The drive towards alternative liquid fuels is mainly a result of the more favourable facility of storage relative to hydrogen. The electrolysis of CO_2 to produce, in the first instance, carbon monoxide (CO) is a necessary step towards deriving these alternative fuels. In this aspect, although this thesis does not primarily address co-electrolysis of $CO_2 + H_2O_{(g)}$ to produce syngas (H_2 + CO) at ambient pressures and, quite possibly, methane (CH_4) directly at high pressures, it has been introduced as a possible allied benefit of the rSOC technology.

SOEs have been shown capable of CO_2 electrolysis [19], [20] and syngas (H_2+CO) production by co-electrolysis of H_2O+CO_2 at current densities similar to steam electrolysis [21], [22]. However, since the area specific resistance (ASR) for electrolysis of CO_2 is generally higher than that of H_2O [17], it has been hypothesised that in 'co-electrolysis', only the H_2O undergoes electrolysis and H_2 from the electrolysis of H_2O reacts with the CO_2 in a reverse water gas shift (endothermic reaction with ΔH = +40.4 kJ/mol), [Equation 1-8], to produce syngas (H_2+CO). The mechanism for the CO_2 reduction in 'co-electrolysis' is thus not well defined or determined [16].

$$\boldsymbol{CO + H_2O \underset{RWGS}{\overset{WGS}{\leftrightarrow}} H_2 + CO_2} \qquad \boldsymbol{Equation\ 1-8}$$

1.1.4.4 Reversible Solid Oxide Cell Technology

Reversible solid oxide cell technology, capable of seamless operation in both SOFC and SOE modes as presented in Sections 1.1.4.2 and 1.1.4.3, is clearly very attractive and highly desirable (also see Equation 1 - 9). The technology, whilst operating in SOE mode, seeks to reduce H_2O or H_2O + CO_2 using electricity to produce H_2 or syngas (H_2+CO). Syngas can be used as an intermediate resource in several applications, as mentioned in Section 1.1.3, and may be used as feed fuel for rSOCs in fuel cell mode to produce electricity. This versatility of the rSOC technology, serving as a power-to-gas or fuel (P2G), gas/fuel-to-power (G2P) or power-to-gas-to power (P2P) device, and several other permutations, makes it a key asset in any energy integration policy or green energy landscape [23].

$$\boldsymbol{H_2 + \frac{1}{2}O_2 \underset{\underset{SOE}{\longleftarrow}}{\overset{\overset{SOFC}{\longrightarrow}}{\leftrightarrow}} H_2O} \qquad \boldsymbol{Equation\ 1-9}$$

In conclusion, rSOCs, as envisaged, will utilise the setup of an SOFC operating in electrochemical reverse mode. This philosophy of operation has several significant advantages:

1. The end-product of water electrolysis is hydrogen, which is valuable in various industries;
2. The possible end-products of high temperature co-electrolysis (H_2O + CO_2 as feed) are all chemicals which could be used as fuel for heating, transportation, electricity generation, as fuel for SOFCs, or even as chemical raw materials (e.g. for plastics production). This introduces significant flexibility into the energy matrix by integrating or promoting crossovers in the electrical grid, heating and mobility fuel infrastructure, as well as with the chemical industry;
3. Co-electrolysis, which seeks to utilise CO_2 as a commodity, will result in a financially beneficial industry in the fight against climate change when compared to other excess CO_2 combating industries such as Carbon Capture and Storage (CCS);
4. The presently most widespread, largest scale, and possibly most promising renewable power sources (photo-voltaics and wind) fluctuate with regards to power output. Therefore, as they are generally characterised as peak and trough systems, high temperature electrolysis / co-electrolysis would serve as a bridging or balancing technology to convert any excess electrical energy produced during peak-times into fuels to be converted back to electrical energy during trough-times. As an example, coupling rSOC to a solar cell system would convert and store any excess electrical energy produced during the day for use at night. Moreover, the fuels produced could also be diverted into the gas and transport fuel networks;
5. The economics of a high temperature SOFC system that is also capable of seamless reversible operation in electrolyser mode are more favourable relative to stand-alone,

separate SOFC and SOE systems. The reversibility of the rSOC device thus improves its cost-effectiveness significantly since a single device would be providing two services. The two services provided by a single device also improve its annual utilisation rate, providing a further cost-effective benefit;

6. In the future renewable energy economy, several symbiotic dependencies exist with electrolysis and other systems. As an example, concepts combining electrolysis with biomass-based plants [12] exist where the oxygen produced in the SOE unit can be used for the gasification of biomass, and the feed-steam for the SOE can be generated in the gasification plant. In addition, SOE generates hydrogen that is required to convert all the carbon in the biomass to products such as methanol (MeOH), dimethyl ether (DME), biodiesel, and synthetic natural gas (SNG) [16];
7. There is also the potential for large-scale energy storage [5] since the possible end-products; hydrogen, synthetic methane and syngas, are potentially compatible with the existing natural gas infrastructure, and can also be stored in underground geological formations;
8. It may be possible that the reversibility of the device would slow down its performance degradation, as compared to a standalone SOE system, thus increasing the effective design life of the device. This would be the case if a significant percentage of cell degradation during electrolysis mode were recovered under fuel cell mode, and possibly vice versa. This possibility will be investigated in this thesis.

A minimum design/operating life of 40,000 hrs [24] [25] have been set for SOFCs primarily based on the long-term stability of the conductivity of the electrolyte and durability / reliability of BoP components on a stack or system level. rSOCs must therefore also meet this criterion as a minimum, in terms of the performance stability of the electrodes as well as the long-term stability of the conductivity of the electrolyte.

1.2 Problem Statement

Since rSOCs are operated at high temperatures, a significant advantage is that the electrode polarisation is typically small. Theoretically, the overall decomposition voltage due to Ohmic resistance plus concentration and electrode polarisations during SOE operation should also be low or similar to those for SOFCs. However, the SOE operation is usually SOFC components functioning in electrochemical reverse. These components are thus subjected to strong cyclical reducing and oxidising environments when undergoing reversible operation in SOFC and SOE modes at these high operating temperatures. Therefore, although SOFC and SOEs may be regarded as reversible electrochemical reactors, the lack of seamless reversibility in operation was identified in the 1990s [26]**.** Significant challenges regarding component stability, degradation and material selection remain.

rSOC single cells and multi-cell stacks have already been fabricated and their cyclic operation has been demonstrated. Although SOFC and SOE are regarded as reversible electrochemical reactors, the lack of seamless reversibility in operation is a significant challenge [26]. Unit cell and stack performance in SOE mode typically show higher degradation rates than those in SOFC mode [27]*.* The root causes for this difference are however not fully understood. It was shown more than two decades ago [26] that the magnitude of the polarisation of the cell electrodes was strongly dependent on the mode of operation. It was observed that, with YSZ electrolytes, the polarisation of Ni-YSZ (hydrogen/fuel electrode) and LSM (oxygen/air electrode) in SOFC mode were minimal but significant in SOE mode. Conversely, the polarisation of Pt (hydrogen/fuel electrode) and LSC (oxygen/air electrode) were minimal in SOE mode but significant in SOFC mode. This was an early indicator that although SOFC and SOE may be considered as reversible electrochemical reactors, given an identified set of materials of construction, the efficiency of operation in one mode may not be replicated in the reverse mode due to the different operating environments/conditions.

1.3 Research Hypotheses

The performance of an oxygen/air electrode, which is stable in SOFC mode, may deteriorate rapidly in SOE mode because of oxygen evolution at the electrode/electrolyte interface leading to delamination [27]. This mode of failure has been reported for oxygen electrodes which are primarily based on electronic conducting oxides (e.g., LSM) when they are not specifically designed to minimise oxygen pressure build-up at the electrode/electrolyte interface during operation. If the oxygen electrodes are based on mixed ionic electronic conducting (MIEC) oxides (e.g., LSCF), even with similar microstructures, electrode delamination may still occur but at significantly higher current densities. This is because the ionic conductivity of the MIECs extends the active sites over the entire mixed conductive oxide electrode/electrolyte interface (i.e. both internal and external interfaces). This leads to lower electrode over-voltages. Note that for the electronic conducting oxide electrodes, the reactions can only occur at the electrode/electrolyte interface (i.e. the triple phase boundary, TPB, where the electrolyte, electrode and gas are in contact), leading to high electrode over-voltages [28]*.* Therefore MIECs would be used in the present work.

The performance stability of rSOC electrodes is also very dependent on the microstructures of the electrodes. Irrespective of conductor type, whether electronic or ionic-electronic, oxygen electrode microstructures must be designed to prevent the build-up of oxygen pressure at the electrode/electrolyte interface in SOE mode. The microstructures of hydrogen/fuel electrodes must also be designed to promote water, carbon dioxide, hydrogen and carbon monoxide transport to and from the reaction sites [16]. Electrodes are therefore typically designed with high porosities, whilst ideally incorporating networks of the electrolyte material, to increase the total surface area of the TPB. It is expected that the use of electrodes with electrolyte material networks would increase cell performance/durability and decrease cell degradation relative to the traditional cell architectures.

1.4 Project Scope

The BALANCE project on which this thesis was based, on a unit cell level, sought to develop and test alternative electrode materials and different electrode architectures in order to improve the electrochemical performance and durability of rSOC cells relative to existing capacities. *Table 1-1* presents the project target conditions as against existing capacity. A key criterion was to attain optimum performance of the rSOC cells under operation at high current densities (≥1 A/cm^2) and relatively lower temperatures (≤ 750^{o}C). At the unit cell level, critical test parameters and material combinations influencing the electrochemical performance and the durability of the rSOC would be clearly delineated.

A more detailed overview, and the achievements, of the BALANCE project are presented in Chapter 2.

Table 1-1: Project unit cell target performance as against existing capacity.

Parameter	Existing Capacity	EU BALANCE Project Target
Cell ASR	0.2 Ω-cm^2, 800°C in SOE, 1 A/cm^2 0.15 Ω-cm^2, 800°C in SOFC mode	0.2 Ω-cm^2, 750°C in SOE, 1.25 A/cm^2 0.15 Ω-cm^2, 750°C in SOFC mode
Cell Degradation	~ 0.5% /1000 h, 800°C in SOE, 1 A/cm^2 0.5 %/1000 h, 800°C in SOFC mode	< 0.5% /1000 h, 750°C in SOE, 1.25 A/cm^2 < 0.5 %/1000 h, 750°C in SOFC mode

1.5 Project Objectives

The scope of this thesis sought to address the following objectives:

1. Design a high temperature rSOC test apparatus that accommodates reversible high temperature electrolysis and standalone SOFC/SOE operations;
2. Investigate the reversible operation performance of different unit cell architectures to aid in identifying any necessary unit cell prerequisites for optimum performance.
3. Investigate operating conditions (e.g. temperature, current density, cycling rate, switching time, fuel flow rates or fuel utilisation, etc) necessary to promote seamless and reversible operation of the experimental test-apparatus with minimal performance degradation, and identify possible mechanisms that counteract symmetrical and reversible operation of the system;
4. Investigate the possibility that the reversibility of the device would slow down its performance degradation, as compared to a standalone SOE system, thus increasing the effective design life of the device. This would be the case if a significant percentage of

cell degradation during electrolysis mode were recovered under fuel cell mode, and possibly vice versa;

5. Structural characterisation of the as-fabricated cells, and post-test analysis of the cell components to understand their electrochemical performance evolution.

1.6 Novelty Statement

This research work used next generation cell architectures designed specifically for rSOCs to investigate various process parameters as outlined in sections 1.2 to 1.5. This helped to accelerate the presently low TRL rSOC technology to a post TRL 5 technology by defining both steady state (such as temperature and current density) and transient (such as switching time) processes involved at the unit cell level (see Chapter 3, specifically 3.5, and the results and discussion chapters 5 to 8 for more details).

1.7 Thesis Outline

Chapter 2 of the thesis presents a general overview of the EU BALANCE project to help explain the genesis of some of the test variables adopted for the work as reported in Chapter 4. It would also aid better understanding of the subsequent results and discussions presented in the chapters 5 to 7 of this thesis.

Chapter 3 (Literature Review) deals specifically with only the elements addressed under the experimental sections of the work. The literature review thus covers:

1. material selection (unit cell design and materials of fabrication);
2. effects of cell operating temperature and current density;

3. comparative assessment of rSOC degradation rates under SOFC and SOC operation;
4. effects of fuel electrode reactant utilisation on performance and degradation;
5. effect of switching time on rSOC performance and degradation rates; and,
6. test apparatus design issues which impact operating efficiency (specifically any dependencies of rSOC performance efficiency on test apparatus orientation relative to reactant composition and chemical/physical characteristics).

Chapter 4 (Methodology) details the experimental approach and equipment employed for the project.

Chapter 5 presents the qualitative and quantitative results of Cell Type 1 tested at different temperatures, current densities, reactant flow rates and /or fuel utilisations.

Chapter 6 presents the qualitative and quantitative results of Cell Type 2 tested at different temperatures, current densities, reactant flow rates and /or fuel utilisations.

Chapter 7 discusses the highlights of the results presented in Chapters 5 and 6. It then focusses on comparing the performance of Cell Types 1 and 2, and seeks to delineate a link between cell architecture and the observed performance.

Chapter 8 summarises the work done and the main highlights and recommends areas requiring further work to enable a more comprehensive understanding of the technology.

2 OVERVIEW OF THE BALANCE PROJECT

2.1 Introduction

This chapter presents a general overview of the EU BALANCE project to aid better understanding of the subsequent results and discussions presented in the following chapters of this thesis. It would also help explain the genesis of some of the test variables adopted for the work.

2.2 Project Background and Purpose

The multifaceted and inter-related challenges of perceived climate change, as well as ensuring the competitiveness and security of energy supply, require a coordinated and robust response. The EUs reaction to these challenges, from an energy perspective, is the Strategic Energy Technology Plan, hereafter referred to as 'SET-PLAN'. The SET-PLAN is a far-reaching jigsaw of policy measures to reduce Europe's greenhouse gas emissions by 60-80% by 2050, whilst creating a competitive internal energy market, i.e., without sacrificing Europe's standard of living.

The SET-PLAN incorporates 13 themes and 10 key actions. The SET-PLAN themes and key actions are listed in *Table 2-1*.

The BALANCE project sought to address the SET-PLAN themes and key actions by investigating rSOC as a key enabling technology as illustrated in *Figure 2-1*.

Table 2-1: SET-PLAN themes and key actions (*[29]*).

No.	SET-PLAN Themes	SET-PLAN Key Actions
1	Engaging consumers	Performant renewable technologies integrated in the system
2	Smart technologies for consumers	Reduce costs of technologies

No.	SET-PLAN Themes	SET-PLAN Key Actions
3	Energy efficiency in buildings	New technologies & services for consumers
4	Energy efficiency in heating and cooling	Resilience and security of energy system
5	Energy efficiency in industry and services	New materials and technologies for buildings
6	Modernising the electricity grid	Energy efficiency for industry
7	Energy storage	Competitive in global battery sector (e-mobility)
8	System flexibility	Renewable fuels
9	Smart cities and communities	Carbon capture storage/use (CCS/U)
10	Development of renewables	Nuclear safety
11	Carbon capture storage/use (CCS/U)	
12	Nuclear energy	
13	Biofuels, fuel cells & hydrogen, alternative fuels	

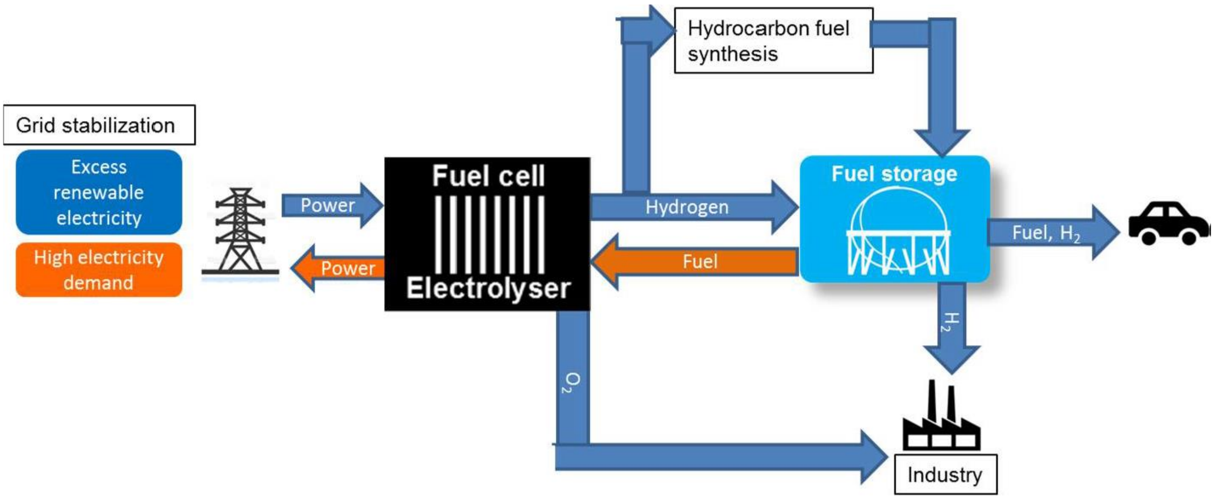

Figure 2-1: rSOC concept and its role as a key integrator of the different energy vectors, as investigated in the BALANCE project *[3]*.

The role of rSOC in a green energy economy, primarily addresses themes 7, 8 and 13 of the SET-PLAN and key actions 1, 2, 3, 4, 6 and 8 as given in *Table 2-1*.

The rSOC technology also provides a platform to promote the development and efficiency of other technologies that address the other SET-PLAN themes and key actions. For instance, waste heat from a nuclear plant could be utilised by an rSOC system to decrease the amount of electricity required to produce a unit of fuel, whilst an rSOC system can also utilise captured CO_2 (CCU) to be converted to syngas, methane and/or Fischer-Tropsch fuel.

The rSOC is therefore considered a key technology to enable the broad penetration of renewable electricity into the energy matrix, whilst also integrating the green energy landscape (electrical, natural gas and transport fuel grids). The BALANCE project aimed to accelerate the research and development of a low-TRL European rSOC technology into a sufficiently mature technology (~TRL 6) for later industry deployment qualification (TRL 7 to TRL 9).

2.3 Project Participants and Scope

The scope of the BALANCE project encompassed all the activities required to ascertain the state of rSOC in Europe. It involved experimental research to optimise all necessary facets of the technology, technology demonstration at system level including system modelling to quantify end-user synergies such as the production of aviation fuel, as well as project dissemination activities (technical and strategic knowledge transfer) to ensure parastatal agencies and private industry players were adequately informed for technology deployment decisions.

The BALANCE project would develop the next generation of rSOC cells, optimise cell-integration into stack assemblies, and investigate constraints on reversible operation at system level and upon integration with the energy grid (*Figure 2-1*. Techno-economic analyses of feasible integration strategies of the rSOC technology in various industrial applications were performed to provide industry and other stakeholders with clear cost-benefit bases for adopting and/or promoting the technology.

The overall scope of the BALANCE project comprised six (6) work packages and was delivered by eight (8) participants (see *Table 2-2*) over a 36-month project duration. The participants in the BALANCE project were CEA (France), DTU (Denmark), ENEA (Italy), EPFL (Switzerland), Institute of Energy (Poland), TU Delft (The Netherlands), University of Birmingham (UK) and VTT (Finland).

Table 2-2: BALANCE project work packages and participants.

WP No.	Work Package Description	Lead Participant	Package Participants
1	Project coordination and EU Agenda alignment	VTT	All
2	Integrated European Research Agenda for rSOC (Analysis of national activities, outcomes, barriers and gaps)	ENEA	All
3	Electrochemical process development	DTU	All
4	Modelling and rSOC System Verification	VTT	CEA, DTU, EPFL, IEn, TU D
5	Power-to-commodity-to-power systems	TU D	ENEA, EPFL, VTT
6	Knowledge management, communication and dissemination	CEA	All

Each work package consisted of several main tasks and deliverables. Work package 3, for instance consisted of 7 main tasks as follows:

1.1 Development of high performing and robust electrodes for stable rSOC;

1.2 Cell Integration and manufacturing;

1.3 Electrochemical characterisation of single cells in reversible mode;

1.4 Evaluation of steel grades and coatings for interconnects;

1.5 Stack design optimisation for reversible operation;

1.6 Manufacturing and characterisation of SRU/short stacks in reversible mode; and

1.7 Structural characterisation.

The subsequent sections of this chapter deal mainly with the BALANCE activities under task 3.3 (Electrochemical characterisation of single cells in reversible mode) since it is the task related to the main themes of this thesis. The chapter ends with the main conclusions from the overall BALANCE project.

2.4 Unit Cell Testing Activities

Unit cell testing activities under the BALANCE project were focussed on the electrochemical characterisation of single cells in rSOC mode.

2.4.1 Cell configurations and Test Protocol

Three different unit cell configurations as shown in *Figure 2-2* were subjected to the BALANCE unit cell test protocol detailed in *Table 2-3*.

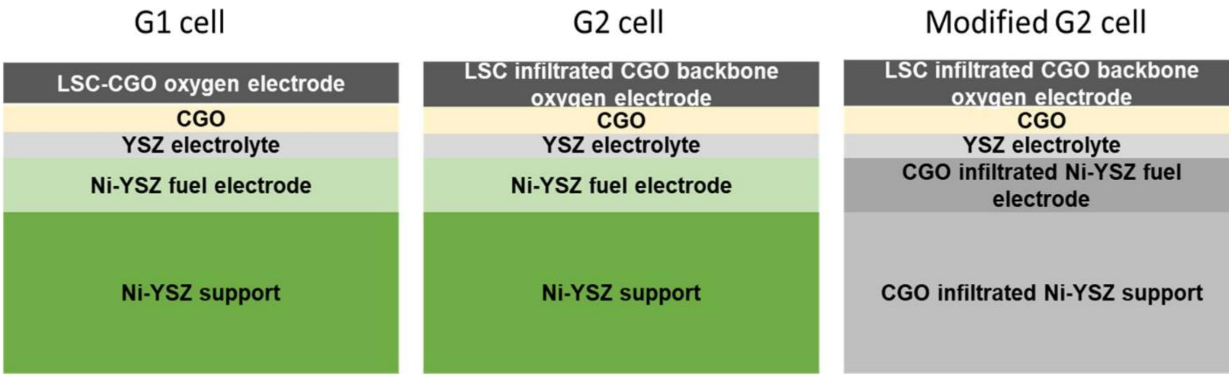

Figure 2-2: BALANCE generation 1 (G1), generation 2 (G2) and modified generation 2 (Modified G2) cell configurations.

As seen in *Figure 2-2*, the main difference between G1 and G2 cells was the oxygen electrode. G1 cells had a composite LSC-CGO oxygen electrode with a pure CGO barrier layer to mitigate deleterious reaction between the oxygen electrode material and the YSZ electrolyte forming an insulating layer of strontium zirconate. G2 cells had an LSC infiltrated CGO backbone oxygen electrode, also with a pure CGO barrier layer to mitigate deleterious reactions. The modified G2 cells also incorporated CGO infiltrants in the Ni-YSZ fuel electrode and the Ni-YSZ support.

These cells were subjected to the test matrix and protocol outlined in *Table 2-3*. The rationale for the selected profiles is given in Section 2.4.2.

Table 2-3: BALANCE unit cell test matrix for G1, G2 and Modified G2 Cells.

Test ID NOTE 1	Temp °C	SOE Current Density A/cm^2	SOFC Current Density A/cm^2	H_2 or H_2O Conversion NOTE 2	SOE/SOFC Period NOTE 3
A1	750	-0.5	+0.5	~50%	20/3
B1 & C1	700	-0.5	+0.5	~50%	20/3
A2	750	-0.75	+0.75	~50%	20/3

Test ID NOTE 1	Temp °C	SOE Current Density A/cm^2	SOFC Current Density A/cm^2	H_2 or H_2O Conversion NOTE 2	SOE/SOFC Period NOTE 3
B2 & C2	700	-1	+1	~50%	20/3
A3	750	-1	+1	~50%	20/3
B3 & C3	700	-1.25	+1.25	~50%	20/3
A4	700	-0.5	+0.5	~50%	20/3
B4 & C4	700	-0.5	+0.5	~75%	20/3
A5	750	-0.5	+0.5	~50%	8/3
B5 & C5	700	-0.5	+0.5	~50%	8/3
A6	750	-0.5	+0.5	~75%	20/3

1. Test IDs A, B and C refer to G1, G2 and Modified G2 cells, respectively, see *Figure 2-2*.
2. H_2 or H_2O conversion, also known as 'fuel utilisation' is a ratio of the molar flow of electrons over the molar flow of reactants (hydrogen atoms), also see Section 3.3.3.
3. The rationale for the reversible test protocols is explained in Section 2.4.2.

2.4.2 Rationale for Selected Test Periods / Profile

As shown in *Figure 2-1*, the rSOC technology is envisaged to play three key roles in a green energy economy. The concept is to couple the rSOC device to intermittent solar and wind power generators in order to provide grid stabilisation, energy/fuel storage and facilitate hydrocarbon fuel synthesis. Grid stabilisation would utilise both modes of operation (SOE/SOFC) of the rSOC device to provide electricity top-up during down-cycle periods of the solar/wind generators and convert any excess electricity to fuel during up-cycle periods of the solar/wind power generators. Energy/fuel storage would utilise SOE mode of operation to convert renewable electricity to fuel to be utilised later for electricity production or put to some other use. For hydrocarbon fuel synthesis, the device would be coupled to a methanation set-up or Fischer-Tropsch reactor to further process the raw gas produced by the rSOC system.

Therefore, due to the drive to decarbonise transportation fuels, the production of green fuels is likely the more important of the rSOC operating modes, since other technologies with possibly higher efficiencies may be available for electricity generation/production. Also, the intermittent solar power generators are on the average limited to approximately 8 hours for electricity generation (sunlight hours). Whilst, theoretically, wind power generators may produce electricity for 24 hours a day, practically, they are limited to about 20 hours a day on average [30] due to factors such as wind speed limitations (too little or too much wind) and shutdowns for maintenance/repairs or due to failure inspections/breakdowns.

The BALANCE project thus chose 20 hours SOE followed by 3 hours SOFC, and 8 hours SOE followed by 3 hours SOFC test periods as the most useful rSOC operation scenarios. These test periods also serve to subject the rSOC device to the most conservative test regimes since the literature suggests that degradation rates during SOE operation are significantly higher than degradation rates during SOFC operation [27].

2.4.3 Selection of Unit Cell Test Results and Discussion

A selection of the single test results based on the test matrices outlined in *Table 2-3* are presented in this section.

Figure *2-3* shows comparable OCVs (1143 - 1200 mV in SOFC mode and 890 - 910 mV in SOE mode) for the G1 cells tested at three different participating laboratories. The j-V curves were captured prior to subjecting the cells to the test protocol, and thus represent the initial condition of the G1 cells. The calculated initial ASRs (gradient of the linear region of the j-V curves) of the G1 cells was 0.41 Ω.cm^2 for SOFC mode and 0.3 Ω.cm^2 for SOE mode.

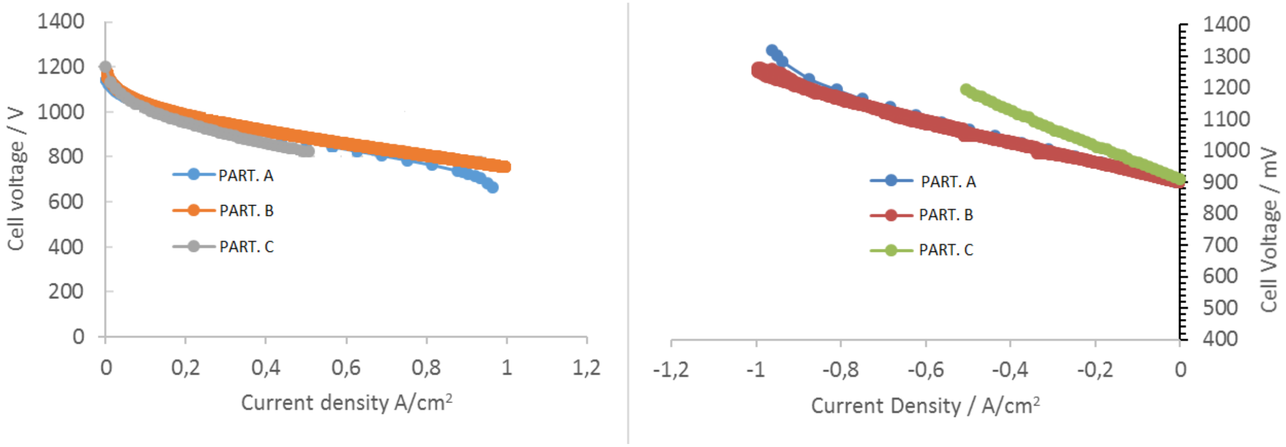

Figure 2-3: Initial j-V curve comparisons of G1 cells tested at three different participating Labs.

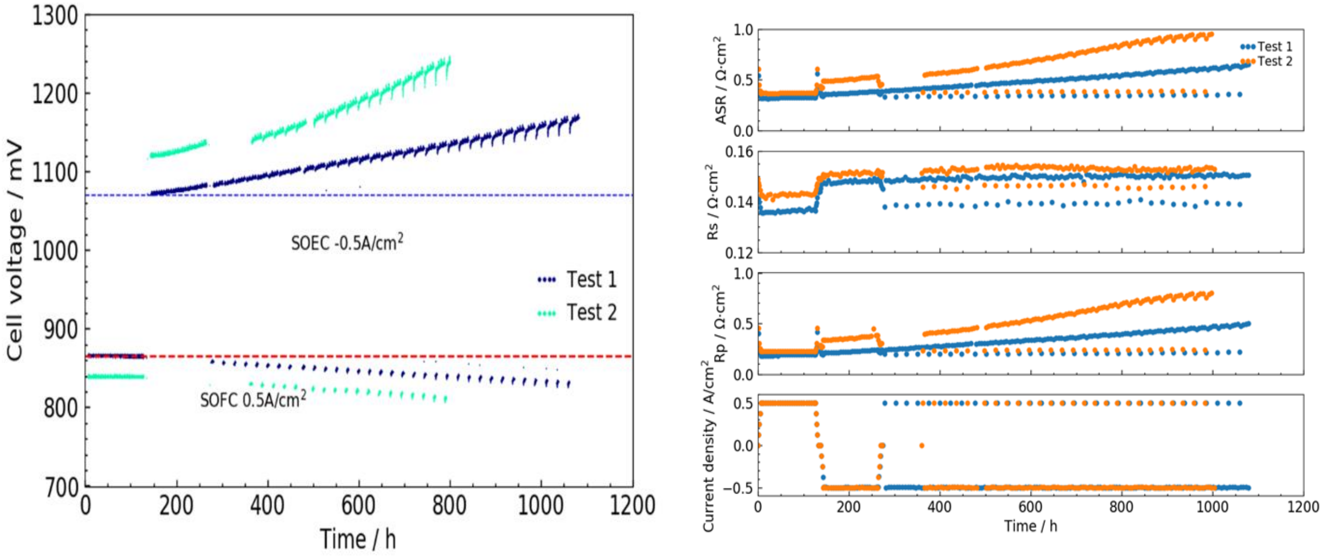

Figure 2-4: Voltage evolution comparison of BALANCE G1 Cell (Test 1) with commercial cell (Test 2).

Figure 2-4 is a comparison of the voltage evolution characteristics of a G1 cell and a state-of-the-art commercial cell subjected twice to test matrix A1 as given in *Table 2-3*. The BALANCE G1 cells show superior performance in both tests, indicating that the project cells were to very good standards. Both cells show minor degradation in SOFC and higher degradation in SOE modes. Also discernible is relatively higher degradation rate at the initial rSOC cycles and stabilising over further cycles in reversible operation.

As seen in *Figure 2-5*, the series resistance (Rs) is quite stable whereas the polarisation resistance (Rp) increased significantly over the test duration. Also, most of the degradation occurred during the reversible operation.

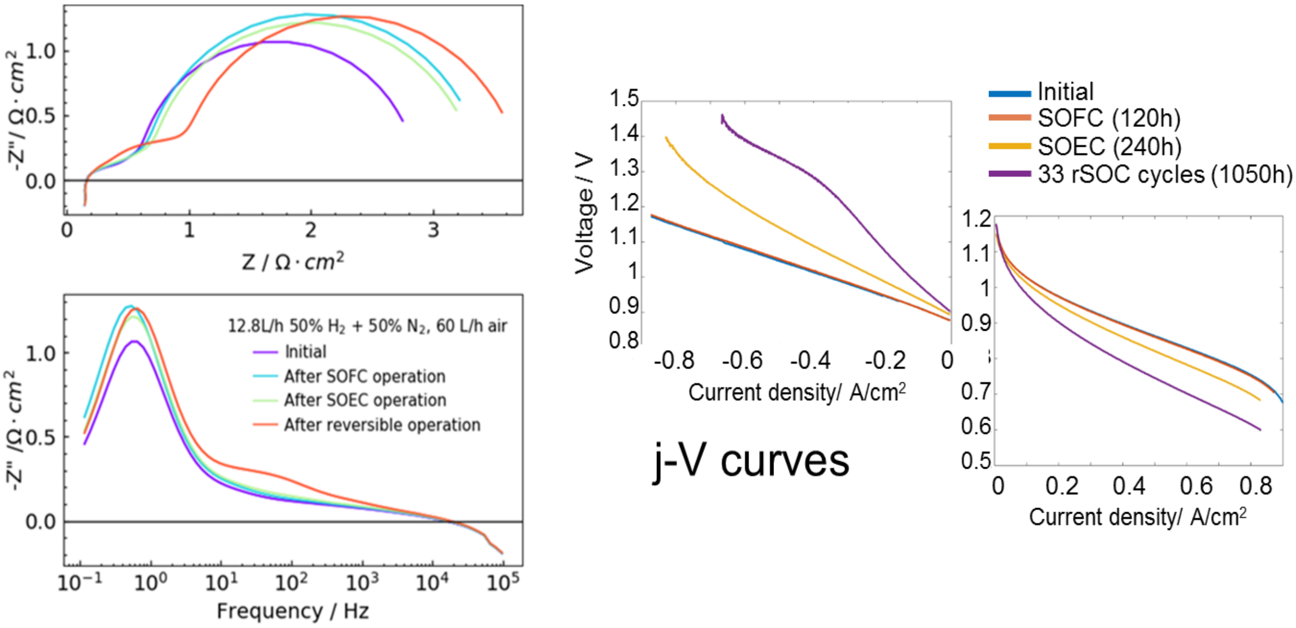

Figure 2-5: j-V and EIS curves of BALANCE test matrix A1.

Decreasing the SOE cycle duration (from 20 hrs to 8 hrs, test matrix A5) during reversible operation appears to have reduced the degradation rate, see *Figure 2-6* compared with *Figure 2-5*. During steady state operation (initial 280 hrs in *Figure 2-6*), the performance was similar to Test A1 (*Figure 2-5*) since the conditions were the same. The only difference between test matrix A1 and A5 being the reduced SOE cycle time for test A5 (8hrs) compared to test A1 (20hrs).

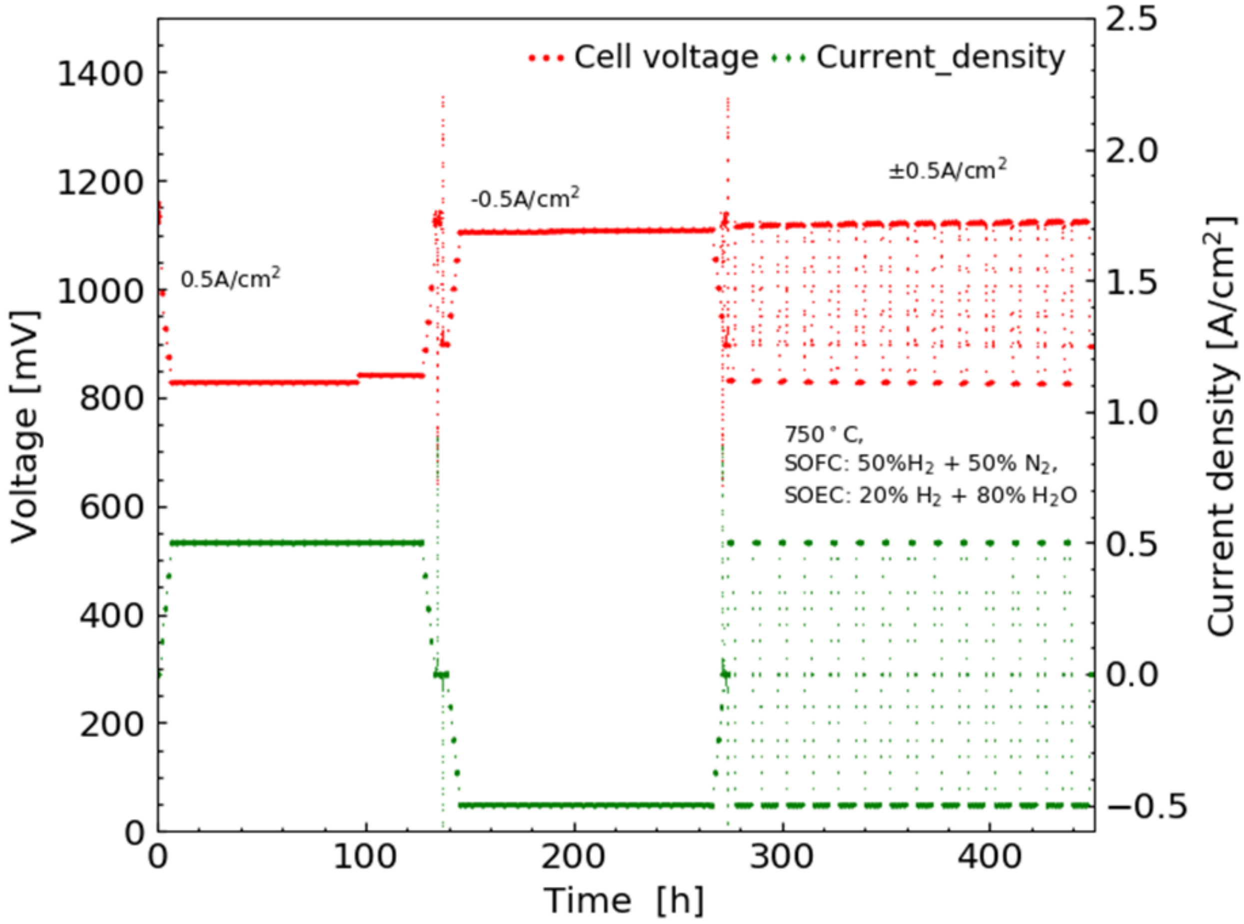

Figure 2-6: Voltage evolution of G1 cell tested under test matrix A5.

Figure 2-7 compares the initial performance of the Generations 1 (G1) and 2 (G2) cells, prior to subjecting them to the test protocol.

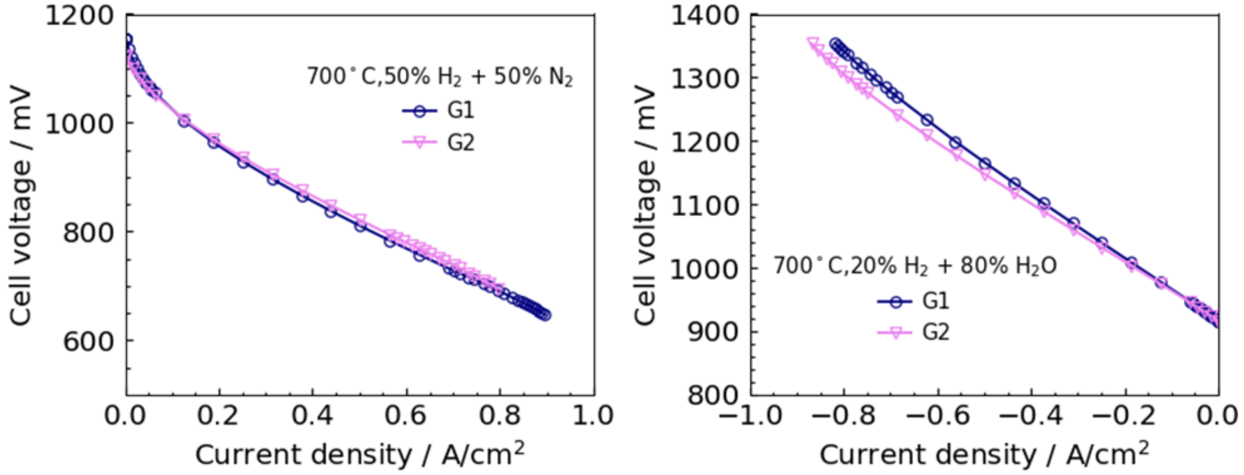

Figure 2-7: Comparison of G1 and G2 cells' initial performance.

The results show similar performance with the G2 cell being slightly better.

The voltage evolution (i.e. cell durability) of the cells subjected to the rSOC test protocol were also compared, and is shown in *Figure 2-8*. The G1 cell was subjected to the A4 test procedure from the test matrix (i.e. 700°C, 0.5 A/cm^2, ~50% fuel utilisation and 20 hrs SOE followed by 3hrs SOFC cycle period), whilst the G2 cell was subjected to the identical B1 test procedure.

The durability of the G2 cell was better than that of the G1 cell, albeit with still relatively high degradation as reported in .

Table 2-4: G1 and G2 cell voltage degradation rates in different operating modes.

Degradation Rate, %/1000h	Constant Operation		Reversible Operation	
	SOFC Mode	SOE Mode	SOFC Mode	SOE Mode
A4	1.7	7.7	3.8	7
B1	~0	3.7	2.5	4

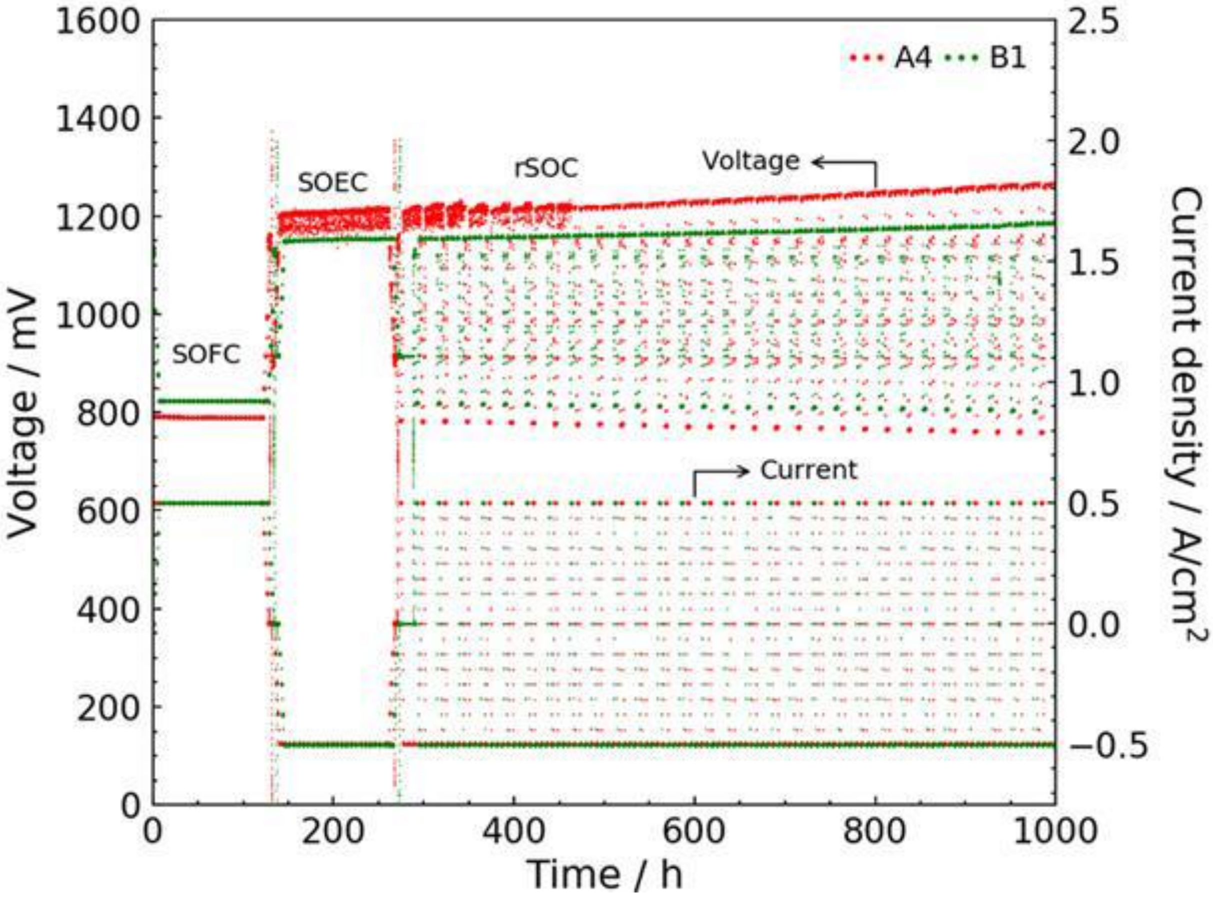

Figure 2-8: Comparison of voltage evolution of G1 and G2 cells.

A comparison of the stability of the G2 and Modified G2 cells is presented in *Figure 2-9* and . It is evident that the modified G2 cell is relatively more stable.

As reported in , the modified G2 cell shows significantly lower degradation, especially for the reversible operation mode.

Table 2-5: G2 and Modified G2 cell voltage degradation rates in different operating modes.

Degradation Rate, %/1000h	Constant Operation		Reversible Operation	
	SOFC Mode	SOE Mode	SOFC Mode	SOE Mode
G2	~0	3.7	2.5	4
Modified G2	3.6	2	0.97	0.5

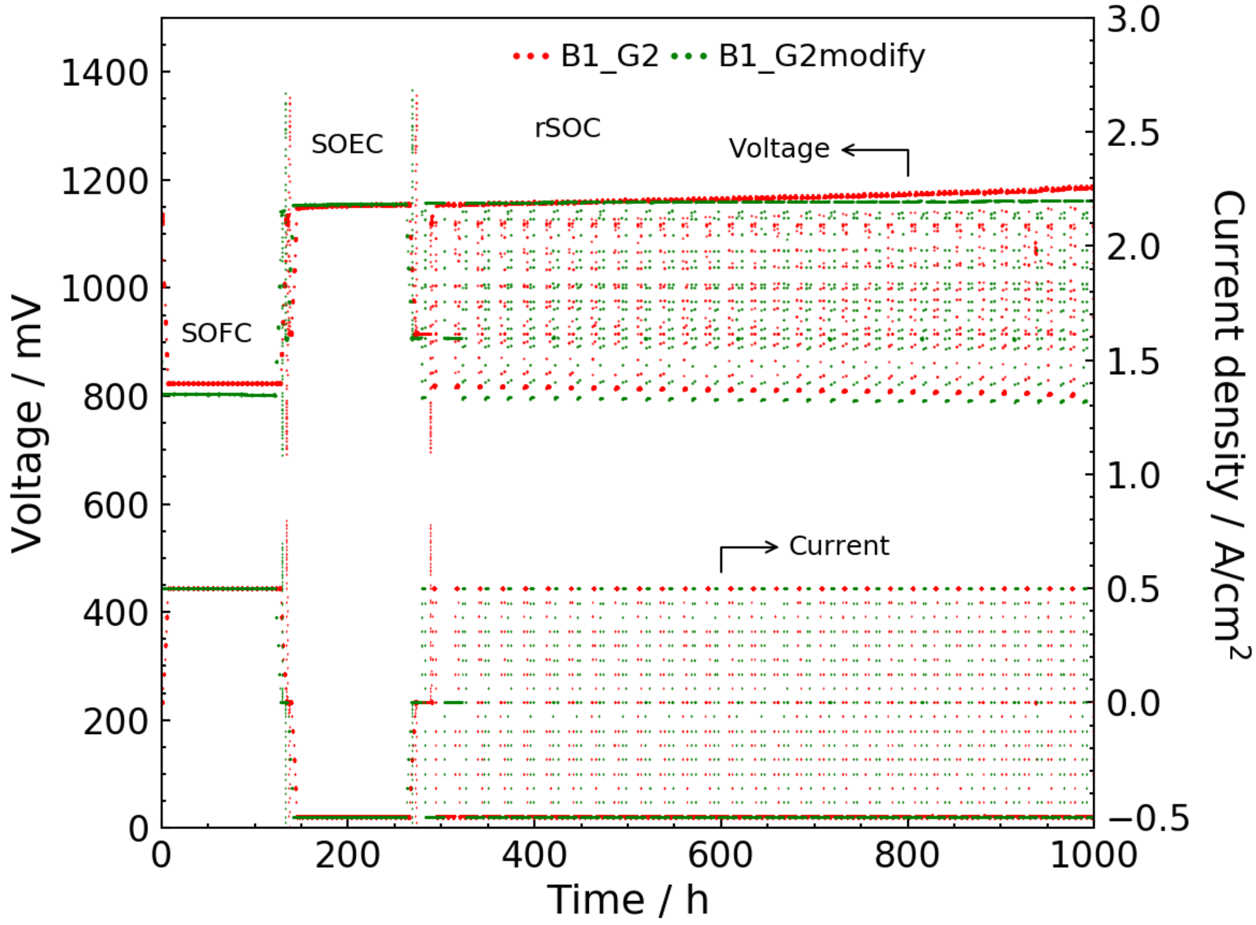

Figure 2-9: Comparison of voltage evolution of G2 and Modified G2 cells.

2.5 CONCLUSIONS

Whilst the G1 cell performance targets were generally achieved by the project, the rather ambitious targets of the project for the performance of G2 cells was not realised (see *Table 2-6*). Nevertheless, good progress was made in the lower temperature operation regime (at 700°C) and important lessons have been learned.

Table 2-6: BALANCE unit cell testing performance targets and achievements.

Parameter	SotA (G1) Cells		G2 Cells	
	Project Target	Project Result	Project Target	Project Result
Cell Area Specific Resistance (ASR)	0.2 Ω-cm^2, 800°C in SOE, 1 A/cm^2	0.191 Ω-cm^2, 800°C in SOE, 1 A/cm^2	0.2 Ω-cm^2, 700°C in SOE, 1.25 A/cm^2	0.53 Ω-cm^2, 700°C in SOE, 1.25 A/cm^2
		0.3 Ω-cm^2 750°C in SOE, 0.25 A/cm^2		
	0.15 Ω-cm^2, 800°C in SOFC, 1 A/cm^2	0.157 Ω-cm^2, 800°C in SOFC, 1 A/cm^2	0.15 Ω-cm^2, 700°C in SOFC, 1.25 A/cm^2	0.32 Ω-cm^2, 700°C in SOFC, 1.25 A/cm^2
		0.41 Ω-cm^2, 750°C in SOFC, 0.25 A/cm^2		
Cell Degradation Rate	0.5% / 1000h, 800°C in SOE, 1 A/cm^2	3.3% / 1000h, 750°C in SOE, 0.5 A/cm^2	< 0.5% / 1000h, 700°C in SOE, 1.25 A/cm^2	7.3% / 1000h, 700°C in SOE, 1.25 A/cm^2
	0.5% /1000h, 800°C in SOFC, 1 A/cm^2	0.2% / 1000h, 750°C in SOFC, 0.5 A/cm^2	< 0.5% /1000h, 700°C in SOFC, 1.25 A/cm^2	-0.1% /1000h, 700°C in SOFC, 1.25 A/cm^2

The cell designs that were based on extensive SOFC experience still require significant optimisation in the SOE field, particularly their degradation rates. The lowering of the target operation temperature to 700°C, whilst beneficial in terms of industrial commercialisation, may have exacerbated the G2 cell degradation rates in SOE mode.

2.5.1 Knowledge Management, Communication and Dissemination

The BALANCE project hosted a website which was created in 2016 at the beginning of the project and was deactivated at the end of the project with all deliverables transferred to the EU website [3]. Over the project timeline, the website had over 4000 visits and 11,200 page views, and had all the project deliverables accessible as open data. The BALANCE project was also involved in the organisation of three annual industry workshops in Brussels (led by UoB) over the project duration. The project also engaged in education efforts by hosting both summer and winter schools over the project period.

Furthermore, 17 scientific papers were published by the project, in addition to 47 oral and poster presentations which are all accessible as open data and are current hosted on the EU website [3].

3 LITERATURE REVIEW

3.1 General

This chapter of the thesis deals specifically with only the elements addressed under the experimental sections of this work. These are:

1. test apparatus design issues which impact operating efficiency (specifically any dependencies of rSOC performance efficiency on test apparatus orientation relative to reactant composition and chemical/physical characteristics);
2. unit cell design and materials of fabrication;
3. effects of cell operating temperature and current density;
4. comparative assessment of rSOC degradation rates under SOFC and SOC operation;
5. effects of fuel electrode reactant utilisation on performance and degradation;
6. effect of switching time on rSOC performance and degradation rates.

3.2 Materials and their Degradation

Although the conversion of chemical energy directly to electrical energy via fuel cell technology was demonstrated more than a century ago, its commercialisation has been hampered mainly by materials issues [31]. Specifically, for SOFCs, the development of materials and manufacturing routes which would render the technology cost-effective, relative to the conventional electric power technologies, has been challenging and thus slow. Material developments in standalone SOE, and more so rSOC, technologies are even more nascent, typically piggy-backing on materials developments in the more advanced SOFC technology [32].

For almost five decades, yttria-stabilised zirconia (YSZ) has been the established material of choice for the electrolyte; Nickel/yttria-stabilised zirconia (Ni/YSZ) for the fuel electrode; and Lanthanum Strontium Manganate, $La_{1-x}Sr_xMnO_{3-\delta}$, (LSM) for the oxygen electrode. Further research had mainly focussed on addressing their drawbacks by modifying and optimising compositions, morphologies, etc. Whilst this is possibly adequate for SOFC-only systems, SOE/rSOC operation may require different materials for optimum operation [26]. Materials properties (type, strength, electrode stability, physical and chemical characteristics, manufacturability*, etc.) are thus areas of intensive research in SOE/rSOC systems [33]-[34][35],[38], [44] - [45][46][31] [47], [52]. This philosophy of research ensures that materials are formulated which are suitable and targeted for rSOC systems. Instead of SOE/rSOC mainly leveraging advances in SOFC technology, the increased focus on developing novel materials for rSOCs, taking into account the different exposure environments under SOFC and SOE modes, ensures all possible avenues for optimising the technology are suitably explored.

This sub-section presents a review of materials from the point of view of rSOCs.

3.2.1 Electrolytes

The cell electrolyte must meet the following requirements: stability under both oxidising and reducing atmospheres with a sufficiently high ionic conductivity [57], [58]; easy to make dense thin films; and with good mechanical and thermal properties [31], [58]. The electronic conductivity at the cell operating temperature must be negligible. Some researchers have however suggested that the development of high pressures at the oxygen electrode due to oxygen evolution on the oxygen electrode at high current densities (≥ 0.5 A/cm^2), a major concern in SOE mode, may be avoided by introducing some electronic conduction in the electrolyte [59].

In addition, it has been theoretically and experimentally shown that mixed ionic electronic conductor (MIEC) electrolyte-based cells can be designed to operate as efficiently in both SOFC and SOE modes, as cells made with solely ionic conducting electrolytes [56].

Traditionally, Yttria-stabilised zirconia (8YSZ) has been the preferred electrolyte [5] due to its high ionic and negligible electronic conductivity. It is also stable under both reducing and oxidising atmospheres. The conductivities of YSZ with 8 mol% Y_2O_3 (8YSZ) are 0.1 S/cm and 0.03 S/cm at 1000°C and 800°C, respectively. In order to reduce the contribution of the electrolyte to overall cell resistance, the conductivity of the electrolyte should not be significantly less than 0.1 S/cm at the cell operating temperature. It has been shown [60] that 10YSZ, 10YbSZ and 8 to 12ScSZ all have conductivities greater than 0.1 S/cm at 1000^{o}C, with 11 ScSZ having the highest conductivity (0.3 S/cm at 1000°C). The conductivity of 11 ScSZ and 12 ScSZ at 800°C was 0.12 S/cm, showing their potential for use as cell electrolytes at intermediate temperatures. The three-point bending strength and the thermal expansion coefficient of 12 ScSZ were also shown to be comparable to that of YSZ. Such results have led to increased work on the use of alternative electrolytes which may be more tailored and suitable for rSOC [56], [57], [61], although all the scandia-doped zirconia compositions are more expensive relative to YSZ [5].

The performance of the electrolyte depends mainly on the thickness and the material properties of the electrolyte, as well as on the operating temperature of the system. Irrespective of the material used for the electrolyte, cell performance will improve with decreasing electrolyte thickness and increasing operating temperature. Thermodynamically, it is always advantageous to operate the cells at high temperatures because the ionic conductivities of the electrolyte materials increase with increasing temperature. Also, the electrochemical processes are thermally activated, leading to lower overall cell resistances at high temperatures [26], [57], [61].

Electrolyser cells fabricated with protonic conductors have attracted some interest due to the possible simplicity in system design and operation, with regards to hydrogen separation. In the case of steam electrolysis, protonic electrolytes present the opportunity of introducing both the 'fuel' (steam) and oxygen feed at the oxygen electrode. The product, hydrogen, will then be harvested at the hydrogen electrode with no need to separate the hydrogen from the effluent water. rSOCs with proton conducting electrolytes have been demonstrated, and relatively low ASR values have been reported at temperatures as low as 700 ^{o}C [50]. For co-electrolysers, although the CO_2 will still have to be introduced at the hydrogen electrode, proton conducting electrolytes offer similar advantages in system design and operation [62]. This system also lends itself to a better understanding of the CO_2 reduction mechanism in co-electrolysis, i.e., whether it's via direct electrolysis or a reverse water gas shift reaction.

Nevertheless, instability is a major concern in proton conducting materials, and extensive tests addressing the stability of proton conducting electrolytes are needed before they can be considered as viable rSOC electrolytes. Some research has been undertaken on proton conducting electrolyte candidates such as $BaZrO_3$ and promising results have been reported [63] - [64] [65].

Due to the objectives and scope of this thesis, as outlined in sections 1.4 and 1.5, the more established YSZ electrolytes would be used for the work.

3.2.2 Air / Oxygen Electrodes

The material for the air/oxygen electrode of an rSOC cell needs to be a good electronic conductor with a high catalytic activity for oxygen reduction / evolution [31]. It must also be compatible with the other cell components. Platinum is electrochemically suitable for the oxygen electrode and was used in the early development stages of SOFC technology. However, due to platinum's high cost and extensive SOFC materials research over the years, less expensive perovskites are now the preferred materials for the oxygen electrode for SOFC cells [58], and hence for rSOC cells as well.

The performance, stability and degradation of the presently used oxygen electrodes for rSOC cells seem to differ under SOFC and SOE modes. Some studies have suggested that the oxygen electrodes suffer higher voltage losses under SOE mode relative to SOFC mode. This relative difference in potential losses seems to be independent of the oxygen partial pressure, which is a function of the operating current density, at the oxygen electrode side of the cell. It has also been observed that subsequently operating the cell in SOFC mode positively affects the maximum power density and the potential losses, and depending on the relative operating times under SOE and SOFC mode, either:

1. Entirely reverses the degradation sustained under SOE mode [66]; or
2. Partially reverses or recovers the degradation sustained under SOE mode [67][68][69] - [70].

The stability of the oxygen electrodes is lower under SOE mode relative to SOFC mode. This low stability is more pronounced for purely electronic conducting oxygen electrodes (such as LSM) than for the mixed ionic electronic conducting (MIEC) oxygen electrodes such as LSCF/LSC [16], [71]. This already points to the impact of the available triple phase boundary (TPB) region.

Traditionally, the most widely used oxygen electrode material for SOFC, and hence SOE and rSOC, has been $La_{1-x}Sr_xMnO_{3-\delta}$ (LSM) [5]. Overall, the literature reports two main degradation mechanisms for LSM oxygen electrode materials under SOE / rSOC operation. These are:

1. Electrode delamination due to high oxygen pressure build-up across the oxygen electrode / electrolyte interface [59], [72][73] - [74]; and
2. Oxygen electrode passivation due to poisoning by contaminants such as chromium, silica and/or elemental denudation via cation migration such as strontium segregation [75][76][77] - [78].

The reported main cause of oxygen electrode performance degradation under SOE mode is electrode delamination from the electrolyte as a result of oxygen pressure build-up across the electrode-electrolyte interface. This is usually manifested at high current densities [73]. Prior to this, polarisation losses for the oxygen evolution reaction at high current densities are caused by structural and chemical changes in the oxygen electrode, which also decrease the interfacial pressure threshold required for physical delamination [72], [74], [79].

LSMs poor ionic conductivity limits the performance of the cell because the reactions can only occur in a narrow area where the gases, electrolyte and LSM electrode are in physical contact. This active area, the triple phase boundary (TPB), is limited to the interface of the electrolyte/electrode sandwich. Therefore, to increase cell performance with LSM electrodes, the material is synthesised to be highly porous to gas, hence increasing the rate of gas diffusion to the TPB for oxygen electrode reactions. The LSM can also be combined with the electrolyte material to form an oxygen electrode in the form of an LSM-electrolyte material composite [80], [81]. This consists of an LSM matrix with electrolyte networks, thus increasing the ionic conductivity of the electrode, and therefore extending the TPB area for oxygen electrode reactions [80]. However, it is difficult to fabricate a uniformly composed LSM-electrolyte composite to extend the TPB region (LSM/electrolyte/gas) [82].

Effectively, most of the degradation mechanisms reported for the LSM electrode indicate that increasing the TPB area significantly would mitigate cell degradation. These degradation mechanisms: delamination due to oxygen pressure build-up and interfacial formation of lanthanum zirconate ($La_2Zr_2O_7$); development of porosities at electrolyte (YSZ) grain boundaries; and morphological changes due to formation of nanoparticles in LSM grains adjacent to the electrolyte/oxygen-electrode interface, are all related to the narrowness of the TPB [41], [73], [83]. Therefore, it should be possible to improve the stability of the cell (under SOE mode in particular) by extending the sites for the reactions at the oxygen electrode. Infiltration with an ionic conductor effectively shifts the reaction sites from the oxygen electrode / electrolyte interface to incorporate the oxygen electrode matrix material / infiltrate material interfaces in the bulk oxygen electrode. This hypothesis led to the successful formulation and test of cells fabricated using the infiltration technique [84] - [85] [86].

LSM based oxygen electrodes are infiltrated at the nanoscale (oxygen electrode nanostructured technology) with suitable ionic conductors. Preferably, the electrolyte material is the infiltrate to promote or ensure cell stability / material compatibility. However, this is not a hard and fast rule and the infiltrate material may not necessarily be the electrolyte material. Initial tests conducted using cells with nano-infiltrated oxygen electrodes indicate superior performance relative to the traditional LSM electrodes due to increased electro-catalytic activity and stability under SOE mode [36], [37], [40], [42]. Since infiltration is primarily intended to increase the TPB, the extent of the infiltrated network has a positive correlation with cell performance. For instance, the polarisation behaviour of two LSM based oxygen electrodes, infiltrated with gadolinium doped ceria (GDC) nanoparticles, to form continuous networks of up to 0.5 mg/cm^2 and 1.5 mg/cm^2 were investigated at 800^{o}C. The resistance reported for the cell with the 0.5 mg/cm^2 of GDC infiltrated network was 0.39 Ω cm^2 and that for the 1.5 mg/cm^2 of GDC infiltrated network was 0.09 Ω cm^2. These are all significantly lower/better relative to the resistance reported for a cell with pristine LSM oxygen electrode at 800^{o}C, which was 8.2 Ω.cm^2. Aside increasing the TPB area, the high thermal stability of GDC nanoparticles in the oxygen rich environment present at the oxygen electrode, under SOE mode, contributes to the overall stability of the LSM-GDC infiltrated microstructure and hence improved cell performance [85].

As mentioned earlier, another way to improve the performance of the LSM oxygen electrode, aside nanoparticles infiltration, is by adding an ionic conducting secondary phase to the structure to impart or increase ionic conductivity of the electrode. This also increases the extent of the TPB reaction sites. This could be done by simply adding an ionic conducting phase to the LSM or by substitution of the A and/or B sites of the LSM material. The general structure of LSM, ABO_3, lends itself to several permutations when utilising the substitution technique to impart or increase ionic conductivity. The A site element, Lanthanum (L), could be replaced by similar members from the lanthanide series such as Praseodymium (Pr). The B site element, Manganese (Mn), could be replaced by either Iron (Fe) and/or Cobalt (Co) [87]. Upon substitution, such as when Mn is replaced by Co or Fe–Co, the ionic conductivity of the electrode increases with a simultaneous increase in the electro-catalytic activity for oxygen reduction / evolution. This is because the substituted oxygen electrode acts as a mixed ionic electronic conductor (MIEC) [5].

The electrode performance of some of the permutations (substituting only the B-site element) has been mapped as follows: $La_{0.8}Sr_{0.2}CoO_{3\delta}$ (LSC) < LSM < $La_{0.8}Sr_{0.2}FeO_{3\delta}$ (LSF) < LSCF [54]. This indicates that oxygen electrode materials with MIEC characteristics are generally better electrochemical performers relative to solely electronic conducting electrodes. LSC, also a MIEC, only performs poorly relative to LSM due to the formation of poorly conducting secondary phases with chromium (at SRU, stack or system level). This makes it presently only suitable in conjunction with protective layers for the stack interconnects since the current collectors for stack and system operations contain Cr, which typically evaporates from the materials at the high operating temperatures and in presence of water. Aside from the loss of ionic conductivity resulting from the formation of the poorly conducting secondary phases, the LSC-Cr layer at the electrode/current-collector interface also dissociates, leading to a deterioration in the electronic conductivity of the cell. These conductivity related failures make the degradation of the LSC oxygen electrode cell worse than that of the LSM electrode cell under SOE mode at SRU, stack or system level [78].

Therefore, aside LSC which is only suitable where Cr evaporation in interconnect systems is otherwise mitigated, the other mixed ionic electronic conductors are receiving increasing attention as the most suitable air electrode materials. Under rSOC conditions, MIECs such as LSCF have shown significantly improved electrolytic performance and cell stability relative to poorly ionic conducting LSM electrodes. Some resistance values measured for LSCF electrodes with two different electrolyte materials and at different temperatures are as follows: 0.68 Ω cm^2 for YSZ electrolyte at 750°C, and 0.81 Ω cm^2 for ScSZ-GDC at 650°C. These results indicate that LSCF, and more generally MIECs, have excellent potentials as electrode materials for intermediate to low temperature rSOC operation irrespective of the electrolyte material. LSCF oxygen electrodes employed and tested in SOFC stacks, show good performance with reported cell degradation rates ranging from 0.6 to 1.4%/1000 hours [88], [89]. Comparatively, when LSCF was used as an oxygen electrode and tested in an SOE stack, significantly higher degradation rates of ~5.6%/1000 hours were reported for continuous SOE operation up to 4000 hours [90]. This further illustrates the magnitude of the cell degradation differences under SOFC and SOE operation. Clearly therefore, more work is required, not only to optimise the LSCF microstructure for rSOC operation, but also to determine the optimum rSOC operating conditions required to mitigate overall cell degradation: such as reactant flow rates; cycle rate and time; switching regime including switching time and applied current step-size; and potentiostatic vs galvanostatic characteristics. LSCF has also been tested under CO_2 electrolysis mode and it performed better than an LSM-YSZ composite electrode. It showed negligible performance degradation when operated for 9 hours at a high current density (1.2 A/cm^2) and a high temperature of 1000°C relative to the LSM-YSZ composite electrode [91].

A degradation mechanism reported for LSCF oxygen electrodes under rSOC operation involves cation (e.g. Sr) segregation under both SOFC and SOE modes of operation [33], [92]. However, apparently irrespective of the cell architecture, the polarisation resistance of the LSCF electrode under SOE mode was reported to be significantly higher than its polarisation resistance under

SOFC mode; and approximately 3 times higher than the polarisation resistance of the corresponding Ni-YSZ fuel/hydrogen electrode in either mode. Therefore, generally, oxygen electrode polarisation and its degradation, especially under SOE mode, seems to be a major limiting parameter of rSOC systems [93]. It has been reported [26] that applying layers of samaria-doped ceria (SDC) on the LSCF oxygen electrode side of a YSZ electrolyte is effective in lowering the resistance without an attendant deterioration in the open circuit voltage. Therefore, similar to other air electrode materials, the incorporation of SDC or GDC layers onto the LSCF oxygen electrode side of the electrolyte eliminates the formation of non-conductive interphases that may also increase the risk of delamination under SOE mode [92]. Experiments conducted to compare the performances of LSC and LSCF oxygen electrodes showed that LSC performed better initially but the initial performance deteriorated under long-term tests, and it was more likely to delaminate (as previously discussed), even at relatively low current densities and with an SDC/GDC layer [94]. The electrochemical performance of cells with LSCF air electrodes was apparently improved even further by adding the SDC to the LSCF oxygen electrode. For a given nominal cell degradation rate, a cell with 40 vol% SDC added to the oxygen electrode could be operated at current densities that were up to 5 times higher than the cell with a pure LSCF oxygen electrode [33]. Cells of this type, which incorporate a GDC barrier layer and a GDC+MIEC composite oxygen electrode (see description of Cell type 1 in section 4.1.2.1 and chapter 5), would be used to investigate the objectives under the scope of this thesis.

Although the increase in ASR for YSZ electrolyte cells with an SDC/GDC interlayer are lower and the cells are more stable [92], [95], [96], during long term tests (9000 h) under SOE mode, as mentioned earlier, even LSCF oxygen electrodes degrade appreciably along with the electrolyte material. Observed re-structuring of grain surfaces in the electrolyte, and voids formation along the electrolyte grain boundaries compromise its mechanical properties and increase overall Ohmic resistance. The increase in Ohmic resistance would be exacerbated by the observed formation of horizontally oriented pores at the YSZ/GDC interface and the formation of a dense and insulating interphase layer ($SrZrO_3$) at this interface. For the LSCF electrode, compositional fluctuations may also increase the Ohmic resistance whilst recrystallisation of its electrochemically active centres may decrease its catalytic activity [74], [97].

To mitigate the delamination issues of even MIEC based oxygen electrodes such as LSCF, it has been suggested to incorporate a second layer between the GDC interlayer and the electrolyte. Experiments conducted with oxygen electrodes fabricated by adding a second layer of $Ce_{0.43}Zr_{0.43}Gd_{0.1}Y_{0.04}O_{2\delta}$ (CZGY) in between the LSCF-GDC interlayer and YSZ electrolyte reported improved stability, with a relative decrease in cell ASR from 0.45 to 0.35 Ω cm^2. The cell was also reported to have sustained long-term testing without delamination [98].

Other substituted MIEC oxygen electrodes such as $Ba_{0.5}Sr_{0.5}Co_{0.2}Fe_{0.8}O_{3\delta}$ (BSCF) have been tested. BSCF, in SOFC mode, exhibits very small polarisation resistances (approximately 0.1 Ω cm^2) even at temperatures as low as 600°C [99]. This polarisation resistance is considerably lower than that observed for the other perovskite-based MIEC oxygen electrode materials. That for LSC under equivalent test conditions, for instance was 1.48 Ω cm^2 [100]. However, cells made with BSCF oxygen electrodes undergo significant performance decay under SOE mode. A BSCF cell operated under SOE mode deteriorated significantly after just 20 hours of operation, relative to an LSM-YSZ composite oxygen electrode cell that performed stably for more than 20 hours under the same operation conditions [51]. It may therefore seem that BSCF air electrodes are not suitable candidates for rSOC cells.

A third method of improving the performance of the LSM electrode at high current densities may combine the above two approaches, i.e. nanoparticles infiltration and elemental substitution. This concept involves the integration of a porous electrode backbone onto the electrolyte to facilitate a strong adhesion between the electrode and electrolyte. Highly active electrocatalytic materials, such as substituted perovskite based MIECs like LSC, LSF or even LSCF, can then be integrated into the porous backbone using nanostructured infiltration techniques. Theoretically, this can be done for both the oxygen and hydrogen electrode materials. Since it has already been demonstrated that the infiltrated nanostructure electrodes perform much better than their bulk counterparts due to the TPB increase, this concept would primarily increase the interface strength between electrode and electrolyte to mitigate delamination under long-term operation. In addition, these nanostructured electrodes are also expected to have better durability due to the reduction in the effective current density per unit surface area. Thus, unit cells of this type would also be used to investigate the objectives under the scope of this thesis (see the description of Cell type 2 as given in section 4.1.2.2 and chapter 6.

Other oxygen electrode materials have been proposed and tested such as the Ruddlesden-Popper series or A_2BO_4-type oxides. These materials may be considered as natural heterostructures, comprising alternating blocks of perovskites and rock-salt with the rock-salt layer providing a very mobile pathway for oxygen. Specific formulations which have been proposed have an $A_2NiO_{4+\delta}$ structure, with A=La, Nd or Pr. These have been somewhat investigated for rSOC applications due mainly to their oxygen transport properties which can be further enhanced by appropriate B-site doping [101] - [102] [103]**.** Experiments comparing the electrochemical behaviour of these nickelate-type materials have suggested Nd-nickelate (NNO) as having the highest activity. Other experiments have indicated $Pr_2NiO_{4+\delta}$ (PNO) as the phase with the highest oxygen diffusion rate and the lowest cathodic ASR [104], [105]. A significant disadvantage reported for the nickelate-based electrodes is their reactivity with both YSZ and GDC electrolytes, which therefore necessitates the use of alternate electrolyte materials and / or effective barrier layers for any possible use of Nickelate-based electrodes [106], [107]. Alternatively, the cells must be operated at temperatures below the threshold temperature at which the adverse reactions take place. These thresholds have been investigated for some of the nickelates, reporting: 900^{o}C for $La_2NiO_{4\text{þ}\delta}$ (LNO) with a YSZ electrolyte and 700^{o}C with a GDC electrolyte; and 1000^{o}C for NNO with both YSZ and GDC electrolytes (the test was reported to be inconclusive for the Pr-derivative due to the decomposition of $Pr_2NiO_{4+\delta}$) [106] - [107][108] [109]. It should be noted that since sintering temperatures are usually higher than 1000^{o}C for the electrode to be adequately strong and to achieve proper adhesion at the electrode/electrolyte interface with an interconnected microstructure; the materials would react and degrade during fabrication. Therefore, the infiltration of nickelate salt precursors followed by calcination is used to fabricate these cell types [108].

3.2.3 Fuel/Hydrogen Electrodes

The hydrogen electrode needs to be electronically conducting and porous to both the reactants and the products [31]. Traditionally, it has been fabricated from a Nickel – Yttrium stabilised Zirconia cermet (Ni/YSZ) [5]. Nickel provides the primary electronic conduction and functions as a catalyst, whilst the YSZ phase builds the durable ceramic backbone and increases the reactions sites by extending the TPB. Some ionic conductivity in the hydrogen electrode is thus desirable.

Degradation of Ni/YSZ hydrogen electrode has been widely reported [28], [75], [81], [95], [96]. However, unlike the traditional LSM oxygen electrodes, long-term tests have indicated that Ni/YSZ hydrogen electrode degradation is not a direct function of the applied current density. It is rather due to adsorbed impurities such as silica in the Ni/YSZ hydrogen electrode [28], [67], [75], [80]. The presence of Zr-oxide nanoparticles on the surface of Ni grains has also been identified as one of the major degradation mechanisms for Ni–YSZ hydrogen electrodes under SOE operation. Similar to the trend observed for oxygen electrode degradation, the observed degradation of hydrogen electrodes seems to be higher under SOE mode than under SOFC mode [95], [96]. Other degradation mechanisms or contributing factors reported for Ni/YSZ hydrogen electrodes during operation are: Ni particle oxidation, steam starvation, layer peeling and grain coarsening [26], [32], [110] - [111][112] [113]**.** Degradation by Ni particle oxidation is primarily a result of the high operating temperatures combined with the oxygen partial pressure increase from water splitting, and secondarily due to concentrated electrolysis currents at preferential regions of the Ni/YSZ electrode [110]***.*** The time-dependence decrease in performance of Ni/YSZ electrodes has been attributed to the deposition of impurities such as sulphur, Si oxide or Zr oxide particles on the surface of Ni grains or in the pores of the electrode [76]. The TPB is reduced when impurities deposit in the pores of the electrodes. More generally, the impurities may also poison the electrode leading to significant electrode polarisation resistance [95], [96].

Hydrogen electrodes based on Ni-YSZ have another rSOC related problem, in that; they serve as catalysts for carbon formation [5]. This hampers their potential use in co-electrolytic cells, especially at low temperature, since co-electrolysis of H_2O (g) and CO_2 would lead to carbon formation on the electrodes thus decreasing their performance. Research is therefore focussing on alternate hydrogen electrode materials suitable for co-electrolysis at low temperature (less than approx. 750^{o}C). Some of these potential carbon tolerant hydrogen electrode materials are doped strontium titanate and other high-performance hydrogen electrode materials based on doped cerium oxide (CeO_2).

The objectives for tailoring of the traditional Ni/YSZ cermet are not limited to improvements in coking resistance under co-electrolysis. The main objective, like the air electrode architecture design, is reaction sites extension (increase in TPB area) to promote stability and catalytic activity. This is done through substituting some elements of the Ni/YSZ cermet and/or introducing 'beneficial impurities' (doping) to increase vacancies, introducing active layers, and by refining the microstructure. A copper cermet (60Cu:40YSZ) has been tested. This replaced the Ni with Cu for the hydrogen electrode. Although slightly higher hydrogen production rates (up to 1.8 cm^3/min, compared to 1.4 cm^3/min for 60Ni:40YSZ) were achieved, the conductivities of sintered Cu-YSZ are extremely low. The conductivity of 40Cu-60YSZ is 0.11 S/cm and that of 60Cu-40YSZ is only relatively better at 2.1 S/cm. These are relatively paltry compared to a conductivity of 10000 S/cm for 40Ni-60YSZ [114]*.*

The drawbacks of Cu-YSZ hydrogen electrodes are not limited to low electronic conductivities. Inimical and undesirable phases such as Y-rich cubic and monoclinic zirconia are formed even at low CuO (~1 wt%) contents. Partial reduction of zirconium from Zr^{+4} to Zr^{+3} has also been reported, increasing the cell resistance by about 25%. Although manufacturing methods and regimes have been proposed to mitigate these negative chemical changes, such as the impregnation method and manufacturing at low temperatures (< ~850^{o}C and ~700^{o}C for oxidising and reducing atmospheres, respectively), Cu-YSZ hydrogen electrodes are presently not ideal replacements for the Ni-YSZ hydrogen electrode even for low temperature (<700°C) cells [115].

For reversible solid oxide cells for electrolysis, and potentially more importantly for co-electrolysis, a more promising hydrogen electrode architecture is the mixed ionic and electronic conductor (MIEC) ceramics. MIECs have been receiving increasing attention as hydrogen electrode materials because they homogenously extend the reaction sites (TPB area) to the whole electrode thus significantly decreasing cell polarisation. MIECs are typically perovskites (ABO_3) and related phases. These electrode materials are more compatible with the traditional electrolyte materials, are more stable, and are more resistant to coking relative to the metal components in Ni-YSZ electrodes, for instance [116].

These MIEC materials are however not without their challenges. A common drawback reported in the literature is a relatively low catalytic activity for the fuel electrode reactions. The composition of perovskites such as $BaZr_{0.1}Ce_{0.7}Y_{0.2-x}Yb_xO_{3\delta}$ also need to be highly optimised in order to resist coking under the typical rSOC conditions [117] - [118] [119]. This has resulted in the formulation of double perovskite materials (e.g. Sr_2FeNbO_6, - SFN) with exceptionally high catalytic activities coupled with high conductivities. These double perovskite materials seem very promising as hydrogen electrode materials for the rSOC technology [49], [119].

Other symmetrical electrode compositions [120] and perovskites present an interesting scope of research as fuel electrode materials due to their characteristically low ASR, low polarisation, and high chemical stability, especially coking resistance. Some of the perovskites in this category that have been studied and reported in the literature are $La_{0.3}Ca_{0.7}Cr_{0.3}Fe_{0.7}O_3$ (LCFCr),

$La_{0.3}Sr_{0.3}Cr_{0.3}Fe_{0.7}O_3$ (LSCrF), $La_{0.8}Sr_{0.2}Cr_{0.5}Mn_{0.5}O_3$ (LSCM), $La_{0.3}Sr_{0.7}TiO_3$ (LST), and $La_{0.7}Sr_{0.3}VO_3$ (LSV) [35], [43], [55], [121] - [122][123][124] [125].

Perovskites, due to their unique properties, lend themselves as electrode materials for symmetrical cells, where both the hydrogen and oxygen electrodes are made of the same material. Symmetrical cells with $La_{0.8}Sr_{0.2}Cr_{0.5}Mn_{0.5}O_3$ (LSCM) electrodes, using YSZ as electrolyte, perform relatively well with low ASR at low temperatures (700 °C). They also present low polarisations in both air and hydrogen. At 900°C, the polarisation in air was ~0.27 Ω cm^2 and ~0.34 Ω cm^2 in hydrogen [126]. At 850°C, the polarisation in air was ~0.29 Ω cm^2 and ~0.59 Ω cm^2 in hydrogen [127]. The results from these experiments indicate that LSCM may be a candidate material for both the hydrogen and oxygen electrode for symmetrical rSOC cells. However, these results are for operation in fuel cell mode. For electrolysis, because LSCM has relatively low electrical conductivity in reducing environments, the material needs modification for its performance to be similar to its fuel cell mode performance. The electrical conductivity of LSCM in reducing environments is ~38 S/cm in air and ~3 S/cm in hydrogen [128], [129]. In non-reducing environments, such as for electrolysis of CO_2, the performance of LSCM in electrolysis mode is similar to that in fuel cell mode [19]. Modification to impart increased electrical conductivity in reducing environments is effected by adding between 35 and 45 wt% Ni (high electron conducting secondary phase) [130]. Using this modified composite with increased electrical conductivity, the electrode was relatively stable under SOE mode for direct steam electrolysis but with limited cell performance [131]. LSCM based materials therefore seem suitable for rSOC systems with CO_2 electrolysis but not for steam electrolysis or co-electrolysis. However, incorporating catalysts such as CeO_2 (2.8 vol%) and Pd (0.5 vol%) improved co-electrolysis cell performance [132].

Other perovskites such as $La_{0.3}Sr_{0.3}Cr_{0.3}Fe_{0.7}O_3$ (LSCrF) and $La_{0.3}Ca_{0.7}Cr_{0.3}Fe_{0.7}O_3$ (LCaCrF) have been investigated as possible electrode materials for symmetrical rSOCs. Relative to LSCM, both LSCrF and LCaCrF are very stable under both reducing and oxidising atmospheres, and like LSCM, are resistant to coking. Although they perform better under electrolysis mode than under fuel cell mode, they may still be suitable materials for both the hydrogen and oxygen electrodes of rSOCs [43], [35], [55], [121], [125], [133].

$La_{0.7}Sr_{0.3}VO_3$ (LSV), at present, exhibits limited catalytic activity. Although this activity could be enhanced by doping with CeO_2 and Pd catalysts for both electrolysis and co-electrolysis, for co-electrolysis, the degradation rate of the doped LSV is unacceptably high (i.e. approximately 2.3 mV/h) [124], [132].

Due to the objectives under the scope of this thesis, Ni-YSZ, which is the more established fuel electrode material, would be employed for the experimental work covered by this thesis.

3.3 Effects of Cell Operating Variables on Performance and Degradation

3.3.1 Cell Operating Temperature

Generally, given a set of cell materials, cell performance in both SOFC and SOE modes decreases with decreasing temperature [81] due to differences in both the transport rate of reactants and products to and from the reaction sites (principally due to decreasing ionic conductivity of the electrolyte), as well as the activation energies required for catalysis. As mentioned in Section 1.1.3, the thermodynamics of the process and the electrochemical kinetic conditions are more favourable at higher temperatures [48], [134]. This is in fact the reason why solid oxide cells promise such significant operating efficiencies relative to low temperature electrolysis technologies such as alkaline and PEME fuel cells.

Although the YSZ-based cells perform better at high SOFC temperatures (≥800^{o}C) [135], it is more economic to operate rSOCs at lower temperatures since it permits a wider choice in materials of construction for balance of plant components at the system level. Therefore, the tests performed under the scope of this thesis would be at temperatures ≤750^{o}C.

3.3.2 Cell Current Density/Mode

At low to intermediate current densities (i.e. up to approximately 0.5 A/cm^2), the overall cell degradation has been attributed mainly to oxygen electrode degradation [59], [68], [70], [73], [83], [85], [136], if the inlet gases (including steam) to the fuel electrode are cleaned from undesirable impurities to prevent fuel electrode poisoning [66] [137]. This is especially the case for operation at intermediate current densities since cell degradation is minimal at low current densities (i.e. < 0.5 A/cm^2). This is apparently independent of rSOC cycle duration. However, since the reported cell degradation rates in electrolysis mode appear to be significantly higher than cell degradation in fuel cell mode, it should follow that any cell degradation, even at low current densities, should correlate with both the rSOC cycle number and relative SOFC and SOE cycle durations during rSOC. On the other hand, at high current densities (i.e. above ≥ 0.7 A/cm^2), overall cell degradation is attributable to both the oxygen and hydrogen electrodes, and is also strongly dependent on rSOC cycle duration [79], [138]. This rule of thumb (negligible cell degradation at low current densities – significant cell degradation at high current densities), therefore seems to be independent of duration of cell operation or cycle rates and/or cycle duration of rSOC operation. The rule of thumb seems to hold true for cells operated under short-term and long-term test conditions. Cells operated for over 1000 hours at a low current density (< 0.5 A/cm^2) exhibit negligible degradation or delamination, regardless of cycling condition. rSOC systems can therefore sustain stable operation at low current densities (or possibly be operated at low current densities without any appreciable degradation); however, this may not be ideal relative to the economics of fuel utilisation and heat energy input since the cell may be significantly under-utilised at low current densities. On the other hand, rSOC systems operated at high current densities degrade significantly with the degradation rates seemingly increasing with increasing current density [72], [74]**.**

Current related degradation rates may not be limited to the magnitude of current densities. The mode of current supply under electrolysis operation also seem to affect cell degradation characteristics. The rate of degradation of the rSOC system is apparently less for variable current operation (potentiostatic) relative to constant current (galvanostatic) electrolysis operation. This is to be expected due to the hypothesised degradation mechanisms, involving the formation of new phases and/or voids, oxygen electrode delamination, all of which require an incubation time or minimum thresholds [59], [66], [72], [73], [83]. Taking the case of oxygen electrode delamination as an example, under potentiostatic SOE operation, since the current through the cell is a function of the electrode reactions and ion transport through the electrolyte, when oxygen ions begin to accumulate at the interface of the electrolyte and air electrode, the cell resistance increases whilst the current decreases in accordance with Ohm’s law since the voltage is constant (i.e. potentiostatic). Therefore, the rate of electrode reactions and ion transport through the cell also decrease, thus mitigating the pressure build-up at the electrolyte – air electrode interface. Under galvanostatic SOE operation, the current through the cell is held constant and therefore the cell voltage and resistance could increase linearly till the interfacial pressure threshold for electrode delamination is reached. Nevertheless, for commercialisation, galvanostatic operation is desired due to the direct correlation between hydrogen production rate (and stable electricity supply) and the operation current density. Therefore, galvanostatic operation would be employed for the tests under the scope of this thesis.

3.3.3 Effects of Reactants (Fuel Electrode) Utilisation

Similar to the observed low degradation rates when the rSOC unit cell is operated at low current densities (3.3.2), low degradation rates have been attained by operating the unit cell at low fuel electrode reactant utilisations [16]. However, operation at low fuel utilisation requires an effective exhaust fuel recirculation system to ensure economic efficiency. The fuel utilisation (U_F) is defined as the ratio of the flow rate of electrons [Equation 3 – 1] to the flow rate of hydrogen atoms [Equation 3 – 2].

$$\boldsymbol{n_{\dot{e}} = \frac{I}{2F}} \qquad [\boldsymbol{Equation\ 3-1}]$$

$$\boldsymbol{n_{\dot{m}} = \frac{\rho V}{M}} \qquad [\boldsymbol{Equation\ 3-2}]$$

$$\boldsymbol{U_F = \frac{n_{\dot{e}}}{n_{\dot{m}}}} \qquad [\boldsymbol{Equation\ 3-3}]$$

Where:

$n_{\dot{e}}$ = Molar flow of electrons;

$n_{\dot{m}}$ = Molar flow of hydrogen atoms;

I = Current (Ampere);

F = Faradays constant (96,485 C/mol);

ρ = Density of hydrogen gas (g/m^3), at standard temperature, 273.15 K and pressure,101.325 kPa;

V = Volumetric flow rate of hydrogen gas (m^3/s);

M = Molar mass of hydrogen gas (g/mol).

rSOCs may thus be readily operated with a desired constant fuel utilisation by running the system under constant current (galvanostatic) in both SOFC and SOC modes, and with defined fuel flow rates.

3.3.4 Comparative Assessment of rSOC Degradation Rates under SOFC and SOE Operations

Although the durability of rSOC cells is more complex than a simple relationship with the time of operation in SOFC mode relative to the time of operation under SOE mode, rSOC cells operated for longer durations in SOFC relative to SOE mode seem to perform better than cells operated for longer periods under SOE mode [16], [66].

A direct correlation of the absolute time the cell operates under SOE mode to overall cell degradation has also been observed. Cells cyclically operated for 1000 hours but changing from SOE to SOFC mode after every 1 hour indicate lower degradation rates compared to similar cells operated for 1000 hours but changing from SOE to SOFC mode after every 12 hours [72]. Cell degradation may therefore be mitigated by frequently switching current direction before the electrode polarisation threshold (i.e. end of the so-called break-in mechanism), which is relative to the operating current density, is breached.

A solar power based rSOC cell in locations and during periods of longer days and shorter nights thus seem to be the most conservative usage scenario. This is because the cell would be operated under SOE mode for longer periods to convert excess solar power to chemical energy. It may then be operated for relatively shorter periods to convert the stored chemical energy back to electrical power during the times of limited or no sun exposure. In addition, whilst wind power generators may theoretically produce electricity for 24 hours a day, practically, they are limited to about 20 hours a day on average [30] due to factors such as wind speed limitations (too little or too much wind) and shutdowns for maintenance/repairs or due to failure inspections/breakdowns.

Therefore, the cycling duration chosen for the work reported in this thesis is 3 hours SOFC operation followed by 20 hours SOE operation (see section 4.2.2 for further details). This is expected to enable an investigation of performance and degradation under the most conservative usage scenario.

3.3.5 Effect of other Operation Variables on rSOC Performance and Degradation Rates

During reversible cell operation under either galvanostatic or potentiostatic modes, the current or voltage is ramped from the open cell voltage (OCV) to the required operating current or current density. Also, during switching from one mode to the other (SOFC to SOE and vice versa), it is expected that the cell may require some time to recover back to initial OCV prior to ramping up for the next cycle. The author has not found any mention in the literature of the effects (if any) of both the ramping rate and the switching time /frequency on the subsequent performance and degradation of the cell, although the effect of such transient processes on stack performance have been studied at a system level [139] [140]. A key question to be answered would be the necessity of running the cell with reactants but without load for a period to enable the cell to recover or stabilise prior to ramping under load. This would only be necessary if switching directly from one mode to the other without recovering the cell to OCV affects cell performance and degradation rates, due to the obvious waste of reactants during the recovery period.

These would be investigated.

3.4 Summary of Conditions Necessary for Symmetrical and Reversible Operation

As noted in the preceding sections, an rSOC cell must operate efficiently in both SOFC and SOE modes and must be stable under the desired and inherent cyclic operation [16]**.** An rSOC must be operated cyclically for the technology to live up to its promise.

Generally, the hydrogen electrode shows symmetrical performance between fuel cell and electrolyser modes. The oxygen electrode, however, only shows symmetrical performance at current densities less than about 0.5 A/cm^2 [72] [141]. rSOC systems can therefore sustain stable operation at low current densities (or possibly be operated at low current densities without any appreciable degradation); however, this is not ideal since the cell is significantly under-utilised at low current densities. Although stable operation of rSOC at low current densities is thus feasible, the performance will be low for hydrogen and/or electricity production. The oxygen electrode may exhibit irreversibility at current densities greater than about 0.5 A/cm^2 in electrolysis mode [59], [72], [73]. Operation at these high current densities mostly results in delamination, due to O_2 evolution on the oxygen electrode, leading to oxygen pressure build-up across the electrolyte/electrode interface. This causes structural and chemical changes in the oxygen electrode [66], [141]. The irreversibility shown by the oxygen electrode has been indicated to depend on a number of factors such as electrode microstructure (see 3.2.2), material type (see 3.2) and cell operating parameters (see 3.3) [27].

3.5 Conclusions

For the state-of-the-art rSOC, Ni-YSZ is presently the optimum solution for the fuel electrode material due to its relatively superior catalytic activity, durability and reliability. However, to fully exploit the benefits of the solid oxide cell technology to ultimately produce liquid fuels such as methane, methanol, and synthetic diesel via syngas (H_2+CO) production, research is ongoing on alternative fuel electrodes with similar catalytic activity, durability and reliability characteristics to Ni-YSZ, and with the additional requirement of coking resistance. For the oxygen electrode, although LSM works very well in SOFC mode, it degrades significantly under SOE mode. Therefore, for rSOC, MIEC materials such as LSC and LSCF are the material of choice due to their comparable performance to LSM under SOFC mode, and relatively superior durability under SOE mode. YSZ electrolyte materials remain the solution for intermediate and high temperature solid oxide cells. Some work has been done on alternative electrolyte materials based on doped ceria and scandium stabilised zirconia for low to intermediate temperature ($\leq 650^{o}$C) SOC.

Therefore, for the purposes of this thesis, Ni-YSZ / YSZ / MIEC cells would be used.

Some work has been done on the effect of operating variables on cell performance, durability and reliability. Generally, cell performance increases with increasing temperature due to increasing catalytic activity and ionic conduction, as well as decreasing electric energy demand in

SOE mode. Cell durability also generally increases with decreasing operating current density and fuel utilisation (as a function of fuel flow parameters and current density). However, the effects of the interplay between these operating variables is not sufficiently understood to determine the optimal cell operating conditions, which may be a compromise between temperature, current density, fuel flow rates and utilisation.

Specifically, for rSOCs, cells operated for shorter periods under SOE mode relative to the periods of operation under SOFC mode, show improved durability relative to cells operated with the opposite philosophy. Finally, not much work has been done on the effect of the transient processes during mode switching on subsequent rSOC performance, durability and reliability. This would be a topic, as pointed out later, of future work.

4 METHODOLOGY

4.1 Materials Tested

Two types of cells, with different electrolyte - oxygen electrode configurations, were tested in this work. Both cell types utilised a Ni-YSZ hydrogen electrode (with a Ni-YSZ support) and a YSZ electrolyte. Cell type 1 had a pure GDC barrier layer between the YSZ electrolyte and an LSC-GDC composite oxygen electrode (with an LSC contact layer on the oxygen electrode). Cell type 2 also had a pure GDC barrier layer between the YSZ electrolyte and an LSC infiltrated GDC backbone oxygen electrode (with an LSC contact layer on the oxygen electrode). Therefore, the main difference between cell type 1 and cell type 2 was the LSC infiltrated CGO oxygen electrode. The intended role of the of the GDC barrier layer in both cell types was to mitigate deleterious reactions between the YSZ electrolyte and the LSC-GDC oxygen electrode since YSZ and LSC form insulating interfacial phases such as $SrZrO_3$ and $La_2Zr_2O_7$ [5] [142].

All tested cells were supplied by a member of the BALANCE consortium (DTU, Denmark).

Typical dimensions of the cells used in the experimental work are detailed in *Table 4-1*. The overall thickness of the cells tested was 0.1 mm.

Table 4-1: Project SOC dimensions

	Cell Diameter (cm)	Active cathode area (cm^2)	Layer Thicknesses (µm)					
			Ni-YSZ support	Ni-YSZ fuel electrode	YSZ Electrolyte	GDC barrier layer	LSC-GDC oxygen electrode	LSC contact layer
Cell type 1	3	5.3	30	15	15	5	8	20
Cell type 2	3	5.3	30	10	10	8	20	20

4.1.1 Fuel Electrode Material

The composition of the fuel electrode material, assessed via EDX, is indicated in *Table 4-2* and *Figure 4-1* . Note that EDX does not give exact compositional data and is mainly useful for positive material identification (PMI) purposes. The fuel electrode in this work is thus definitely a Nickel / Yttrium stabilised zirconia cermet as indicated in *Table 4-2* and *Figure 4-1*.

Table 4-2: Indicative composition of the fuel electrode material (assessed via EDX).

```
Element   AN  Series     Net unn. C norm. C Atom. C Error
                            [wt.%]  [wt.%]  [at.%]   [%]
--------------------------------------------------------
Oxygen     8  K-series 23457  22.77   23.89   51.69   2.6
Nickel    28  K-series 37964  34.94   36.67   21.62   1.1
Carbon     6  K-series  2008   4.46    4.68   13.48   0.7
Zirconium 40  L-series 88857  31.45   33.00   12.52   1.2
Yttrium   39  L-series  4487   1.67    1.76    0.68   0.1
--------------------------------------------------------
                      Total:  95.29  100.00  100.00
```

The microstructure of the Ni/YSZ fuel electrode material, Figure 4-2, shows a uniform particle size of approximately ≤ 2µm, with finely distributed interstitial porosity for optimum transport of reactants, and products, to, and from, all Ni / YSZ boundaries.

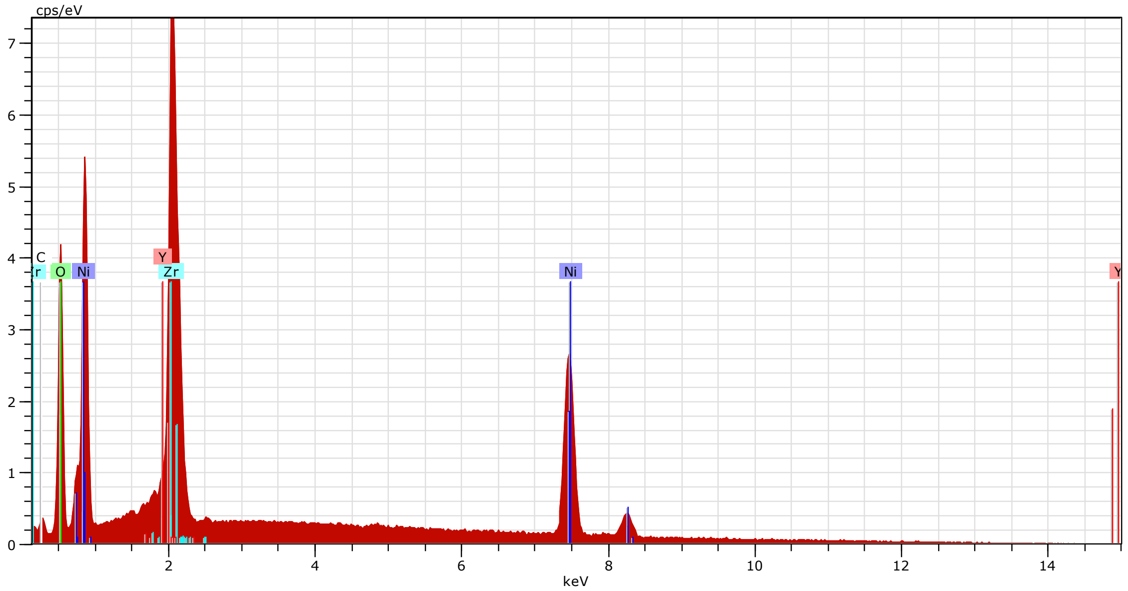

Figure 4-1: Energy-dispersive X-ray spectrograph of fuel electrode material.

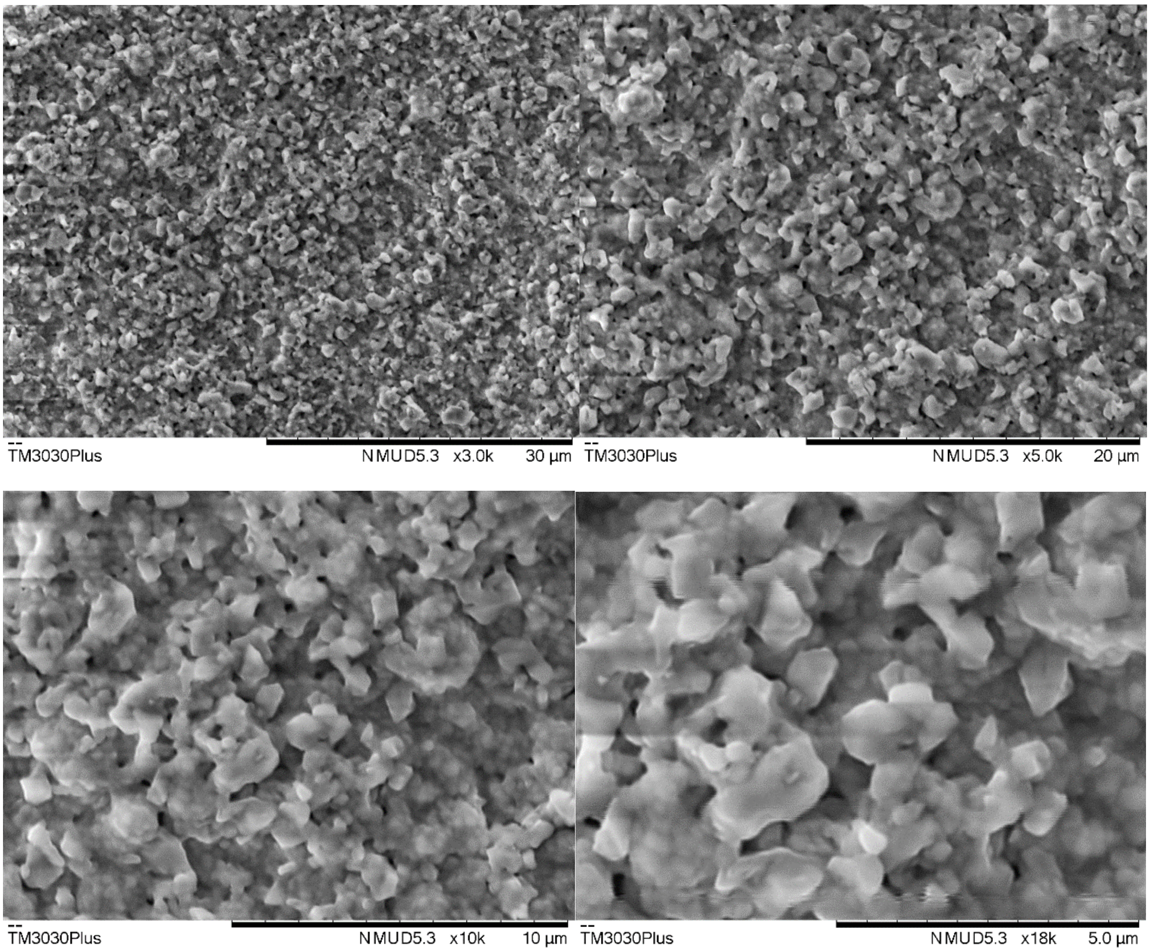

Figure 4-2: Scanning electron micrograph of the virgin fuel electrode material.

4.1.2 Oxygen electrode material

4.1.2.1 *Cell type 1 (LSC+ GDC Composite)*

The oxygen electrode material as seen in Table 4-3 and *Figure 4-3* is a composite of lanthanum strontium cobaltite and gadolinium doped ceria ceramics. Since LSC electrodes are prone to the formation of deleterious phases such as $SrZrO_3$ and $La_2Zr_2O_7$ with YSZ electrolytes [142], barrier layers (see 4.1.2.2) are typically incorporated between the LSC electrode and YSZ electrolyte to mitigate any harmful solid-state reactions. SEM images of the oxygen electrode showing a uniform grain structure of approximately ≤2µm grain size and finely distributed interstitial pores is shown in Figure 4-4 and *Figure 4-8* .

Table 4-3: Indicative composition of the oxygen electrode material (assessed via EDX).

```
Element     AN  Series     Net unn. C norm. C Atom. C Error
                               [wt.%]  [wt.%]  [at.%]   [%]
-----------------------------------------------------------
Oxygen      8  K-series 16337  14.30   14.02   41.61   1.7
Cobalt      27 K-series 26374  28.98   28.41   22.89   0.9
Carbon      6  K-series  1961   3.56    3.49   13.80   0.5
Lanthanum   57 L-series 58290  37.73   36.99   12.64   1.1
Strontium   38 L-series 21401  15.50   15.20    8.24   0.6
Yttrium     39 L-series  1252   0.85    0.83    0.44   0.1
Cerium      58 L-series  1352   0.91    0.89    0.30   0.1
Zirconium   40 L-series   220   0.16    0.16    0.08   0.0
Gadolinium  64 L-series     0   0.00    0.00    0.00   0.0
-----------------------------------------------------------
                       Total: 101.99  100.00  100.00
```

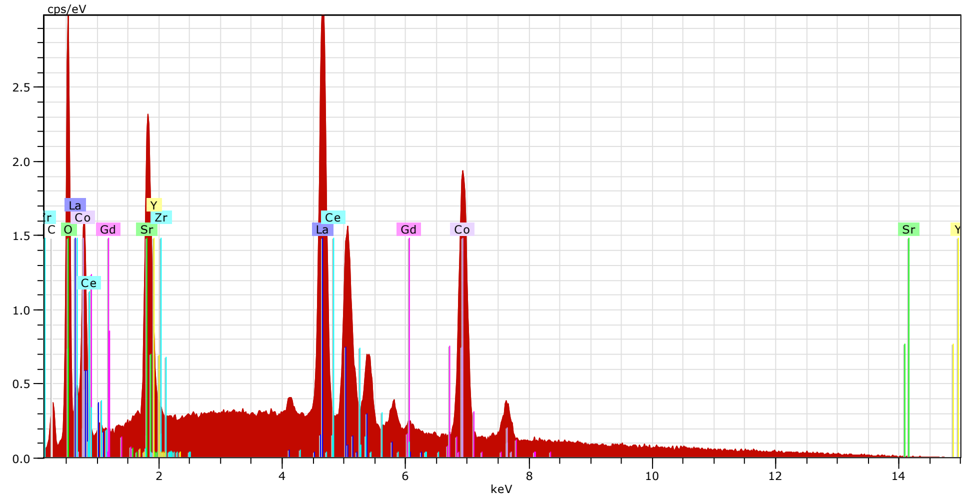

Figure 4-3: Energy-dispersive X-ray spectrograph of oxygen electrode material.

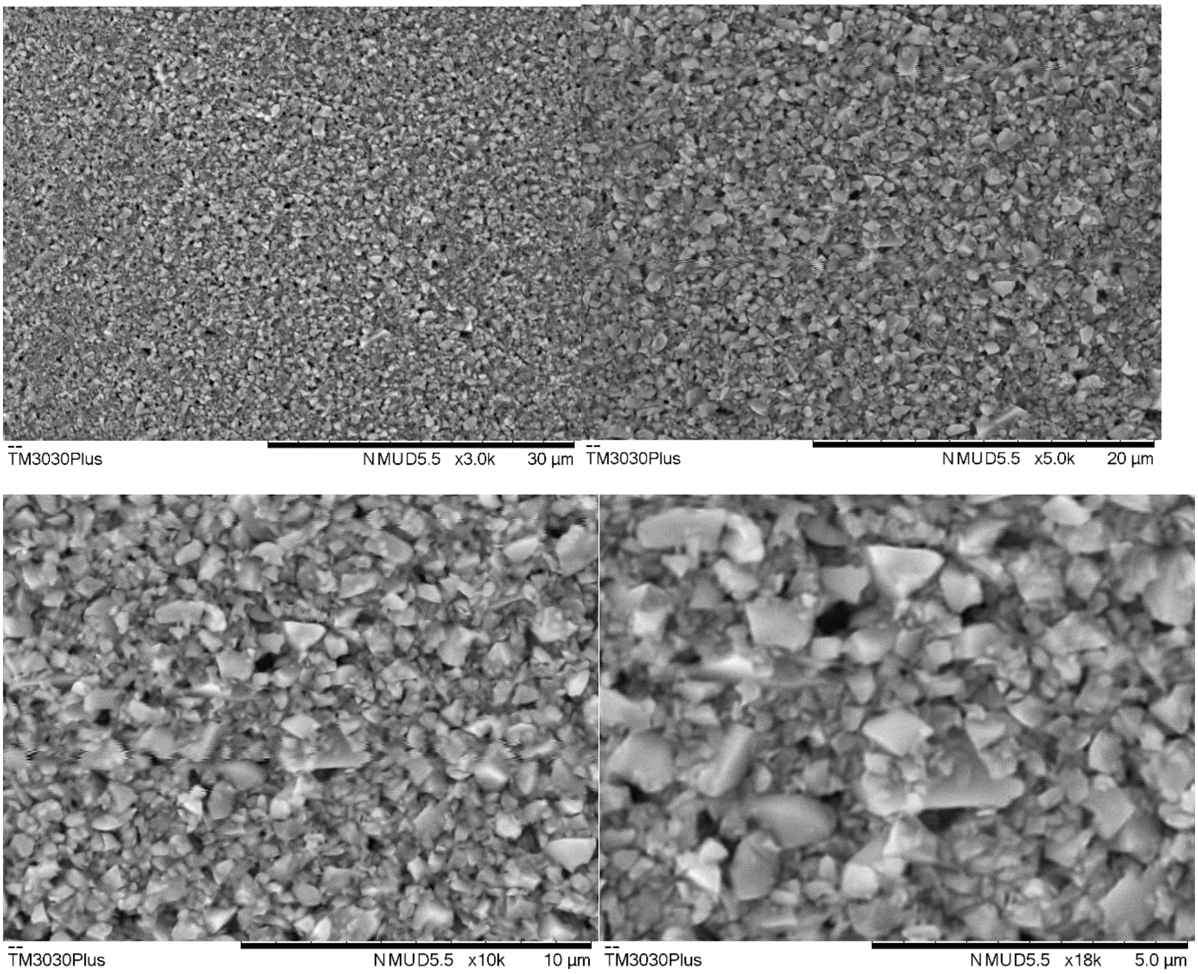

Figure 4-4: Scanning electron micrograph of oxygen electrode material for cell type 1 (also see *Figure 4-8*).

4.1.2.2 Cell type 2 (LSC infiltrated GDC backbone)

The oxygen electrode for cell type 2 was an LSC infiltrated GDC backbone. This is shown in Figure 4-5, and its usage has not been reported in the literature. Like the LSC+GDC composite, the LSC infiltrated GDC backbone also increases the TPB for electrode catalytic reactions.

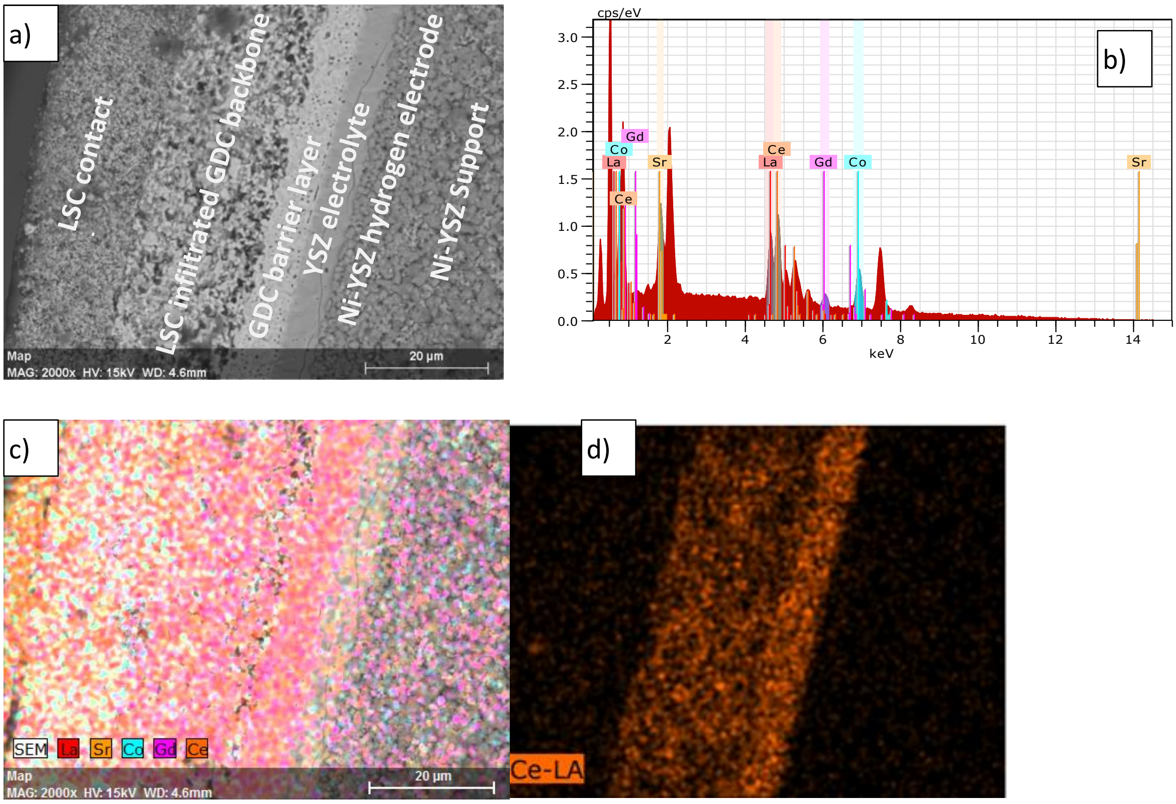

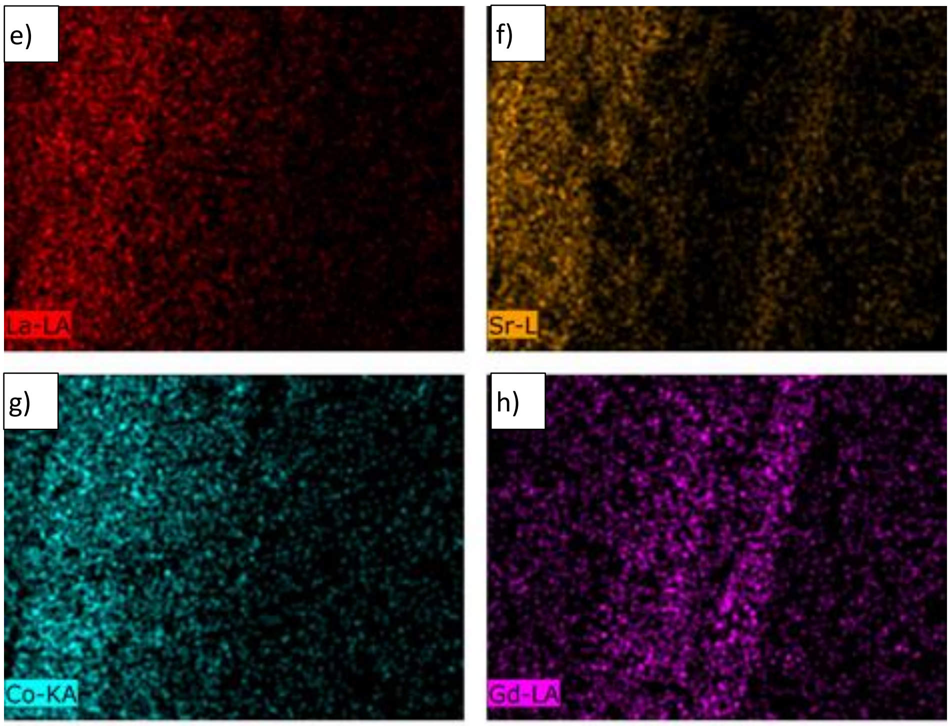

Figure 4-5: Cross-section of cell type 2 showing LSC infiltrated backbone oxygen electrode between pure GDC interlayer LSC contact layer. a) complete cell cross-section, b) to h) EDX scan showing elemental distribution across the SOC cross-section.

4.1.3 Electrolyte / Oxygen electrode interlayer

Table 4-4 and *Figure 4-6* identify the YSZ electrolyte / LSC electrode interlayer material as gadolinium doped ceria (GDC). This layer is used to mitigate harmful reactions, at the high operating temperatures, between the YSZ electrolyte and LSC containing layers (see 4.1.2). *Figure 4-7* and *Figure 4-8* show the microstructure of the GDC interlayer, having a grain size of approximately ≤ 1µm and finely distributed interstitial spaces to facilitate mass transport.

Table 4-4: Indicative composition of the electrolyte / oxygen electrode material (assessed via EDX).

```
Element     AN  Series      Net unn. C norm. C Atom. C Error
                                [wt.%]  [wt.%]  [at.%]   [%]
-----------------------------------------------------------
Oxygen      8  K-series  38833  15.40   16.88   64.03   1.7
Cerium      58 L-series 133185  66.85   73.30   31.74   1.9
Gadolinium  64 L-series   8854   7.62    8.36    3.22   0.2
Cobalt      27 K-series    561   0.50    0.54    0.56   0.0
Lanthanum   57 L-series   1493   0.69    0.75    0.33   0.0
Strontium   38 L-series    336   0.15    0.17    0.12   0.0
```

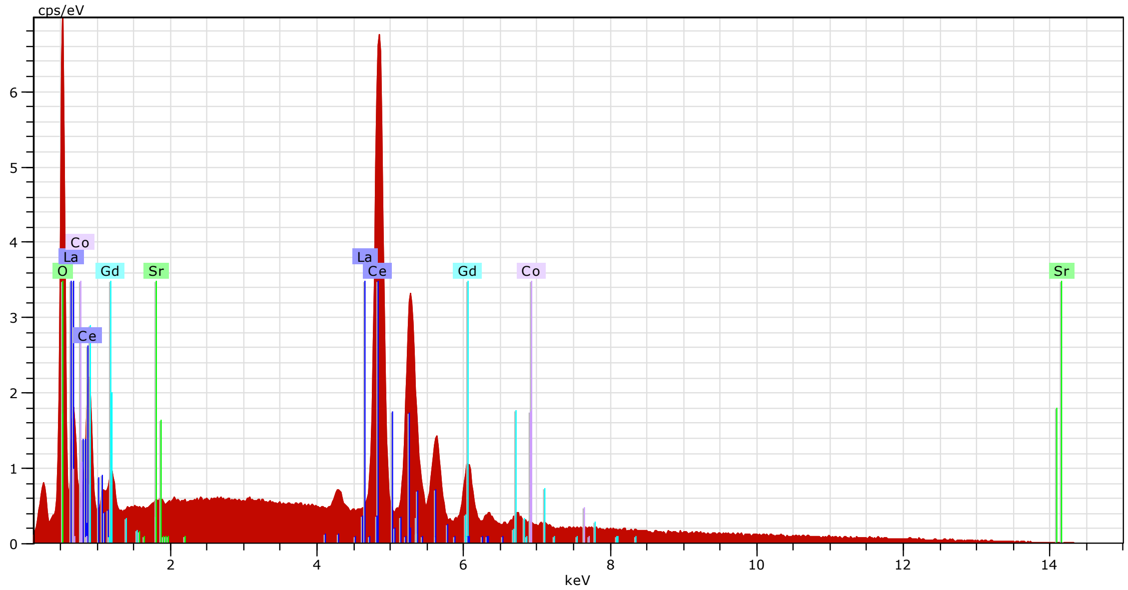

Figure 4-6: Energy-dispersive X-ray spectrograph of electrolyte / oxygen electrode interlayer material.

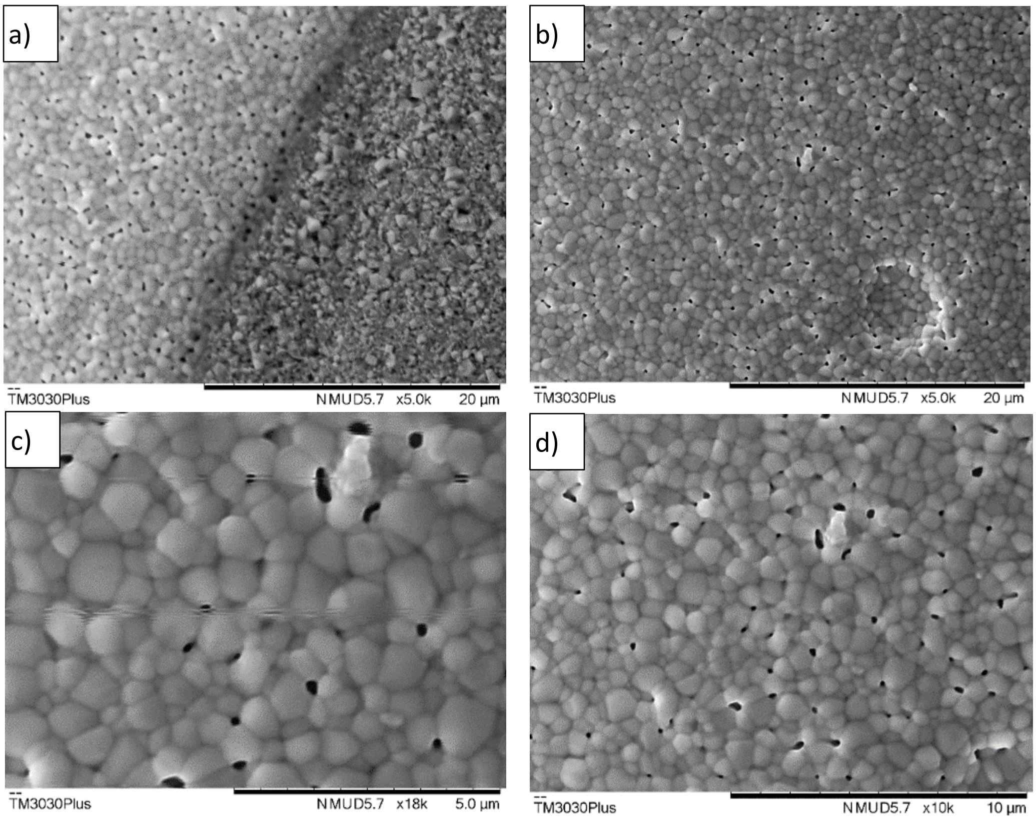

Figure 4-7: Scanning electron micrograph of the GDC interlayer (surface image of the exposed GDC interlayer at the rim of the oxygen electrode, see Figure 4-10 b)).

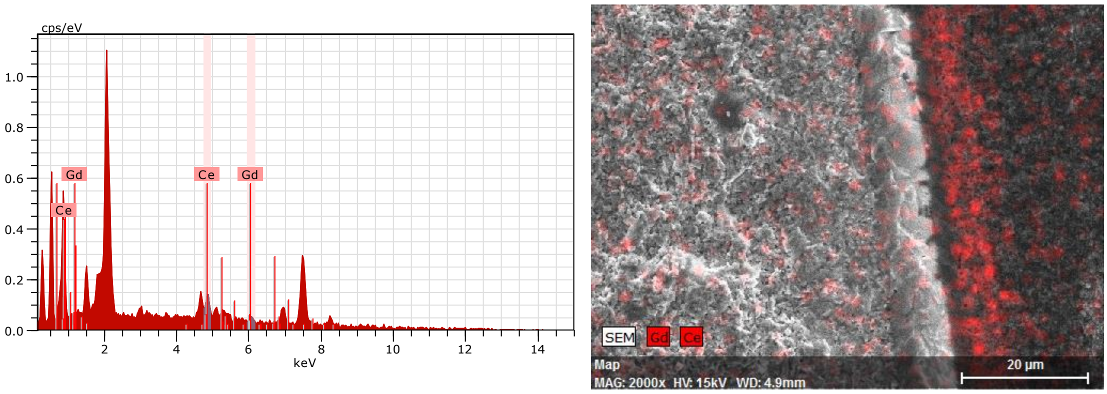

Figure 4-8: Cross-section of cell type 1 showing GDC layer between electrolyte and oxygen electrode.

4.1.4 Electrolyte

The electrolyte material used for all tests reported in this thesis was yttria stabilised zirconia (YSZ). YSZ electrolyte cells were used for the rSOC tests due to the reasons explained in Section 3.2.1.

As can be seen from *Figure 4-9* a), the YSZ electrolyte was thin (≤ 15µm) and extremely dense due to the reasons detailed in Section 3.2.1.

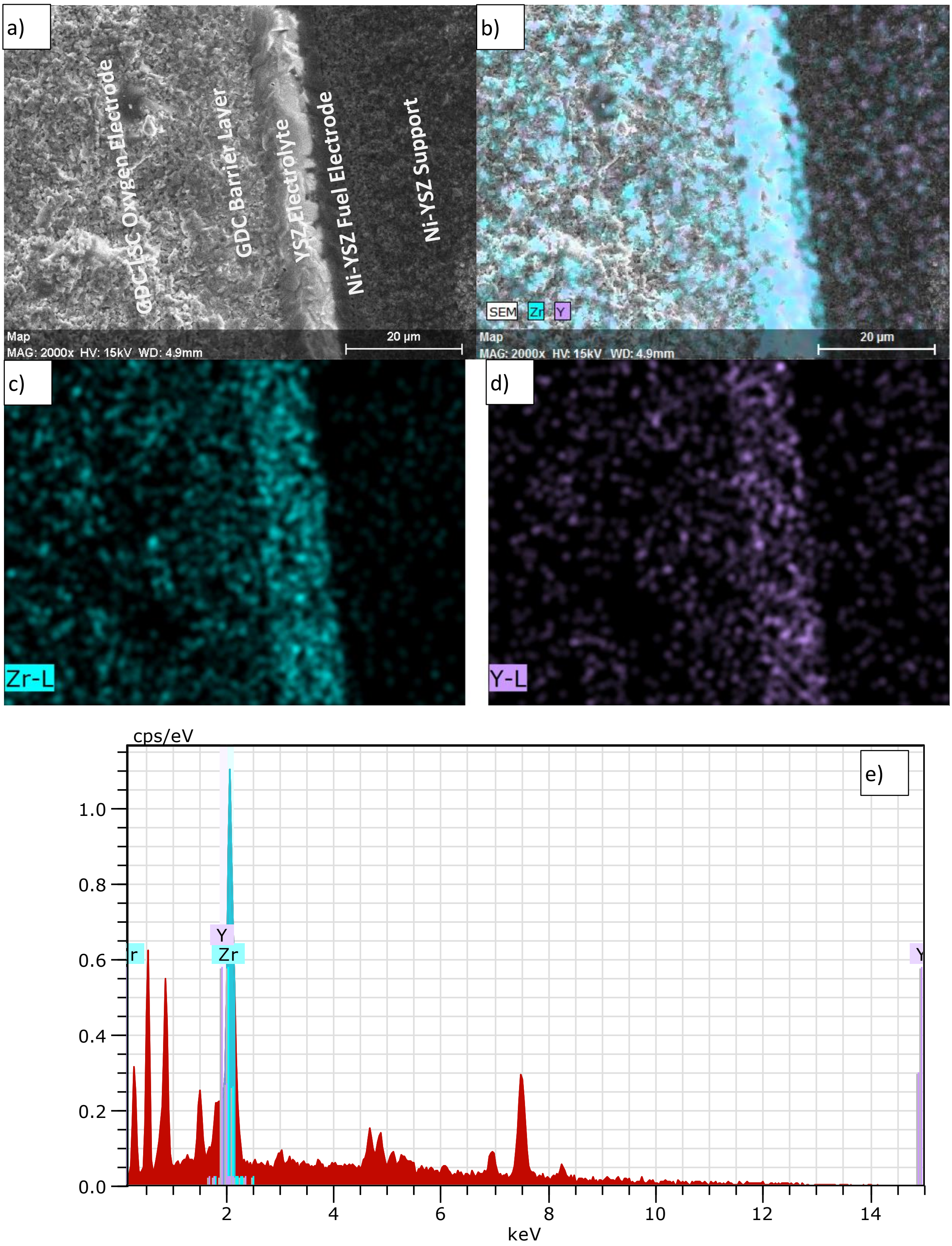

Figure 4-9: YSZ electrolyte material for both cell types 1 and 2.

4.1.5 Current collection materials

Two different current collection systems were employed. The first system was based on silver wires and paste. The silver paste was embossed on the electrode surfaces and was also used to attach the silver wires to the electrode surfaces, *Figure 4-10*. To prevent breaking of the silver wires at the high operating temperatures and current densities (up to 2.65 A/cm^2), several strands (3 or 4) of 0.3 mm diameter silver wires were wound together.

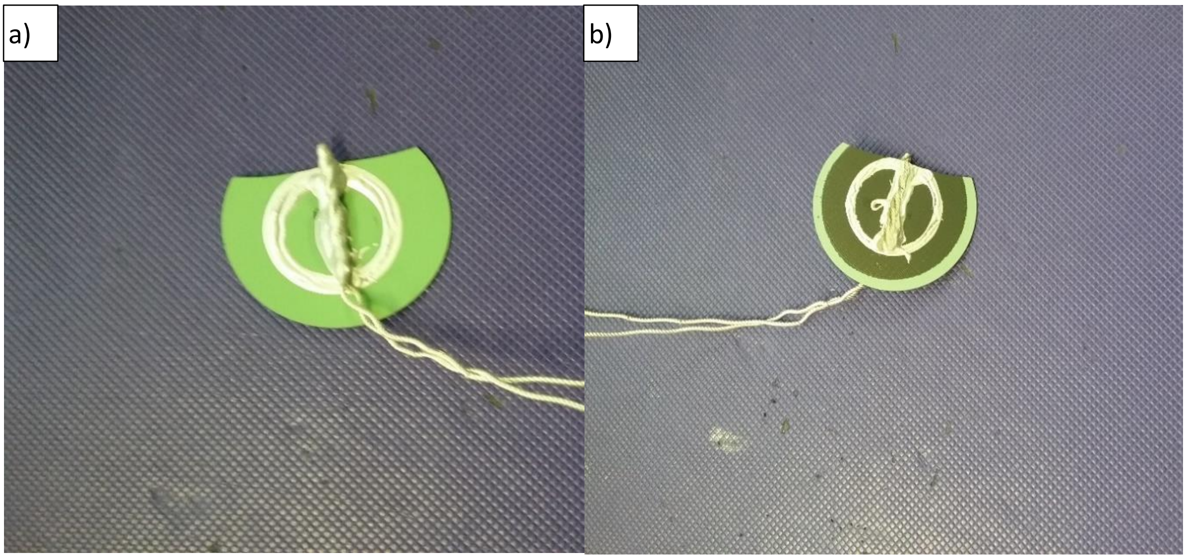

Figure 4-10: Silver-based current collection system attached to a) fuel electrode and b) oxygen electrode.

The following figures display some of the raw data generated using the silver-based current collection system. *Figure 4-11* shows the open cell voltage (OCV) of the tested cell operating under SOFC mode conditions (*Table 4-5*). The measured OCV of approximately 1V was as expected (see *Figure 1-3*). The actual OCV of fuel cells is less than the ideal OCV at all temperatures (e.g. $\Delta G_f/nF$; ≈237300/2*96485; ≈1.23V for the case of hydrogen fuels as in the present work) due to inherent inefficiencies in apparatus system design plus losses attributable to electrode activation and mass transport potentials.

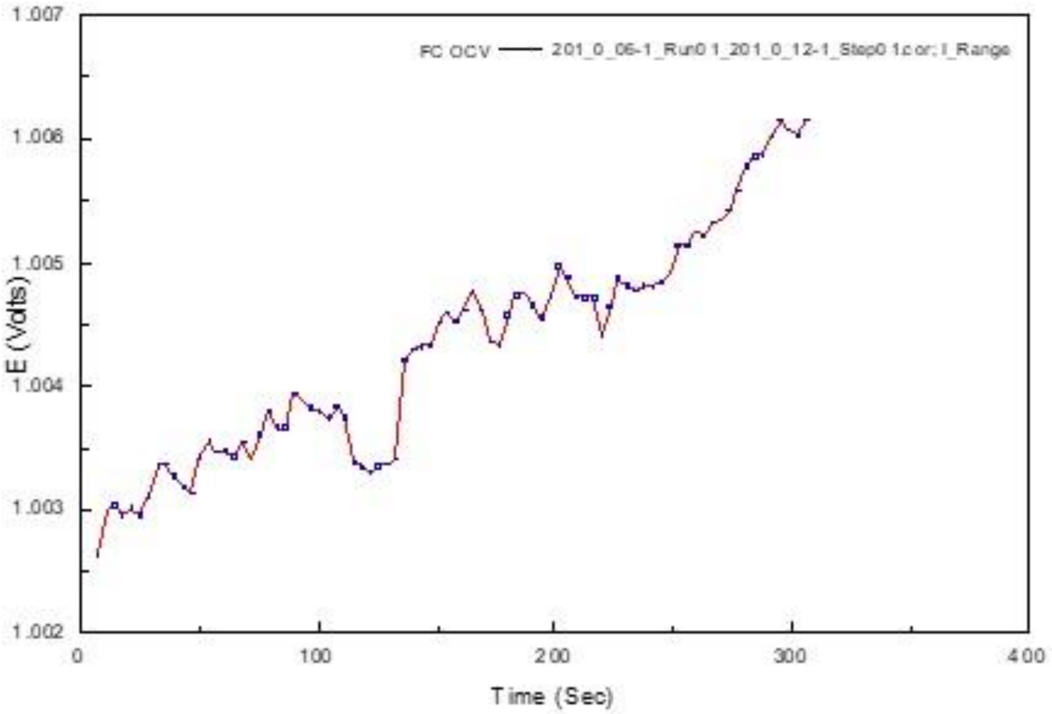

Figure 4-11: SOFC mode OCV at 750 °C.

Figure 4-12 shows the current-voltage characteristics of the cell under a current density ramp rate of approximately 0.025 A/cm^2/min. For every 0.025 current density ramp up per minute cycle, there was a corresponding loss of about 0.01V. These losses were mainly a result of four factors: fuel crossover, activation, Ohmic and mass transport. Fuel crossover losses were due to the reactant fuel (i.e. hydrogen in the present work) crossing over to the oxygen electrode by passing through the electrolyte or other possible leak paths. Activation losses were due to slow reaction kinetics at the electrode/electrolyte interfaces. Ohmic losses were due to resistances to ionic and electronic transfer through the electrodes, electrolytes and current collection system, as applicable.

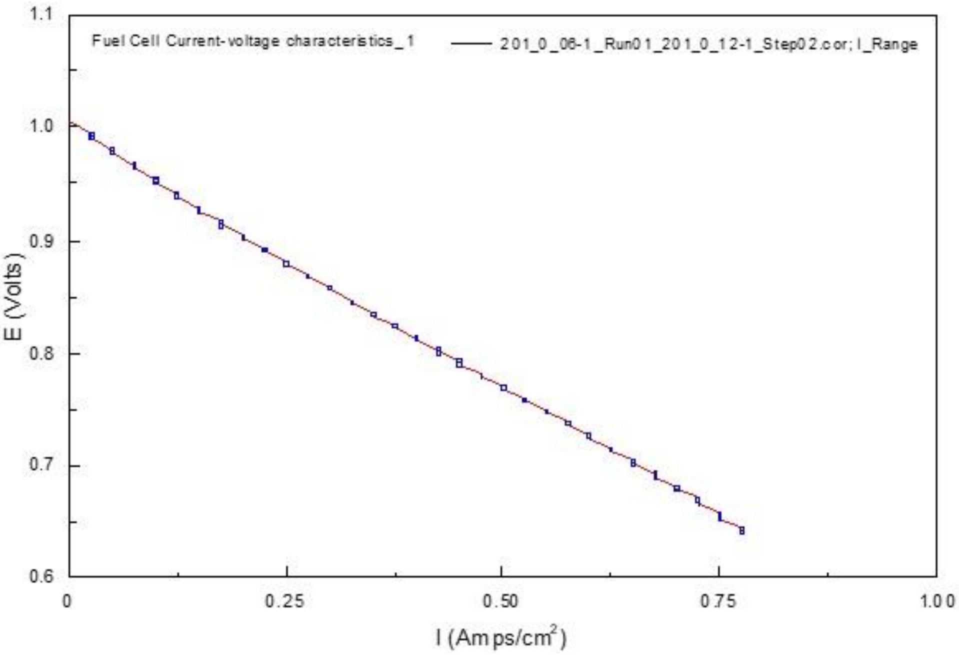

Figure 4-12: Current - voltage characteristics in SOFC mode at 750 °C.

A more general trend of these voltage losses are shown in the long-term constant current operation results under SOFC mode as presented in *Figure 4-13* and Figure 4-14.

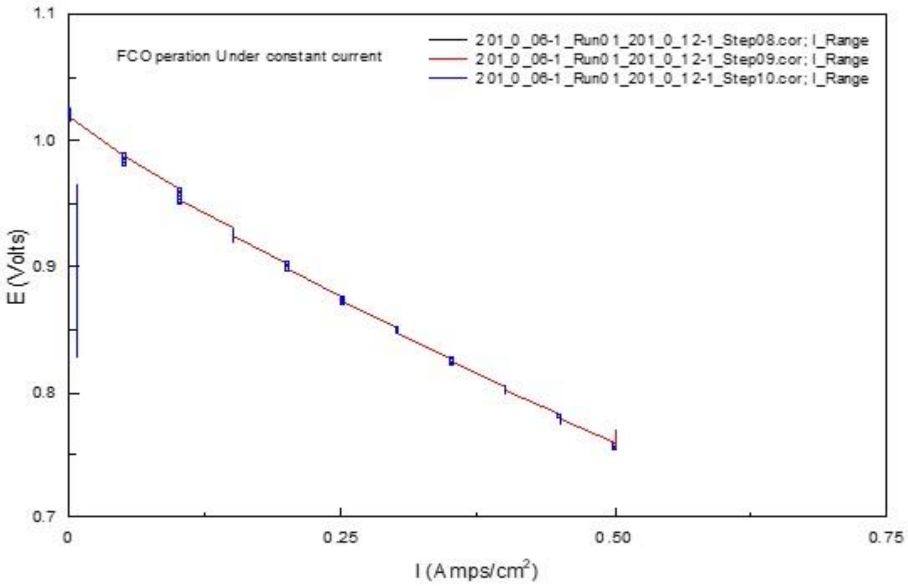

Figure 4-13: *j-V* characteristics under a ramp rate of 0.05 Amps/cm^2/min prior to operation in SOFC under constant current at 750 °C.

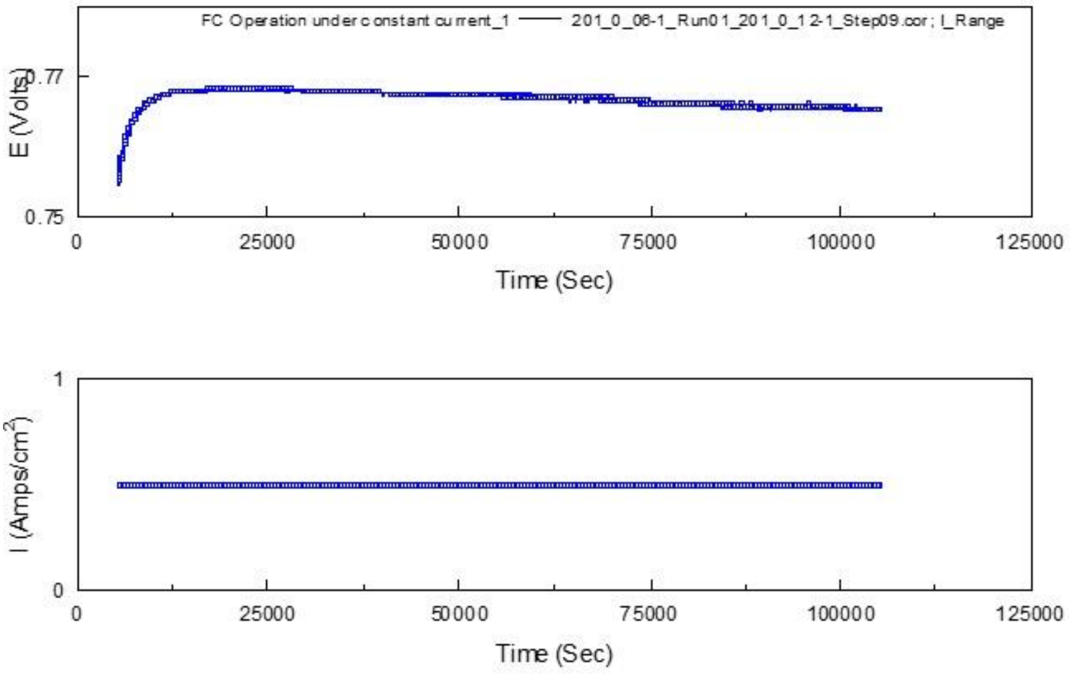

Figure 4-14: Operation in SOFC mode under constant current at 750 ^{o}C.

Figure 4-15 and *Figure 4-16* show the impedance characteristics of the cell under the SOFC conditions of operation. A good quality impedance spectra allows for a more detailed analysis of cell performance by enabling a delineation of the different polarisation losses. This is because the different loss factors are prominent under different frequency regimes. Thus by cycling the cell under different frequency regimes, an indication of the magnitude of the contributions from the different polarisation losses (i.e. activation, Ohmic, mass transport) may be gleaned. *Figure 4-15* is the 'Nyquist plot' of the cell, and the corresponding Bode Plot is given by *Figure*

4-16. There was considerable scatter in the mass transport region (i.e. low frequency region) of the Nyquist Plot, most likely as a result of instabilities in the steam generating CEM.

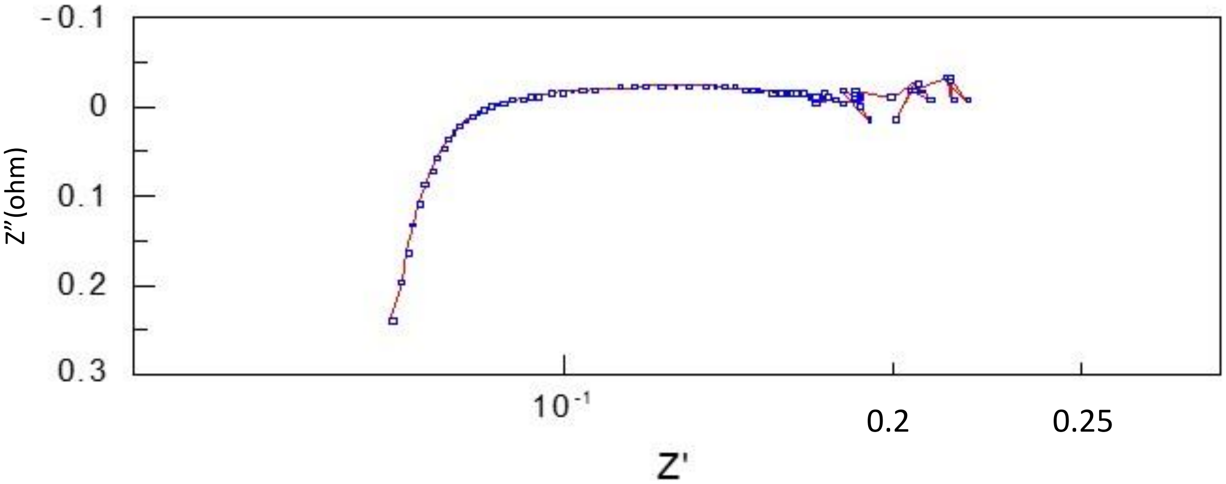

Figure 4-15: SOFC mode Nyquist plot.

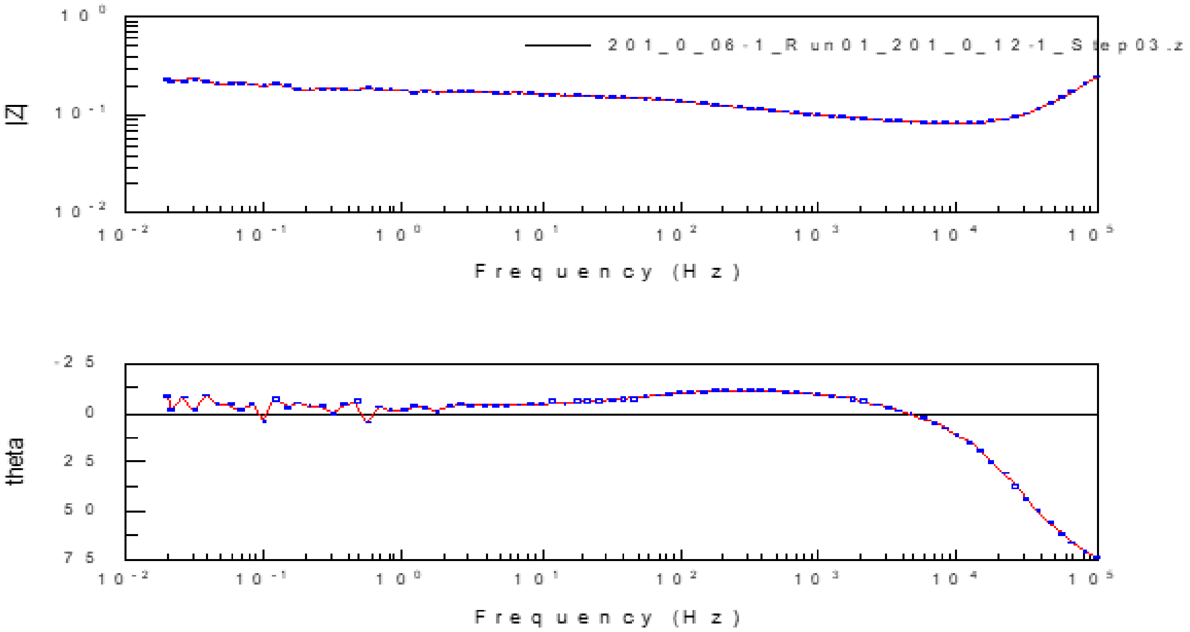

Figure 4-16: SOFC mode Bode plot.

The corresponding SOE results for the SOFC results presented in *Figure 4-11*, *Figure 4-12*, *Figure 4-15*, and *Figure 4-16* are presented in *Figure 4-17*, *Figure 4-18*, *Figure 4-19*, and *Figure 4-20* respectively. The recorded OCV under SOE conditions was approximately 0.85V in accordance with *Figure 4-17*. *Figure 4-18* indicates a voltage loss of at least 0.015V per minute for every 0.025 A/cm^2 current density ramp. This is greater than the ~0.01V voltage loss per ramp observed for the SOFC mode of operation. The SOE 'Nyquist' and 'Bode' plots are presented in *Figure 4-19* and *Figure 4-20*, respectively.

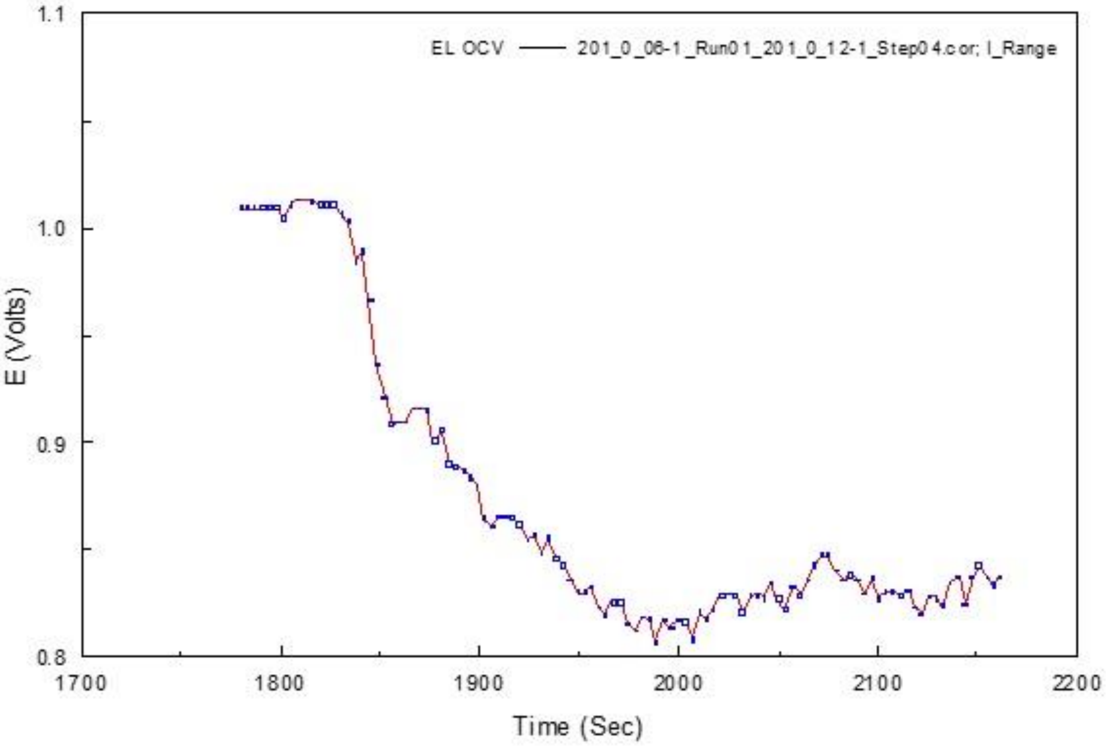

Figure 4-17: SOE mode OCV at 750 ^{o}C.

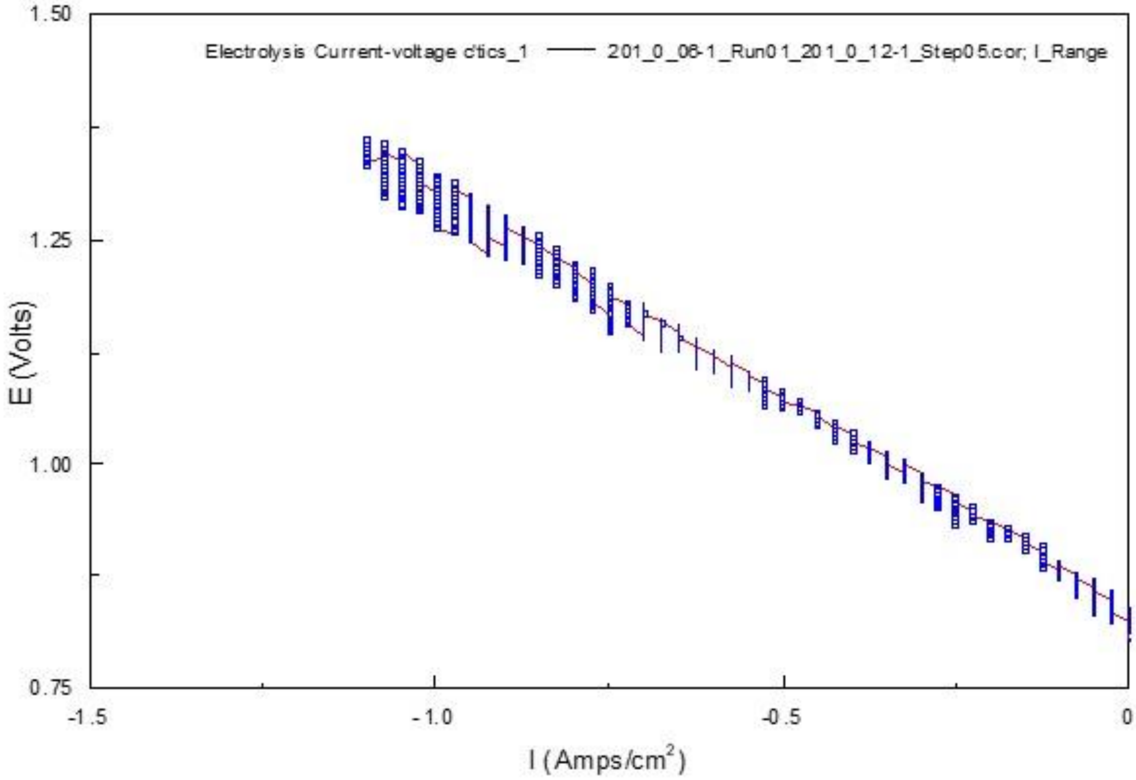

Figure 4-18: Current - voltage characteristics in SOE mode at 750 °C.

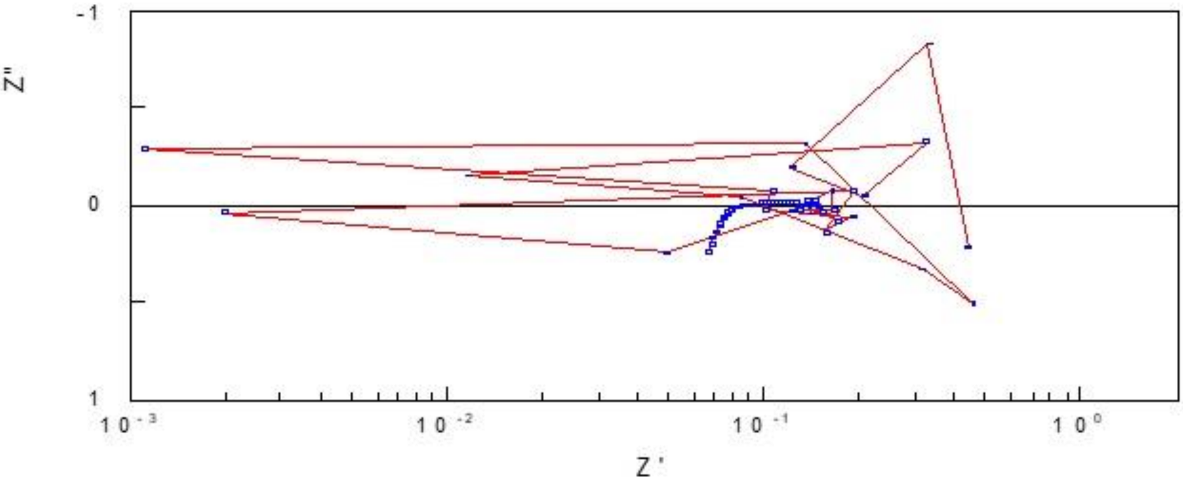

Figure 4-19: SOE mode Nyquist plot (significant scatter in the mass transfer region).

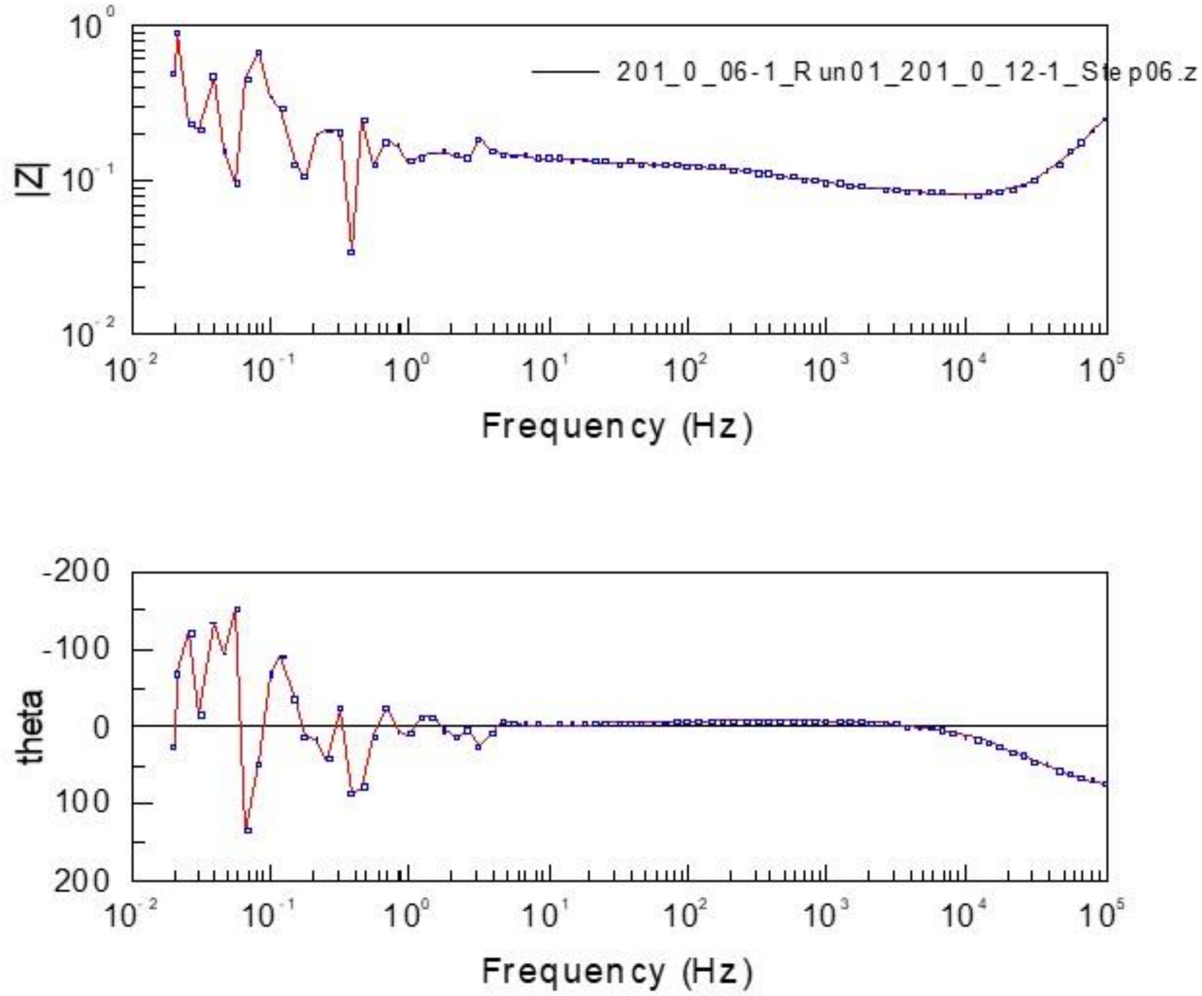

Figure 4-20: SOE mode Bode plot.

It was not possible to capture any results for operation in SOE mode under constant current (the SOE equivalent of Figure 4-14) using the silver-based current collection system. This silver-based current collection system was found to be suitable for short term testing (≤1 week) only. For longer term testing, the embossed silver paste and wires on the oxygen electrode surface oxidised/combusted and disbonded leading to test failure, Figure 4-21.

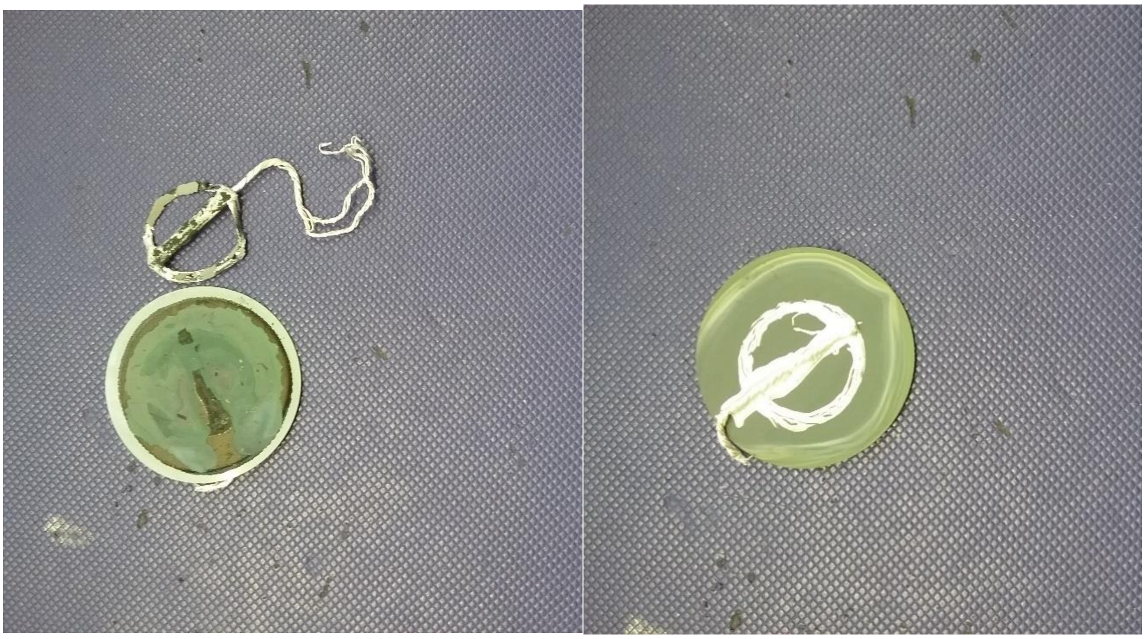

Figure 4-21: Degradation of the silver-based current collectors under test conditions.

Therefore the 2nd current collection system was used for all long-term tests to deliver the test protocol detailed in Section 4.2.2. This system consisted of nickel wires and mesh current collectors on the fuel electrode side, and gold wires and mesh on the oxygen electrode side (see Figure 4-22).

All the results (i.e. subsequent work) reported in Chapters 5, 6 and 7 of this thesis utilised nickel wires and mesh current collectors on the fuel electrode side, and gold wires and mesh on the oxygen electrode side.

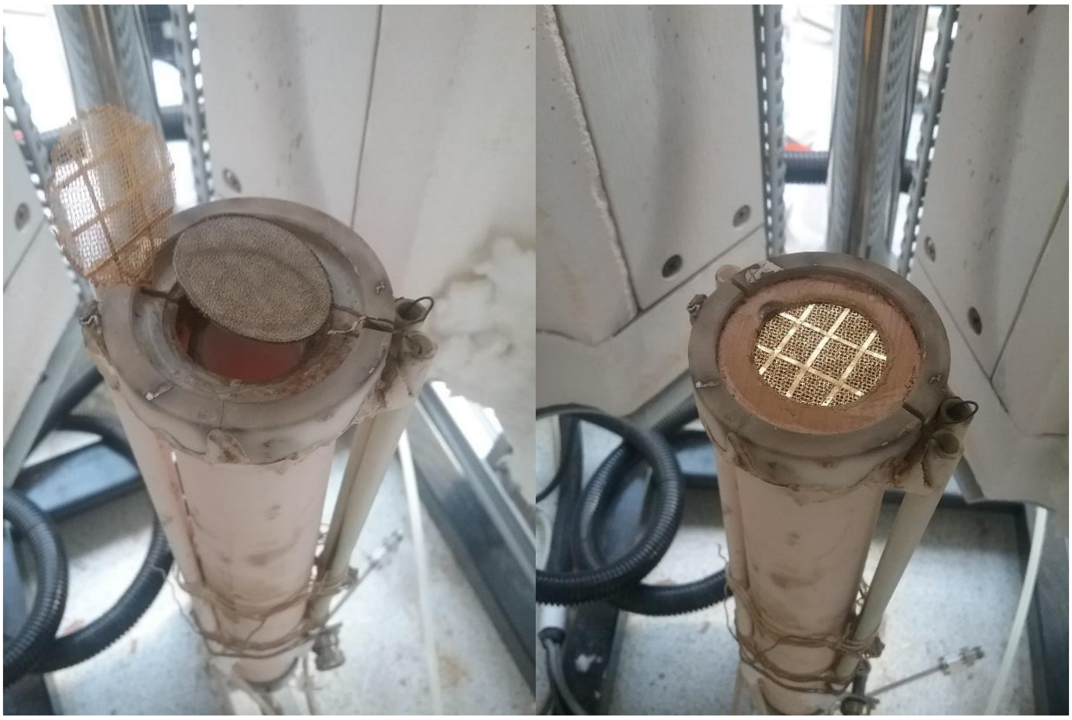

Figure 4-22: Gold and nickel mesh/wires current collection system

4.2 Experimental Methods

4.2.1 Description of test apparatus

The experimental test hardware designed and constructed for the rSOC testing is shown in Figure 4-23 and Figure 4-24 . Gas mass flow controllers (MFCs) were connected in parallel to individually measure and deliver required gas quantities via a main outlet pipe to a controlled evaporator mixer (CEM). The delivered gases were nitrogen and hydrogen, used as required in different combinations and quantities for fuel cell and electrolysis modes, respectively. A liquid MFC to measure and deliver water to the CEM was also connected.

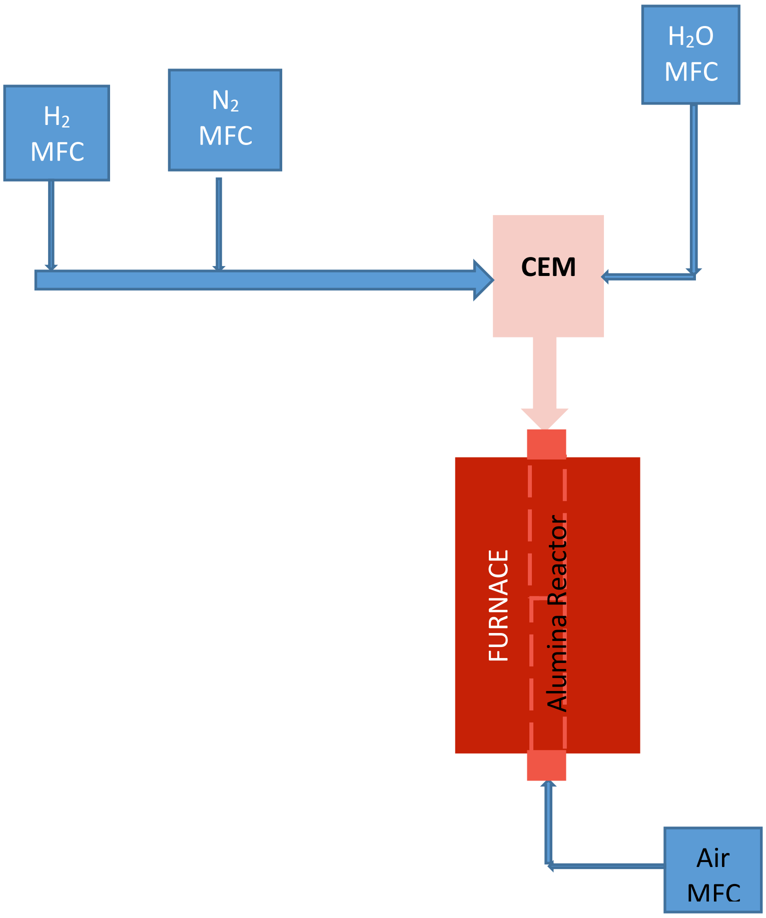

Figure 4-23: Schematic of rSOC experimental test apparatus.

The CEM heated up and evaporated the water, mixing it with the other gases before delivering the gas mixture to the hydrogen electrode. A separate gas MFC measured and delivered air/oxygen to the oxygen electrode.

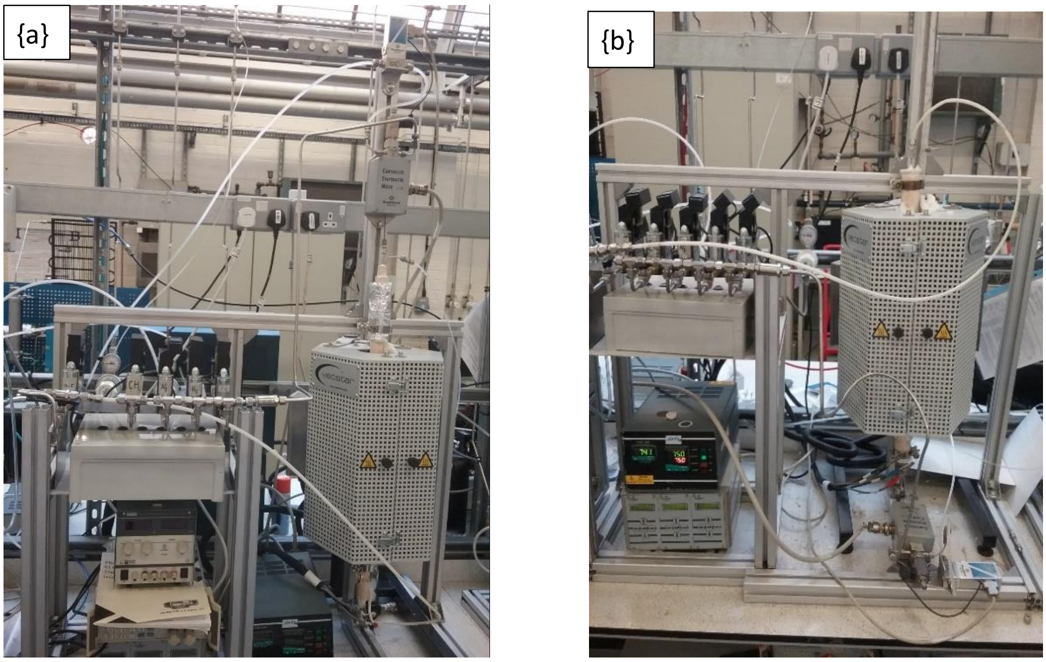

Figure 4-24: rSOC experimental test apparatus with the CEM for delivery of the reactants to the fuel electrode located at the top {a), and CEM for delivery of the reactants to the fuel electrode located at the bottom {b}.

Two different vertical test apparatus configurations were employed for the experimental work to investigate any possible effect of gravity on cell performance (i.e. mass transport effects) during reversible operation. The feed gases to both the hydrogen and oxygen electrodes would thus be delivered against gravity and with gravity. It is probable that for vertical rSOC set-ups, delivery of the feed gases to the hydrogen electrode against gravity would be beneficial in SOFC mode whilst the reverse should hold for SOE mode due to the differential densities of the reactant gases and products, despite the high temperatures and a pseudo-closed system. Test apparatus {a}, which has the same configuration as the schematic in *Figure 4-23*, should therefore be more suited to SOE operation whilst test apparatus {b} should be more suitable for SOFC operation. If proven, this may necessitate a flexible test apparatus design to accommodate both configurations in order to optimise the rSOC mass transport variables.

The unit cell, comprising of a hydrogen electrode, an electrolyte and an oxygen electrode was housed in an alumina tube-in-tube reactor (see Figure 4-25). The alumina reactor was then centrally located in a Vecstar furnace. The alumina half-reactor was fabricated with two alumina tubes, an inner and an outer tube. The inner tube was connected to the piping from the CEM outlet to receive the reactant gases to the hydrogen electrode. The annulus of the tube-in-tube construct was fitted with an exhaust piping to convey the product gases (and unreacted reactant gases) from the hydrogen electrode. The product gases were then routed to a gas chromatograph / flow meter for quantification or analysis and then to the lab exhaust gas system for disposal when operating in electrolysis mode, or the product gases were routed directly to the lab exhaust gases system for disposal when operating in fuel cell mode. The other half-reactor was similarly fabricated for conveying air/oxygen to the oxygen electrode via the inner tube and exhaust gases via the annulus to a gas chromatograph and/or the lab exhaust system, depending on the mode of operation.

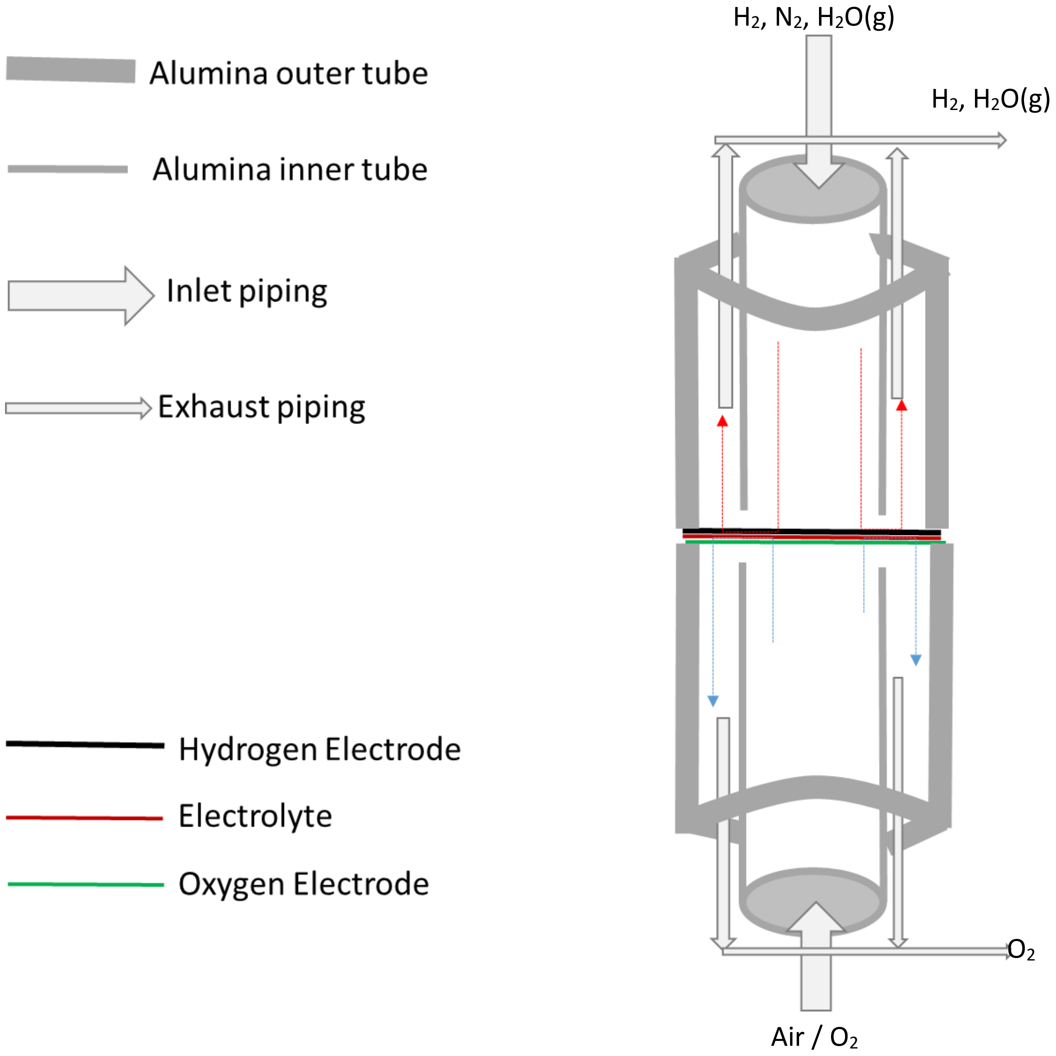

Figure 4-25: An illustration of the alumina tube-in-tube reactor in accordance with test apparatus configuration {a}.

Sealing / gas-tightness of the alumina tube was a significant problem because of the need to connect wires to the electrodes for current collection/delivery. As shown in Figure 4-26, the wires stood proud of the tube edges thus preventing complete tube closure. Encasing the wires in a circular rim of gas-tight mica around the tube edges did not help much due to insufficient relative compression of the half-reactors.

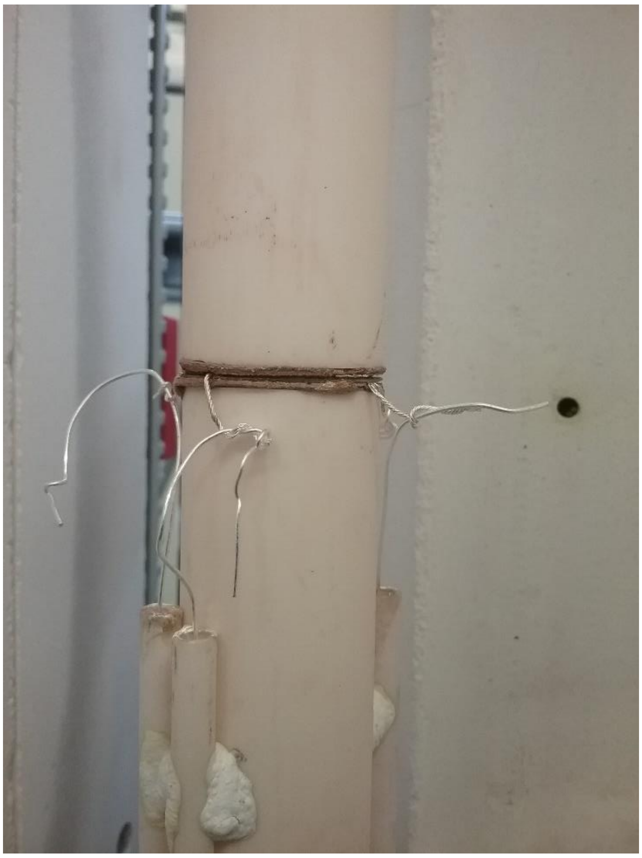

Figure 4-26: Lack of gas tightness / adequate sealing at the alumina tube edge around the unit cell.

A sealing mechanism or closure piece for the alumina tube edges was thus fabricated from MACOR®, a machinable ceramic. This consisted of male- and female- like connectors (see Figure 4-27) fitted onto an outsized alumina tube-in-tube fabrication with a groove for the current collector/delivery wires. An outsized alumina tube-in-tube was employed in order to, as far as practicable; contain any leaks within the tube annulus and prevent mixing of the anode and cathode reactants and products.

Two cables, one for voltage sensing or potential measurement, and the other for carrying current, were connected to both the anode and cathode, respectively. Different cables were used for potential measurement, and thus separate from those carrying current, in order to avoid errors due to voltage drop.

Figure 4-27: Male and female end closure connectors designed to improve leak-tightness.

4.2.2 Operating variables

The operating variables utilised in the present work to investigate the performance of the state-of-the-art cells are given in *Table 4-5*. These variables were used for investigating cell performance by the BALANCE project consortium and have been implemented in this project as the base case test condition to serve as a useful benchmark for all work done under the scope of the PhD research.

Table 4-5: Operating variables for single cell testing.

Mode of Operation	Temperature	Gas composition to fuel electrode compartment*	Gas to oxygen electrode compartment	Current Density	Fuel electrode reactant utilisation at 0.5 $A \cdot cm^{-2}$	Operating period
SOFC mode	≤ 750°C	0.8 $L \cdot h^{-1} \cdot cm^{-2}$ of 50% H_2 + 50% N_2 (0.4 $L \cdot h^{-1} \cdot cm^{-2}$ H_2 + 0.4 $L \cdot h^{-1} \cdot cm^{-2}$ N_2)	3.75 $L \cdot h^{-1} \cdot cm^{-2}$ Air	≥ 0.5 A/cm^2 (+ve)	≥ 52.3%	3 hrs
SOE mode		0.5 $L \cdot h^{-1} \cdot cm^{-2}$ of 80% H_2O + 20% H_2 (0.1 $L \cdot h^{-1} \cdot cm^{-2}$ H_2 + 0.4 $L \cdot h^{-1} \cdot cm^{-2}$ H_2O)	0.75 $L \cdot h^{-1} \cdot cm^{-2}$ Air	≥ 0.5 A/cm^2 (-ve)	≥ 52.3%	20 hrs

In order to study the effect of the various parameters (temperature, current density, reactant flow rates and fuel utilisation), different operating variables to the base case (Table 4-5) were also employed. The various magnitudes of operating current density and reactant flow rates gave the theoretical fuel utilisations employed, as calculated using Equations 3 - 1 to 3 - 3, and detailed in Table 4-6.

Table 4-6: Test fuel utilisations

Test ID	CT1_0.5_750#1	CT1_0.5_700#1	CT1_0.7_750	CT1_1.25_750	CT1_1.39_750	CT1_2.65_750	CT2_0.5_700	CT2_0.5_750	CT2_0.7_750
Cell Type	1	1	1	1	1	1	2	2	2
Temperature (°C)	750	700	750	750	750	750	700	750	750
Current Density (A/cm^2)	0.5	0.5	0.7	1.25	1.39	2.65	0.5	0.5	0.7
H_2 Flow Rate (ml/min)	35.3	35.3	35.3	55.3	70	97.6	35.3	35.3	35.3
FUEL UTILISATION (%)	**52.3**	**52.3**	**73.2**	**83.5**	**73.4**	**100**	**52.3**	**52.3**	**73.3**

The base case flow rates employed (see sections 4.2.2.1.2 and 4.2.2.2.2), coupled with the minimum current density used for the work (see sections 4.2.2.1.3 and 4.2.2.2.3) resulted in a fuel utilization of 52.3 % (see *Table 4-6*). In accordance with [Equation 3 – 3], the fuel utilisation affects the mass transport of reactants and products, ionic transport of chemical species and electronic transport. It was therefore expected that at low fuel utilisation, the contributions of both electrode polarisation resistance and electrolyte ionic conduction would be low, thus lowering the overall cell degradation rate. At high fuel utilisation, due to the increased demands placed on both electrode mass transport and catalytic activity, and ionic transport through the electrolyte, as well as electron transfer of all relevant cell components, observed cell degradation is more likely to be high due to the cell degradation mechanisms described in Section 3.2. Therefore, fuel utilisations greater than 50% in both SOFC and SOC modes were used in the work reported in this thesis in order to benchmark cell performance and degradation under ideal commercial operating conditions.

4.2.2.1 SOFC Mode

4.2.2.1.1 Temperature

750^{o}C was the base case temperature employed in this work. Some tests were also performed at a lower temperature of 700^{o}C to investigate cell performance at relatively lower temperatures. Good cell performance at lower operating temperatures are generally more desirable for commercial operation due to the associated decreased energy required (lower heat and electric energy input) and the possibility of utilising less expensive balance of plant component materials. In addition, the stability of stack materials decreases with increasing operating temperature [5].

4.2.2.1.2 Feed and Flow rates

Under SOFC mode, 0.4 L/hr/cm^2 of hydrogen gas (H_2) was fed to the hydrogen electrode. For the 3 cm unit cells, with approximately 5.3 cm^2 oxygen electrode active area (i.e. an active area diameter of 2.6 cm), used for the work, 35.3 ml/min H_2 was fed to the hydrogen electrode. A similar flowrate of nitrogen gas (N_2) was utilised as the H_2 carrier gas.

3.75 L/hr/cm^2 (i.e., 331.25 ml/min) of compressed air was fed to the oxygen electrode.

4.2.2.1.3 Electric current operation/supply

All the tests were performed under galvanostatic mode. This means that during SOFC operation, a constant current of ≥ +0.5 A/cm^2 (approximately 2.65 A) was drawn from the cell. Changes in cell voltage were thus used to monitor qualitative performance of the cell.

Also, due to the active area of the cells (5.3 cm^2), the highest current density employed in the tests was 2.65 A/cm^2, chosen based on the 2.65 A nominal current required at the lowest current density used for the tests (0.5 A/cm^2).

4.2.2.2 SOE Mode

4.2.2.2.1 Temperature

Under a given set of conditions for SOFC operation, the operating temperature under SOE mode was the same as that under the SOFC mode.

4.2.2.2.2 Feed and Flow rates

Under SOE mode, 0.4 L/hr/cm^2 of steam (approximately 35.3 ml/min of $H_2O_{(g)}$), was fed to the hydrogen electrode. This translated into approximately 1.3 g/hr of liquid water to the controlled evaporator mixer (CEM) used for generating the steam supply (i.e. using a steam density of 600 g/m^3). 0.1 L/hr/cm^2 of hydrogen gas (approximately 8.8 ml/min of $H_{2(g)}$) was added to the hydrogen electrode fuel mix to prevent instantaneous oxidation of the nickel catalyst used in the hydrogen electrode.

0.75 L/hr/cm^2 (66.25 ml/min) of compressed air was fed to the oxygen electrode under SOE mode.

4.2.2.2.3 Electric current operation/supply

Under SOE galvanostatic mode of operation, a minimum of 0.5 A/cm^2 (2.65 A) of current was supplied to the cell to electrolytically produce hydrogen from steam.

4.2.3 Test Protocol

The SOC was first conditioned (hydrogen electrode reduced) by holding the furnace temperature at about 850^{o}C for about 2 hours with double the operating gas rates given in Section 4.2.2 (i.e., 0.8 L/h/cm^2 of H_2 plus 0.8 L/h/cm^2 of N_2). The test programme, began after cell conditioning, by ramping down the reactor temperature to the required test temperature and adjusting the flow rates of the reactant gases to the respective reactor (i.e. anode and cathode) compartments. Relatively low operation temperatures were utilised (700°C or 750°C) in order to compare performance with work done with similar SOCs at higher temperatures (800°C to 850°C), as reported in the literature [5]. Acceptable performance at lower temperatures would enable the use of a wider variety of balance of plant materials at the system level, thus relatively lowering the overall technology cost.

After holding the reactor temperature at the operating temperature, the open cell voltage (OCV) of the test cell was recorded (see 4.2.4 below for electrochemical data acquisition). If the

OCV was as expected (i.e. between approximately 1000 to 1200 mV in accordance with the thermodynamic parameters for the electrolysis of H_2O given in *Figure 1-3*), then j-V and EIS characterisations were undertaken to examine the performance of the virgin cell. If the virgin cell performance was as expected, the test programme proceeded with constant current SOFC regime at the defined current density and for the required duration, with the given SOFC gas composition and flow rates supplied to the fuel electrode and oxygen electrode compartments. The required galvanostatic current density was attained by ramping the test current density from 0 to the required test current density via a step magnitude equal to 10% of the required current density with 60 seconds hold-time per step. Therefore, for testing at 0.5 A/cm^2, the test current was increased at 0.05 $A/cm^2/min$.

After the constant SOFC operation, j-V and EIS characterisations were undertaken again to check the cell performance and benchmark any cell degradation following SOFC operation. This was followed by a constant current SOE regime for the same duration and current density as for the preceding SOFC regime, with the given SOE gas composition and flow rates supplied to the fuel electrode and oxygen electrode compartments. The reactant utilisation at the fuel electrode in both SOFC and SOE modes was maintained as a constant, although it may be more efficient to operate the rSOC with higher utilisations in SOE mode relative to SOFC mode (see *Figure 4-28*. The work reported in this thesis corresponds to the Water-Air mode since during electrolysis operation, steam is supplied to the fuel electrode whilst air is supplied to the oxygen electrode).

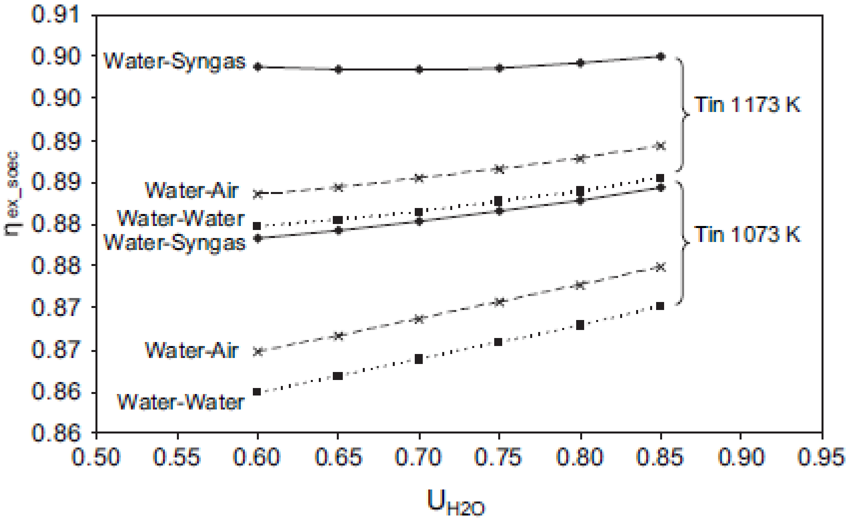

Figure 4-28: SOE efficiencies for different cathode water utilisation and input temperature *[143]*.

After the constant current SOE operation, another performance check of j-V and EIS characterisations was performed. This was followed by reversible SOFC and SOE operation with a cycling duration of 3 and 20 hours, respectively, but otherwise under the same conditions as for the constant current SOFC and SOE operation.

Each reversible operation cycle started with changing the gas composition and flow rates to those required for SOFC operation. The current was then ramped up to the required current density to be drawn from the cell, holding it for 3 hours, and then ramping down to the open circuit voltage to change the gas composition and flow rates to those required for SOE operation. After the reactants' changeover, the current was then ramped up to the required current density to be supplied to the cell for gas production, holding it for 20 hours, before ramping down to OCV.

The overall test flow chart and test profile for the reversible operation are illustrated in *Figure 4-29* and Figure 4-30, respectively. The subject under investigation, as detailed in the following chapters, determines the number of cycles for the reversible operation. The test was completed by running final j-V and EIS characterisations under both SOFC and SOE conditions before shut-down.

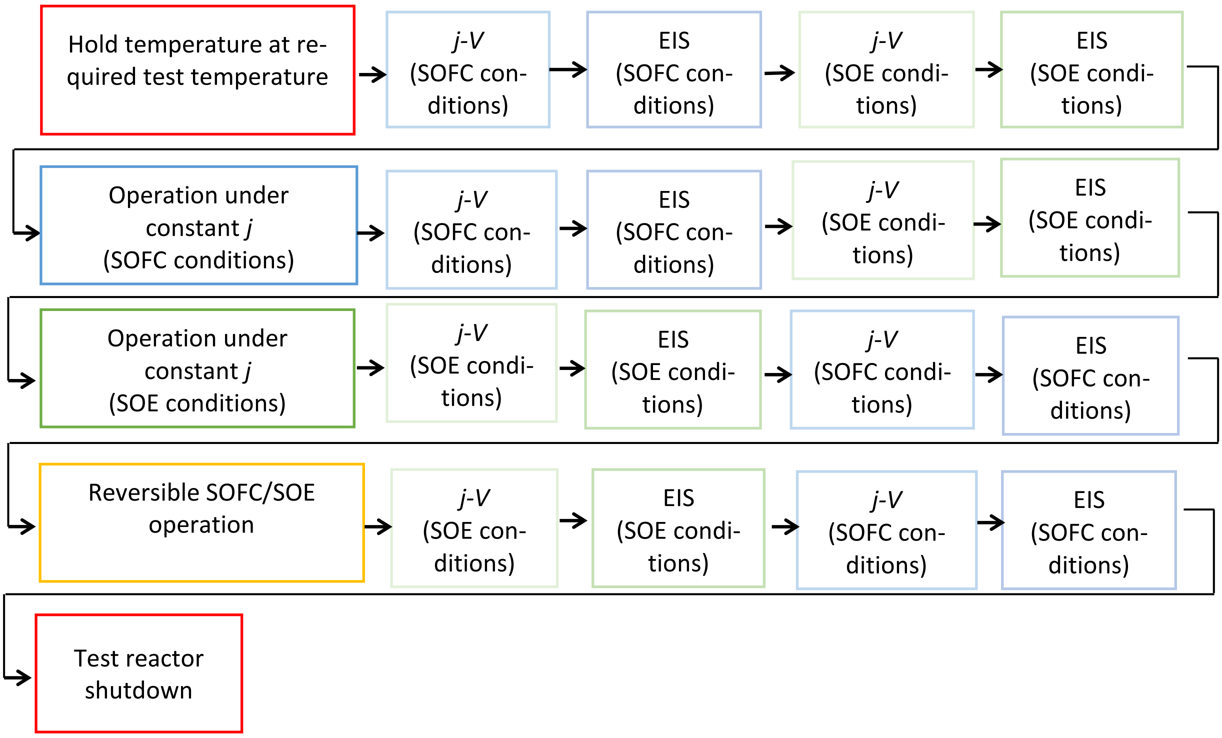

Figure 4-29: Flow chart for the typical test regime used in the work (i.e., power-to-gas-to-power application specific test programme). Switching time between SOFC and SOE modes was approximately 30 minutes.

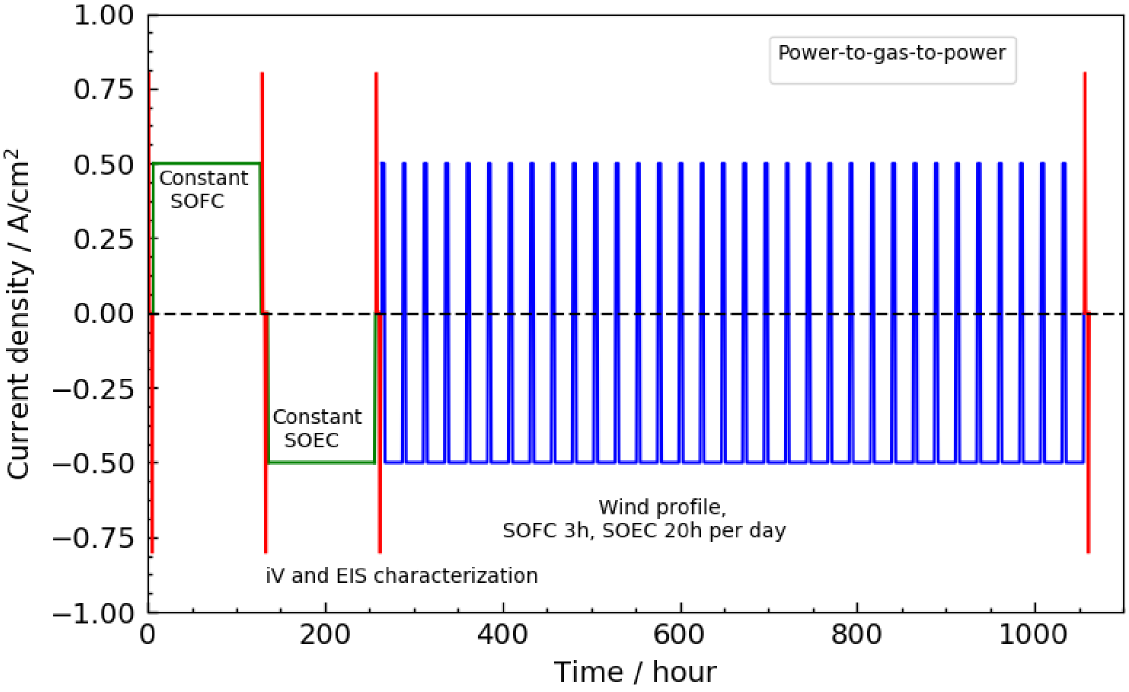

Figure 4-30: Typical profile for the overall test protocol (j = ±0.5 A·cm^{-2} during reversible operation).

4.2.4 Electrochemical data acquisition

All electrochemical testing was controlled and recorded using a galvanostat (Solatron Model 1470E) connected to a frequency response analyser (Solatron 1455 FRA) for impedance measurements. The raw solatron data was deconvoluted using the Multistat software and then analysed using MATLAB. The following sub-sections detail the instrument settings used to interrogate the cell in both fuel cell and electrolysis mode.

4.2.4.1 Current-Voltage characteristics

After capturing the cell OCV, initial cell performance was evaluated by recording its current-voltage characteristics (j-V curve). All j-V curves were performed as galvanostatic stair-steps of ≥ 0.025 A/cm^2 (i.e. step increase of 5% of test current density) with a step duration of 30 seconds. The duration of 30s was found to be enough for the cell to reach steady state before the next step (see *Figure 4-31*). To prevent irreversibly damaging the cell, maximum current density to be drawn from the cell is reached when the corresponding cell voltage falls below 0.65 V under SOFC conditions. The corresponding maximum current density under SOE conditions is when the cell voltage exceeds 1.35 V.

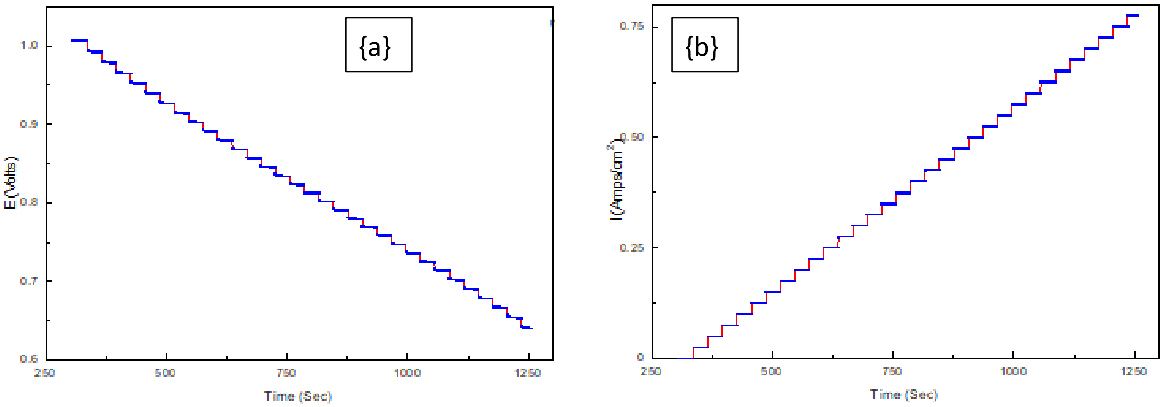

Figure 4-31: Galvanostatic stair-step used for recording SOC j-V characteristics {a} shows voltage drop per step whilst {b} shows current density increase per step.

The j-V curve provided some information on the resistances in the cell and gave the corresponding voltages at various current densities. The j-V curve is a useful tool to compare the performance of different cells and gives indication of the main losses in the cell. However, this information is limited. An example j-V curve for a cell operated under fuel cell and electrolysis modes is shown in *Figure 4-32*.

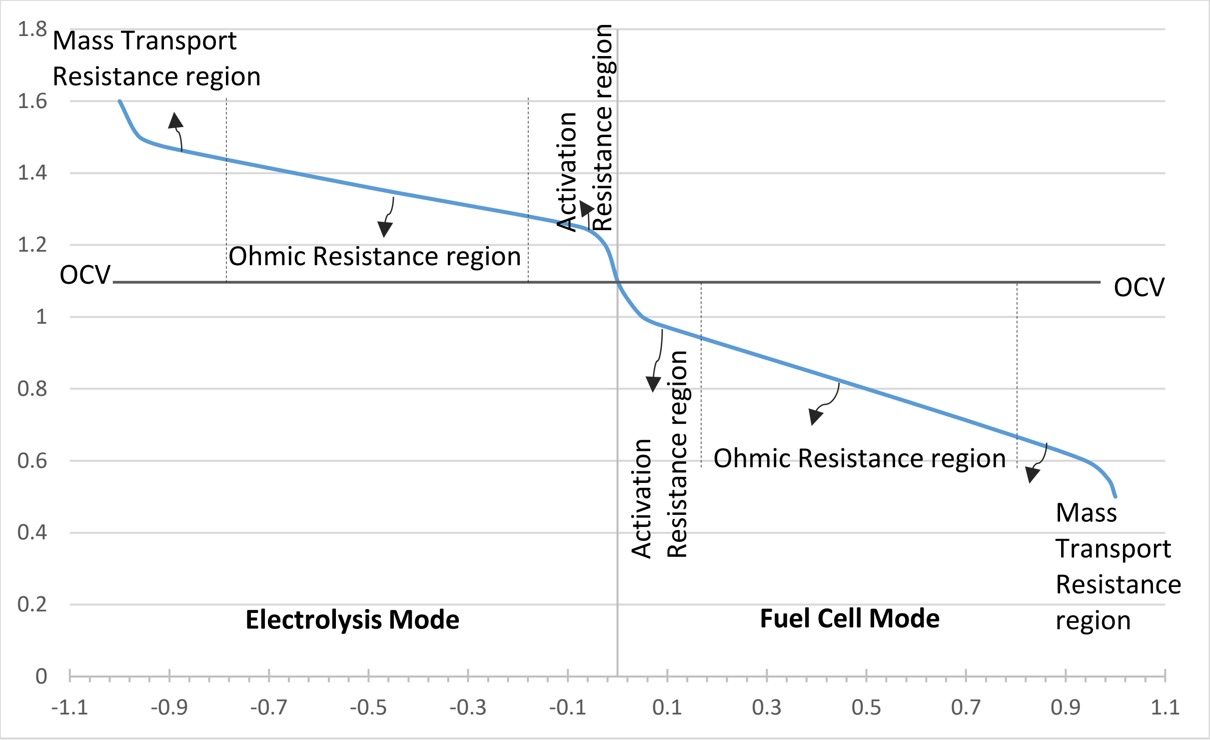

Figure 4-32: Fuel cell and electrolysis example j-V curve.

The j-V curve indicates the activation, Ohmic and mass transport resistance contributions (overpotentials) to effective cell voltage. The high operating temperatures of the SOFC technology result in typically small activation overpotentials. The area specific resistance (ASR) of the cell may be calculated as the gradient of the linear (Ohmic resistance) region of the curve, outside the activation or concentration overpotential regions.

4.2.4.2 Electrochemical impedance spectroscopy (EIS)

The use of j-V curves provides top-level, but limited information about the resistances to ideal cell performance. The area specific resistance (ASR), which is akin to the Ohmic cell resistance, is the most useful information that can be gleaned from the j-V curve, by calculating the gradient of the linear region of the j-V curve. Therefore, electrochemical impedance spectroscopy (EIS) is commonly used in-situ to interrogate the various individual contributions to the overall cell degradation. Impedance is analogous to the resistance from Ohms law, since it is also the ratio between voltage and current. However, it does not only indicate the ability of a circuit to resist the flow of electrical current (i.e. the 'real impedance' term) as is the case for the Ohms law resistance, but it also demonstrates the ability of the circuit to store electrical energy, like a capacitance or inductance (i.e. the 'imaginary impedance' term). Therefore, impedance may be more correctly defined as the 'complex resistance' encountered when alternating current (AC) flows through a circuit composed of various resistors, capacitors and inductors [82].

EIS is based on the measurement of a transfer function due to a disruption of the electrochemical system under consideration. Since impedance is analogous to Ohms law resistance, pseudolinearity of the transfer function must be ensured by limiting the applied disruption. Therefore, since the measurements carried in this thesis were done in galvanostatic mode, the applied current was set equal to 0A with a small AC amplitude (10mA) for alternating current flows.

The main processes, which lead to losses in a fuel cell, are related to Ohmic resistance (ionic and electronic charge transfer overpotentials), activation overpotential, and mass transport overpotentials. Before charge transfer across an electrochemical interface, there needs to be mass transport of reactive species across the bulk phase (often coupled with chemical reactions), electrode adsorption of the reactive species, and interfacial electrochemical and chemical reactions. EIS seeks to dissect the various individual electrochemical contributions to fuel cell performance or degradation [82], [136].

Due to the more detailed cell performance information which EIS provides, EIS was used in this work to quantify the different contributions to the overall cell degradation.

Unless otherwise stated, the following settings were used for the EIS measurements: they were made between 100,000 Hz and 0.02 Hz as a logarithmic frequency sweep with 12 frequency points per decade (starting from 100 kHz to 20 mHz). This frequency range was chosen to enable the capture of low frequency mass transport and electrode polarisation resistance, and the high frequency ohmic resistance.

The EIS was current controlled (galvanostatic operation) with an applied DC current of 0 A (i.e. at OCV) in both fuel cell and electrolysis modes. An AC amplitude of 10mA was applied to the cell to ensure pseudolinearity.

For EIS data analysis, the multistate software based on the distribution of relaxation times (DRT) method [144], [145] was used to deconvolute the impedance spectra, and the electrical equivalent circuit (EEC) method was then employed to interrogate or fit the deconvoluted impedance spectra [82]. *Figure 4-33* show the good agreement between the raw data and the employed EEC model data.

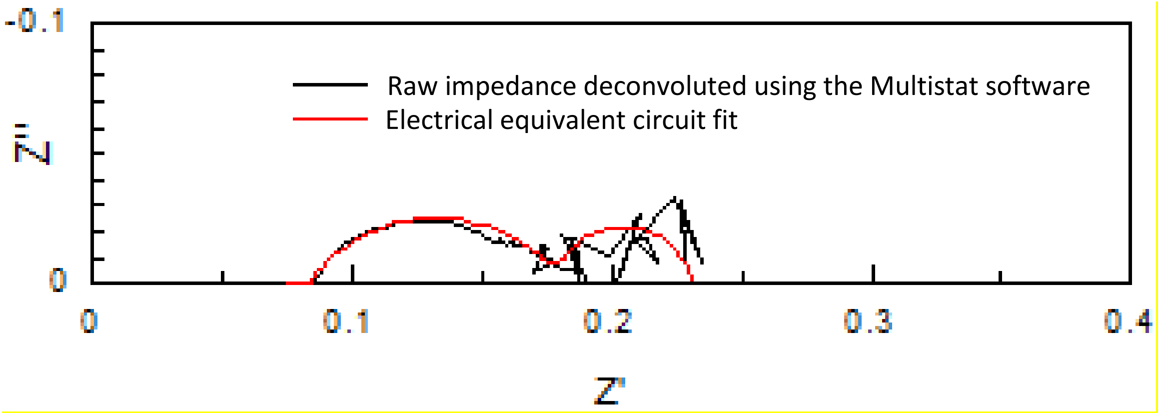

Figure 4-33: Raw impedance spectra and EEC model fit spectra

4.2.4.2.1 Distribution of relaxation times

The distribution of relaxation times, which is a function of the relaxations times (rate constants) and relaxation amplitudes (loss factors), is the primary parameter of interest in the impedance data analysis. However, the relaxation times cannot be measured directly due to interference or perturbation (poor resolution). This is because an impedance measurement at a required frequency also captures significant relaxation time information from adjacent frequencies (i.e. contributions from other physically distinct processes occurring at an inverse frequency magnitude above and below the desired frequency), especially for complex electrochemical systems such as solid oxide cells [82].

A distribution function of relaxation times and relaxation amplitudes of impedance related processes may however be calculated directly from experimental data using a deconvolution method. This method is helpfully known as Distribution of Relaxation Times (DRT) and provides a direct access to the dynamic constants in the impedance data. The calculated distribution of relaxation times also provides information on the kinetic parameters of the prevailing processes. The DRT approach prevents the subjectivity inherent in fitting experimental data to a prior selected electrical equivalent circuit (EEC). It was therefore used in the present work as a pre-identification tool to select the most appropriate EEC [82], [144].

Fourier analysis of the impedance data coupled with digital filtering of the data in the transformed space and extrapolation techniques are required to access the distribution of relaxation of times. For the present work, this was done using the multistat software, and the various steps required to resolve the data are detailed in reference [144].

4.2.4.2.2 Electrical equivalent circuit

The electrical equivalent circuit employed in this work is shown in *Figure 4-34*.

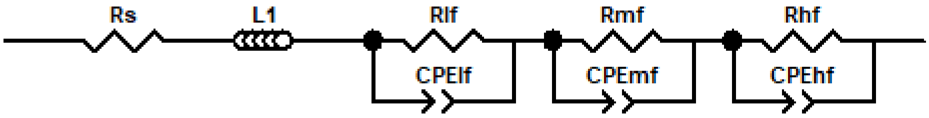

Figure 4-34: Employed EEC model *[82]*, *[144]*, *[146]*.

The Ohmic or series resistance, R_s, is the impedance at the highest frequencies (approx. ≥ 50 kHz) or the frequency independent part of the impedance (i.e. the offset in the high-frequency real part of the impedance). It is analogous to the slope of the j-V curve (*Figure 4-32*), and is dominated by the resistance to ionic transfer between the fuel and oxygen electrodes (i.e. ohmic resistance of the electrolyte, including electrolyte – electrode interfaces), and some contribution from the resistance to electronic charge transport through the electrodes and current collectors.

L1 seeks to capture the inductance of the current collectors, including the current/voltage probes of the electrochemical equipment.

Polarisation resistance, R_p, is the impedance at medium to high frequencies (approx. 10 Hz to 100 kHz) and is analogous to the R_{hf} and R_{mf} in the employed EEC model. It captures resistances due to the electrochemical processes in the electrodes. It is also related to the overall area under the impedance spectrum.

Mass transport resistance, R_m, is the impedance at the lowest frequencies (approx. ≤ 10 Hz) and is analogous to the R_{lf} in the employed EEC model. It is related to gas conversion (reactants and products transport, ad/desorption, ion exchange and diffusion processes). This impedance term is also commonly characterised as 'low frequency polarisation resistance (R_{pLF}) [82], and is losses due to the concentration gradient of the reactants and products across the electrodes.

The capacitance contributes significantly to the impedance at high frequencies as a result of the double layer capacitive effect. This part of the impedance is expected to increase if electrode delamination occurs as a result of the resultant increase in the dielectric properties of the double layer. Nevertheless, since the rSOC system does not lend itself to ideal behaviour, the capacitance components have been replaced with a constant phase element. The constant phase element (CPE) thus captures the phase angle of the AC frequency independent portion of the circuit [82], and thus for our EEC model CPElf = CPEmf = CPEhf.

4.2.4.3 Calculation of ASR and cell degradation rate

The cell degradation rates (based on cell durability tests) and ASRs (based on j-V characterisations) reported in the following chapters of this thesis were calculated using the equations below.

Cell degradation under the galvanostatic operation modes utilised in the study were calculated with the following equations:

$$\left|\frac{\boldsymbol{V_t - V_{t_0}}}{\boldsymbol{t - t_0}} \times \mathbf{1000}\right| \qquad \frac{\mathrm{mV}}{1000\mathrm{h}} \qquad\qquad \boldsymbol{Equation\, 4-\ 1}$$

and;

$$\left|\frac{\mathbf{V_t - V_{t_0}}}{\mathbf{(t - t_0)V_{t_0}}} \times \mathbf{100 * 1000}\right| \qquad \% \frac{}{1000\mathrm{h}} \qquad\qquad \boldsymbol{Equation\, 4-\ 2}$$

Where:

V_t = cell voltage at time 't' (mV);

V_{t0} = cell voltage at time 't0' (mV);
t0 = reference time or time at the beginning of the test (minutes);
t = elapsed test time relative to the reference time (minutes).

The ASR were calculated from the j-V characterisations at 50% of the test current density. Therefore, for a cell tested at 0.5 A/cm^2, the ASR was calculated as follows:

$$\left| \boldsymbol{ASR\ @0.25\ A/cm^2 = \frac{V\ @\ 0.2\ A/cm^2 -\ V\ @\ 0.3\ A/cm^2}{j\ @\ 0.3\ A/cm^2 -\ j\ @\ 0.2\ A/cm^2}} \right| \qquad \boldsymbol{Equation\ 4-\ 3}$$

Where:
V = cell voltage (mV);
j = cell current density (A/cm^2).

4.2.5 Structural characterisation

Upon completion of all electrochemical testing, a record of the last test condition, i.e., temperature, test atmosphere (SOFC or SOE) at completion and during cooling to ambient, etc., which the unit cell experienced was taken. Pictures were then taken to record the physical condition of the tested cell. If the cell was cracked or if visible delamination of the layers is observed, the pictures are taken with special attention to them.

The following factors were taken into consideration when selecting the position of the cell to sample for its structural examination / characterisation:

2. Test conditions used;

3. Electrochemical performance of the sample;

4. Most probable position of interest for understanding the observed behaviour.

The samples were then explicitly marked with the record of the cell position selected.

A virgin cell was also sampled to serve as a benchmark for the structural characterisation of tested cells.

4.2.5.1 Post-test sample preparation

After sampling, the cell sample was embedded in epoxy under vacuum in accordance with the resin manufacturer's recommendations [147].

After the cold mounting procedure using an epoxy resin, the sample is polished with a Struers machine utilising semi-automatic settings. The following sample polishing procedure resulted in polished samples which gave the best quality images:

1. Grinding the cross-section with progressively finer grinding media and with increasing times: e.g. 125 µm for approximately 1 minute, 75 µm SiC for 2 minutes, 45 µm for 3 minutes, 15 and 9 µm diamond suspension with disc for 4 minutes;

2. Wash the sample between each grinding stage with water and soap solution to remove ceramic particles and organic matter;

3. After washing, check the level of scratching in an optical microscope to determine if the effects of the coarser grinding step have been replaced by that of the finer stage. Keep the discs used clean and wash with water to avoid cross-contamination;

4. Polishing the cross-section with progressively finer polishing media and with increasing times: e.g. cloth polishing with 3 µm diamond suspension for 5 minutes, 1 µm diamond

suspension for 6 minutes, 0.3 µm diamond suspension for 7 minutes, and 0.05 µm diamond suspension for 10 minutes;

5. Repeat steps 2. and 3. between each polishing step, ensuring that the effects of coarser polishing steps have been replaced by that of the proceeding finer steps.

4.2.6 SEM analysis

Scanning electron microscopy, and where required, e.g. for grain size measurement, in conjunction with full EDX mapping, was used to systematically gather the following information in each layer and at each interface of the cell sample. Any other specific features of interest were also investigated.

1. Fuel electrode examination entailed the capturing of the following basic information:

    - Nickel agglomeration, distribution and surface condition;
    - The condition of the Ni and YSZ interfaces;
    - Particle size of Ni and YSZ.

2. For the examination of fuel electrode and electrolyte interface:

    - Cracking and delamination;
    - Ni agglomeration, distribution and surface condition adjacent to the fuel electrode and electrolyte interface.

3. For electrolyte examination:

    - Cracking due to oxygen evolution.

4. Examination of electrolyte (and barrier layer interface):

    - Physical and/or electrochemical delamination.

5. Examination of barrier layer and oxygen electrode interface:

    - Delamination;
    - Chemical analysis.

Phase analysis, including possible identification of impurities and secondary phases was carried out using the backscatter electron mode in SEM. EDX was used for chemical analysis of impurities and secondary phases in all components of the cells.

All SEM analysis was performed using a table-top SEM (TM3030Plus, Hitachi), equipped with Energy Dispersive X–ray (EDX) detection (Quantax70, Bruker Nano GmbH).

5 CELL TYPE 1 REVERSIBLE OPERATION

5.1 Introduction

As mentioned in Section 0, Cell type 1 included a pure GDC interlayer between the YSZ electrolyte and LSC-GDC oxygen electrode in order to mitigate possible deleterious chemical reactions, as indicated in Chapter 3, between the YSZ electrolyte and LSC containing layers (oxygen electrode and contact layer). The configuration of cell type 1 is illustrated in Figure 5-1.

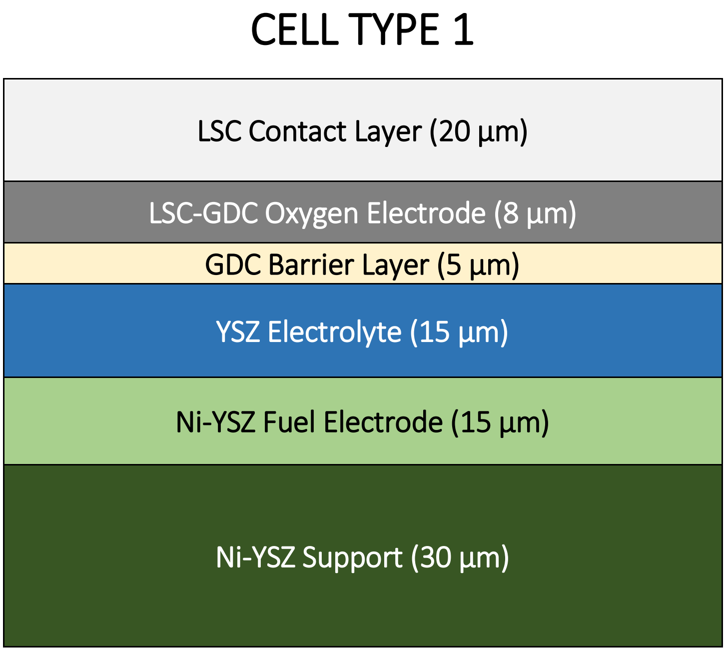

Figure 5-1: Configuration of cell type 1

Different cells of this type were subjected to the test protocol detailed in Chapter 4, under different fuel flow rates, with current densities ranging from 0.5 A/cm^2 to 2.65 A/cm^2, and at temperatures of 700^{o}C and 750^{o}C. The base case flow rates used for the tests (unless otherwise indicated) were as follows:

1. During fuel cell operation, a dry mixture of 35.3 ml/min each of H_2 and N_2 was delivered to the fuel electrode, whilst 331.25 ml/min of air was delivered to the oxygen electrode;
2. During electrolysis operations, 1.3 g/hr of $H_2O_{(l)}$ (approximately 35.3 ml/min of $H_2O_{(g)}$) mixed with 8.8 ml/min H_2 was delivered to the fuel electrode, whilst 66.25 ml/min of air was delivered to the oxygen electrode.

These flow rates corresponded to the fuel and oxygen electrode compartment gas compositions, and fuel electrode reactant utilisations given in for 3 cm diameter unit cells with 5.3 cm^2 effective cathode area (see) tested under a current density of 0.5 A/cm^2.

The results, detailing the cell voltage evolution under test, j-V and impedance characteristics are reported in Sections 5.2 to 5.9, and summarised in Section 5.10. It is very important to bear in mind when reading the results presented in this chapter 5 and the following chapter 6, as well as the discussion presented in chapter 7, that since all the tests were carried out under galvanostatic mode (rather than potentiostatic):

1. voltage decreases during SOFC operation when current was being drawn from the cell indicate increases in resistances across the cell, whilst voltage increases indicate decreases in resistance across the cell and thus improving cell performance;

2. voltage decreases during SOE operation when current was being supplied to the cell indicate decreases in resistances across the cell, whilst voltage increases indicate increases in resistance across the cell and thus deteriorating cell performance;
3. the H_2/H_2O conversion rates (same as 'fuel utilisation') stated in *Table 5-1* and *Table 6-1* are based on the amount of substance required to produce the amount of electrons being supplied (SOFC mode) or used-up (SOE mode) by the chemical reactions across the cell. These would be constants with no error margins due to the galvanostatic (or constant current-density) approach taken for the tests (also see section 3.3.3).

The different tests are identified using Cell IDs. The Cell IDs comprise 3 parts, separated by an underscore (e.g. CT1_0.5_750). The first part is alphanumeric and identifies the cell type, i.e., CT1 for cell type 1 (see *Figure 5-1*). The second part of the cell ID is the test current density in A/cm^2, and the third part is the test temperature in degrees Celsius. Some tests were repeated with other variables (apart from cell type, current density and temperature) being changed, and these are identified by #1 or #2 added to the Cell ID.

The test matrix for the cell type 1 tests reported in this Chapter 5 is detailed in *Table 5-1*.

Table 5-1: Test matrix for cell type 1 tests

TEST IDs	Temp. (°C)	Current Density (A/cm^2)	H_2/H_2O Conversion (%)	Further Details
CT1_0.5_750#1	750	0.5	52.3	Section 5.2
CT1_0.5_700#1	700	0.5	52.3	Section 5.3
CT1_0.5_750#2	750	0.5	52.3	Section 5.4
CT1_0.5_700#2	700	0.5	52.3	Section 5.5
CT1_0.7_750	750	0.7	73.3	Section 5.6

CT1_1.39_750	750	1.39	73.3	Section 5.7
CT1_1.25_750	750	1.25	83.5	Section 5.8
CT1_2.65_750	750	2.65	100	Section 5.9
CT1_1.5_750#1	750	1.5	83.5	Appendix A.1
CT1_1.5_750#2	750	1.5	83.5	Appendix A.2

5.2 Test at 0.5 A/cm^2 Current Density (CT1_0.5_750#1)

This cell (CT1_0.5_750#1) was tested at 750°C and a galvanostatic current density of 0.5 A/cm^2 under all operating modes (SOFC, SOE & rSOC), resulting in a fuel utilisation of 52.3%. The voltage evolution, which gives an indication of the change in cell resistance over time, is illustrated in *Figure 5-2*. As can be seen, the voltage remained relatively stable during the initial 120- hours of constant SOFC operation with a voltage degradation rate of 28 mV/1000h (3.1% / 1000h). During the subsequent 120 hours of constant SOE operation, the voltage remained relatively stable over the first approximately 20 hours. It then increased steadily, with the rate of increase seemingly increasing with time as can be seen from the 120 hours to 240 hours portion of *Figure 5-2*, with an overall voltage degradation rate of 99.9 mV/1000h (10.3% / 1000h). The cell voltage evolution trend continued during the 33 rSOC operation cycles of *Figure 5-2*, from 240 hours to 1000 hours. Throughout the rSOC operation, the rate of voltage degradation in SOE mode (voltages corresponding to -0.5 A/cm^2 in *Figure 5-2*) was higher than that in SOFC mode (voltages corresponding to +0.5 A/cm^2 in *Figure 5-2*). Since the period of the SOE operation (20 hrs) was longer than the SOFC period (3 hrs), the apparent higher dragradation under SOE mode could be attributed solely to the relative length of exposure to the respective conditions.

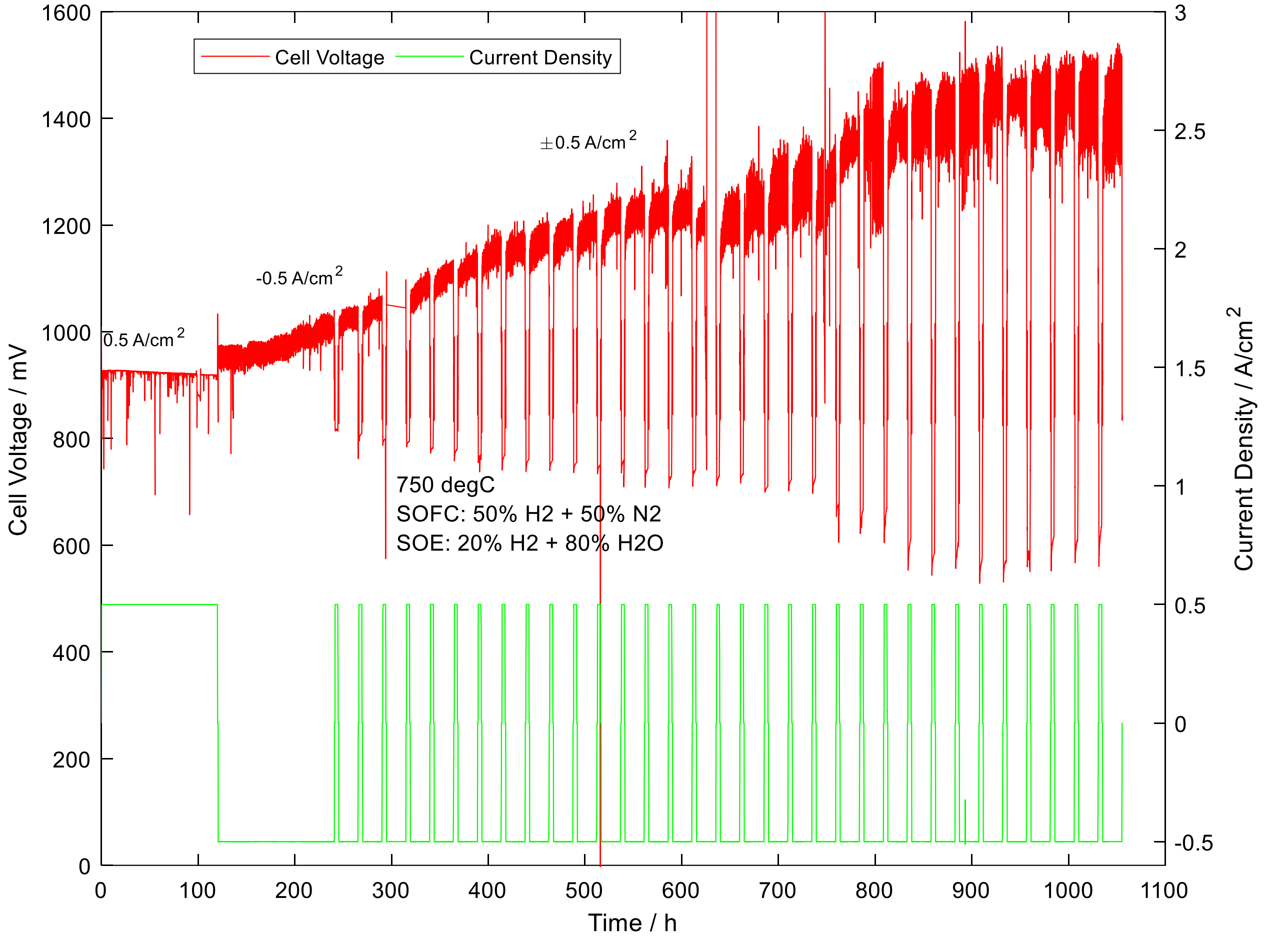

Figure 5-2: Voltage evolution characteristics of CT1_0.5_750#1 tested at 750°C and ±0.5 A/cm^2 current density.

(The voltage spikes at approximately 520 hrs during an SOFC cycle, and at 600 hrs & 750 hrs during SOE cycles occurred as a result of malfunctions in the laboratory hydrogen supply and the compressed air system, respectively).

However, as can be seen in *Figure 5-3*, which is a blow-up of the SOFC mode voltages of *Figure 5-2*, there seems to be a repeated cell voltage recovery during the constant SOFC operation mode during rSOC operation. As already mentioned, rSOC operation entailed 3 hours of SOFC operation followed by 20 hours of SOE operation, with approximately 1 hour for switch-over. Thus, *Figure 5-3* shows continous voltage increases (positive voltage recovery) throughout the

3 hours of SOFC operation, and repeated for all the 33 SOFC cycles which comprised the rSOC test protocol. This voltage recovery in SOFC mode under rSOC operation is therefore a positive contribution to the cell's overall rSOC performance. The observed higher degradation in SOE mode was therefore not as a result of the relative length of exposures, and may be due to:

1. Different underlying (electro-) chemical processes occuring during the SOE and SOFC modes which comprised the rSOC cycles (SOFC - SOE - SOFC - SOE -, etc); and / or
2. Same processes occuring during operation in SOE and SOFC modes, but at different relative rates.

These possibilities are further investigated below, using electrochemical impedance spectroscopy (EIS), especially to more definitively determine the possible reasons for the apparent difference in degradation rates under SOE and SOFC cycles.

Figure 5-3 also indicates that the rate of voltage recovery when operating in SOFC mode during rSOC cycling increases with cycle number. At cycle one, the recovery during the 3 hours of SOFC operation was minimal (approximately from 815 to 817 mV, see *Figure 5-3*a). Whereas the rate is relatively steep during the final cycles (approximately from 566 to 638 mV for the final cycle, see *Figure 5-3*c). This also coincides with the observed trend in voltage degradation during SOE operation, i.e., the rate of voltage degradation during SOE operation increases with both time (during constant SOE operation) and cycle number (during rSOC operation). The voltage recovery during SOFC operation is therefore most likely linked to some reversal in at least one of the processes responsible for the voltage dedradation during SOE operation.

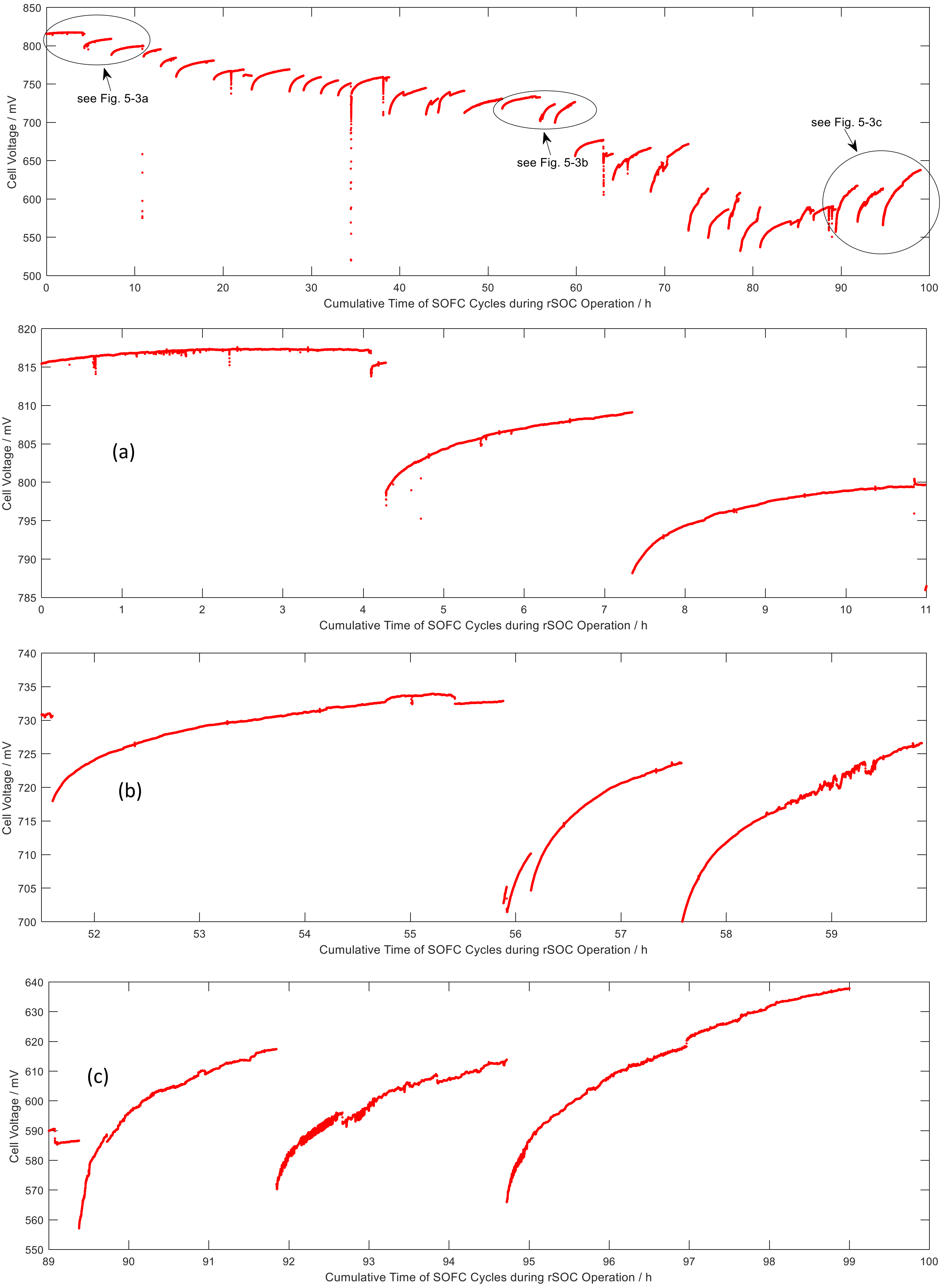

Figure 5-3: Cell voltage recovery under SOFC cycles during rSOC operation.

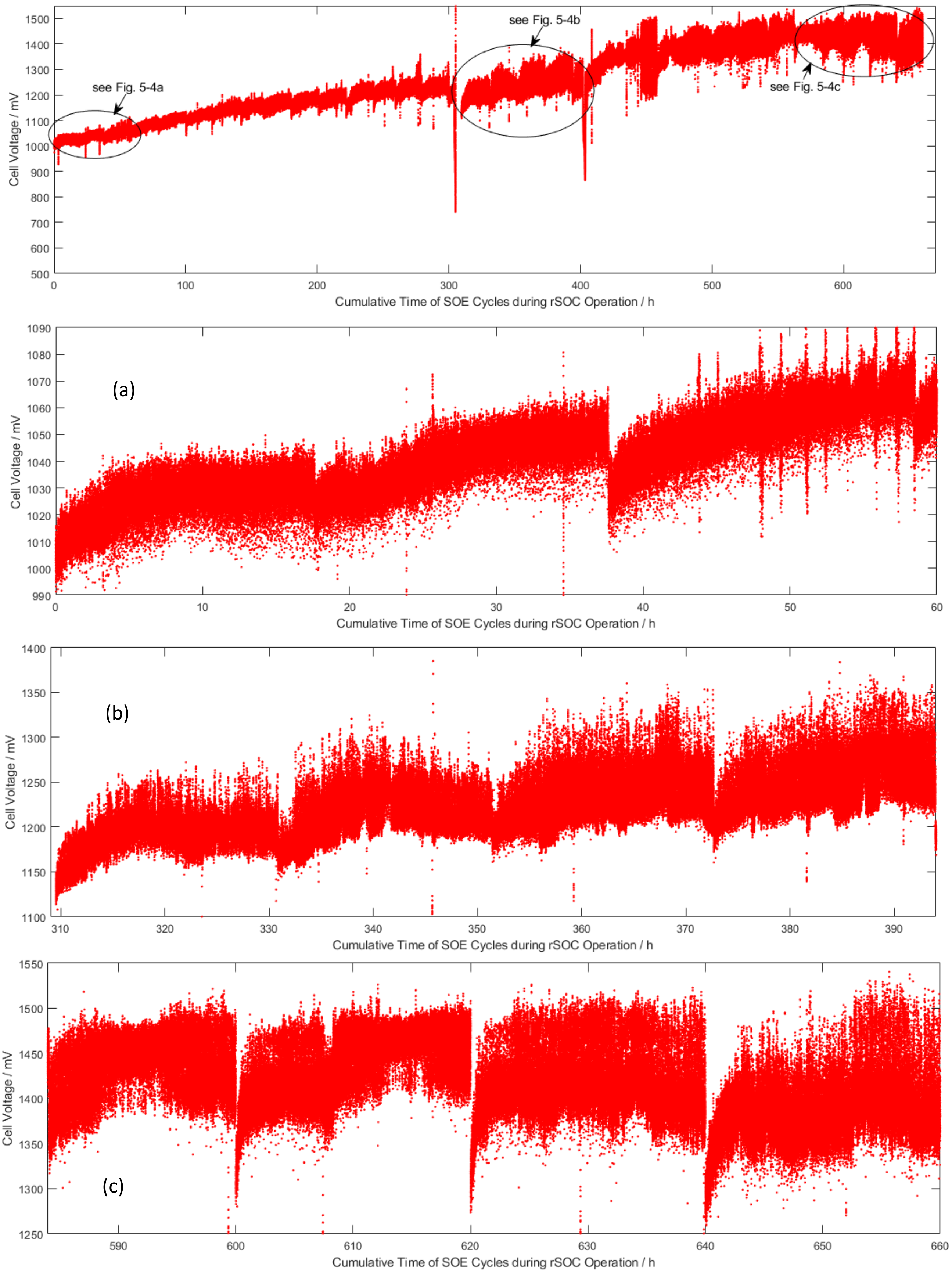

Figure 5-4: Cell voltage evolution during SOE cycles during rSOC operation.

As shown by *Figure 5-2* and Figure 5-4, the observed cell voltage recovery in SOFC mode (Figure 5-3) was not replicated at any stage of the SOE operation during rSOC cycles. As seen especially in Figure 5-4, during all the 20 hour, 33 SOE mode operation during rSOC cycling, the general trend was a continous voltage increase. Nevertheless it may be seen from Figure 5-4a to Figure 5-4c that the starting voltage for every subsequent SOE cycle was relatively lower than the ending voltage of the previous SOE cycle. This seems to reflect the positive contribution of the SOFC cycles during the rSOC operation. However, the increasing rate of cell degradation with SOE cycle number was indicated by the observation that the ending voltage of all subsequent SOE cycles was greater than the ending voltage of the previous cycle (see Figure 5-2 and Figure 5-4.

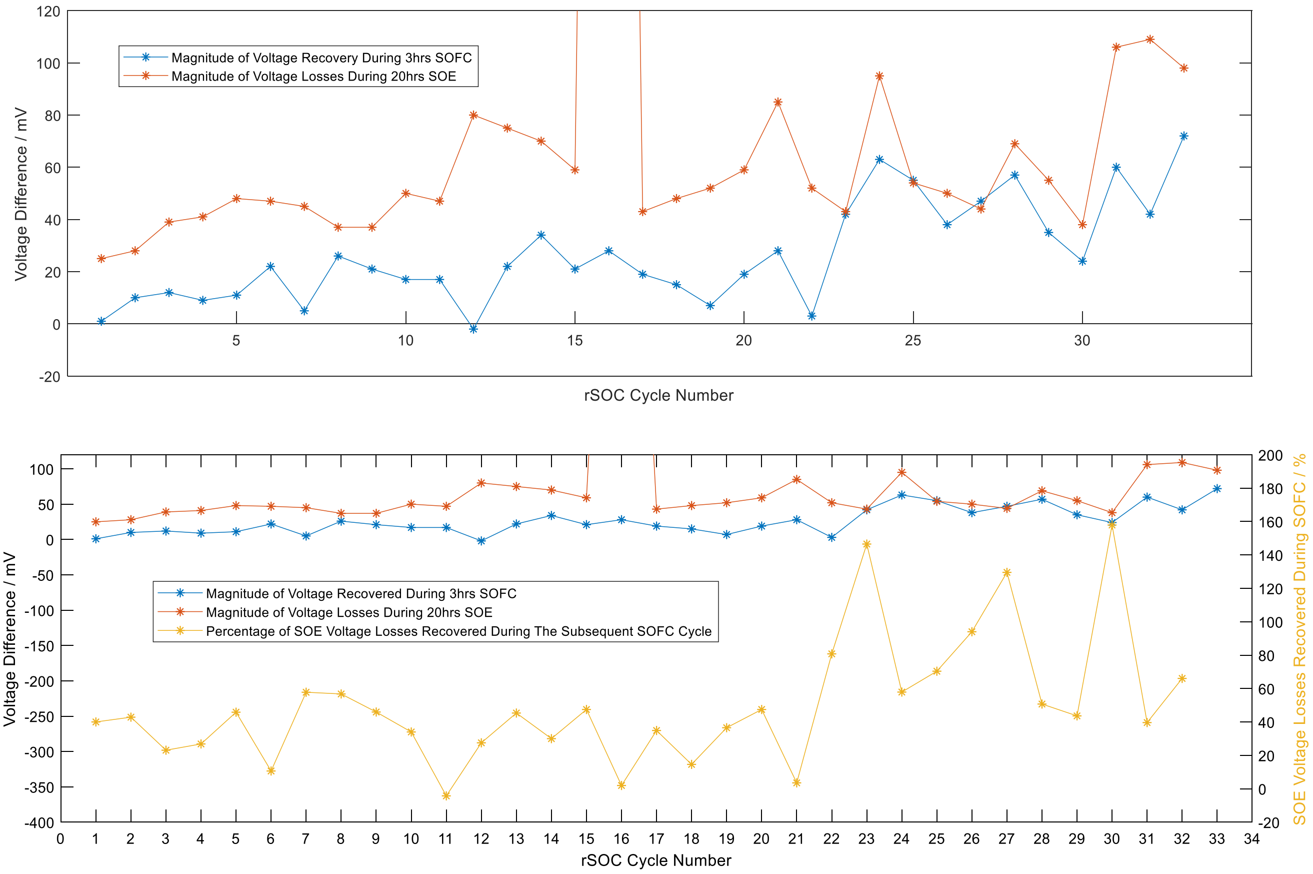

Figure 5-5: Difference in magnitude between voltage losses during SOE and voltage recovery during SOFC.

A comparison of *Figure 5-3* and *Figure 5-4* (presented separately as Figure 5-5) also shows that until the cell was irreversibly damaged after cycle 21 (see Figure 5-2 to Figure 5-4) the magnitude of voltage degradation during SOE mode operation was significantly greater than the equivalent voltage recovery during SOFC mode operation. *Figure 5-5* shows that approximately 40% of the voltage losses in SOE mode was recovered during the following SOFC mode operation. This may either be as a result of the longer time of SOE operation relative to the SOFC operation, or as already mentioned, irreversibility of at least one of the processes responsible for the voltage degradation in SOE mode. After the cell was irreversely damaged (as indicated by SOFC operating voltages of approximately 600 mV) from cycle 21, *Figure 5-5* indicates that some voltage recoveries during subsequent SOFC mode operation were greater than the voltage losses during the previous SOE operation. Nevertheless, the overall cell performance after rSOC cycle 21 was significantly poorer relatively to the preceeding rSOC cycles.

The rSOC voltage recovery during SOFC mode suggests that the rSOC technology is suitable, in terms of overall system degradation, to schemes which allow at least an hour of SOFC operation time between SOE cycles. Examples would be solar-power based rSOC operation in climatic zones with at least 8 hrs of sunshine (for continous SOE operation), or even better still, wind-power based rSOC operation with at least 12 hrs of wind power generation (for SOE operation). The rSOC system may then be partially regenerated, during the night or when the wind speed is not sufficient for power generation, by operating it in SOFC mode to convert some of the hydrogen generated back into power.

Furthermore, during all the SOE tests carried out, there was considerable scatter in instantaneous cell voltage at a given current density. The amplitude of the scatter in cell voltage also seemed to increase with increasing cycle number (see Figure 5-2 and *Figure 5-4*). This scattering was probably related to the characteristics or limitations inherent in the CEM steam supply equipment used, i.e., intermittent steam starvation and oversupply, thus introducing dynamic changes in $H_2O_{(g)}$ reactant flow rates at the hydrogen electrode. During electrolysis operations, 1.3 g/hr of $H_2O_{(l)}$ (converted to 35.3 ml/min of steam by the CEM), mixed with 8.8 ml/min of H_2 was delivered to the hydrogen electrode, whilst 66.25 ml/min of air was delivered to the oxygen electrode.

Also, the voltage spikes in *Figure 5-2*, at approximately 520 hrs during an SOFC mode operation, and at ~600 hrs & 750 hrs during SOE mode operation occured as a result of malfunctions in the laboratory hydrogen supply and the compressed air system, respectively. During fuel cell operations, 35.3 ml/min of both H_2 and N_2 was delivered to the fuel electrode, whilst 331.25 ml/min of air was delivered to the oxygen electrode. The equipment malfunctions, and the possible resultant cell stresses induced due to reactant starvation under constant current density load, may have contributed to the large drop in cell performance observed after about 600 hours in Figure 5-2, i.e. after rSOC cycle 21 (equivalent timeline to approximately 60 hours in Figure 5-3).

The significant drop in performance from 60 hours to 75 hours in *Figure 5-3* coincided with, and was therefore due to, the hydrogen starvation of the cell during an SOFC mode operation (also see cell voltage at 520 hours in Figure 5-2) and air starvations at 600 hours and 750 hours during SOE cycles.

Figure 5-6 (a) and (b) show the voltage responses to current density changes of the virgin cell, and also of the cell after the 120 hours contant SOFC operation, after the subsequent 120 hours of SOE operation, and finally after the 33 rSOC cycles (33 cycles of 3 hrs SOFC followed by 20 hrs SOE). Figure 5-6 (a) show the current density - voltage characteristic captured with the cell under the SOFC fluid flow rates or under the SOFC operating conditions, whilst (b) show the current density – voltage characteristic recorded with the cell under the SOE fluid flow rates or SOE environment. Relative to the theoretical current density – voltage response depicted in Figure 4-32, there are no clearly discernible transition regions for the captured activation, Ohmic and mass transport resistances in Figure 5-6. This suggests that:

1. the magnitude of the various contributions to the Ohmic resistance in the laboratory test set-up (especially at the low and high current density regimes) are significantly high enough to overshadow the activation resistance (i.e. activation resistance at ≥700°C is negligible) and the mass transport resistance (i.e. currents are low enough to not reach transport limitation); and/or

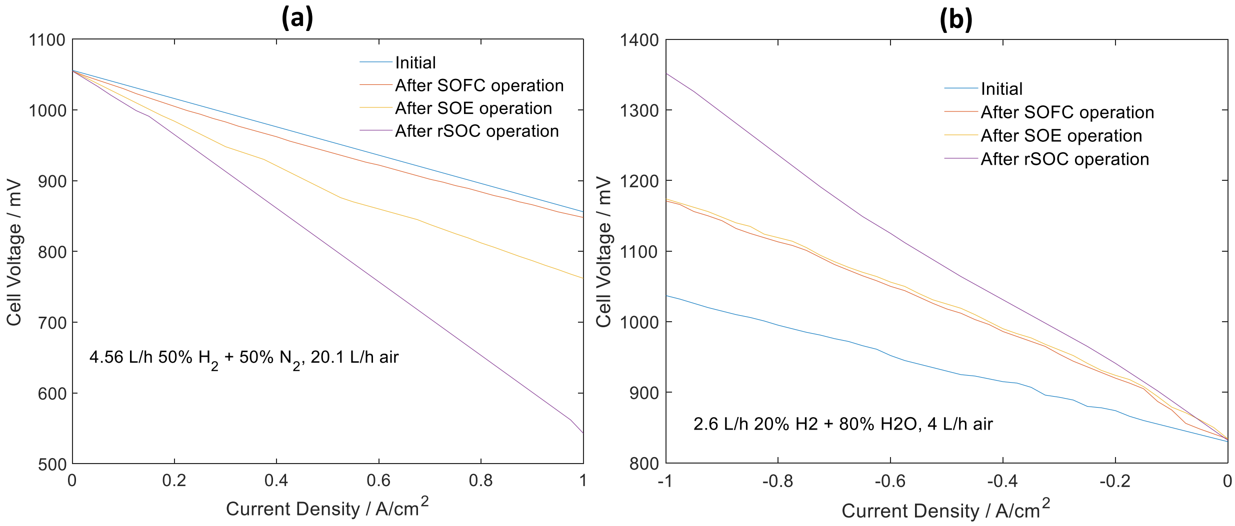

Figure 5-6: Comparison of j-V characteristic of CT1_0.5_750#1 before and after SOFC, SOE and rSOC operation testing (captured under SOFC (a) and SOE (b) conditions).

2. Both the activation resistance at low current densities, and the mass transport resistance at high current densities are negligible due to the cell's architecture (material composition, design and structure) thus accounting for the lack of discernible activation, ohmic and mass transport trasition regions in the captured j-V curve.

The equivalent electrochemical impedance spectroscopy (EIS) of the cell would shed further light as to which of the above proposed explanations is the reason for the morphological deviation of the j-V curves from the theoretical form.

Nevertheless, as should be expected, under both SOFC and SOE environments, the ASRs were lowest for the virgin cell (the 'initial' curves in *Figure 5-6* (a) and (b)). The ASRs calculated from the j-V curves (*Figure 5-6*) are given in *Table 5-2* and *Figure 5-7*.

Table 5-2: ASRs calculated from j-V curves at 0.25 A/cm^2

SOFC environment ASRs (*Figure 5-6*(a)) Ω.cm^2				SOE environment ASRs (*Figure 5-6*(b)) Ω.cm^2			
Initial	After 120 hrs SOFC	After 120 hrs SOE	After 33 rSOC cycles (3hrs SOFC / 20 hrs SOE)	Initial	After 120 hrs SOFC	After 120 hrs SOE	After 33 rSOC cycles (3hrs SOFC / 20 hrs SOE)
0.22	0.225	0.32	0.81	0.2	0.32	0.34	1.1

Under SOFC environment (Figure 5-6 (a)), the slope of the j-V curve after 120 hrs of SOFC operation was similar to that for the virgin cell. The ASR of the cell after 120 hrs SOFC operation was 0.225 Ω.cm^2, which compares favourably with the 0.22 Ω.cm^2 calculated for the virgin cell. The similar ASR for the virgin cell and of the cell after 120 hours of SOFC operation was in accordance with the 'stable voltage evolution' observed in the constant SOFC operation portion of *Figure 5-2*. The similar ASRs of the virgin cell and of the cell after SOFC operation was however not replicated in the cell's j-V response captured in an SOE environment. The equivalent initial ASR was 0.2 Ω.cm^2, and increased to 0.32 Ω.cm^2 after the 120 hrs of constant SOFC operation (see Figure 5-6 (b), *Table 5-2* and *Figure 5-7*). This could be due to the cell's instantaneous response to the SOE environment (i.e., instantaneous losses related to re-oxidation or other processes occuring in the SOE environment) masking the true condition of the cell after the 120 hrs of constant SOFC operation. It is generally known that SOCs undergo initial passivation when operated in SOE mode before subsequent activation depending on operating duration and current density [18], [21], [66]. Nevertheless, the slope of the j-V curve (and ASR) after the constant SOFC operation was still lower than the slope of the curve which captures the cells condition after the subsequent 120 hours of constant SOE operation (Figure 5-6 (b)).

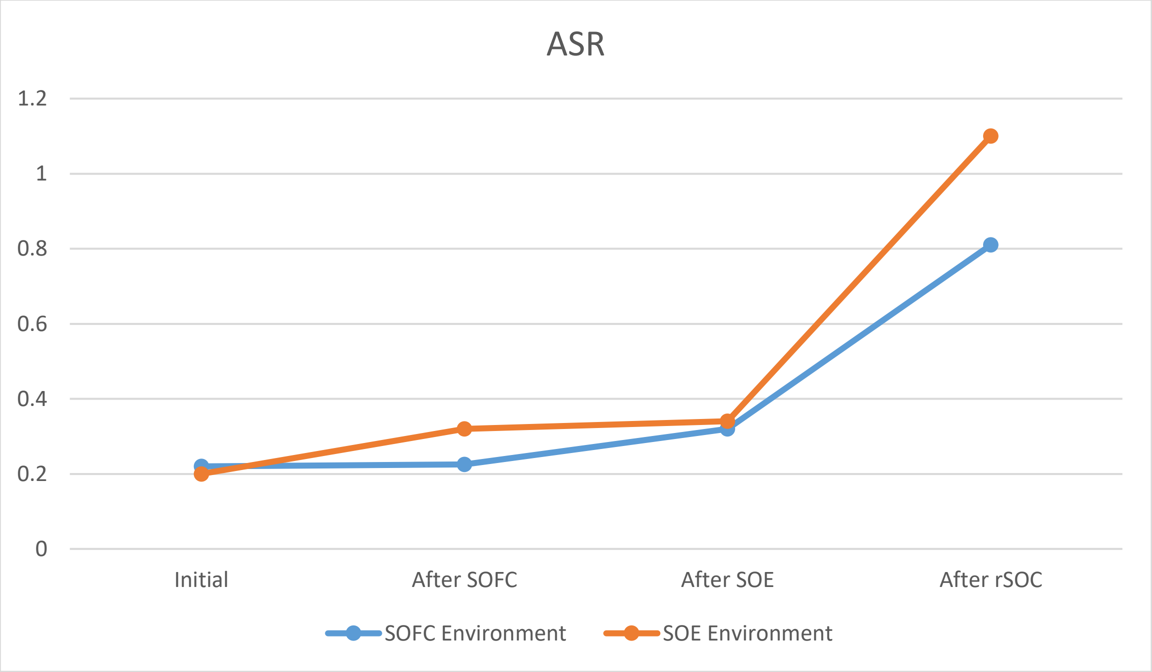

Figure 5-7: Change in cell ASR with mode of operation, as captured under SOFC and SOE environments for CT1_0.5_750#1

Under both the SOFC and SOE environments, Figure 5-6 (a) & (b), the slope was highest (ASRs of 0.81 Ω.cm^2 and 1.1 Ω.cm^2, respectively) for the cell after the 33 rSOC cycles. Due to the test protocol, the increased deterioration could be a function of both cumulative degradation due to the total operating time (i.e. 120hrs SOFC + 120hrs SOE + 33 rSOC cycles of 3hrs SOFC followed by 20hrs SOE), and also relative degradation due to the particular rSOC operating mode (i.e. incidental cell fatigue stresses due to the cyclic operation mode, and cell environment switching). However, as indicated in Figure 5-2, Figure 5-3, Figure 5-4 and Figure 5-5, the degradation during the rSOC operation may be solely attributed to the 33 SOE cycles due to the cell performance recovery indicated in Figure 5-3 for the 33 SOFC cycles. Based on these results, and as noted above, it is expected that cells operated in standalone SOE mode would degrade more than cells operated for an equivalent time period in rSOC mode. This is because of the percentage voltage recoveries observed during the SOFC operating cycles under rSOC operation, Figure 5-5.

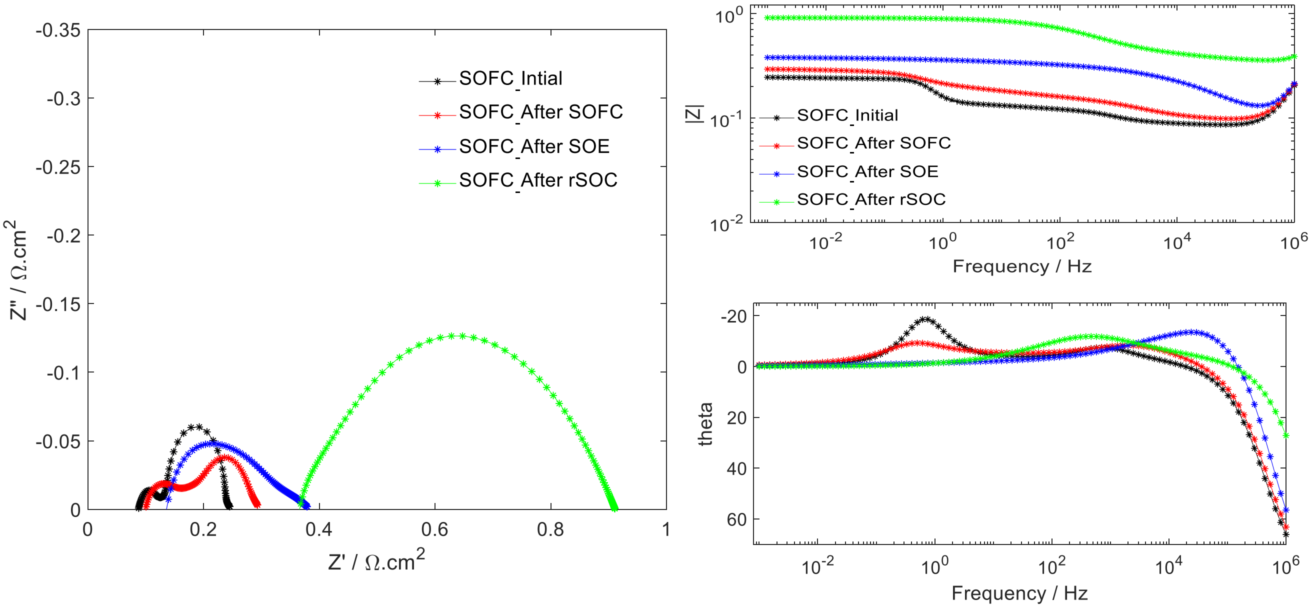

Figure 5-8: Nyquist and Bode impedance plots of CT1_0.5_750#1 before and after SOFC, SOE and rSOC operation testing (captured under SOFC conditions).

Figure 5-8 shows the electrochemical impedance spectroscopy (EIS) equivalent of the j-V information presented in Figure 5-6 (a). As mentioned in Section 4.2.4.2, the j-V curves provide only top-level information on the resistances relative to ideal cell performance (overall ASR). Electrochemical impedance spectroscopy (EIS), on the other hand, can potentially delineate the various frequency-dependent individual contributions to the overall cell degradation, and therefore enable identification of the individual processes responsible for the cell's decreasing performance. This would help in the quest to optimise the various relevant variables, such as cell architecture and operating parameters, to mitigate the performance degradation.

The Nyquist and bode plots of the impedance information captured under SOFC conditions, *Figure 5-8*, show marginal increases in both the Ohmic contribution (real impedance at the high frequency intercept of the spectra) and the polarisation impedance after the cell was operated for 120 hours in SOFC mode, relative to the 'initial' impedance curve for the virgin cell. This corresponds well with the 'after SOFC operation' j-V curve in *Figure 5-6* (a).

Figure 5-8 further shows significant increases in both low and high frequency impedance, as well as a relative increase in the polarisation impedance after the cell was subjected to the 120 hrs of constant SOE operation. After the 33 rSOC cycles, further significant increases in all the impedance components are noticed, indicating further deterioration in the cell's performance compared to the condition of the cell after the 120 hours of constant SOE operation. The Ohmic resistance after the 33 rSOC cycles was 0.38 $\Omega.cm^2$, whilst the polarisation resistance was 0.58 $\Omega.cm^2$, compared to 0.13 $\Omega.cm^2$ and 0.25 $\Omega.cm^2$ respectively after SOE operation.

Figure 5-9 shows the equivalent Nyquist and Bode plots captured under SOE conditions of the virgin cell, and the cell after the 120 hrs of SOFC operation, after the additional 120 hrs of SOE operation, and finally after the 33 rSOC cycles of 3 hrs SOFC followed by 20 hrs SOE operation. Similar to the equivalent j-V curves in *Figure 5-6* (b), significant increases in both the high and low frequency impedances are indicated by the Nyquist plot captured under SOE condition after 120hrs of SOFC operation. Unlike the marginal increase observed in the polarisation impedance for the equivalent Nyquist plot captured under SOFC conditions, the increase is significant for the present case which may be attributed to re-oxidation of the Ni-YSZ grains in the SOE environment.

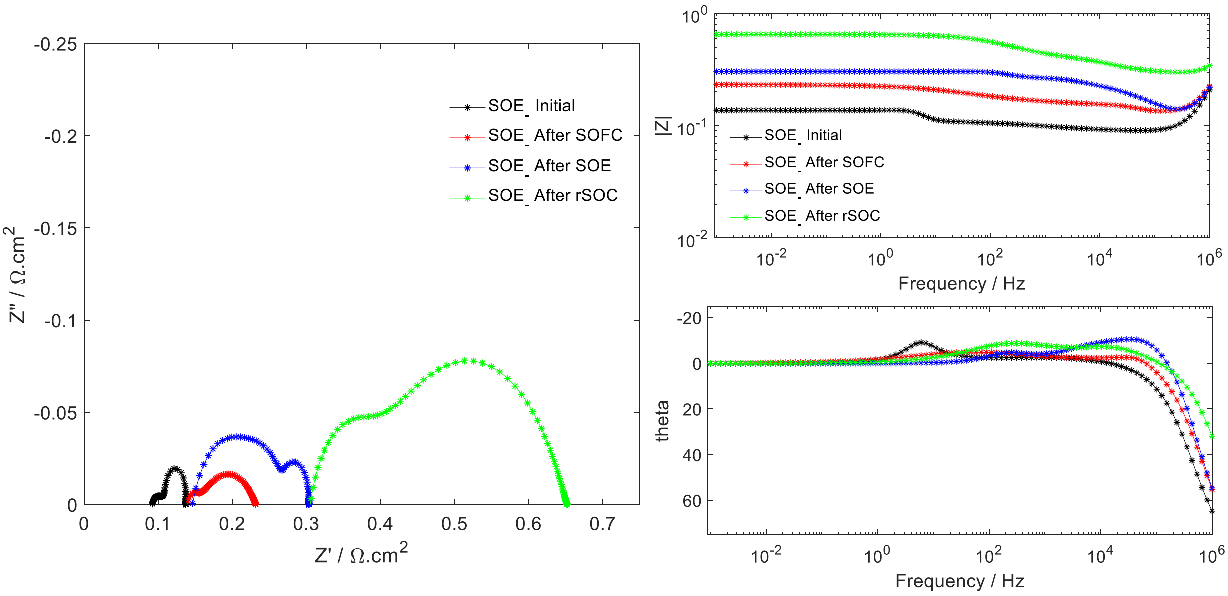

Figure 5-9: Nyquist and Bode impedance plots of CT1_0.5_750#1 before and after SOFC, SOE and rSOC operation testing (captured under SOE conditions).

After the additional 120 hrs of SOE operation, the Nyquist plot captured under SOE conditions, *Figure 5-9*, shows a marginal increase in the high frequency impedance relative to the ‘after 120 hrs SOFC operation’ curve, and a significantly higher polarisation impedance increase which indicates the passivation potential of the SOE environment or gas composition. Another feature of this plot is a low frequency depression resulting in a smaller additional curve in the low frequency region. This suggests a gas conversion or mass transport related process is contributing to the impedance of the cell, as captured under SOE conditions after 120 hrs of SOE operation.

The EIS plot of the cell after the 33 rSOC cycles of 3 hrs SOFC followed by 20 hrs SOE mode shows a more pronounced impedance behaviour relative to the plot taken after the 120hrs SOE operation, *Figure 5-9*. There are significant increases in both high and low frequency as well as polarisation impedance. Furthermore, the additional curve relating to a low frequency regime process seems to have become the dominant contributory process to the overall impedance.

SEM 'structural characterisation' images of the cell before and after testing (i.e. after the complete 120hrs SOFC + 120hrs SOE + 33 rSOC cycles of 3hrs SOFC followed by 20hrs SOE operation) are shown in *Figure 5-10* .

The virgin cell images (*Figure 5-10* a, b & c) show sound boundaries with no cracks. However, during rSOC testing, the cell developed both intra-layer and inter-layer cracks, as well as complete delamination along the boundaries adjacent to the oxygen electrode. The intra-layer cracking was present mainly in the YSZ electrolyte and GDC barrier layers (*Figure 5-10* e & k) adjacent to the oxygen electrode. The inter-layer cracks also ran from the electrolyte to the oxygen electrode (*Figure 5-10* e), whilst the delamination was mainly along the oxygen electrode and barrier layers. All these seem to suggest significant pressure build-up between the electrolyte and oxygen electrode. The observed delamination (i.e. irreversible cell damage) would also have contributed to the precipitous drop in cell performance after approximately 720 hours, Figure 5-2, and the significant increases in ohmic and polarisation resistances after rSOC operation (*Figure 5-8* and *Figure 5-9*).

Figure 5-11 shows the elemental distribution of the cell after testing. It indicates that, despite the GDC barrier layer, there seem to be strontium (Sr) migration from the LSC containing cell layers (oxygen electrode and contact layer) to contaminate the YSZ electrolyte. Nevertheless, this may also have been due to the observed inter-layer cracks creating a contamination pathway between the layers, and not necessarily cation migration through the sound GDC barrier layer. It is known that this sort of inter-layer elemental contamination serves to reduce cell performance [76] - [77] [78].

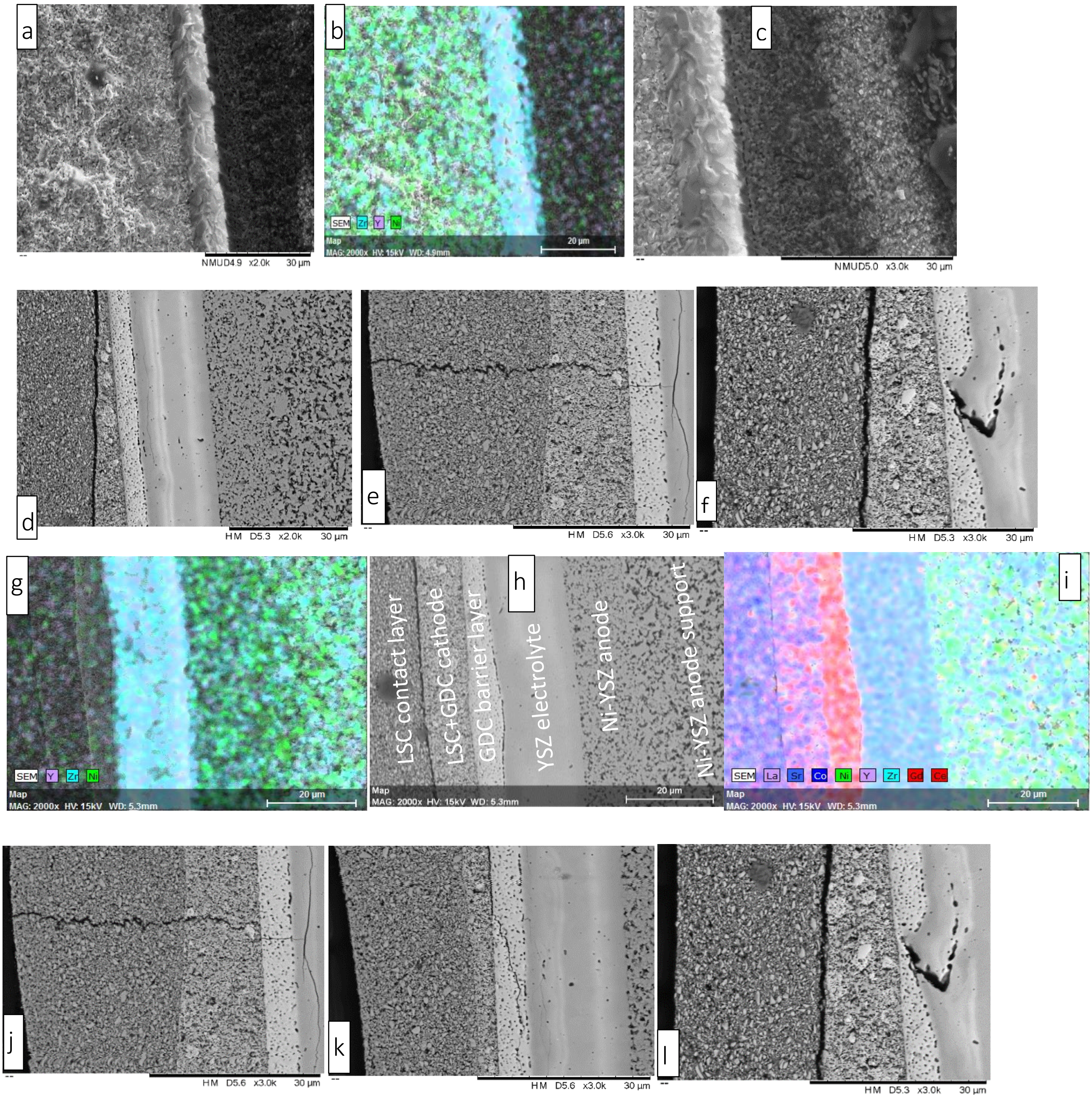

Figure 5-10:Virgin (a, b and c) and post-test (d to l) SEM images of the tested CT1_0.5_750#1

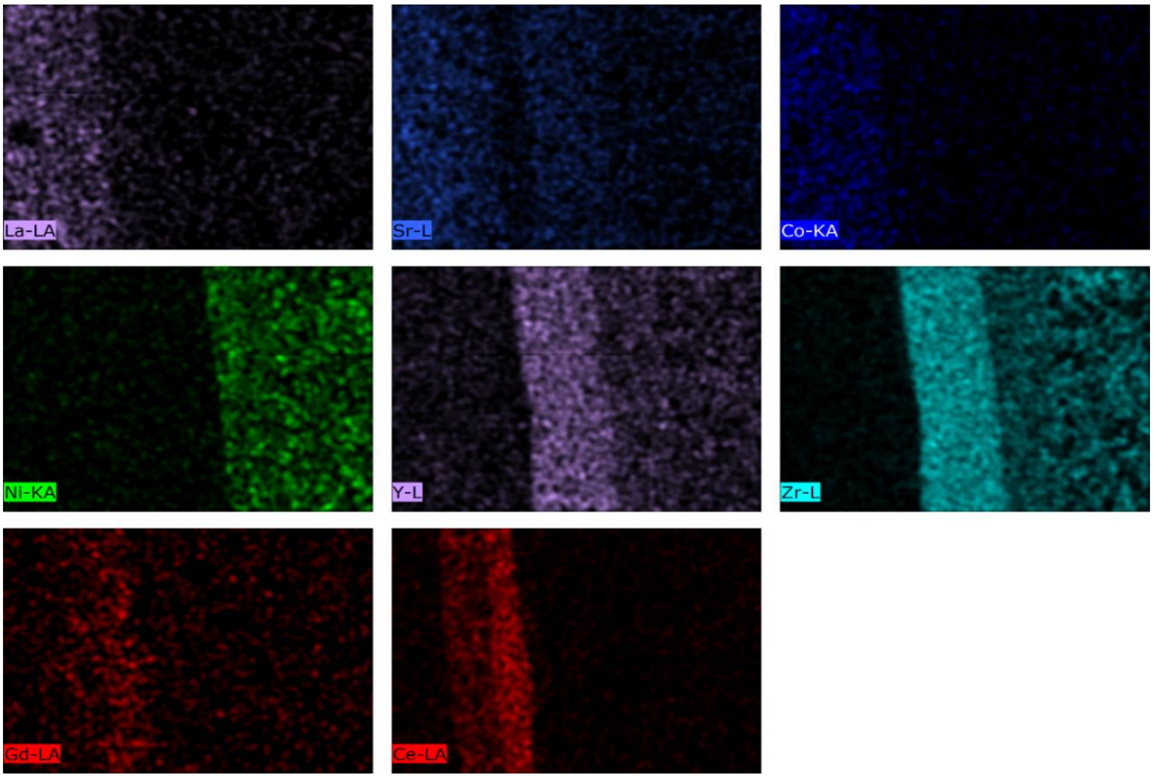

Figure 5-11: Cell elements distribution/identification.

5.3 Test at 0.5 A/cm^2 Current Density (Cell ID: CT1_0.5_700#1)

This test was carried out to investigate the effect of test temperature on cell performance. Therefore, all the other test variables were similar to the test reported in Section 5.2 (CT1_0.5_750#1). This cell (Cell ID: CT1_0.5_700#1) was thus tested at 700°C and a galvanostatic current density of 0.5 A/cm^2, whereas CT1_0.5_750#1 was tested at 750°C and a galvanostatic current density of 0.5 A/cm^2, both under all operating modes (SOFC, SOE & rSOC). As mentioned in Section 5.1:

1. During fuel cell operations, a dry mixture of 35.3 ml/min each of H_2 and N_2 was delivered to the fuel electrode, whilst 331.25 ml/min of air was delivered to the oxygen electrode; and

2. During electrolysis operations, 1.3 g/hr $H_2O_{(l)}$ mixed with 8.8 ml/min H_2 was delivered to the fuel electrode, whilst 66.25 ml/min of air was delivered to the oxygen electrode.

Figure 5-12 captures the durability of the cell under constant SOFC (0.5 A/cm^2), SOE (-0.5 A/cm^2) and rSOC (±0.5 A/cm^2) operation. The constant SOFC portion of the graph (first 120 hours) shows a stable voltage evolution, indicating good performance with minimal losses. The degradation rate, however, was 66 mV/1000h (7.7% / 1000h). This was more than twice the degradation rate of the cell tested at 750^{o}C, which was 28 mV/1000h (3.1% / 1000h). The next portion of the graph, which captures the constant SOE operation (120 hours to 240 hours) also shows relatively stable voltage evolution over the first approximately 40 hours (from 120 hours to ~ 160 hours). The subsequent region of the constant SOE portion of the graph (~160 hours to 240 hours) shows increasing voltage losses with the rate of increase increasing with time under test. The overall (average) degradation rate was 150 mV/1000h (15.3% / 1000h) in SOE operation. The rSOC portion of the graph (240 hours to 350 hours) shows some voltage recovery during the 3 hours of SOFC operation followed by voltage losses during the following SOE operation, like the observations reported under Section 5.2.

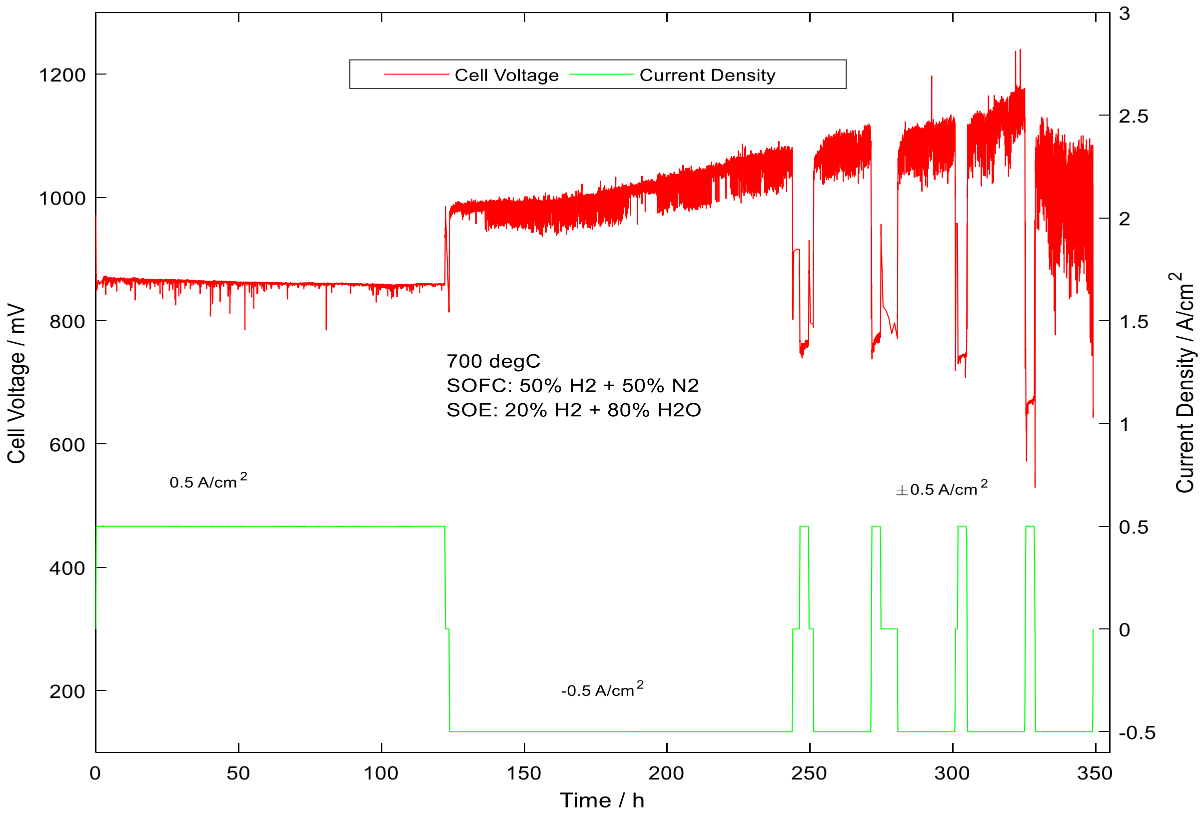

Figure 5-12: Voltage evolution characteristics of CT1_0.5_700#1 tested at 700°C and ±0.5 A/cm^2 current density.

Figure 5-13 shows the current – voltage (j-V) characteristics of the virgin cell, the cell after 120 hours of SOFC, and after an additional 120 hours of SOE operation. The current – voltage characteristics of the cell could not be captured after the rSOC operation due to test failure during the 4th reversible cycle.

As expected, the 'initial' curves, indicating the virgin cells j-V response, show the best performance in both the SOFC and SOE environments, with ASRs of 0.28 Ω.cm^2 and 0.27 Ω.cm^2, respectively. The slope of the cell's j-V response after the constant 120 hours of SOFC operation indicates a negligible drop in cell performance, with an ASR of 0.26 Ω.cm^2 (calculated from the slope of the j-V curve at 0.2 A/cm^2 to 0.3 A/cm^2). The difference in cell performance after the SOFC operation relative to the virgin cell was more pronounced in the j-V response captured under SOE environments (*Figure 5-13*(b)) with an increase in ASR to 0.32Ω.cm^2 compared to the decrease in ASR for the j-V curve captured under SOFC environment (*Figure 5-13*(a)). This was also noted for the cell tested at 750°C (see Section 5.2) and may be due to re-oxidation of nickel grains under the SOE environment. The j-V response of the cell after the constant 120 hours SOE operation indicates significant performance losses and is in line with the observed voltage losses in *Figure 5-12*. The calculated ASRs were 0.39 Ω.cm^2 and 0.5 Ω.cm^2, respectively, for the 'After SOE operation' curves in *Figure 5-13* (a) and (b). The significant difference in OCV after the SOE operation in *Figure 5-13* (a) was due to the presence of residual reactant steam from the preceding SOE operation, resulting in the significant decrease in OCV under SOFC conditions (also see *Figure 1-3*).

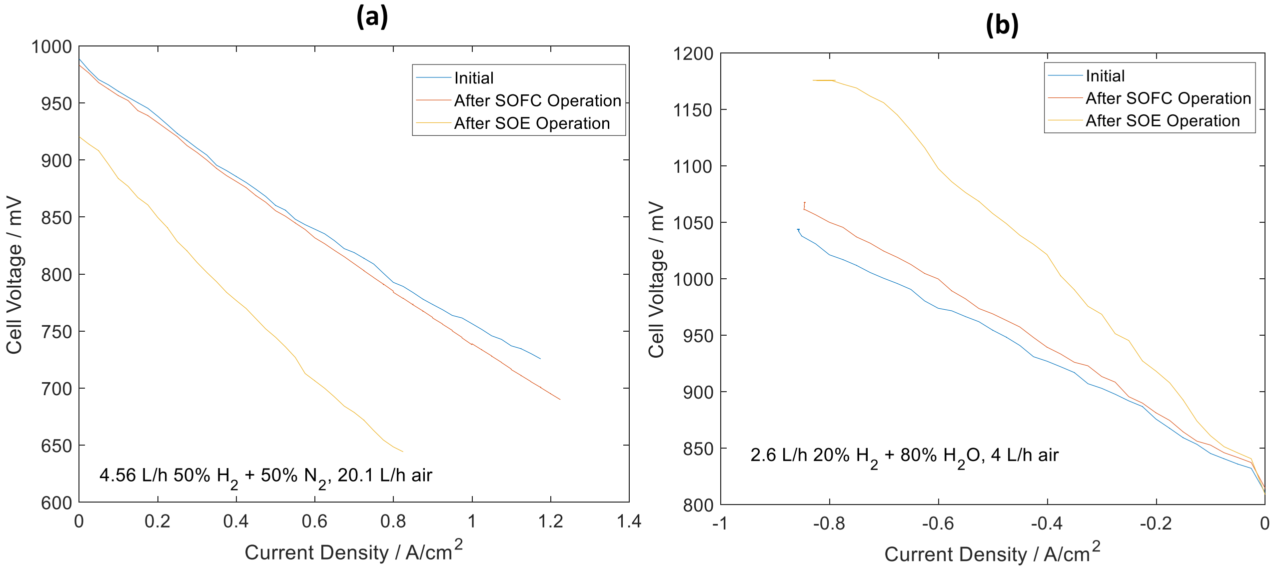

Figure 5-13: Comparison of j-V characteristics of CT1_0.5_700#1 before and after SOFC and SOE operation testing (captured under **(a)** SOFC and **(b)** SOE conditions).

Figure 5-14 shows the electrochemical impedance spectroscopy (EIS) equivalent of the j-V information presented in *Figure 5-13*(a). The Nyquist and Bode plots of the impedance information captured under SOFC conditions, *Figure 5-14*, show no increases in the Ohmic resistance of the cell after the constant 120 hours SOFC operation relative to the 'initial' impedance curve for the virgin cell (0.2 Ω.cm^2). This corresponds generally well with the 'after SOFC operation' j-V curve in *Figure 5-13* (a). However, the EIS data show an increase in polarisation resistance (0.54 Ω.cm^2) of the cell after 120 hours of constant SOFC operation, relative to the polarisation resistance of the virgin cell (0.45 Ω.cm^2). This indicates an increase in resistance to some of the electrochemical processes occurring in the electrodes.

Figure 5-14 further shows a marginal increase in Ohmic resistance (0.23 Ω.cm^2), a significant increase in polarisation resistance (0.65 Ω.cm^2), as well as the development of a gas conversion related low frequency arc, after the cell was subjected to the 120 hrs of constant SOE operation.

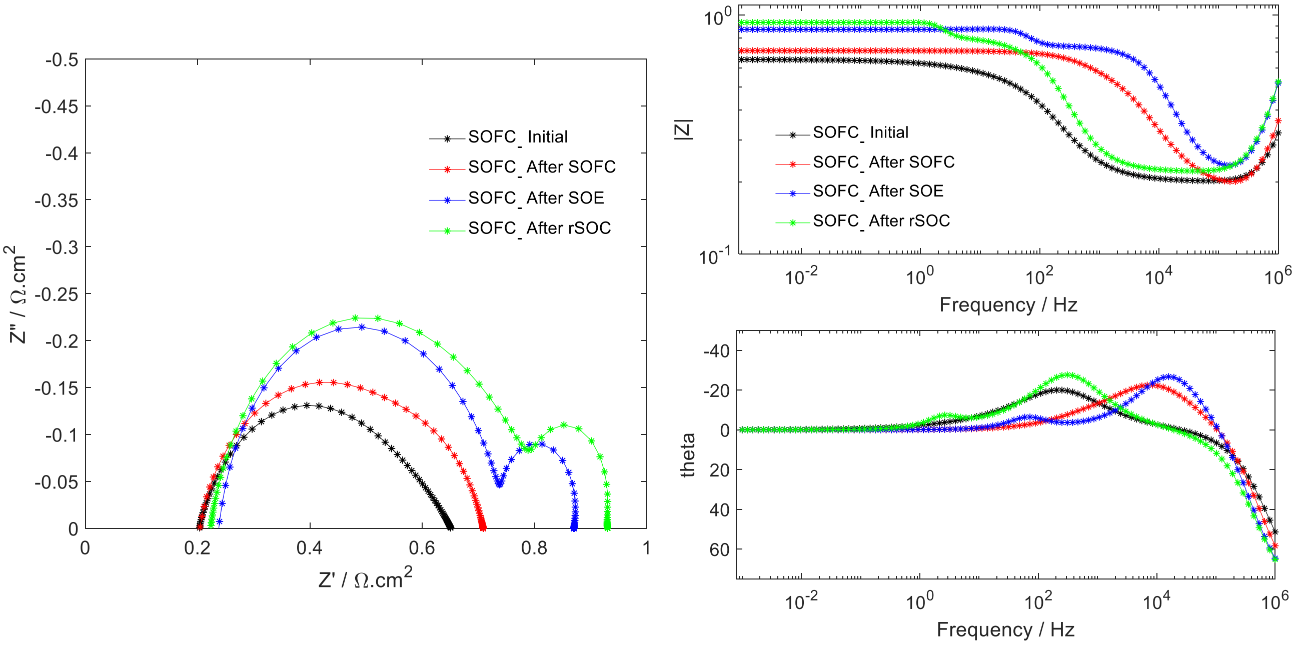

Figure 5-14: Nyquist and Bode impedance plots of CT1_0.5_700#1 before and after SOFC, SOE and rSOC operation testing (captured under SOFC conditions).

After the rSOC cycles (3 hours SOFC followed by 20 hours SOE operation), the Ohmic contribution was relatively unchanged (0.22 Ω.cm^2) and the polarisation resistance had increased to

0.72 Ω.cm^2. This suggests that electrode deterioration during SOE operation, especially, was the major contributor to the cell's performance losses. This is also in line with the significant overall performance loss indicated by the j-V curve of the cell after SOE operation, *Figure 5-13*. In addition, resistances to some gas conversion related processes, which are only active during SOE operation, contributed to the cell performance losses.

Figure 5-15 shows the equivalent Nyquist and Bode plots captured under SOE conditions of the virgin cell, and the cell after the 120 hours of SOFC operation, after the additional 120 hours of SOE operation, and finally after the rSOC cycles of 3 hours SOFC followed by 20 hours SOE. Similar to *Figure 5-14*, increases in both the high frequency Ohmic and polarisation contributions, as well as an increase in resistance to gas conversion processes, are indicated by the Nyquist plot captured under SOE conditions after the 120 hours of SOE operation and after rSOC operation.

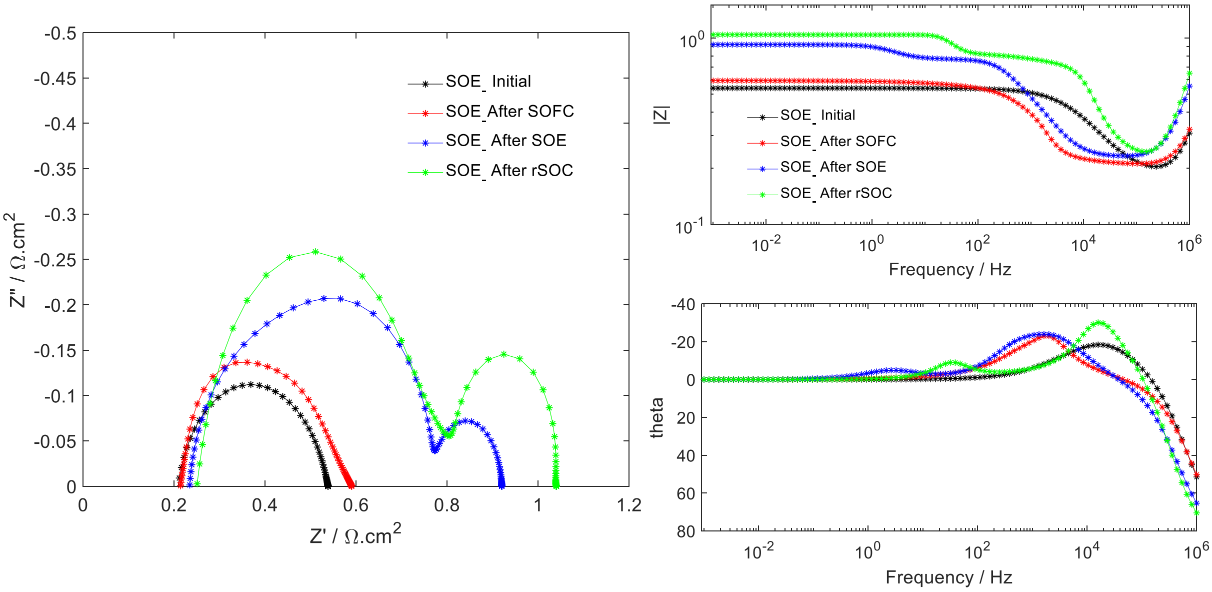

Figure 5-15: Nyquist and Bode impedance plots of CT1_0.5_700#1 before and after SOFC, SOE and rSOC operation testing (captured under SOE conditions).

There were marginal increases in both Ohmic and polarisation losses after the constant 120 hours SOFC operation.

After the additional 120 hours of SOE operation, the Nyquist plot captured under SOE conditions, Figure 5-15, shows a marginal increase in the Ohmic resistance (0.25 $\Omega.cm^2$), relative to the 'after 120 hours SOFC operation' curve (0.2 $\Omega.cm^2$), and a significantly higher polarisation resistance increase (0.65 $\Omega.cm^2$ from 0.42 $\Omega.cm^2$). The EIS plot of the cell after the rSOC cycles of 3hrs SOFC followed by 20hrs SOE shows a more pronounced impedance behaviour relative to the plot taken after the 120hrs of SOE operation, Figure 5-15. There are more significant increases especially in the polarisation impedance (0.75 $\Omega.cm^2$). Furthermore, the gas conversion related process low frequency curve has become more pronounced and is thus contributing more to the overall cell performance losses.

5.4 Test at 0.5 A/cm^2 Current Density "Upside-down test apparatus configuration" (Cell ID: CT1_0.5_750#2)

The 'upside-down vertical test apparatus configuration' was employed in this test and the test reported in Section 5.5 to investigate any possible effect of gravity on cell degradation (i.e. to assess mass transport effects on cell degradation) during reversible operation. The feed gases to the fuel electrode were thus delivered against gravity for these two tests only (this section and the following Section 5.5) – see test apparatus depicted in *Figure 4-24*(b). All the other tests were performed with feed gases delivered to the fuel electrode with gravity. It was hypothesised in Section 4.1 that for vertical rSOC set-ups, delivery of the feed gases to the fuel electrode against gravity (as in this section and Section 5.5) would be beneficial in SOFC mode whilst the reverse should hold for SOE mode. This is due to the differential densities of the reactant gases and products (in-spite of the high rSOC temperatures and the pseudo-closed system). The results presented in this section and Section 5.5 should therefore show better SOFC performance relative to SOE performance, as compared with tests utilising similar variables (results presented in Sections 5.2 and 5.3) but with the opposite test apparatus configuration (as used for all other tests reported in this thesis, see *Figure 4-24*(a)). If proven, this may necessitate a flexible test apparatus design to accommodate both configurations in order to optimise the rSOC global mass transport variables.

The test reported in this Section 5.4 (CT1_0.5_750#2) was thus carried out with the same test variables as the test reported in Section 5.2 (CT1_0.5_750#1), with the exception of flipping over the cell electrode sides and subsequent feed gas flows to assess any gravity effects on global mass transport of the feed gases.

Figure 5-16 indicates the voltage evolution or durability of the cell under test. As can be seen for the constant SOFC portion (first 120 hours), there was significant voltage drop. From an OCV voltage of 1010 mV, the voltage dropped to 700 mV under a current density of 0.5 A/cm^2. The voltage dropped further over the 120 hours under current density load to 430 mV, before a slight recovery to 500 mV towards the end of the 120 hours. This was not as expected, since the hypothesis was that this test configuration should improve SOFC performance, or at least not negatively impact SOFC performance relative to all other tests reported in this thesis (except for the test reported in Section 5.5). The reason for this hypothesis was that, in SOFC mode, H_2 + N_2 feed gases are delivered against gravity (which should not significantly impact global mass transport due to the low density of these gases), whilst gravity facilitates the exit of the produced $H_2O_{(g)}$ from the reaction zone. Conversely, in SOE mode, steam (plus nominal H_2) is delivered against gravity which is expected to hinder the mass transport of the steam to the reaction zone and the exit of the produced H_2 from the reaction zone.

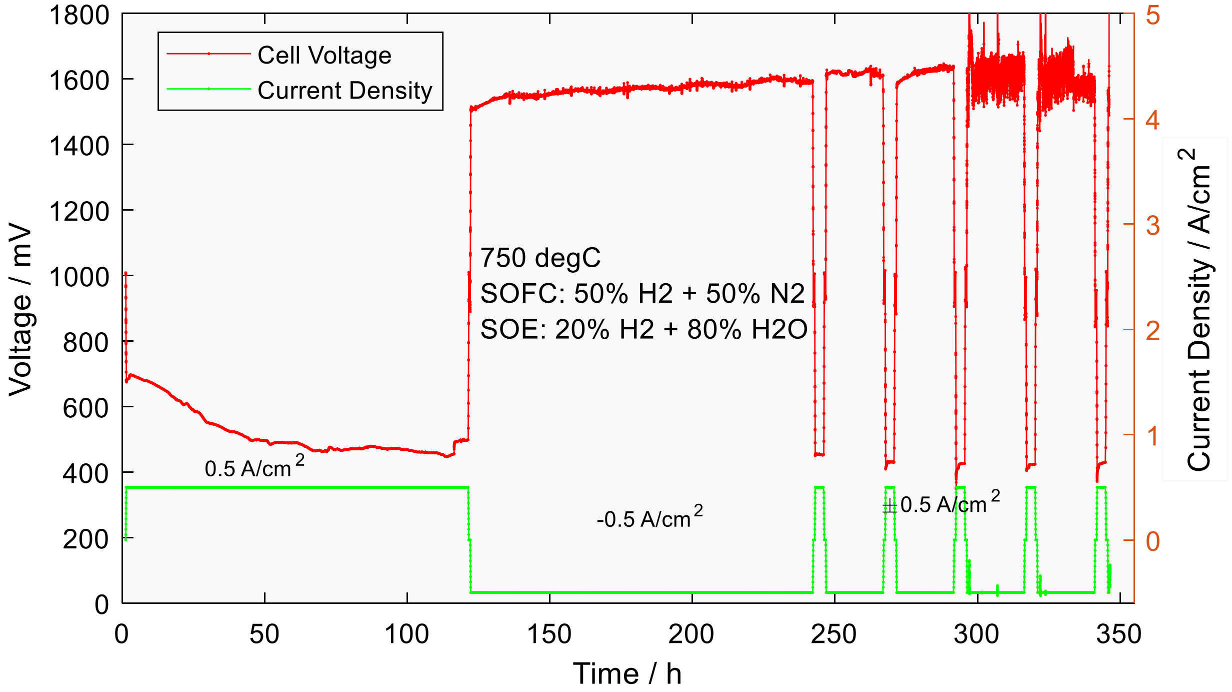

Figure 5-16: Voltage evolution characteristics of CT1_0.5_750#2 tested at 750°C and ±0.5 A/cm^2 current density (upside-down test apparatus configuration, see Figure 4-24 (b)).

Therefore, the voltage evolution trend of the SOFC portion of *Figure 5-16*, with a voltage degradation rate of 2.02 V/1000h did not seem to support the hypothesis. However, exploratory investigations during the test discovered a blockage in the air supply line to the oxygen electrode, limiting air flow to approximately 150 ml/min, thus resulting in oxygen electrode starvation (331.25 ml/min air flow required during SOFC, whilst 66.25 ml/min air flow required during SOE). Attempts to rectify the air obstruction without completely stopping the test were only somewhat successful after about 115 hours of constant SOFC operation.

The required feed gas flows were thus restored to all electrodes during the constant SOE operation. The constant SOE portion of *Figure 5-16*, from 120 hours to 240 hours, shows that a relatively high voltage (1500 mV) was required to sustain the 0.5 A/cm^2 current density, and the voltage degradation rate was 667 mV/1000h (44.2% / 1000h). The SOE starting voltage of 1500 mV was equivalent to the rSOC end voltage under tests performed in similar conditions (except test apparatus configuration) as reported in Section 5.2. This suggested that the vertical test apparatus configuration where steam was fed against gravity during SOE operation was not suitable for stable system performance, since the electric energy input ($\Delta G = \Delta H - T\Delta S$, see Section 1.1.3.2) required to produce a mole of hydrogen was significantly more than the system configuration where steam was fed with gravity.

The j-V characteristics of the virgin cell, of the cell after 120 hours of constant SOFC operation, after 120 hours of constant SOE operation, and finally after rSOC operation, as captured under SOFC and SOE environments, are shown in *Figure 5-17*. *Figure 5-17* (a) are the j-V curves captured under SOFC conditions, whilst (b) are the equivalent j-V curves captured under SOE conditions.

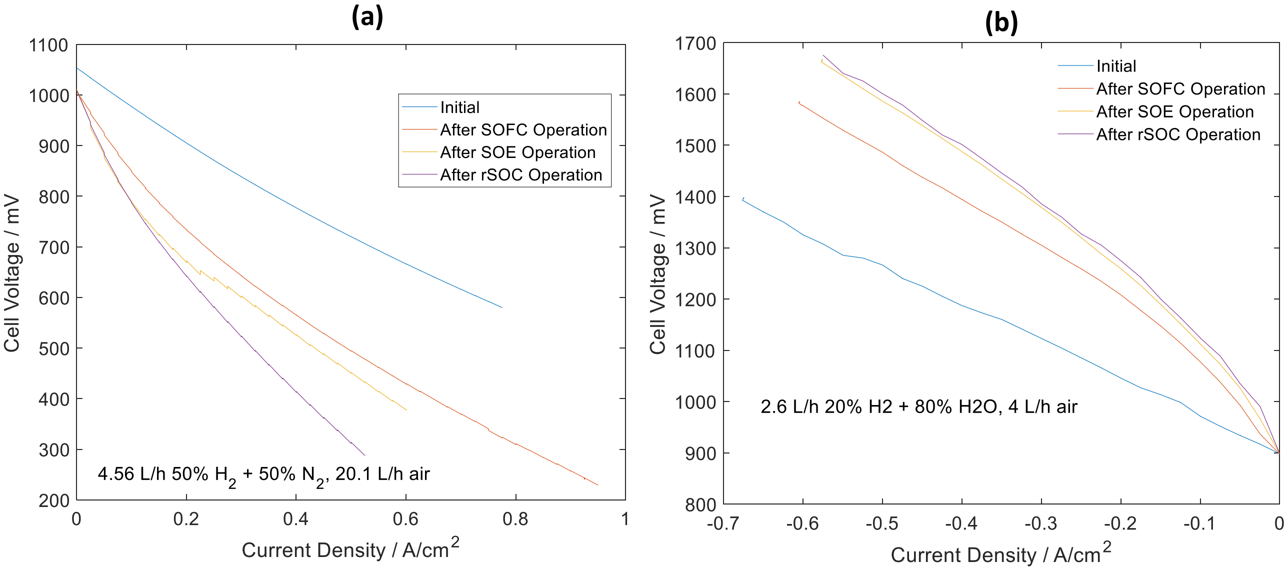

Figure 5-17: Comparison of j-V characteristics of CT1_0.5_750#2 before and after SOFC, SOE and rSOC operation testing (captured under **(a)** SOFC and **(b)** SOE conditions).

Relative to the j-V curve of the virgin cell, in both the SOFC and SOE environments, it is evident that the cell had undergone significant degradation during the 120 hours of constant SOFC operation. The ASR of the virgin cell was 0.67 Ω.cm^2 and 0.77 Ω.cm^2, respectively, in the SOFC and SOE environments. After the 120 hours of constant SOFC, the ASR had increased to 0.9 Ω.cm^2 and 0.97 Ω.cm^2 respectively. This was in line with the significant voltage drop observed in the cell durability results displayed in *Figure 5-16*, and was significantly different to the j-V curves captured under similar conditions (except test apparatus configuration) as reported in Section 5.2, *Figure 5-6* and *Table 5-2*. This poor performance was probably due to significant stresses induced in the cell because of oxygen starvation at the air electrode. It was not attributed to hydrogen starvation at the fuel electrode (as a result of the test apparatus configuration) because the density of hydrogen suggests it would rise against gravity to contact the fuel electrode.

There was further deterioration in cell performance after the additional 120 hours of constant SOE operation, with ASRs of 0.94 Ω.cm^2 and 1.19 Ω.cm^2, respectively, and a further slight deterioration after the rSOC reversible cycles (ASRs of 1.19 Ω.cm^2 and 1.2 Ω.cm^2, respectively).

The OCV of the cell, as captured under SOFC conditions (see *Figure 5-17* (a)), after the 120 hours of constant operation SOFC operation shows a significant decrease relative to the OCV of the virgin cell. This reflects the significant degradation observed as displayed with the cell durability data, *Figure 5-16*, and attributed to oxygen starvation as a result of the blockage discovered in the air supply line to the oxygen electrode.

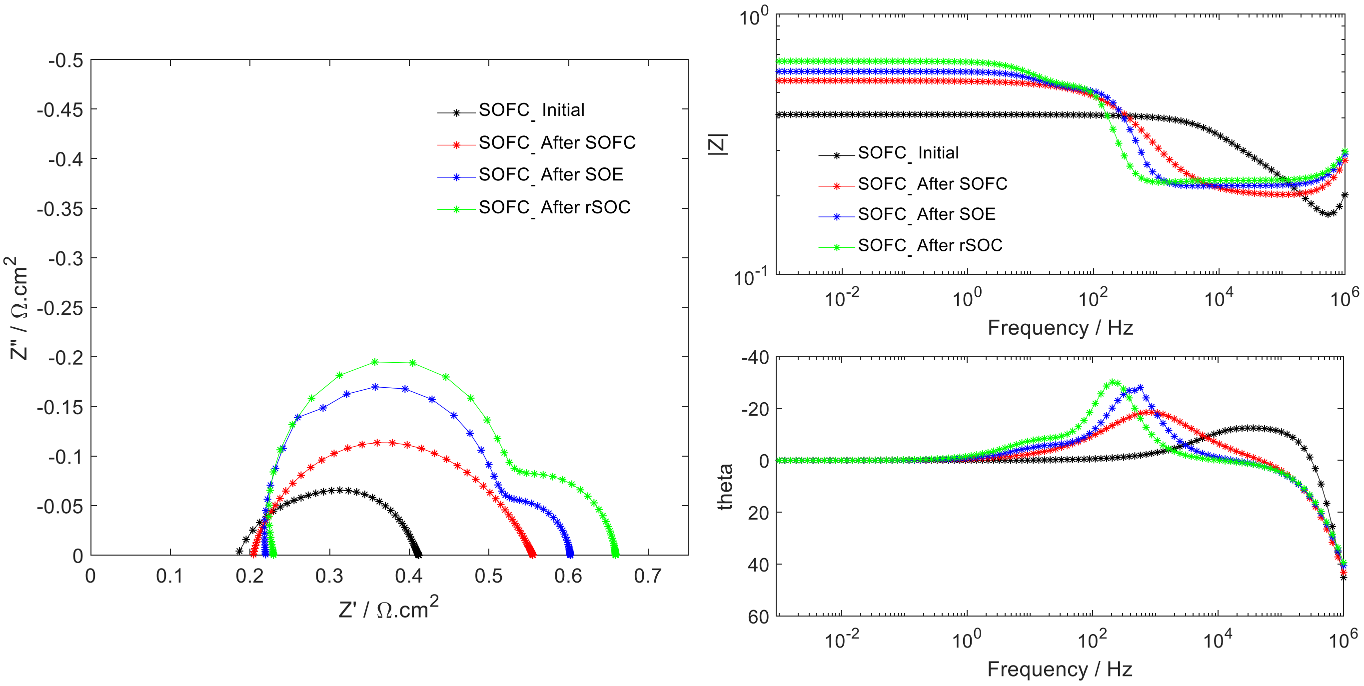

Figure 5-18: Nyquist and Bode impedance plots of CT1_0.5_750#2 before and after SOFC, SOE and rSOC operation testing (captured under SOFC conditions).

The Nyquist and Bode plots captured under SOFC environments as displayed in *Figure 5-18* (equivalent to the j-V curves in *Figure 5-17*(a)) indicate that the polarisation and mass transport resistances contributed the most to the poor cell performance. The ohmic contributions at all stages of the test were similar, ranging from 0.19 Ω.cm^2 for the virgin cell to 0.22 Ω.cm^2 after rSOC operation. The polarisation resistance of the virgin cell was 0.25 Ω.cm^2. It increased to 0.36 Ω.cm^2 after the 120 hours of constant SOFC operation. After the additional 120 hours of constant SOE operation, the polarisation resistance had increased further to 0.42 Ω.cm^2. After the five rSOC cycles, it increased to 0.47 Ω.cm^2.

The Nyquist and Bode plots captured under SOE conditions, as displayed in *Figure 5-19* (equivalent to the j-V curves shown in *Figure 5-17*(b)), was also in line with the cell resistances information given in *Figure 5-17*(b). Moreover, the mass transport depressions observed in the low frequency regime were more pronounced, indicating severe fuel starvation or significant gas concentration gradients at the electrodes under SOE conditions.

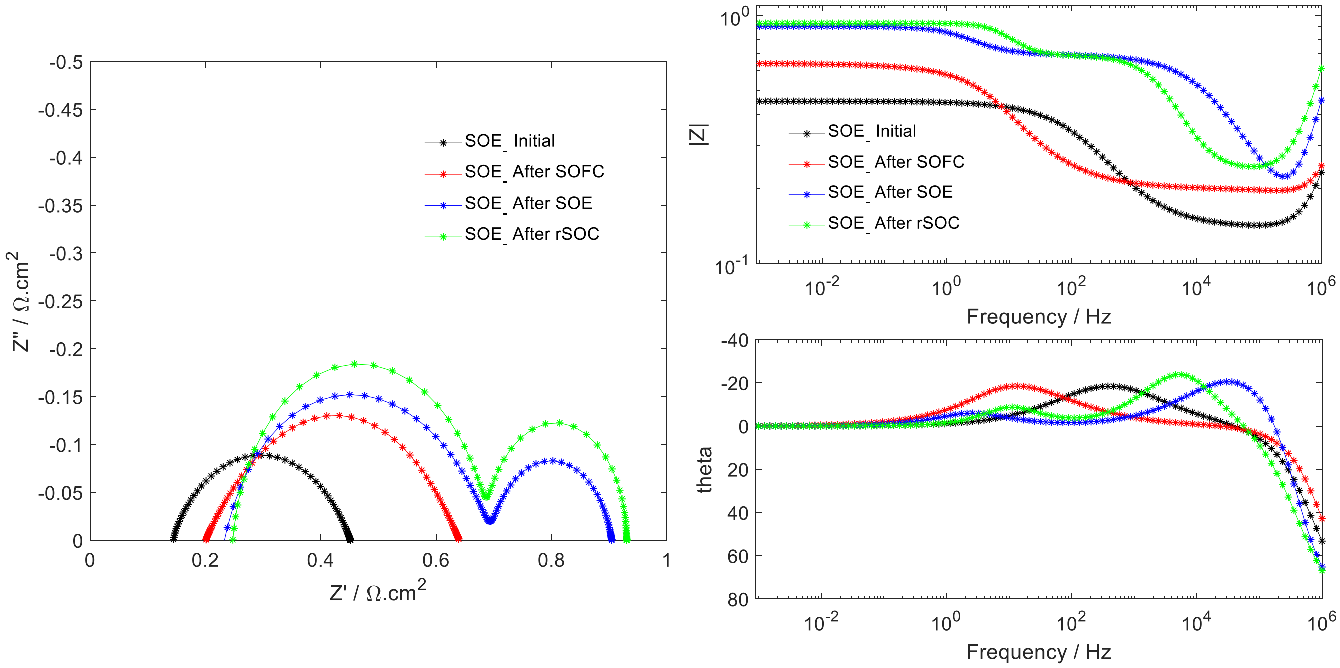

Figure 5-19: Nyquist and Bode impedance plots of CT1_0.5_750#2 before and after SOFC, SOE and rSOC operation testing (captured under SOE conditions).

5.5 Test at 0.5 A/cm^2 Current Density "Upside-down test apparatus configuration" (Cell ID: CT1_0.5_700#2)

This test was conducted as the experimental equivalent to the test reported in Section 5.3, excepting for the modification in test apparatus configuration as described in Section 5.4.

Figure 5-20 shows the cell's voltage evolution under test. This cell gave a relatively low OCV of ~890 mV. The voltage dropped to ~ 650 mV under a current density load of 0.5 A/cm^2, rising to about 710 mV after 2 hours. There was significant fluctuations in the cell voltage all through the constant SOFC operation, prior to the constant SOFC operation failing after 75 hours. The degradation rate prior to test failure was 33 mV/1000h (4.8% / 1000h). Attempts were made to ascertain the cause of the test failure whilst the process was still running. A significant leak was detected at the bottom of the alumina test tube reactor and was subsequently plugged with an alumina adhesive.

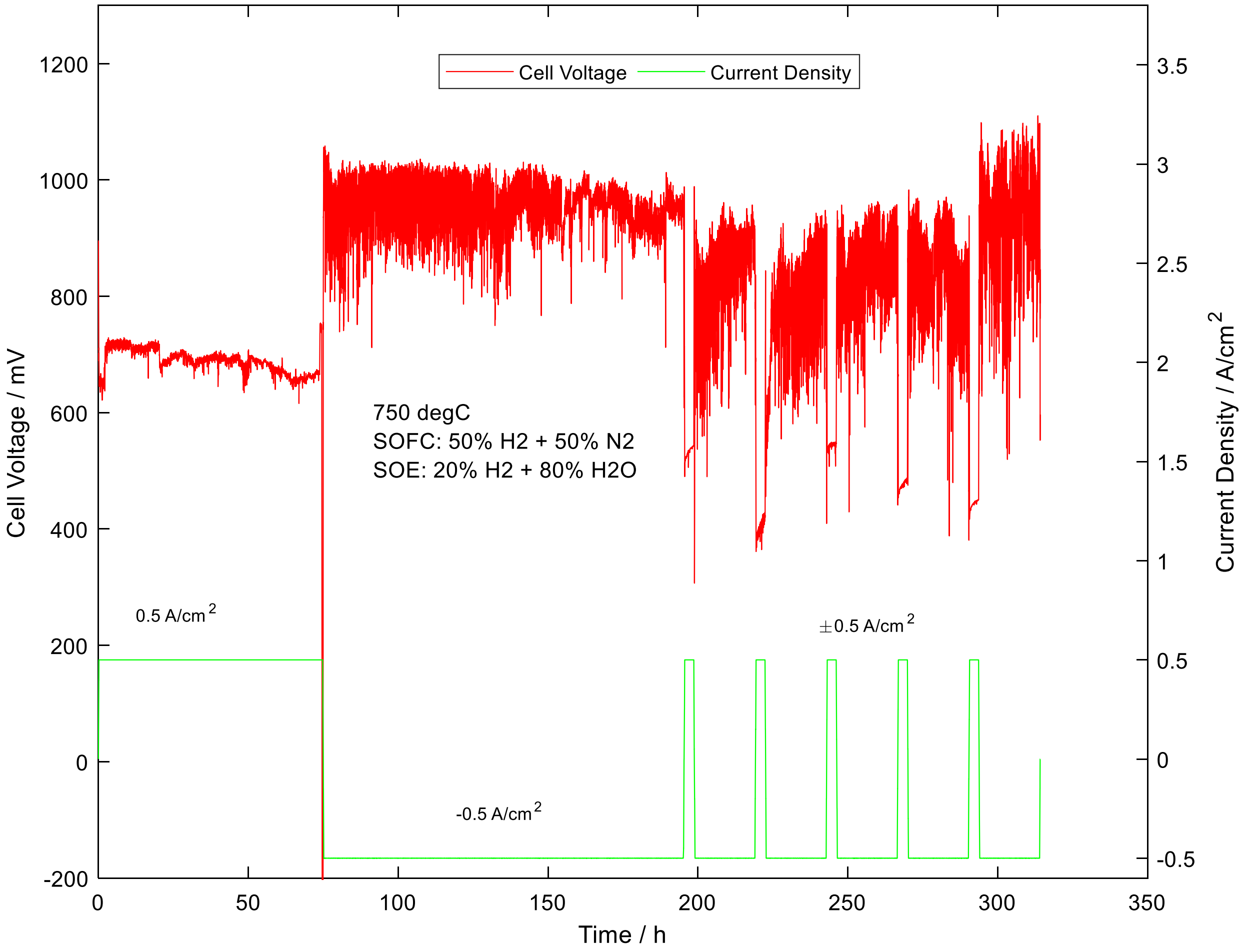

Figure 5-20: Voltage evolution characteristics of CT1_0.5_700#2 tested at 700°C and ±0.5 A/cm^2 current density (upside-down test apparatus configuration).

The test was then continued with the constant SOE operation for 120 hours with an OCV of ~750 mV. Under the -0.5 A/cm^2 galvanostatic load, the test voltage increased to ~1020 mV with significant scatter. The degradation rate during the constant SOE operation was 80 mV/1000h (8.5% / 1000h).

The significant voltage scatter continued over 5 rSOC cycles with an amplitude of 200mV. The test was therefore terminated.

After test termination, a pool of produced and/or reactant water (SOFC = $H_2 + O^{2} \rightarrow H_2O + 2^{e-}$ / SOE = $H_2O + 2^{e-} \rightarrow O^{2-} + H_2$) was found in the inside bottom of the alumina test tube. This had soaked the alumina adhesive joint at the bottom of the test tube, turning it into putty, and hence compromising the integrity of the joint. The resultant leak paths created were most likely the cause of the voltage fluctuations observed in the cell durability tests as displayed in *Figure 5-20*. The upside down vertical test apparatus configuration where the fuel gases (H_2 or H_2O_g) are fed to the fuel electrode against gravity is therefore not recommended due to the possibility of pooling water in the inside bottom of the test reactor, away from the reaction zone, in both SOFC and SOE modes.

Figure 5-21 displays the attempts made to capture the voltage – current characteristics of the cell. However, due to the aforementioned failure of the test reactor due to water pooling, these j-V curves are not considered to have captured the actual cell condition. For instance, the leak paths created by the water pooling were reflected in the significant scatter in OCVs for the virgin cell, after SOFC operation, after SOE operation and after rSOC operation as measured under both SOFC and SOE conditions. Nevertheless, for the j-V curves captured in the SOFC environment *Figure 5-21*(a), as expected, the resistance to ideal cell performance in the virgin cell was the lowest with an ASR of 0.52 $\Omega.cm^2$. The ASR increased to 0.78 $\Omega.cm^2$ after the 75 hours of SOFC operation. After the subsequent 120 hours of SOE operation, the ASR increased to 0.95 Ω.cm^2. After five rSOC cycles of 3 hours SOFC followed by 20 hours SOE, the ASR increased to 1.3 Ω.cm^2.

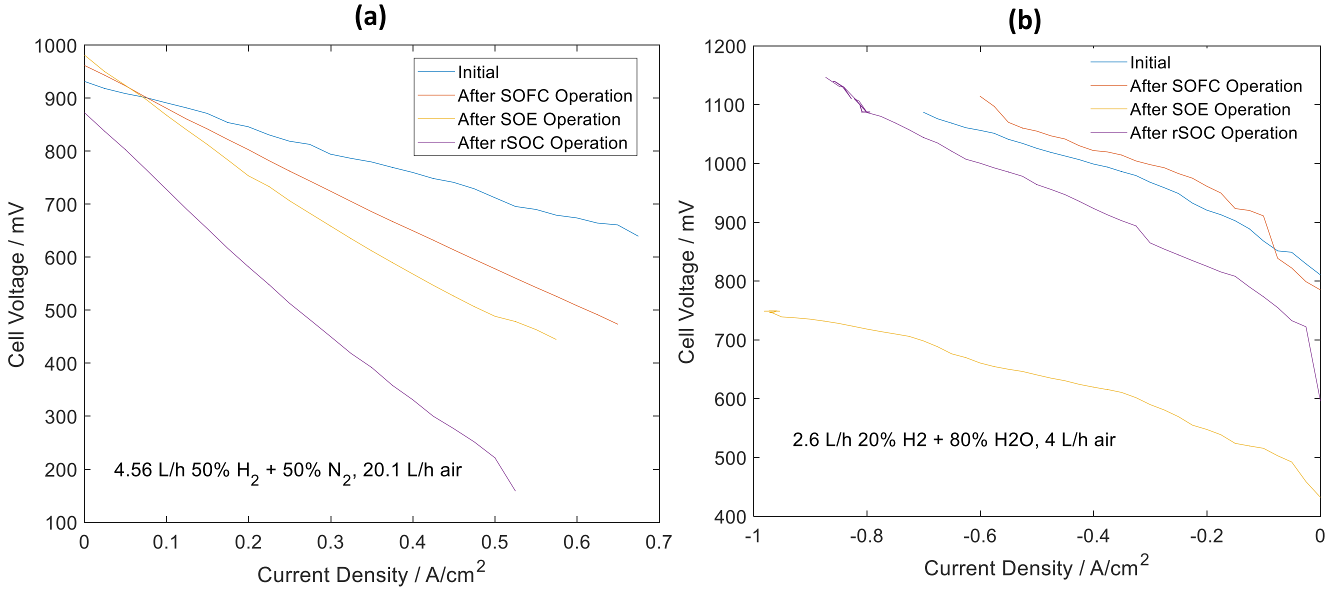

Figure 5-21: Comparison of j-V characteristics of CT1_0.5_700#2 before and after SOFC, SOE and rSOC operation testing (captured under **(a)** SOFC and **(b)** SOE conditions).

However, for the j-V curves captured in the SOE environment *Figure 5-21*(b), the results show that the resistances in the cell were lower after the 120 hours of constant 75 hours of SOFC operation (ASR of 0.37 Ω.cm^2) than the resistances in the virgin cell (ASR of 0.47 Ω.cm^2). This could be due to the significant voltage fluctuations observed during the test. After the 120 hours of constant SOE operation, the ASR in the SOE environment was 0.42 Ω.cm^2, decreasing again to 0.40 Ω.cm^2 after the five rSOC cycles.

The EIS data could provide more accurate cell information since the applied disruption (0A, with an amplitude of 10mA) was minimal in order to ensure pseudolinearity (the impedance being analogous to Ohms law resistance which is a linear function). As a result of the minimal applied

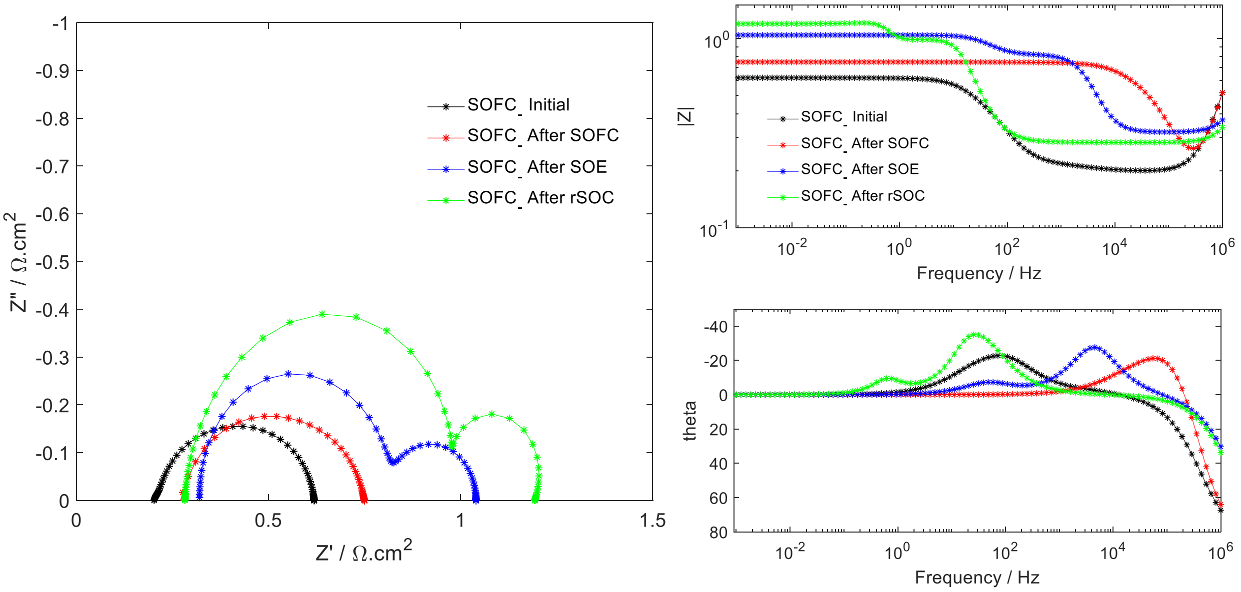

Figure 5-22: Nyquist and Bode impedance plots of CT1_0.5_700#2 before and after SOFC, SOE and rSOC operation testing (captured under SOFC conditions).

disruption, the significant voltage fluctuations due to reactor leakage were expected to be mitigated. *Figure 5-22* shows the Nyquist and Bode plots captured in SOFC environments. Relative to the virgin cell, there were significant increases in both the Ohmic and polarisation contributions of the cell after the 75 hours of constant SOFC operation. The Ohmic resistance increased from 0.22 Ω.cm^2 to 0.25 Ω.cm^2, whilst the polarisation resistance increased from 0.41 Ω.cm^2 to 0.51 Ω.cm^2. After the subsequent 120 hours of SOE operation and the five rSOC cycles, the Ohmic resistances were unchanged whilst the polarisation resistances had increased to 0.73 Ω.cm^2 and 1.0 Ω.cm^2, respectively.

The Nyquist and Bode plots captured in the SOE environment, *Figure 5-23*, show similar trends in the overall cell resistances as for the plots captured in the SOFC environment, *Figure 5-22*.

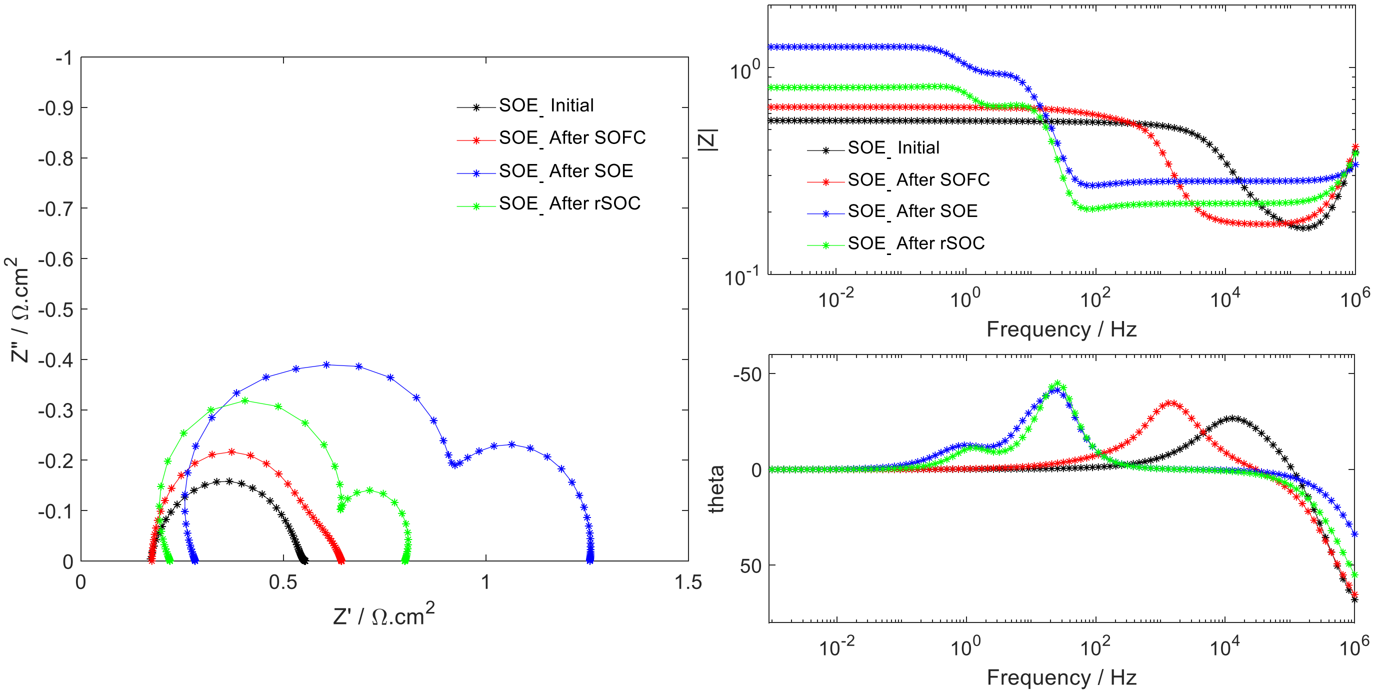

Figure 5-23: Nyquist and Bode impedance plots of CT1_0.5_700#2 before and after SOFC, SOE and rSOC operation testing (captured under SOE conditions).

Additionally, the low frequency depression, which is specifically related to a gas conversion process, was more pronounced in the SOE environment, especially for the cell condition after the constant SOE operation. Similar to *Figure 5-21*(b), the cell seems to have undergone significant recovery after the rSOC cycles. However, this may be a consequence of the reactor failure due to produced and/or reactant water pooling outside the reaction zone resulting in several leak paths through the alumina reactor, especially since the test was terminated after a 20 hour SOE cycle during rSOC operation (see *Figure 5-20*).

5.6 Test at 0.7 A/cm^2 Current Density (Cell ID: CT1_0.7_750)

This test was carried out to study the effect of current density and fuel utilisation on cell performance and degradation characteristics. Fuel utilisation, also known as H_2 or H_2O conversion, is a ratio of the molar flow of electrons over the molar flow of reactants (hydrogen atoms), also see Section 3.3.3. The fuel feed parameters were maintained as a constant, and are as follows (same as the tests previously reported):

1. During fuel cell operations, a dry mixture of 35.3 ml/min each of H_2 and N_2 was delivered to the fuel electrode, whilst 331.25 ml/min of air was delivered to the oxygen electrode;
2. During electrolysis operations, 1.3 g/hr $H_2O_{(l)}$ mixed with 8.8 ml/min H_2 was delivered to the fuel electrode, whilst 66.25 ml/min of air was delivered to the oxygen electrode.

Thus, the only parameter which was changed in order to study the effect of fuel utilisation was the test current density. A current density of 0.7 A/cm^2 was used for this test. This increased the fuel utilisation from the 52.3% used for the previously reported tests (Sections 5.2 to 5.5) to 73.3%. It was expected that this fuel utilisation would increase the induced stresses in the cell (especially at the oxygen electrode interface with the electrolyte during SOE) due to the increased flux of oxygen ions through the cell.

Figure 5-24 shows the durability of the cell under a fuel utilisation of 73.3% (0.7 A/cm^2 current density). The open cell voltage (OCV) in the SOFC environment was 1057 mV, dropping down to 761 mV under the 0.7 A/cm^2 current density load. At the end of the 120 hours of constant SOFC operation, the voltage had dropped down to 705 mV. The OCV at the end of the constant SOFC operation was 1068 mV, possibly indication some further reduction of the nickel grains in the Ni-YSZ fuel electrode during the SOFC operation. The degradation rate during the constant SOFC operation was 208 mV/1000 h (27.6% / 1000h).

The OCV, in the SOE environment, for the subsequent 120 hours of constant SOE operation was 893 mV. This increased to 1232 mV under the -0.7 A/cm^2 current density load. At the end of the 120 hours of constant SOE operation, the cell voltage had increased further to 1310 mV, with a degradation rate of 602 mV/1000h (48.8% / 1000h). This was approximately three times the degradation rate for the preceding 120 hours of constant SOFC operation.

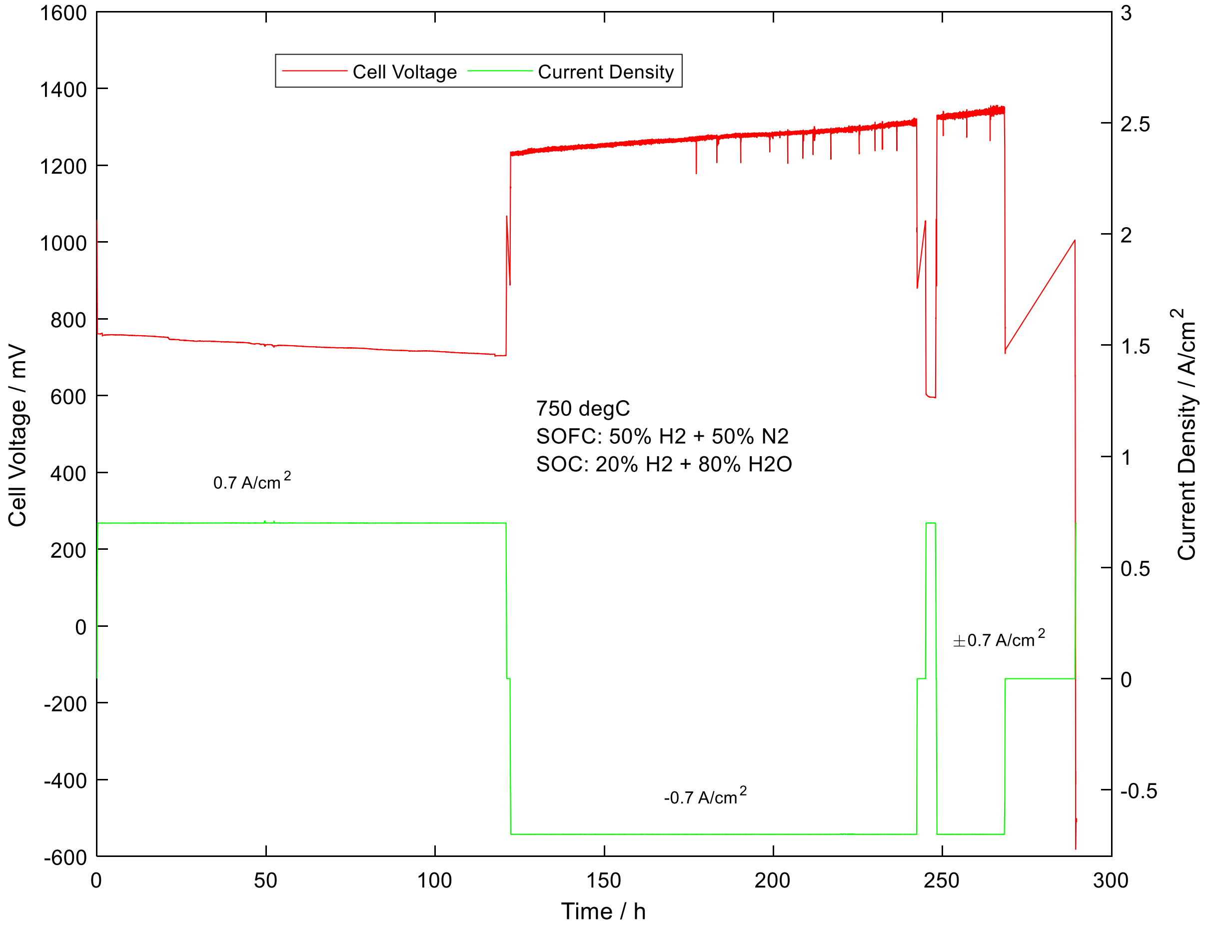

Figure 5-24: Voltage evolution characteristics of CT1_0.7_750 tested at 750°C and ±0.7 A/cm^2 current density.

The OCV for the first SOFC cycle of the rSOC operation was 1056 mV, dropping down to 603 mV under the 0.7 A/cm^2 current density load. Compared to the voltage drop observed at the start of the 120 hours of constant SOFC operation (1057 mV to 761 mV), the 1056 mV to 603 mV drop suggests the constant SOE operation at a current density of -0.7 A/cm^2 (and a fuel utilisation of 73.3 %) had increased the resistances in the cell. At the end of the 3 hours of the first SOFC cycle of the rSOC operation, the voltage had dropped further to 595 mV indicating that the cell had been irreversibly damaged by either the constant SOE operation with a fuel utilisation of 73.3% or during the j-V characterisation of the cell under SOE environment at voltages up to -2250 mV (see *Figure 5-25*(b)). The OCV at the end of this first SOFC cycle was 1059 mV, indicating that the extremely low voltages under load were due to internal restructuring (damage) of the cell and not merely due to surface fluid dynamics.

The SOE environment OCV for the first SOE cycle of the rSOC operation was 893 mV. This increased to 1325 mV under the -0.7 A/cm^2 current density load, slightly increasing further to 1335 mV at the end of the first SOE cycle of the rSOC operation.

After this SOE operation, the cell could not sustain any additional SOFC current density load making it impossible to capture the post-rSOC cell condition via j-V characterisation or EIS assessment. The test was thus terminated.

Figure 5-25 shows the j-V characteristic of the virgin cell, of the cell after the 120 hours of constant SOFC operation and also after the constant SOE operation, in both SOFC and SOE environments. The j-V characteristic of the cell after reversible cycling could not be captured due to cell damage during the rSOC operations.

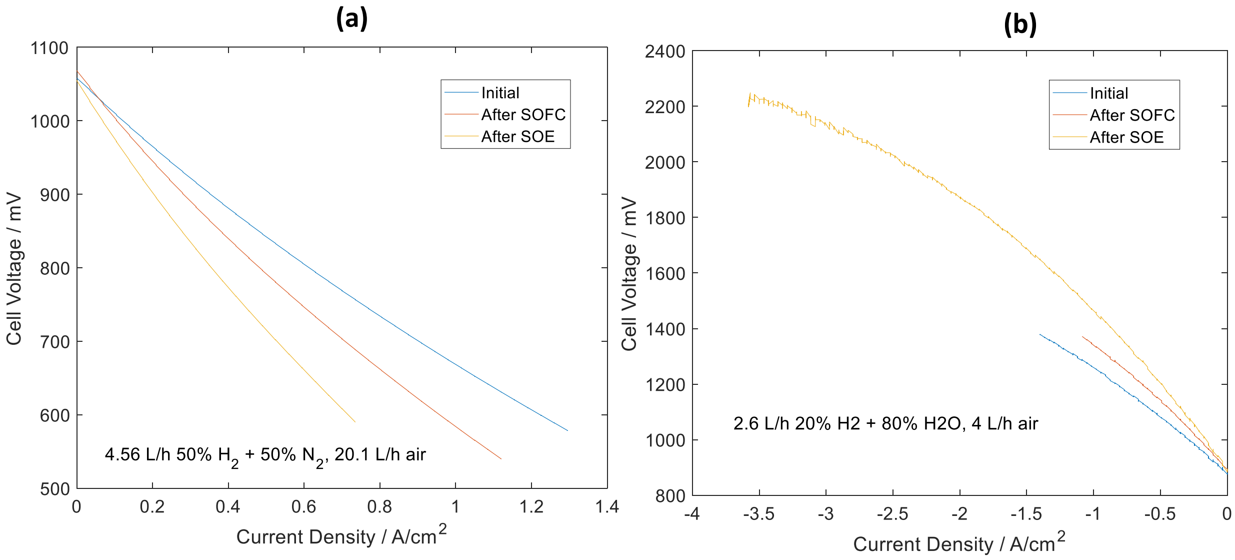

Figure 5-25: Comparison of j-V characteristics of CT1_0.7_750 before and after SOFC and SOE operation testing (captured under SOFC and SOE conditions).

The ASR of the virgin cell (in the SOFC environment, *Figure 5-25*(a)) was 0.43 Ω.cm^2. It increased to 0.54 Ω.cm^2 after the 120 hours of SOFC operation, with a further increase to 0.66 Ω.cm^2 after the subsequent 120 hours of SOE operation. The equivalent ASR of the virgin cell (in the SOE environment, *Figure 5-25*(b)) was 0.45 Ω.cm^2. The ASR increased to 0.50 Ω.cm^2 after the 120 hours of SOFC operation and increased further to 0.57 Ω.cm^2 after the subsequent 120 hours of SOE operation.

The differences in the change in cell ASR under the different environments (SOFC and SOE), *Figure 5-26*, indicate that the process(es) linked to the increase in cell resistance at the 0.7 A/cm^2 current density (73.3% fuel utilisation) may be exacerbated under SOFC conditions relative to cell performance at 0.5 A/cm^2 current density and fuel utilisation of 52.3%. This would be the case if the resistance increases were linked to mass transport limitations and polarisation resistance as a result of the high fuel utilisation.

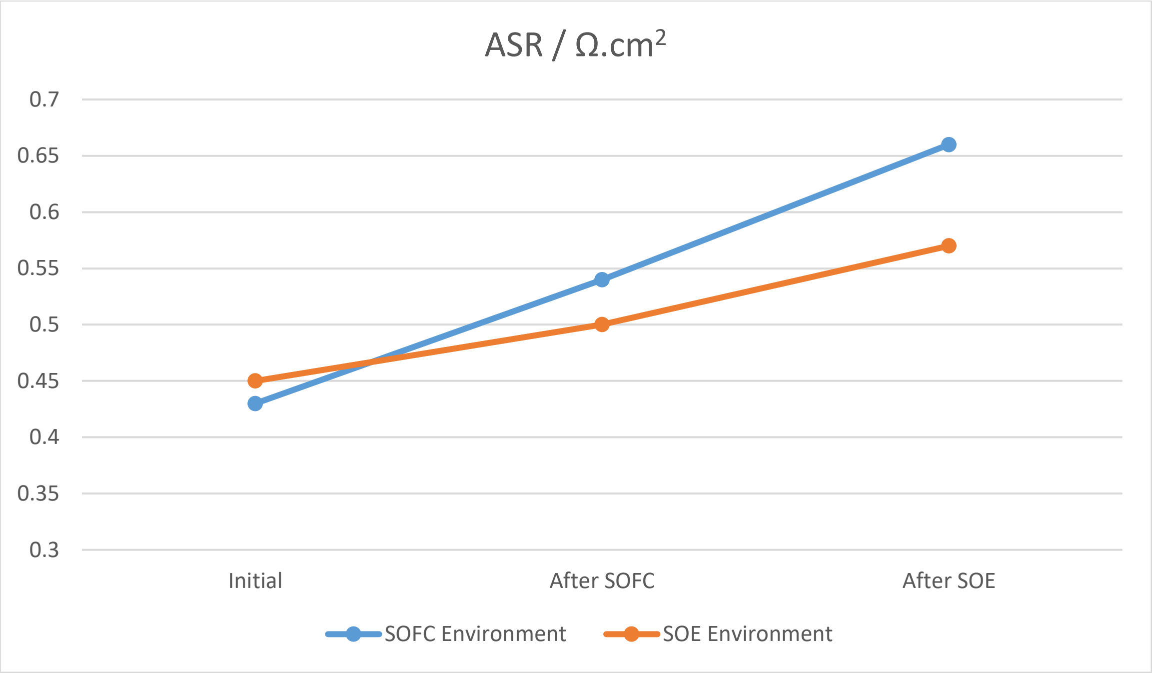

Figure 5-26: Change in cell ASR with mode of operation, as captured under SOFC and SOE environments for CT1_0.7_750.

Electrochemical impedance spectroscopy was also used to interogate the cell. The Nyquist and Bode plots, captured in an SOFC environment, of the virgin cell, and after the constant SOFC and SOE operations are shown in *Figure 5-27*.

Relative to the virgin cell, there was a significant increase in the polarisation resistance of the cell after the constant 120 hours of fuel cell (SOFC) operation (from 0.5 Ω.cm^2 to 0.88 Ω.cm^2), whilst the Ohmic resistance was unchanged. After the subsequent 120 hours of constant SOE operation, the polarisation resistance did not change significantly (0.89 Ω.cm^2). The Ohmic resistance, on the other hand, increased from 0.25 Ω.cm^2 to 0.38 Ω.cm^2.

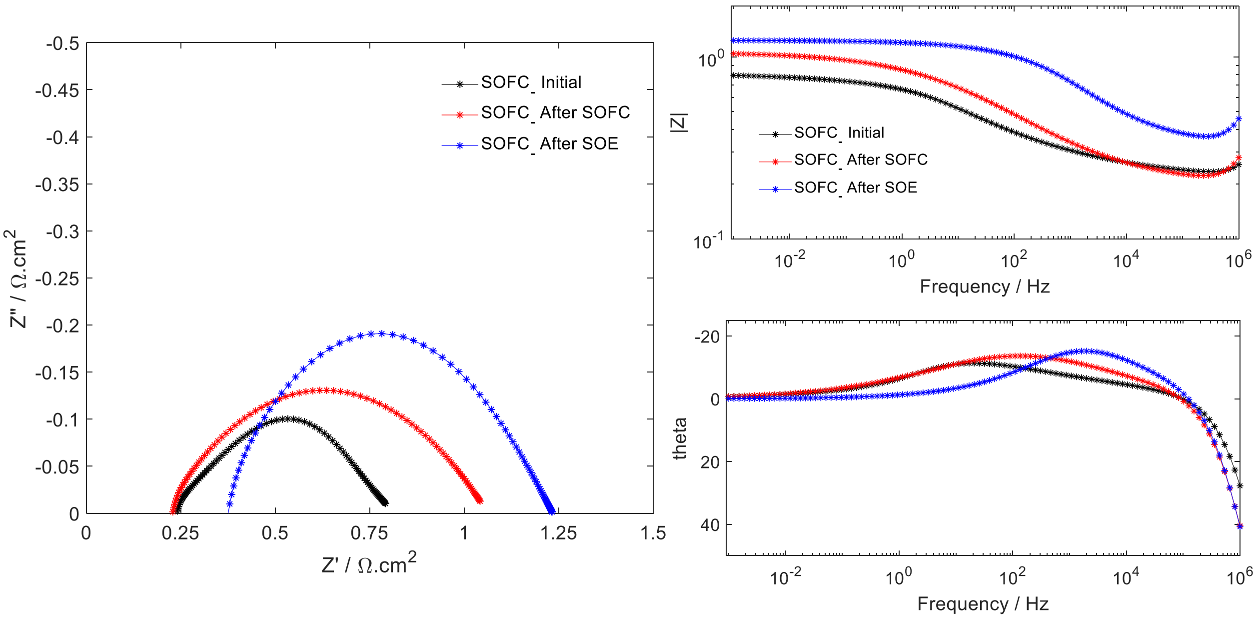

Figure 5-27: Nyquist and Bode impedance plots of CT1_0.7_750 before and after SOFC and SOE operation testing (captured under SOFC conditions).

The equivalent Nyquist and Bode plots captured in the SOE environment show that the Ohmic and polarisation resistances increased from 0.25 Ω.cm^2 to 0.34 Ω.cm^2 and 0.25 Ω.cm^2 to 0.42 Ω.cm^2 respectively, after the 120 hours of SOFC operation, relative to the virgin cell. After the subsequent 120 hours of constant SOE operation, the Ohmic resistance increased to 0.75 Ω.cm^2 whilst the polarisation resistance grew significantly to 0.87 Ω.cm^2. Due to the sequence of operations, it is most likely that the exposure of the cell to the high voltage (~2250 mV) during the j-V characterisation in an SOE environment (see *Figure 5-25*(b)) was responsible for the cell damage rather than the preceding 240 hours of constant SOFC followed by SOE operation. This is because the cell damage was only reflected in the Nyquist and Bode plots captured in the SOE environment after the 120 hours of contant SOE operation (*Figure 5-28*), but not in the Nyquist and Bode plots captured in the SOFC environment after the 120 hours of contant SOE operation, *Figure 5-27*. Note that the j-V characterisation in the SOE environment followed the EIS characterisation in the SOFC environment, which also preceded the EIS characterisation in the SOE environment (see Section 4.2.2 for further details).

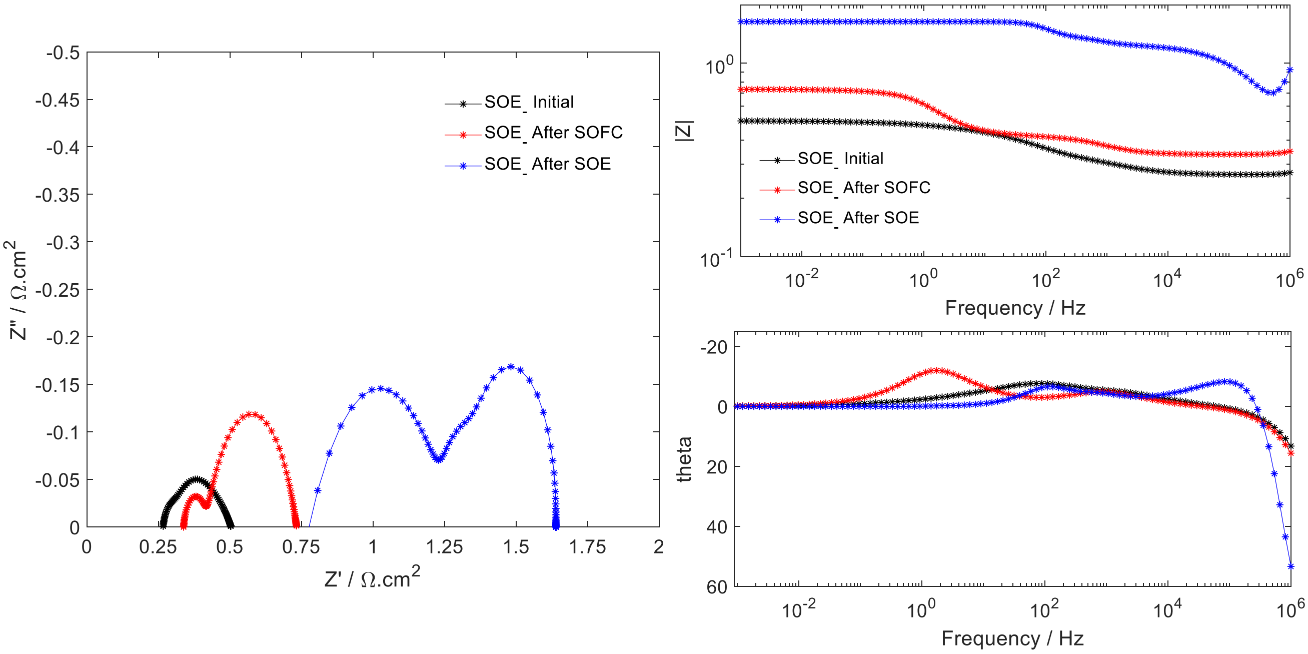

Figure 5-28: Nyquist and Bode impedance plots of CT1_0.7_750 before and after SOFC and SOE operation testing (captured under SOE conditions).

5.7 Test at higher SOE Current Density (Cell ID: CT1_1.39_750)

This test was carried out to study the effects of operating the rSOC device at different current densities (and fuel utilisations) in SOFC and SOE modes. The SOFC mode of this test was therefore conducted at a current density of 1.39 A/cm^2 and a fuel utlisation of 73.4% whilst the SOE mode was conducted at a current density of 2.65 A/cm^2 and a fuel utilisation of 100%. Due to the active area of the cell, the highest current density employed in the tests was 2.65 A/cm^2, chosen based on the 2.65 A nominal current required at the lowest current density used for the tests (0.5 A/cm^2).

To achieve the respective fuel utilisations, the fuel feed parameters used were as follows:

1. During fuel cell operations, a dry mixture of 70 ml/min each of H_2 and N_2 was delivered to the fuel electrode, whilst 331.25 ml/min of air was delivered to the oxygen electrode;
2. During electrolysis operations, 3.5 g/hr $H_2O_{(l)}$ (approximately 97 ml/min $H2O_{(g)}$) mixed with 8.8 ml/min H_2 was delivered to the fuel electrode, whilst 66.25 ml/min of air was delivered to the oxygen electrode.

The above fuel feed parameters, coupled with the 1.39 A/cm^2 current density during SOFC operation and 2.65 A/cm^2 during SOE operation, resulted in fuel electrode reactant utilisations of 73.4% for SOFC regime and 100% for the SOE regime. This type of rSOC operation may be an ideal industrial operation scenario to optimise energy storage or liquid fuel production via SOE operation, whilst also producing some electricity, as required, using the SOFC mode. It should be noted however that a fuel utilisation of 100% with a significantly high current density (2.65 A/cm^2) may expose the cell to excessive internal stresses.

Figure 5-29 presents the voltage evolution or cell durability characteristics of the cell exposed to a higher current density in SOE mode relative to its current density exposure under SOFC mode. In the SOFC environment, the open cell voltage before the start of the 120 hours of constant SOFC operation was 969 mV. This dropped down to 722.7 mV under the 1.39 A/cm^2 SOFC current density. At the end of the 120 hours of constant SOFC operation, the cell voltage had dropped further to 681.7 mV (with an SOFC end open cell voltage of 992.4 mV). The degradation rate was 357 mv/1000 h (49.6% / 1000h).

In the SOE environment, the open cell voltage before the start of the 120 hours of constant SOE operation was 781 mV under SOE fuel conditions. This increased to a voltage of 1388 mV under the SOE current density load of -2.65 A/cm^2.

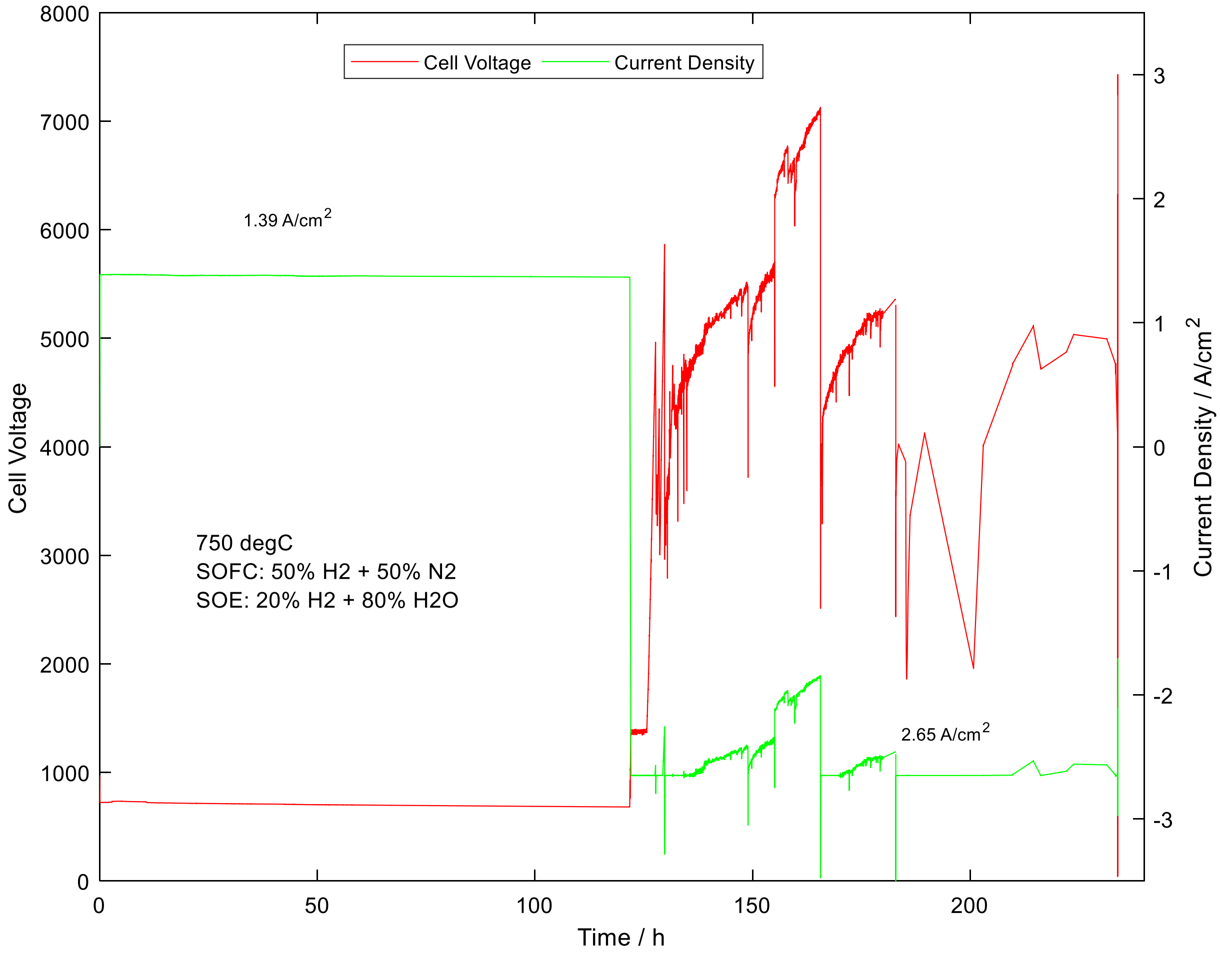

Figure 5-29: Voltage evolution characteristics of CT1_1.39_750 tested at 750°C and at +1.39 A/cm^2 under SOFC conditions and -2.65 A/cm^2 current density under SOE conditions.

The cell sustained this high voltage for approximately 4 hours. The voltage then increased steadily to about 4000 mV over the next hour indicating the progressive occurrence of significant cell damage. Although based on the voltage readings it was evident that the cell had been significantly damaged, the test was left to run its course since the results may provide some useful information on the effect damaged cells may have on an rSOC stack or an rSOC system. *Figure 5-29* indicates that it was not only the cell voltage which was fluctuating due to cell damage. Since all tests were run in galvanostatic mode, the current density should have remained constant throughout the test irrespective of the cell voltage. However, there were significant current density fluctuations as well, indicating that the cell was unable to utilise the supplied -2.65 A/cm^2 current density. Irrespective of the cell damage, theoretically, the cell was still producing hydrogen, albeit at extremely high voltages (i.e. very inefficiently), up until near the 120 hours of constant SOE operation when the test equipment shut down due to unacceptable voltages. Therefore it seems that although cell damage at a stack or system level would affect the efficiency of the system, the damaged cell may still have a positive contribution to the overall performance based solely on hydrogen production rates.

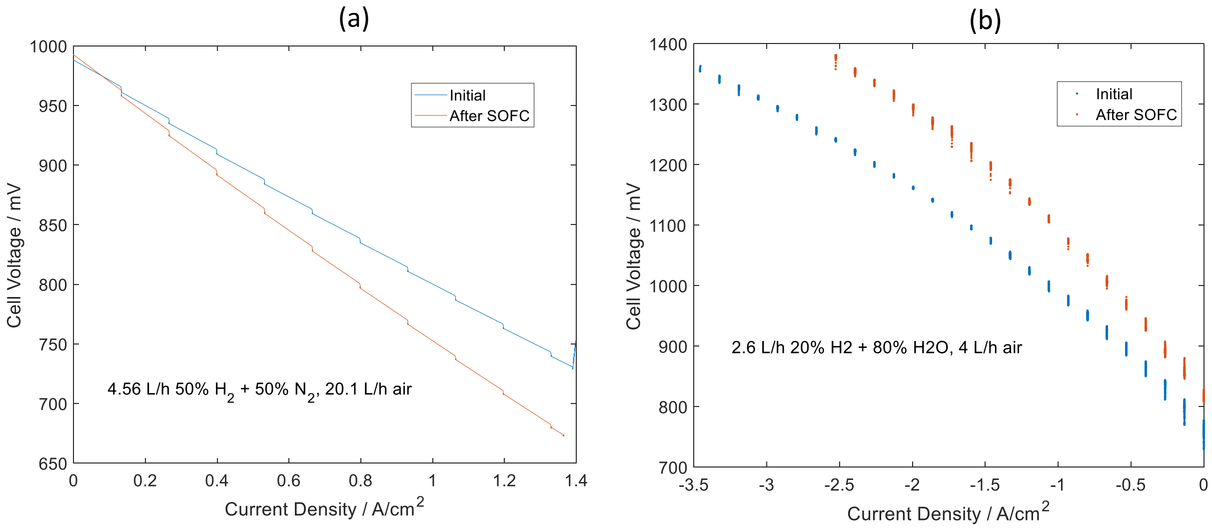

Figure 5-30: Comparison of j-V characteristics of CT1_1.39_750 before and after SOFC operation testing (captured under (a) SOFC and (b) SOE conditions).

Figure 5-30 shows the j-V characteristics of the virgin cell and also after the 120 hours of constant SOFC operation, captured in (a) SOFC and (b) SOE environments, respectively. Due to the significant damage to the cell as a result of the -2.65 A/cm^2 current density (with 100 % fuel utilisation) during the constant SOE operation, the cell was unable to sustain the current required to capture its j-V characteristics after the constant SOE operation. *Figure 5-30* shows that the cell had sustained the 1.39 A/cm^2 SOFC current density with a fuel utilisation of 73.4% really well, and was still in a good condition prior to the constant SOE operation. The ASR, based on the j-V information captured under SOFC conditions, after the 120 hours of SOFC operation was 0.31 Ω.cm^2, compared to 0.25 Ω.cm^2 for the virgin cell. The equivalent ASRs captured under SOE conditions were 0.26 Ω.cm^2 and 0.36 Ω.cm^2, respectively, for the virgin cell and of the cell after 120 hours of SOFC operation.

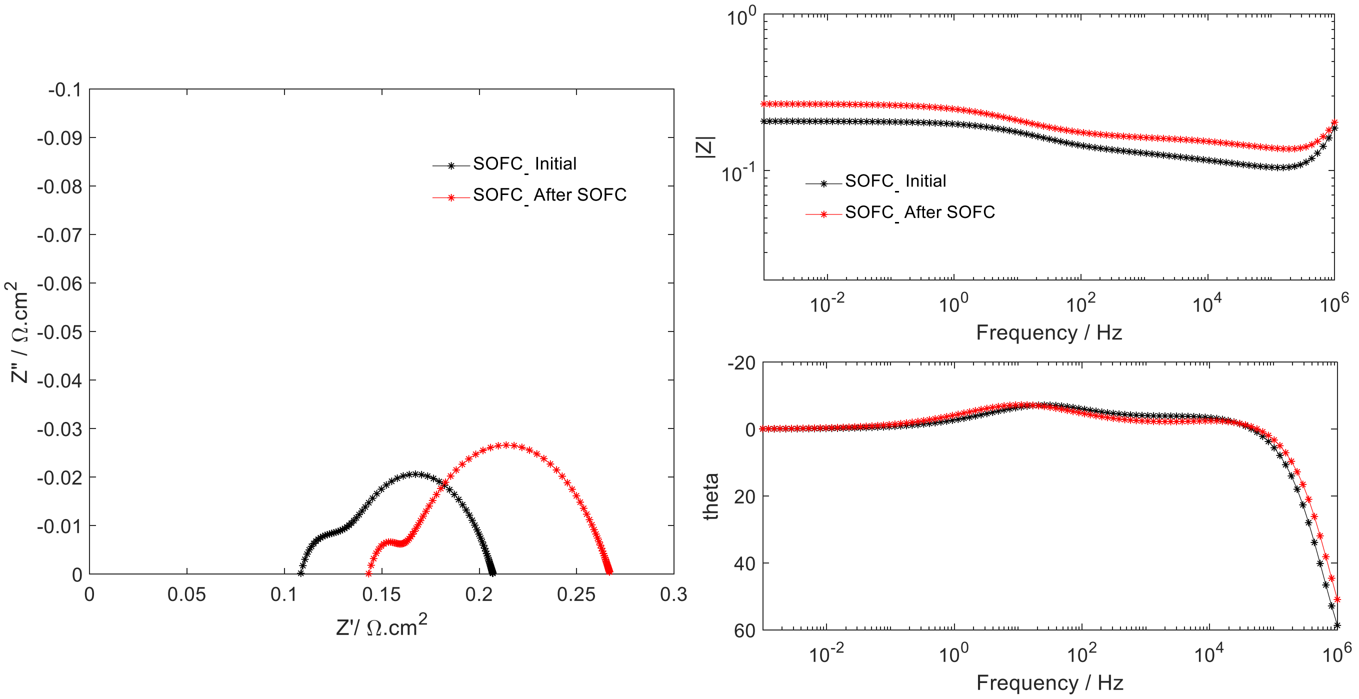

Figure 5-31:Nyquist and Bode impedance plots of CT1_1.39_750 before and after SOFC operation testing (captured under SOFC conditions).

Figure 5-31 presents the SOFC environment Nyquist and Bode plots of the virgin cell and of the cell after the 120 hours of constant SOFC operation. It shows increases in both the Ohmic and polarisation contributions after the 120 hours of SOFC operation, relative to the virgin cell.

Figure 5-32 also presents the Nyquist and Bode plots as captured in the SOE environment. It also indicates significant increases in the Ohmic and polarisation impedances of the cell after the 120 hours of constant SOFC operation, relative to the virgin cell.

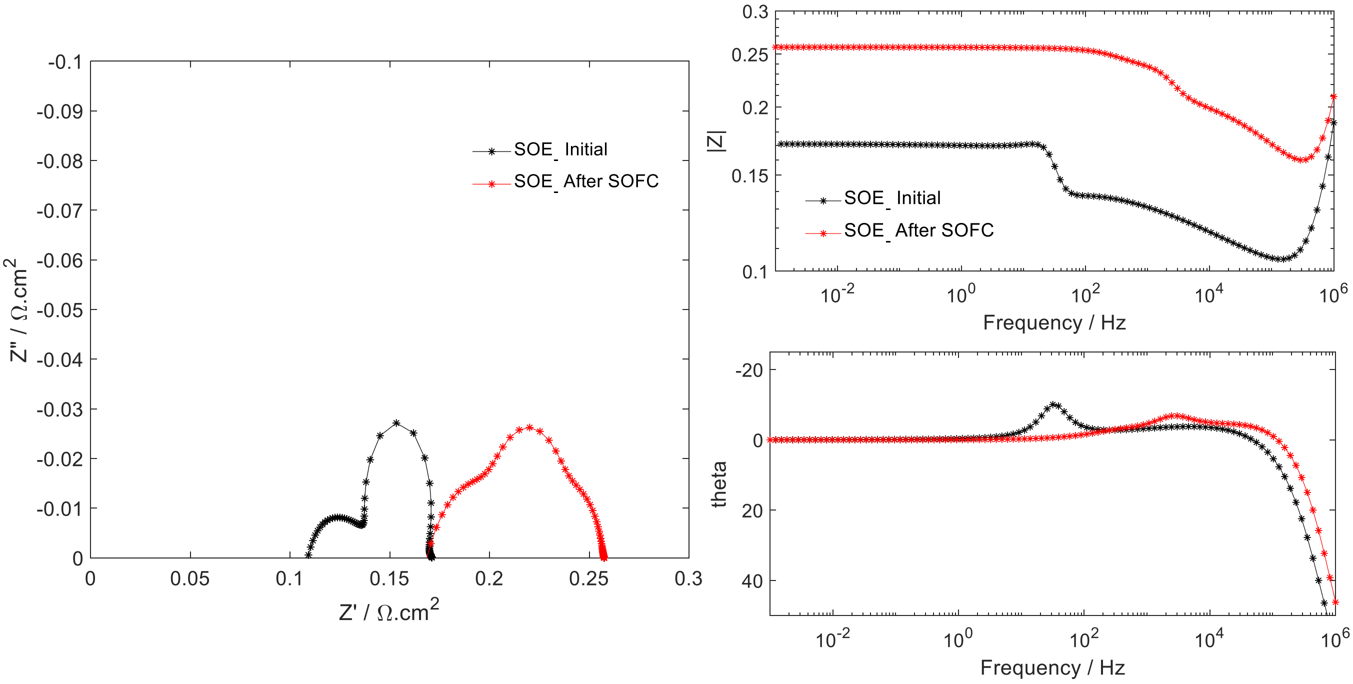

Figure 5-32: Nyquist and Bode impedance plots of CT1_1.39_750 before and after SOFC operation testing (captured under SOE conditions).

5.8 Test at 1.25 A/cm^2 Current Density (Cell ID: CT1_1.25_750)

As a result of the relatively good SOFC performance of CT1_1.39_750 (see Section 5.7) at a current density of 1.39 A/cm2 and fuel utlisation of 73.4%, this test was conducted at a higher fuel utilisation (83.5%) but lower current density (1.25%) in order to tease out the effect on cell performance of any possible correlations between the relative magnitudes of fuel flow rates and test current density. It should be noted that fuel electrode reactant utilisation is a ratio of the molar flow of electrons (parameter related to current density) over the molar flow of reactants (parameter related to fuel flow rates). It would be interesting to find out if an optimised fuel utilisation range exists for both SOFC and SOE operations, and whether this depends on the relative magnitudes of the current density and fuel flow rates. Also, it was expected that in SOFC mode, it would be more economical to operate the system at high fuel utilisations comprising of high current densities and low fuel flow rates. In SOE mode, it was expected that the most economical fuel utilisation would be the relative magnitudes of operating current densities and fuel flow rates that result in the lowest cell degradation rates, especially if waste heat were utilised, since the 'fuel' is water (which has high recyclability and is a relatively low cost 'fuel').

Figure 5-33 presents the voltage evolution or cell durability characteristics of the cell tested at a current density of 1.25 A/cm^2, and a fuel utilisation of 83.5%. The open cell voltage prior to the 120 hours of constant SOFC operation was 1024 mV. Under the 1.25 A/cm^2 current density load, the voltage dropped to 768 mV (it momentarily dropped further to -515 mV due to an interruption in the laboratory compressed air supply). Over the first 46 hours of the constant SOFC operation, the voltage dropped further to 764.5 mV, i.e. voltage degradation rate of 95 mV/1000 h (12.4% / 1000h).

After 46 hours of constant SOFC operation, the voltage dropped further to -2453 mV due to an overnight interruption in the hydrogen supply. When the hydrogen supply was restored a few hours later, the cell had been irreversibly damaged as a result of the galvanostatic operating mode under hydrogen starvation. Therefore the voltage recovered to 620 mV only, which was sustained for approximately 13 hours (with a voltage degradation rate of 686 mV/1000 h), after which the cell was unable to continue producing the 1.25 A/cm^2 current density. The current density thus dwindled down to zero with an OCV of 966 mV. Nevertheless, it was evident from the first 46 hours of constant SOFC operation (prior to the fuel starvation episodes) that the cell was capable of sustaining the 1.25A/cm^2 with a fuel utilisation of 83.5%. The latter stages of the test also indicated that some cell damages lead to cells not able to produce any current at all, irrespective of the operating voltage.

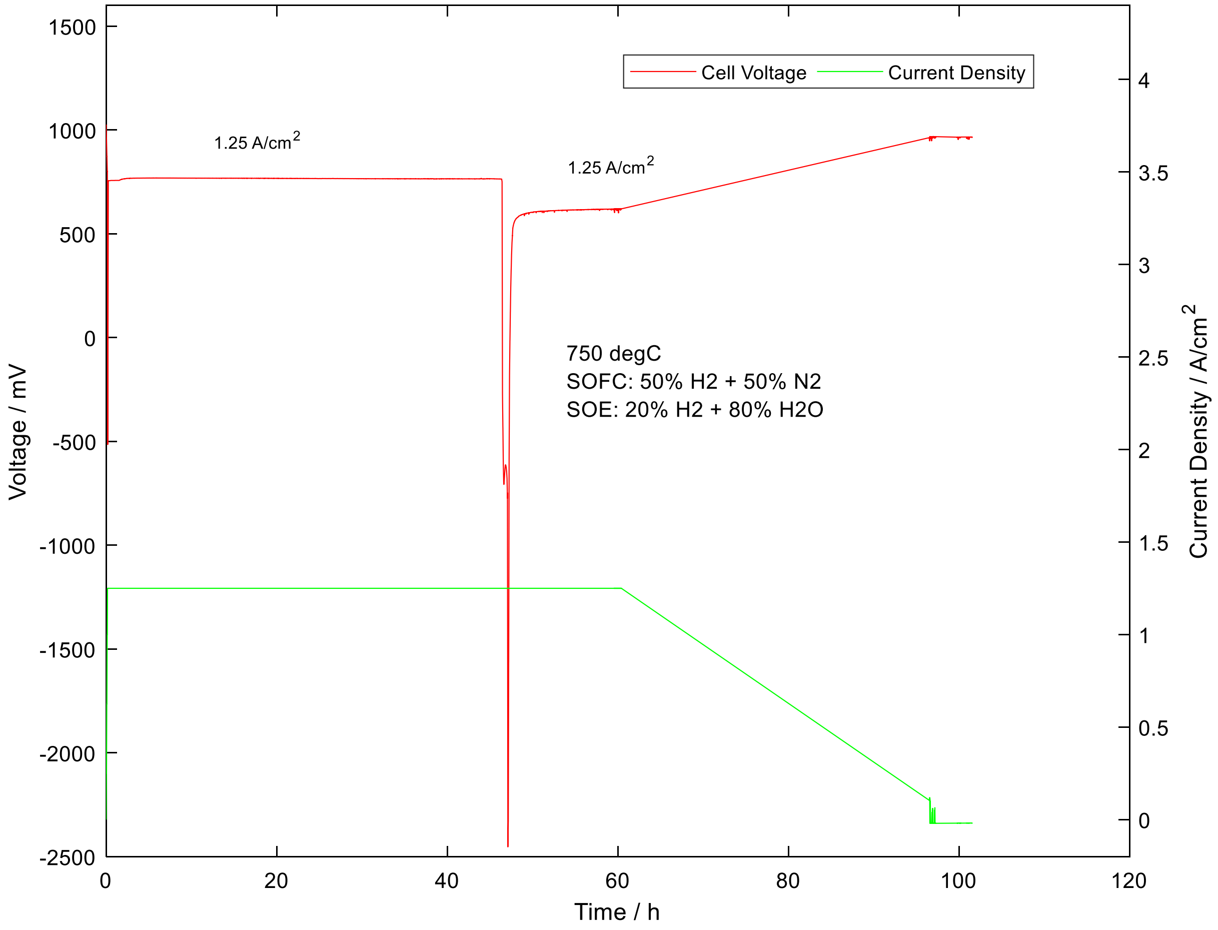

Figure 5-33: Voltage evolution characteristics of CT1_1.25_750 tested at 750°C and ±1.25 A/cm^2 current density.

As a result of the cell damage, the j-V characteristics of the cell could not be determined after the SOFC operation. The cell was unable to sustain any of the current density steps required for the j-V characterisation. *Figure 5-34* show the j-V characteristics of the virgin cell indicating the cell was not damaged prior to the SOFC operation. The ASR of the virgin cell was 0.18 Ω.cm^2 (under SOFC environment) and 0.21 Ω.cm^2 (under SOE environment).

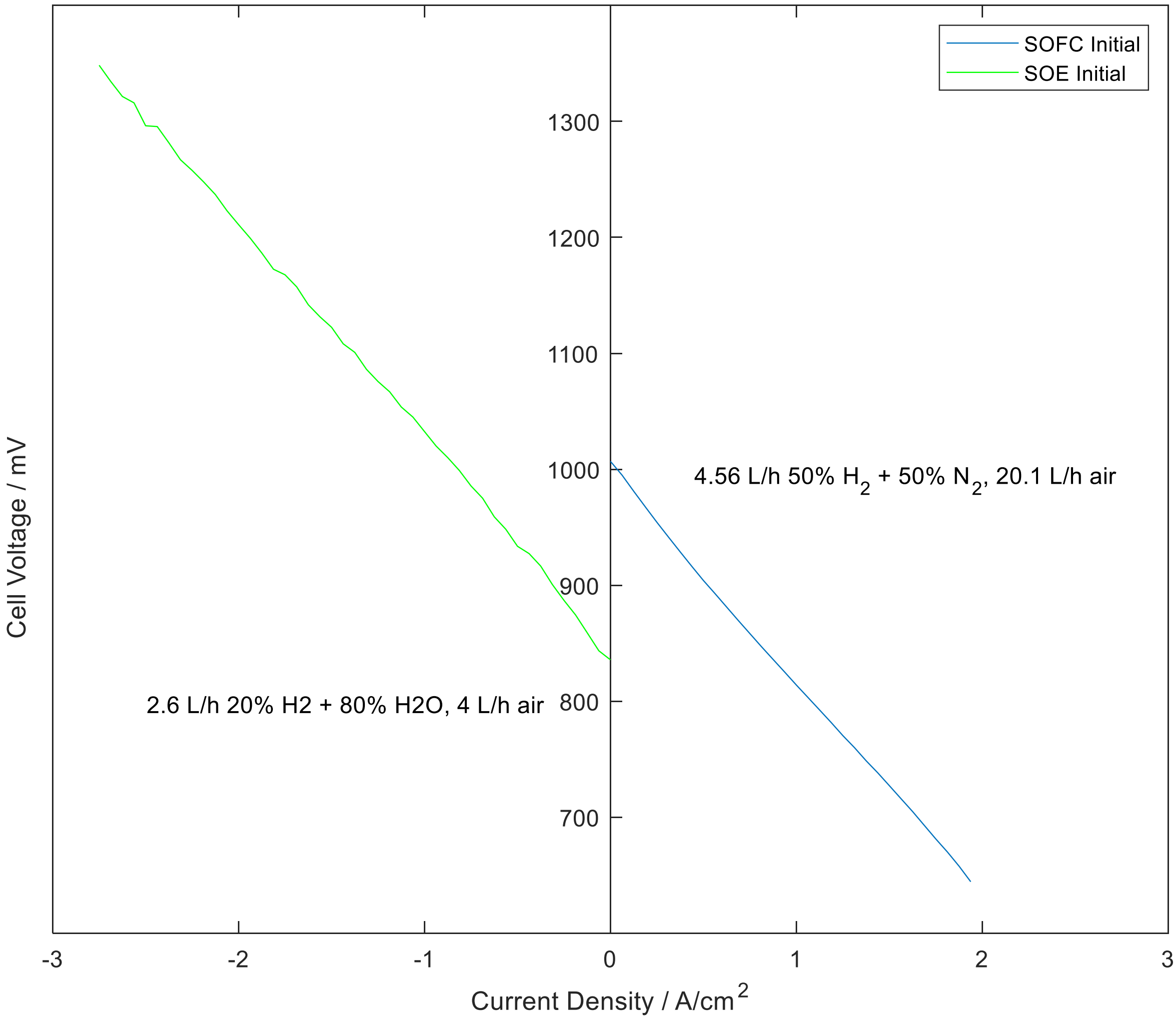

Figure 5-34: Initial j-V characteristics.

5.9 Test at 2.65 A/cm^2 Current Density (Cell ID: CT1_2.65_750)

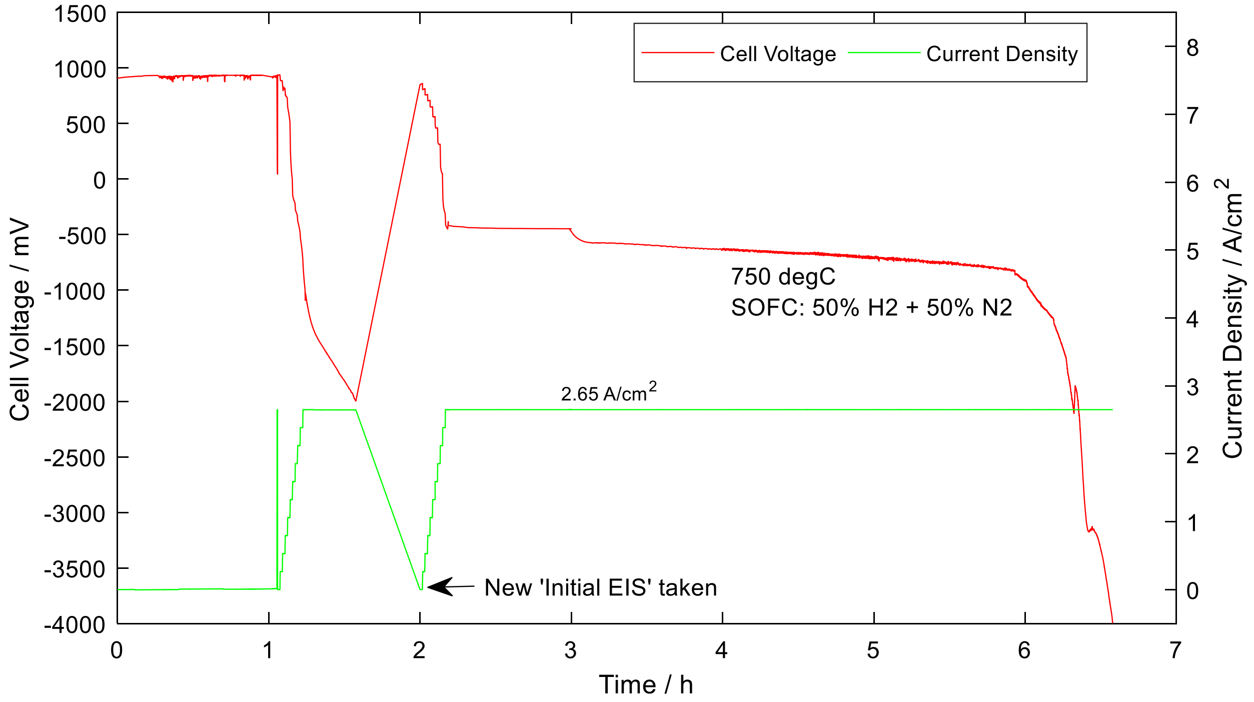

Figure 5-35: Voltage evolution characteristics of CT1_2.65_750 tested at 750°C and ±2.65 A/cm^2 current density.

This test was conducted at a current density of 2.65 A/cm^2, and with a fuel utilisation of 100%. Cell durability information under the 2.65 A/cm^2 current density is presented in . The OCV, prior to commencing the 120 hours of constant SOFC operation was 938.4 mV. Under the 2.65 A/cm^2 current density load, the instantaneous cell voltage dropped to -763 mV. Over the first 30 minutes of the galvanostatic SOFC operation, the cell voltage dropped further to -1997.7 mV. This indicated progressive and irreversible cell damage under the +2.65 A/cm^2 current density load. The current density load was thus removed, and the cell allowed to return to OCV (~861 mV). The condition of the cell was then assessed via electrochemical impedance spectroscopy (i.e. new ‘initial EIS’ taken). A second attempt was made to put the cell under the +2.65 A/cm^2

current density load. At this attempt, the cell voltage observed under the +2.65 A/cm² current density load was -400 mV. This dropped down to -910 mV over 4 hours, before finally crashing.

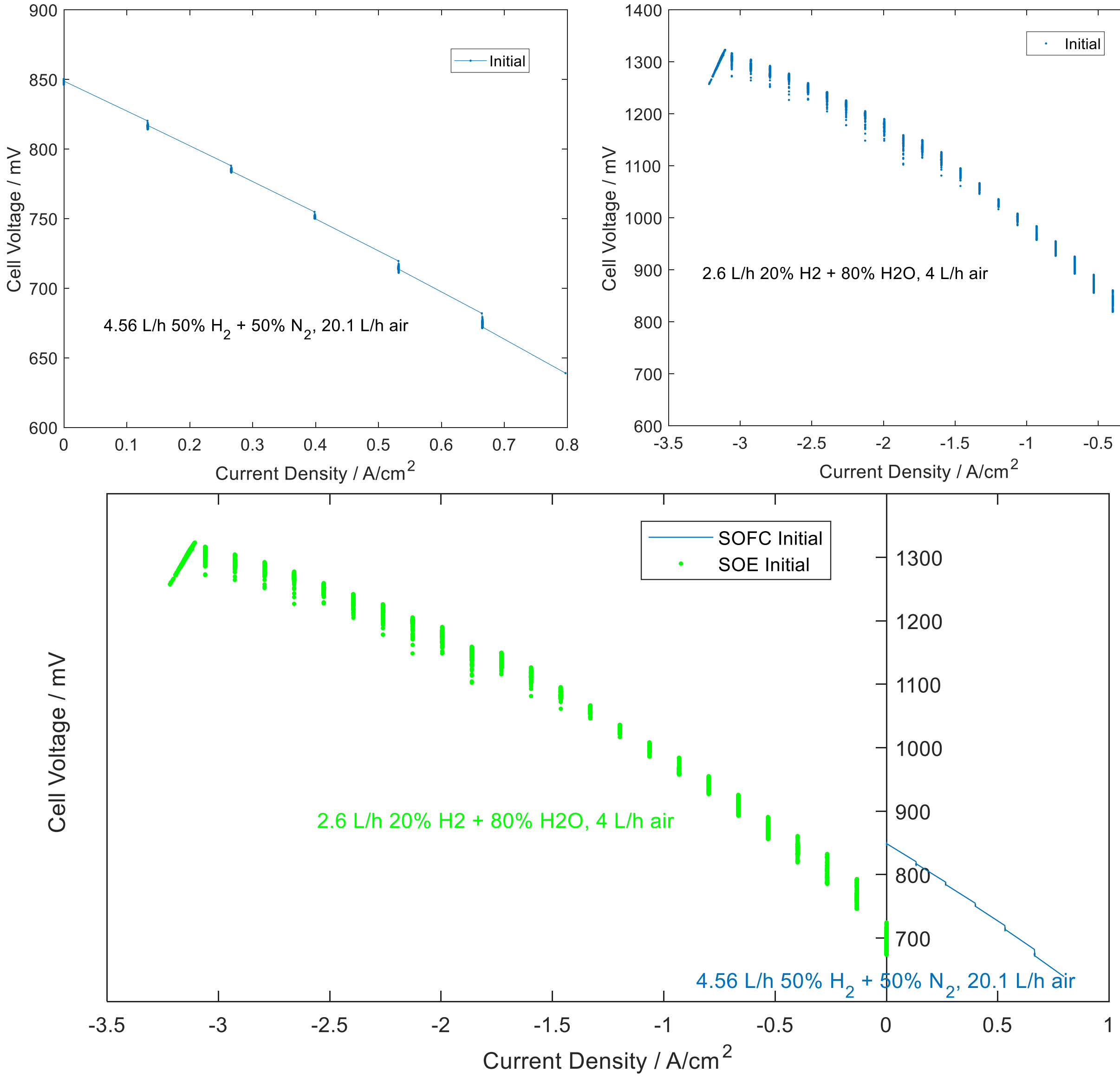

Figure 5-36: Initial j-V characteristic of CT1_2.65_750 tested at 2.65 A/cm² current density.

The j-V characteristics of the virgin cell, *Figure 5-36*, indicate that the cell was of relatively good quality, with ASRs of 0.28 Ω.cm² and 0.25 Ω.cm², respectively, under the SOFC and SOE environments. The reported performance of the cell under the applied current density was therefore due to current density overloading, and not to damaged or poor-quality virgin cell (see virgin cell SEM image in *Figure 5-38*). As a result of the test failure (see test voltage durability results from 6 hours and beyond in), the j-V characteristics of the cell after exposure to the +2.65 A/cm^2 current density could not be captured.

Figure 5-37 shows the impedance characteristics (EIS) of the virgin cell prior to cell exposure to the +2.65 A/cm^2 current density load, and after the current density load was removed after 30 mins of SOFC galvanostatic operation. The Nyquist plot of the cell after the 30 mins of SOFC galvanostatic operation at 2.65 A/cm^2 current density show higher high-frequency impedance and a relatively lower low-frequency impedance compared to the plot of the virgin cell. The decrease in polarisation resistance could be attributed to further reduction of the Ni-YSZ electrode during the constant SOFC operation (or insufficient reduction of the Ni-YSZ electrode prior to capturing the virgin cell EIS information), thus influencing the cell's activation performance (initial OCV was 938.4 mV).

Also, the high frequency depression for the virgin cell plot may be an artefact of the high current density steps used to capture the j-V characteristics of the virgin cell (*Figure 5-36*). Note that during the j-V characterisation, the current density was increased by 132.5 mA/cm^2 per step, with a hold time of 0.5 min per step (see Section 4.2.4.1 for further details). This seemed to have been enough to affect the electrochemical characteristics of the virgin cell, due to the high current density exposure.

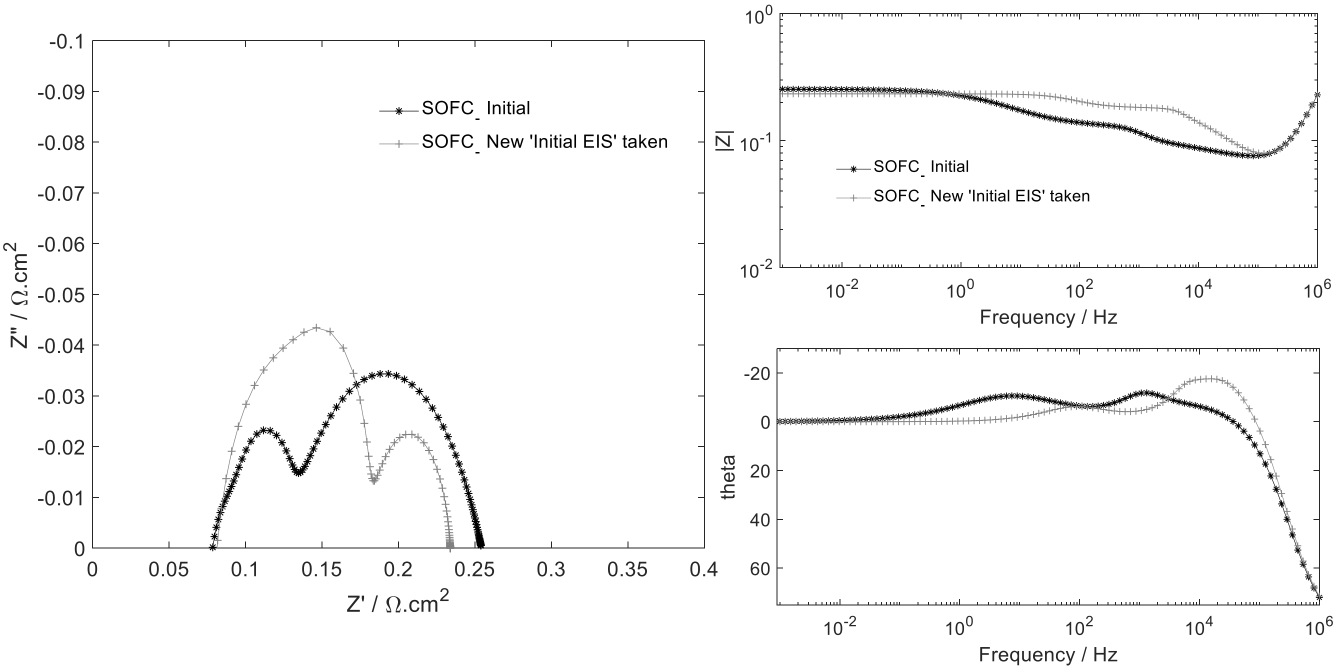

Figure 5-37: Initial Nyquist and Bode plots of CT1_2.65_750 tested at 2.65 A/cm^2.

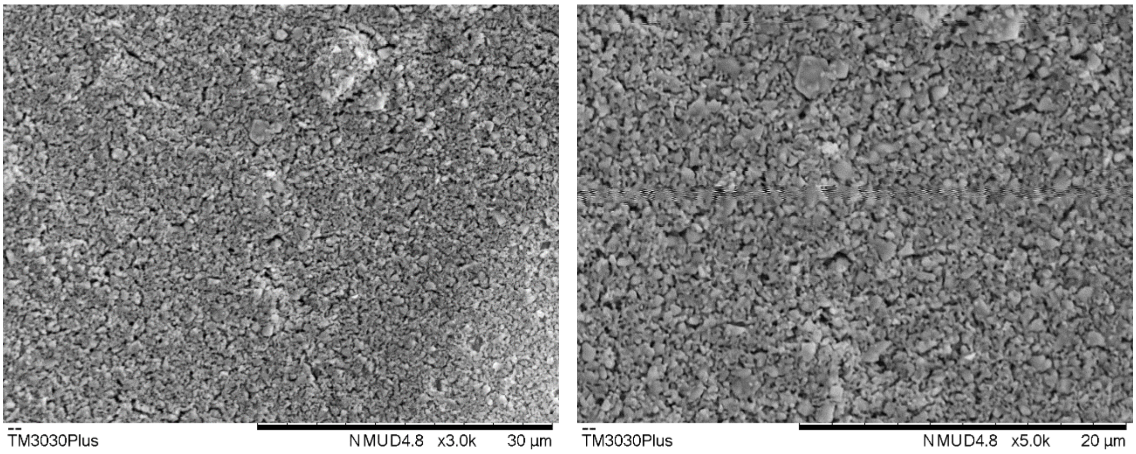

Figure 5-38: Virgin SEM image.

5.10 Summary of Cell Type 1 Results

Cell type 1 was tested at current densities ranging from 0.5 A/cm^2 to 2.65 A/cm^2, and at temperatures of 700^{o}C and 750^{o}C. The cells were subjected to a test protocol which entailed 120 hours of constant SOFC operation followed by 120 hours of constant SOE operation and completed with rSOC cycling comprising 3 hours SOFC operation followed by 20 hours SOE operation. The rSOC cycling was designed to incorporate 33 cycles, however, not all tests could be subjected to the complete test protocol due to various factors such as damaged virgin cells, fuel starvation due to equipment malfunction and cell damage due to high current density exposure.

For all tests, cell performance, as measured by resistance increases and voltage durability, deteriorated under test. The rate of deterioration was higher for constant SOE operation relative to constant SOFC operation. During rSOC cycling, cell performance deteriorated continually under all SOE operation steps, whilst some performance recovery was observed under the subsequent SOFC operation steps.

A more detailed discussion of the results is presented in chapter 7.

6 CELL TYPE 2 REVERSIBLE OPERATION

6.1 Introduction

For effective comparison with the test results for cell type 1 (as reported in Chapter 5), cell type 2 was subjected to the equivalent cell type 1 tests. However, only the successful cell type 1 tests were replicated for cell type 2 testing. Cell type 2 was thus tested at current densities of 0.5 A/cm^2 and 0.7 A/cm^2, as well as temperatures of 700 °C and 750 °C.

As mentioned in Section 0, Cell type 2 has an LSC infiltrated GDC backbone oxygen electrode. It also includes a pure GDC barrier layer between the YSZ electrolyte and the oxygen electrode (and LSC contact layer) in order to mitigate possible deleterious reactions, as explained in Chapter 3, between the YSZ electrolyte and LSC containing layers (oxygen electrode and contact layers). The configuration of cell type 2 is illustrated in *Figure 6-1*.

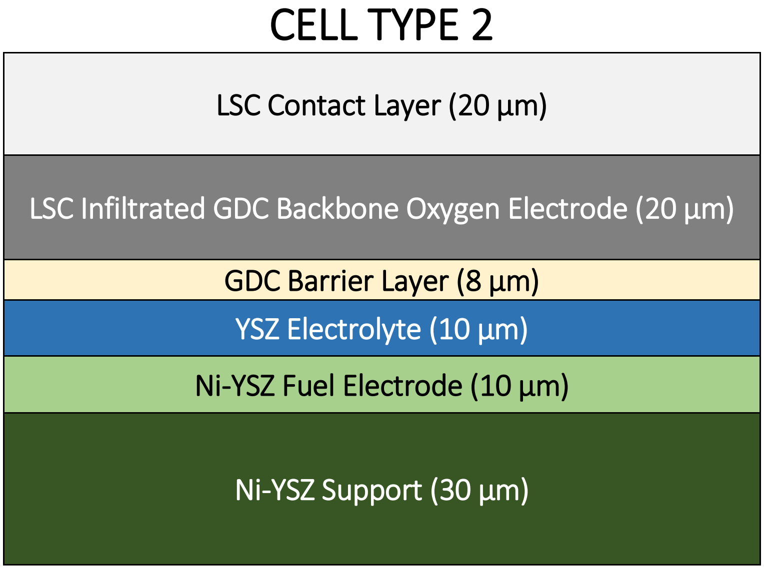

Figure 6-1: Configuration of cell type 2

Different cells of this type were subjected to the test protocol detailed in Chapter 4, under different fuel flow rates, with current densities of 0.5 A/cm^2 and 0.7 A/cm^2, and at temperatures of 750^{o}C and 700^{o}C, respectively. The fluid flow rates used for the tests were as follows:

1. During fuel cell operation, a dry mixture of 35.3 ml/min each of H_2 and N_2 was delivered to the fuel electrode, whilst 331.25 ml/min of air was delivered to the oxygen electrode;
2. During electrolysis operations, 1.3 g/hr of $H_2O_{(l)}$ (approximately 35.3 ml/min of $H_2O_{(g)}$) mixed with 8.8 ml/min H_2 was delivered to the fuel electrode, whilst 66.25 ml/min of air was delivered to the oxygen electrode.

These flow rates corresponded to the fuel and oxygen electrode compartment gas compositions, and fuel electrode reactant utilisations given in for 3 cm diameter unit cells with 5.3 cm^2 effective cathode area (see) tested under a current density of 0.5 A/cm^2.

The results, detailing the cell voltage evolution under test, j-V and impedance characteristics are reported in Sections 6.2 to 6.4. The different tests are identified using Cell IDs. The Cell IDs comprise three parts, separated with an underscore (e.g. CT2_0.5_750). The first part is alphanumeric and identifies the cell type, i.e., CT2 for cell type 2 (see Figure 6-1). The second part of the cell ID is the test current density in A/cm^2, and the third part is the test temperature in degrees Celsius.

The cell IDs for the cell type 2 tests reported in this Chapter 6 are listed in *Table 6-1*.

Table 6-1: Test IDs for cell type 2 tests

Test IDs	Temp. (°C)	Current Density (A/cm^2)	H_2/H_2O Conversion (%)	SECTION
CT2_0.7_750	750	0.7	73.3	6.2

Test IDs	Temp. (°C)	Current Density (A/cm^2)	H_2/H_2O Conversion (%)	SECTION
CT2_0.5_750	750	0.5	52.3	6.3
CT2_0.5_700	700	0.5	52.3	6.4

6.2 Test with 0.7 A/cm^2 Current Density (Cell ID: CT2_0.7_750)

Test CT2_0.7_750 was conducted as the cell type 2 equivalent to the test CT1_0.7_750 reported in Section 5.6. Therefore, this test in isolation also assessed the effect of fuel utilisation on cell performance and degradation characteristics. In combination with the test CT1_0.7_750 reported in Section 5.6, it studied the effect of cell architecture on cell performance.

The fuel feed parameters were as stated in Section 6.1, and with a current density of 0.7 A/cm^2, this resulted in a fuel utilisation of 73.3%. It is expected that this fuel utilisation would also increase the induced stresses in the cell (especially at the oxygen electrode interphases and interface with the electrolyte during SOE) due to the increased flux of oxygen ions through the cell. The test temperature was 750^{o}C.

Figure 6-2 shows the cell durability results over the test protocol which comprised of 120 hours of SOFC operation followed by another 120 hours of SOE operation and ending with rSOC operation cycles of 3 hours SOFC followed by 20 hours SOE. Current density – voltage (j-V) and EIS characterisation were carried out for the virgin cell, after the 120 hours of SOFC operation, after the additional 120 hours of SOE operation, and finally after the rSOC operation. These are shown in *Figure 6-3*, *Figure 6-4* and *Figure 6-5*, and will be discussed further down.

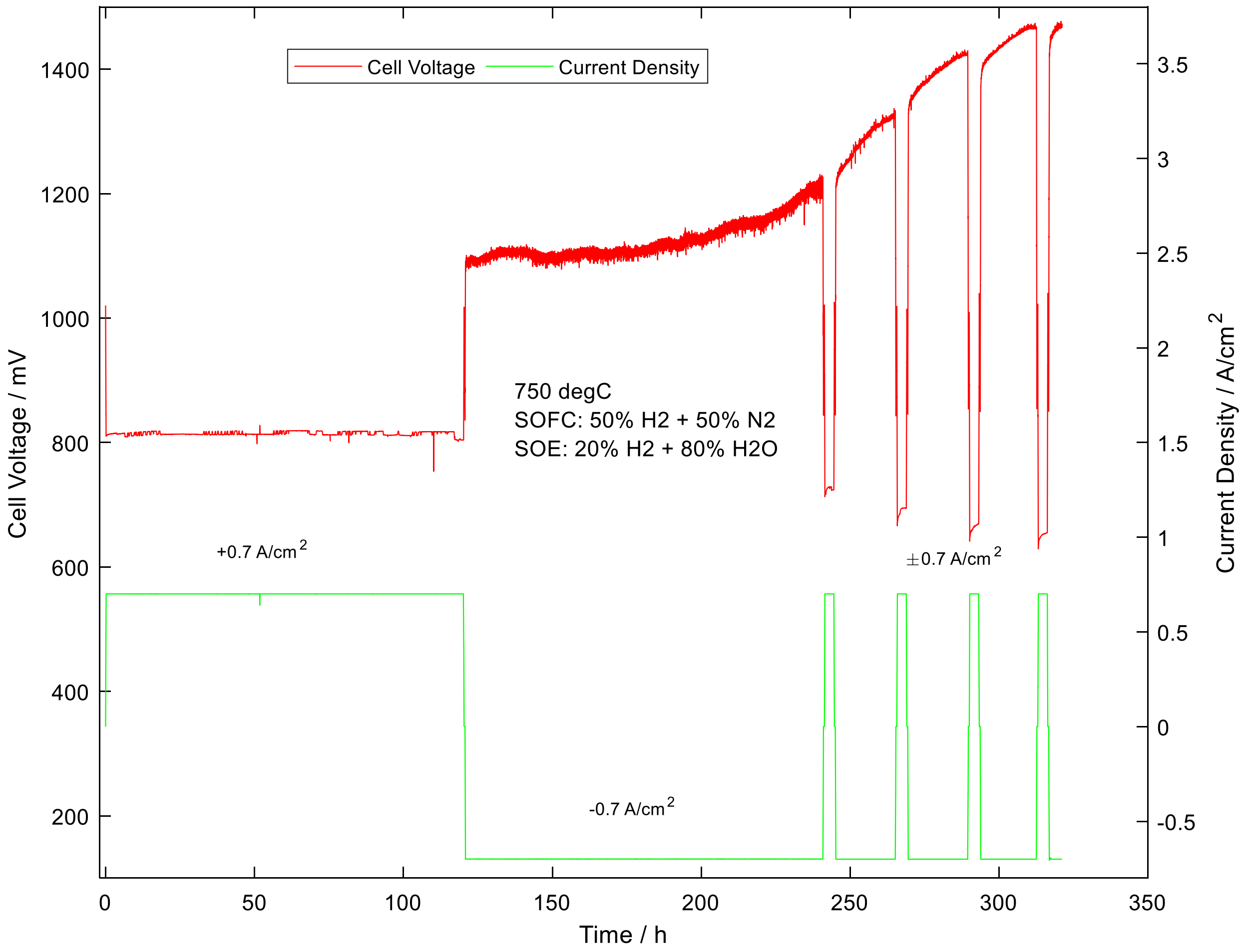

Figure 6-2: Voltage evolution characteristics of test CT2_0.7_750 (750°C and ±0.7 A/cm^2 current density).

The OCV of the cell prior to the 120 hours of SOFC operation was 1019.6 mV (*Figure 6-2*). The cell voltage decreased to 811 mV under the +0.7 A/cm^2 (SOFC) current density load. Over the 120 hours of constant SOFC operation, the voltage increased to approximately 817.5 mV after 117 hours, before dropping to 804 mV over the last 3 hours of the constant SOFC operation. The overall voltage degradation rate was 7.3 mV/1000 h (0.9% / 1000h). This indicated significantly superior SOFC performance compared to the SOFC tests reported in Chapter 5 for cell type 1 (especially for the equivalent CT1_0.7_750 with degradation rate of 208 mV/1000 h).

After the 120 hours of constant SOFC operation, the current density load was removed and the cell returned to OCV, after which the SOFC test environment was evacuated and replaced with an SOE test environment (SOE fluid flow compositions).

The OCV prior to the 120 hours of constant SOE operation was approximately 850 mV. The cell voltage increased to approximately 1084 mV under the -0.7 A/cm^2 (SOE) current density load. Over the 120 hours of SOE operation, the voltage increased further to approximately 1223 mV, with the rate of increase seemingly increasing with time under test. The voltage degradation rate over the first 40 hours was 116 mV/1000 h (10.5% / 1000h). After 40 hours, the degradation rate increased to 1340 mV /1000 h over the remainder of the SOE operation.

As noted for the SOE tests reported in Chapter 5, there was considerable scatter in instantaneus cell voltage at a given current density for all SOE tests. Since all tests were run galvanostatically, the scatter in cell voltage during SOE tests suggested instability in one or more of the cell resistance components (activation, mass transport, Ohmic, etc). The most likely cause was dynamic changes in $H_2O_{(g)}$ reactant flow rates at the hydrogen electrode, hence instability in the mass transport resistance component, due to the characteristics or limitations inherent in the CEM steam supply equipment used, resulting in localised fluctuations of the fuel utilisation parameter.

The significant difference in the voltage evolution under the SOFC and SOE regimes which indicate higher performance losses under SOE operation relative to SOFC operation is in line with results reported in the literature [23] [145] [148].

After the 120 hours of constant SOE operation, the SOFC environment was reinstated for the first 3 hours of SOFC operation for the rSOC cycling. The OCV for the first 3 hours of SOFC operation during rSOC cycling was 1021 mV (i.e. had not appreciably changed from the initial 1019.6 mV). The voltage decreased to 715 mV under the +0.7 A/cm^2 current density load. Over the 3 hours of SOFC operation, the voltage increased (recovered) to 724.4 mV. The OCV for the first 20 hours of SOE mode in the rSOC operation was 854 mV. The voltage increased to 1211 mV under the -0.7 A/cm^2 current density load. Over the 20 hours SOE operation, the voltage increased further (i.e., no recovery) to 1327 mV. This trend of voltage recovery during SOFC followed by further voltage degradation during SOE operation continued for all the SOFC/SOE cycles which constituted the rSOC operation. The OCV for the final 3 hours of SOFC operation during the rSOC cycling was 1022.5 mV (again similar to the OCV at the start of the experiment, thus documenting that there was no physical damage to the cell or unit cell components). Under the +0.7 A/cm^2 current density load, the cell voltage dropped to 632.5 mV. Relative to the 120 hours of constant SOFC operation (1019.6 – 811 mV) and the first SOFC cycle during the rSOC operation (1021 – 715 mV), the voltage drop from 1022.5 to 632.5 mV indicated that the cell had undergone irreversible electrochemical damage during the intervening operations. Over the 3 hours of the final SOFC cycle during the rSOC operation, the voltage recovered from 632.5 mV to 655 mV. This was significantly lower than the cell voltage after the 120 hours of constant SOFC operation (804 mV), thus further underlining the obsevation that the SOE operations were the main cause of cell performance degradation during rSOC operation. The OCV for the final 20 hours SOE cycle during the rSOC operation was 855 mV. The cell voltage increased to 1412.3 mV under the -0.7 A/cm^2 current density load. Over the initial 4 hours of the final 20 hours SOE cycle during the rSOC operation, the cell voltage increased further to 1472.80 mV. After the 4 hours of the SOE cycle, the test was stopped due to logistical issues with the laboratory's hydrogen supply. The j-V characterisation of the cell after the rSOC operation could therefore not be carried out.

Figure 6-3 shows the j-V characterisation of the cell at the various stages, i.e., the virgin cell, the cell after the 120 hours of constant SOFC operation, and the cell after the 120 hours of constant SOE operation. The j-V characteristics captured in the SOFC environment, *Figure 6-3* (a), show that there was not much difference between the resistance characteristics of the cell after the 120 hours of constant SOFC operation, relative to the virgin cell. The area specific resistance (ASR) of the virgin cell was 0.34 Ω•cm^2, whilst the ASR of the cell after the 120 hours of constant SOFC operation was 0.37 Ω•cm^2. After the 120 hours of constant SOE operation, the ASR of the cell had increased to 0.53 Ω•cm^2.

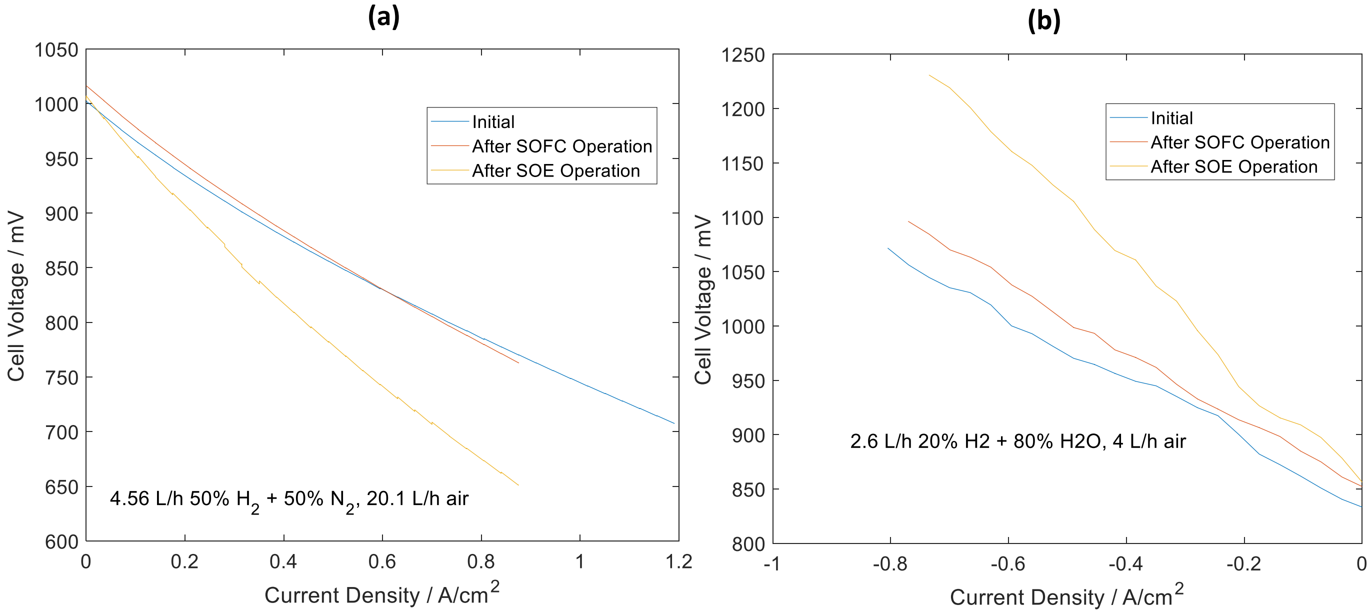

Figure 6-3: Comparison of j-V characteristic of CT2_0.7_750 before and after SOFC and SOE operation testing (captured under (a) SOFC and (b) SOE conditions).

Similarly, the j-V characteristics captured in the SOE environment, *Figure 6-3* (b), show only a small difference between the resistance characteristics of the cell after the 120 hours of constant SOFC operation, relative to the virgin cell. The ASR of the virgin cell (calculated at 0.35 A/cm^2) was 0.38 Ω•cm^2. After the 120 hours of constant SOFC operation, the ASR under SOE conditions increased to only 0.42 Ω•cm^2. However, after the 120 hours of constant SOE operation, the ASR had increased to 0.86 Ω•cm^2. These results serve to reiterate the observation that the increases in cell resistance and the attendant decreases in rSOC cell performance were primarily due to the SOE operation steps rather than the SOFC operation steps.

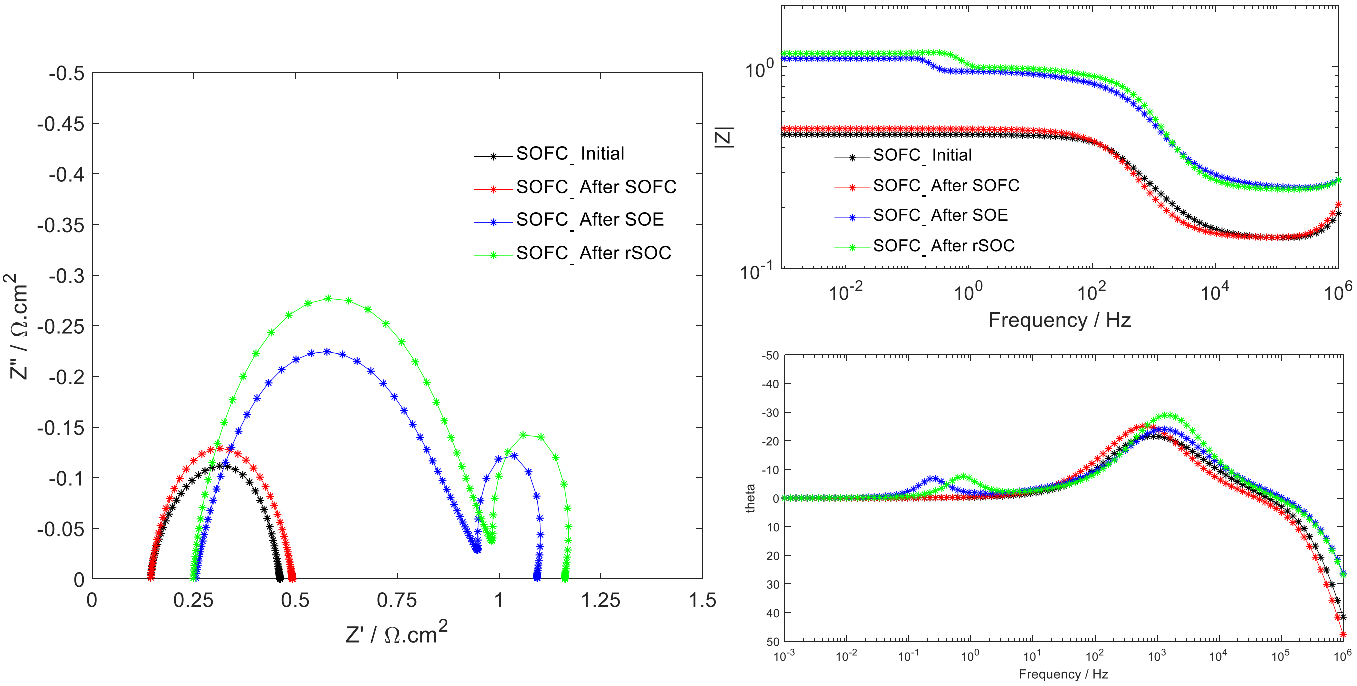

Figure 6-4: Nyquist and Bode impedance plots of CT2_0.7_750 before and after SOFC, SOE and rSOC operation testing (captured under SOFC conditions).

The electrochemical impedance spectroscopy information captured in the SOFC environment is shown in *Figure 6-4*. The Nyquist plot of the cell after the 120 hours of constant SOFC operation show only marginal increases in the polarisation resistance (0.36 Ω•cm^2 to 0.38 Ω•cm^2). There was no difference in the Ohmic contribution. However, after the 120 hours of constant SOE operation, there was a significant difference in the Ohmic part from 0.2 Ω•cm^2 to 0.25 Ω•cm^2, as well as further significant increases in the polarisation resistance (0.69 Ω•cm^2). There was an additional small arc that had developed in the low frequency region. This was most likely due to a low frequency dependent SOE process and may be related to either mass transport (H_2O_g) or ionic transport (O^{2-}) effects through the electrodes.

After the four rSOC cycles, relative to the impedance characteristics of the cell after the 120 hours of constant SOE operation, there were further increases in the cell's polarisation resistance (0.85 Ω•cm^2) indicating progressive worsening in the cell's performance.

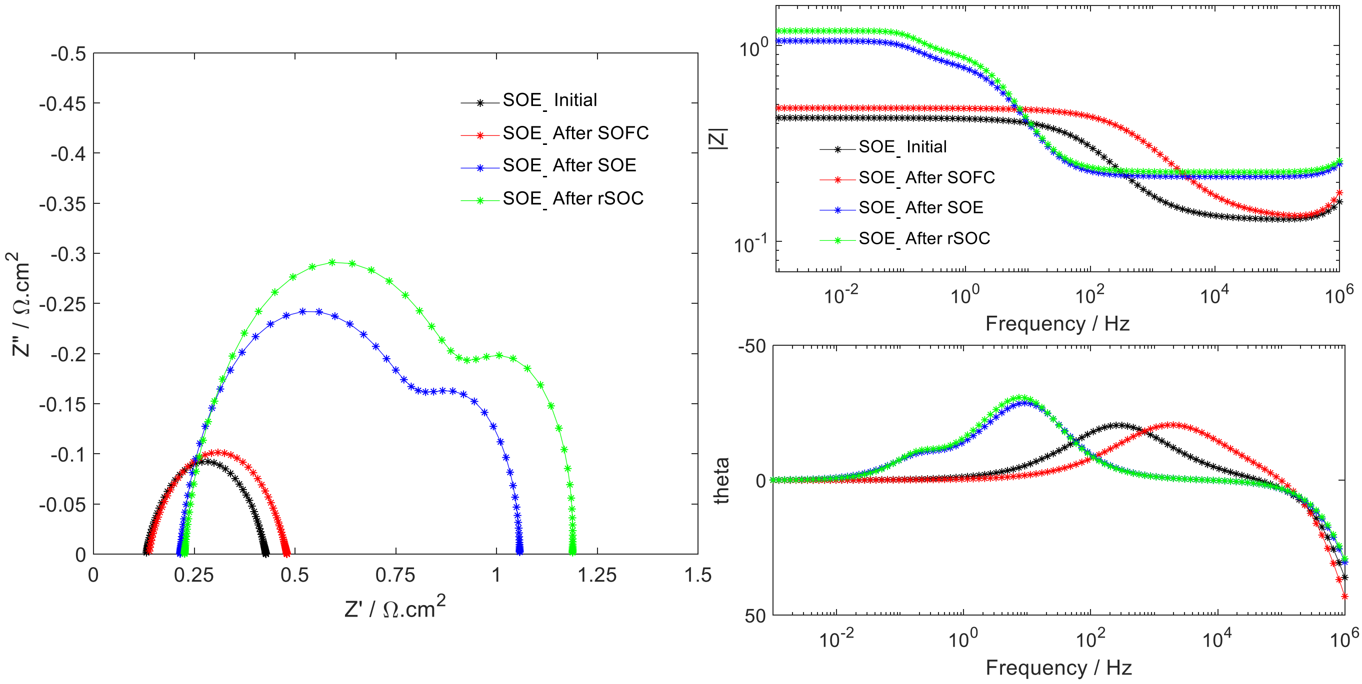

Figure 6-5: Nyquist and Bode impedance plots of CT2_0.7_750 before and after SOFC, SOE and rSOC operation testing (captured under SOE conditions).

The EIS information captured in the SOE environment is shown in *Figure 6-5*. The Nyquist plot of the cell after the 120 hours of constant SOFC operation shows only marginal increases in the polarisation resistance, like the EIS information captured in the SOFC environment. There was no difference in the Ohmic contribution. However, after the 120 hours of constant SOE operation, there was a significant difference in the Ohmic part, whilst the polarisation resistance increased further to 0.85 Ω•cm^2, the same value as in SOFC conditions.

After the four rSOC cycles, relative to the impedance characteristics of the cell after the 120 hours of constant SOE operation, the polarisation impedance increased further to 0.88 Ω•cm^2 indicating progressive worsening in the cell's performance.

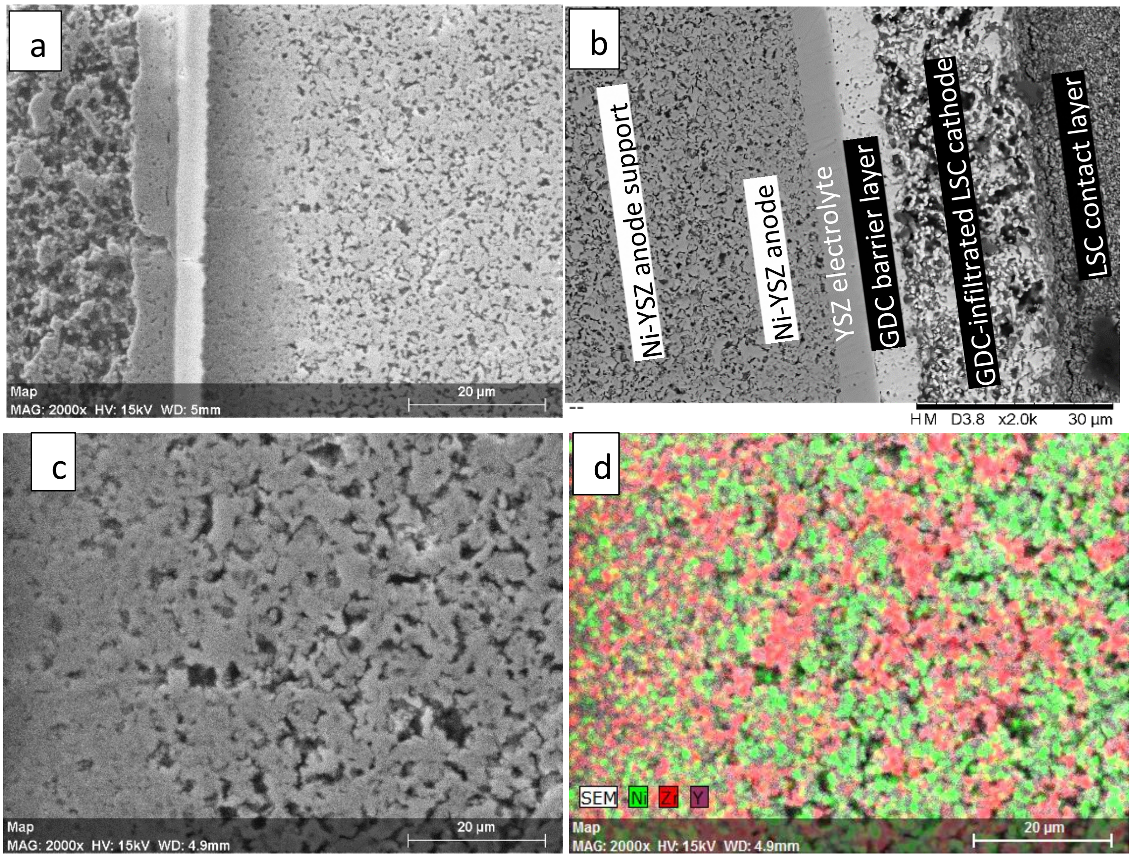

Figure 6-6: Post-test SEM images of CT2_0.7_750.

Figure 6-6 shows the post-test structural characterisation of CT2_0.7_750 via SEM imaging. *Figure 6-6*a shows excellent adherence between the different cell layers, comprising the fuel electrode and electrolyte boundary, the electrolyte and GDC barrier-layer boundary, and the

GDC barrier-layer and LSC infiltrated GDC backbone oxygen electrode boundary. Some discernible delamination may be observed between the LSC infiltrated GDC backbone oxygen electrode and LSC contact layer, *Figure 6-6*b. This may have contributed to the very poor SOE performance reported above, since this LSC contact layer delamination would have led to an increase in the Ohmic resistance of the cell. *Figure 6-6*c and d indicate some Nickel agglomeration in the fuel electrode. This would also have led to an increase in the activation resistance of the cell by decreasing the effective surface area available for catalytic reactions.

6.3 Test at 0.5 A/cm^2 Current Density (Cell ID: CT2_0.5_750)

This test (CT2_0.5_750) was the cell type 2 equivalent of the test reported in Section 5.2 (CT1_0.5_750#1). It was thus conducted at a temperature of 750^{o}C and a galvanostatic current density of 0.5 A/cm^2 under all operating modes (SOFC, SOE & rSOC). Coupled with the following reactant flow rates, the test conditions resulted in a fuel utilisation of 52.3% for the 3 cm diameter unit cell with 5.3 cm^2 effective cathode area (see):

1. During fuel cell operation, a dry mixture of 35.3 ml/min each of H_2 and N_2 was delivered to the fuel electrode, whilst 331.25 ml/min of air was delivered to the oxygen electrode;
2. During electrolysis operations, 1.3 g/hr of $H_2O_{(l)}$ (approximately 35.3 ml/min of $H_2O_{(g)}$) mixed with 8.8 ml/min H_2 was delivered to the fuel electrode, whilst 66.25 ml/min of air was delivered to the oxygen electrode.

The OCV prior to SOFC operation was 968 mV. Under a galvanostatic current density of +0.5 A/cm^2 (SOFC operation), the cell voltage decreased to 811 mV. After approximately 4.5 hours of constant SOFC operation, the cell voltage had increased to 823 mV, indicating an improvement in one or more of the cell resistance components. Due to the thermodynamics of the SOFC operation (see Sections 1.1.3.2, 4.2.4.1 and 4.2.4.2 for further details), the cell resistance component most likely to be improved under SOFC conditions is the activation resistance, due to further Nickel reduction occurring in the Ni-YSZ fuel electrode (anode).

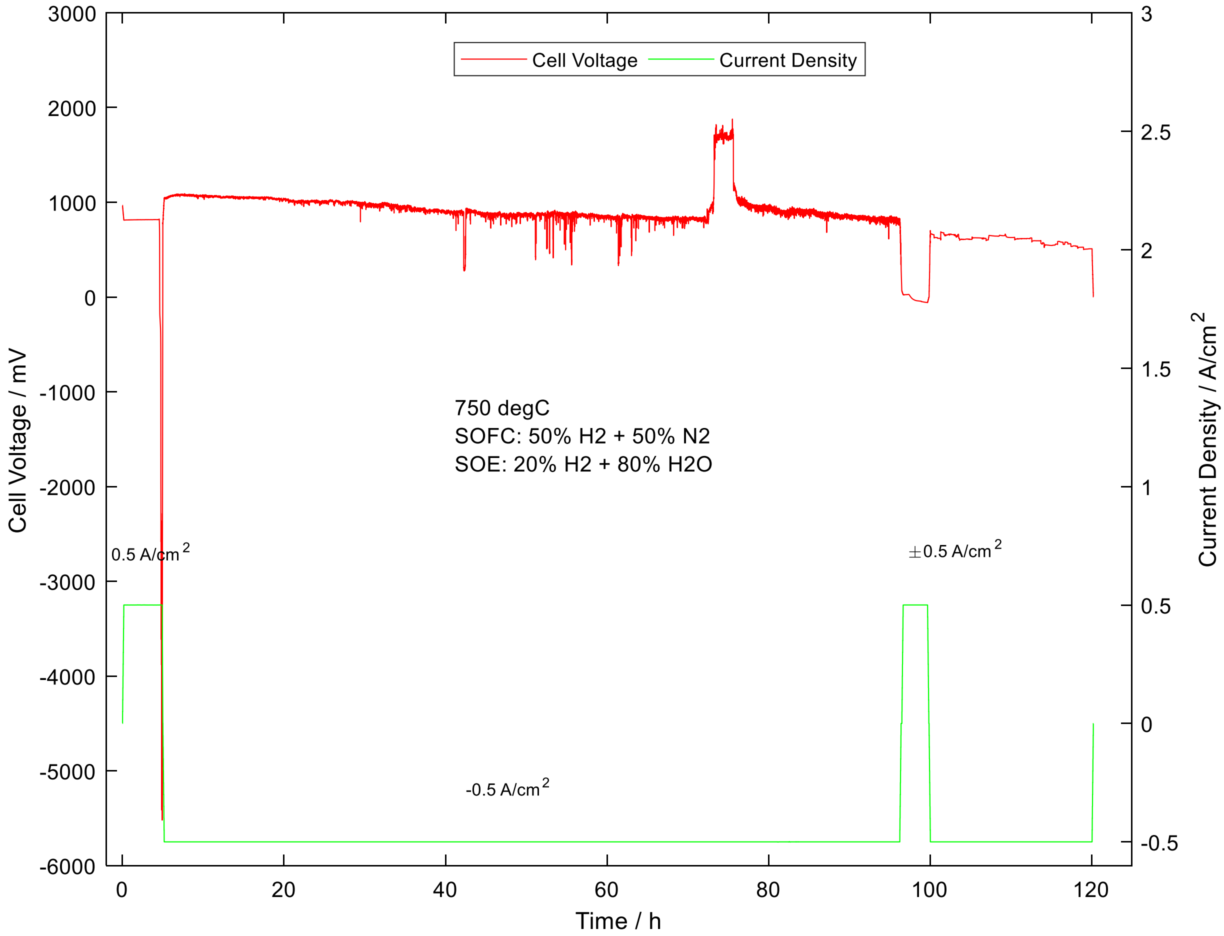

Figure 6-7: Voltage evolution characteristics of CT2_0.5_750 tested at 750°C and ±0.5 A/cm^2 current density.

Due to an interruption in the laboratory hydrogen supply, the cell voltage plummeted to -4522 mV after 5 hours of SOFC operation. The SOFC operation was thus stopped, and the decision made to switch to SOE operation since the reactant hydrogen requirements for SOE operation

(8.8 ml/min) were minimal and could be sustained with the laboratory residual hydrogen supply. The reactor was thus evacuated and the SOE reactant flow compositions instated (35.3 ml/min of $H_2O_{(g)}$ mixed with 8.8 ml/min H_2 was delivered to the fuel electrode, whilst 66.25 ml/min of air was delivered to the oxygen electrode). The OCV under the SOE environment, prior to the start of the SOE operation was 786 mV. Under the galvanostatic current density of -0.5 A/cm2 (SOE operation), the cell voltage increased to 1040 mV. Like all the other SOE tests performed, the voltage increased steadily; but only for the initial 6 hours of SOE operation. After these 6 hours, unlike the other SOE tests, the voltage began decreasing.

This was because the lab residual hydrogen supply had also run out (at approximately 13 hours on *Figure 6-7*). Therefore, from 20 hours (1042 mV) to approximately 70 hours (830 mV), *Figure 6-7*, the SOE operation was being run with a fuel electrode feed gas composition of 35.3 ml/min $H_2O_{(g)}$ and a dwindling hydrogen flow rate (i.e. progressively less than 8.8 ml/min). The decrease in voltage under galvanostatic SOE operation indicates that, in accordance with Ohms law, the cell resistances were also decreasing and hence the electrochemical performance of the cell was improving under test. However, in reality, as indicated by *Figure 6-8* (b) and *Figure 6-10*, the apparent improvement in cell performance based on the observed changes in voltage were due to dynamic fuel composition changes. This was verified by fully opening the hydrogen mass flow controller to increase the residual hydrogen flow, resulting in an instantaneous cell voltage increase to about 1812 mV. Nevertheless, the cell voltage dropped again in line with the hydrogen depletion after the initial surge in hydrogen flow.

These observations indicate that a good understanding of the effect of reactant flow rates on cell voltages (and associated cell performance) is required in order to infer overall cell resistance information from cell voltage durability tests. Furthermore, it would be useful to continuously capture and analyse the SOE/rSOC effluent gas composition, via for instance mass spectroscopy, in order to correlate the cell durability or j-V information with the composition and amount of (product gas) substance. This would enable better understanding of the apparent voltage evolution, especially when operating under potentiostatic mode. This aspect however could not be incorporated into the present body of work due to time and logistical constraints.

The overall voltage degradation rate captured under the SOE conditions was 123.6 mV/1000 h (11.9% / 1000h).

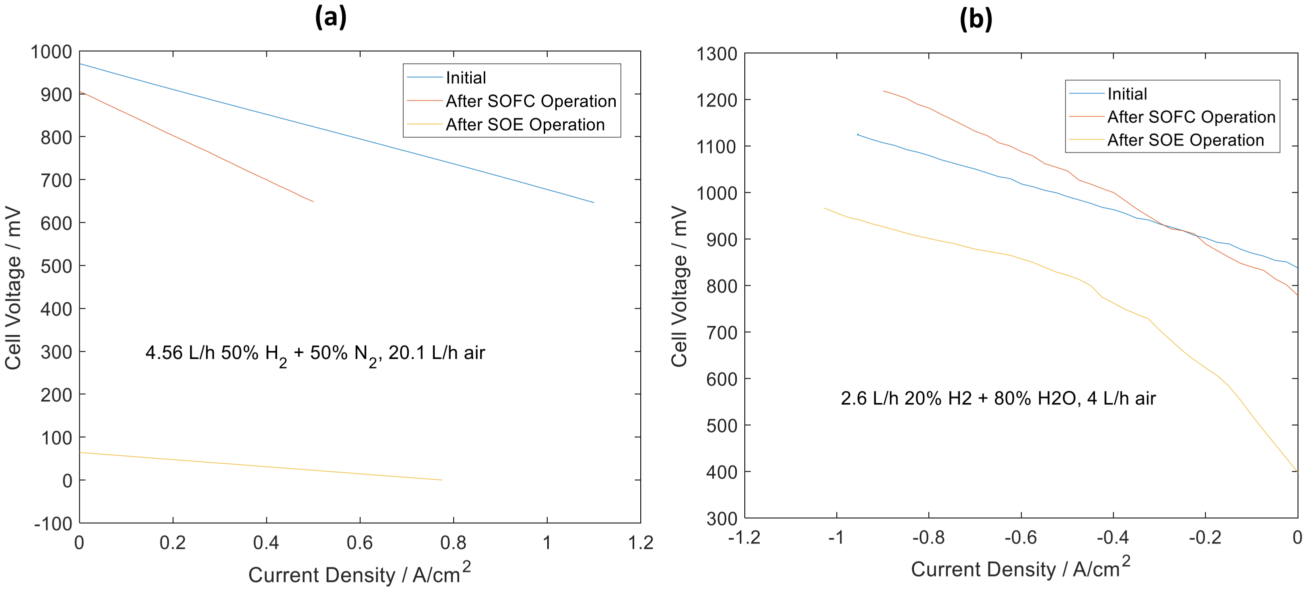

Figure 6-8: Comparison of j-V characteristic of CT2_0.5_750 before and after SOFC and SOE operation testing (captured under SOFC (a) and SOE (b) conditions).

Figure 6-8 shows the j-V curves of the virgin cell, and of the cell after SOFC and SOE operations, captured under SOFC (a) and SOE (b) conditions. *Figure 6-8* shows that the virgin cell, with an ASR of 0.29 Ω•cm^2 in SOFC conditions (a) and 0.30 Ω•cm^2 in SOE conditions(b), was not a damaged cell. After the 5 hours of SOFC operation, the ASR had increased to 0.5 Ω•cm^2 and 0.45 Ω•cm^2, respectively, under SOFC and SOE conditions. The significant increase in cell resistance after the SOFC operation was most likely as a result of the fuel starvation over the last hour of operation (plummeting the cell voltage to -4522 mV, see *Figure 6-7*, which would be the case if the cell was purely driven by the current source).

After the SOE operation, the cell ASR had increased to 0.81 Ω•cm^2 under the SOE conditions *Figure 6-8* (b). A reliable cell ASR could not be captured under the SOFC conditions after SOE operation due to the hydrogen depletion (see *Figure 6-8* (a) and *Figure 6-9*).

Figure 6-9 shows the EIS data of the virgin cell, and of the cell after SOFC and SOE operations, respectively, captured under SOFC conditions. Similar to the corresponding j-V curves (*Figure*

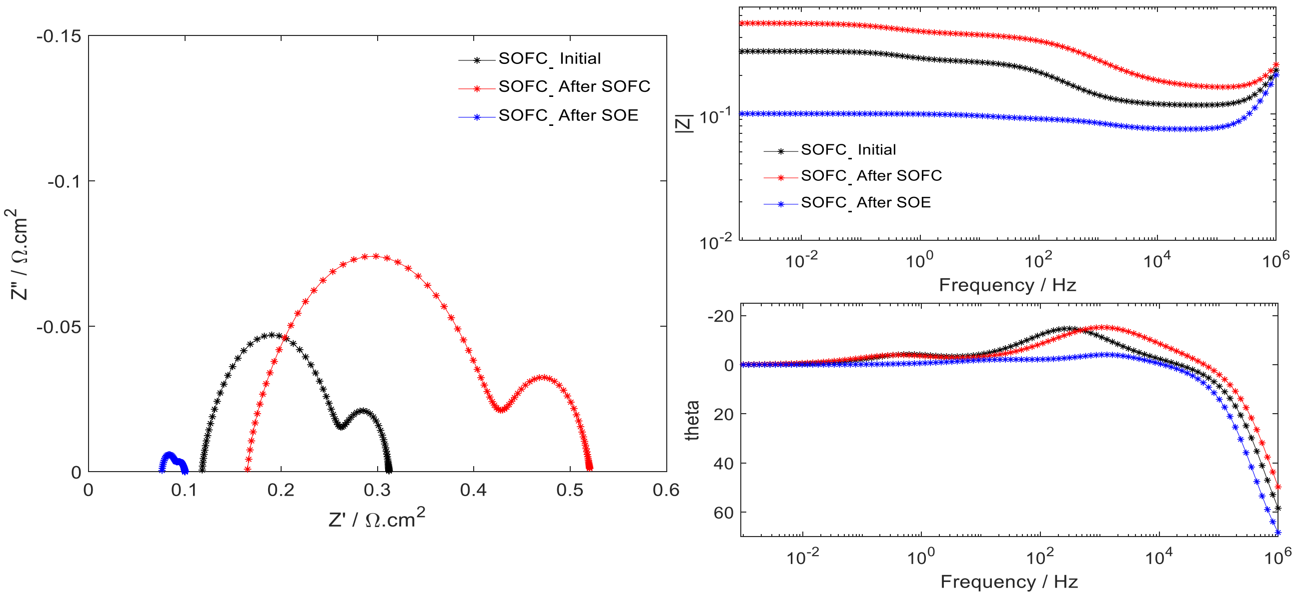

Figure 6-9: Nyquist and Bode impedance plots of CT2_0.5_750 before and after SOFC and SOE operation testing (captured under SOFC conditions).

6-8 (a)); the Nyquist plot shows a significant increase in the cell resistance after the SOFC operation. There were increases in both high and low frequency impedance components relative to the virgin cell. This indicates that for galvanostatic operation, fuel starvation has a significant impact on cell degradation. This is because the system is compelled to maintain the reaction rates without adjusting the reaction dynamics based on the available amount of reactants, thereby inducing significant additional internal stresses in the cell.

Figure 6-10 shows the EIS data of the virgin cell, and of the cell after SOFC and SOE operations, respectively, captured under the SOE conditions.

It shows significant increases, relative to the virgin cell, of all the impedance components after SOFC operation and the subsequent SOE operation.

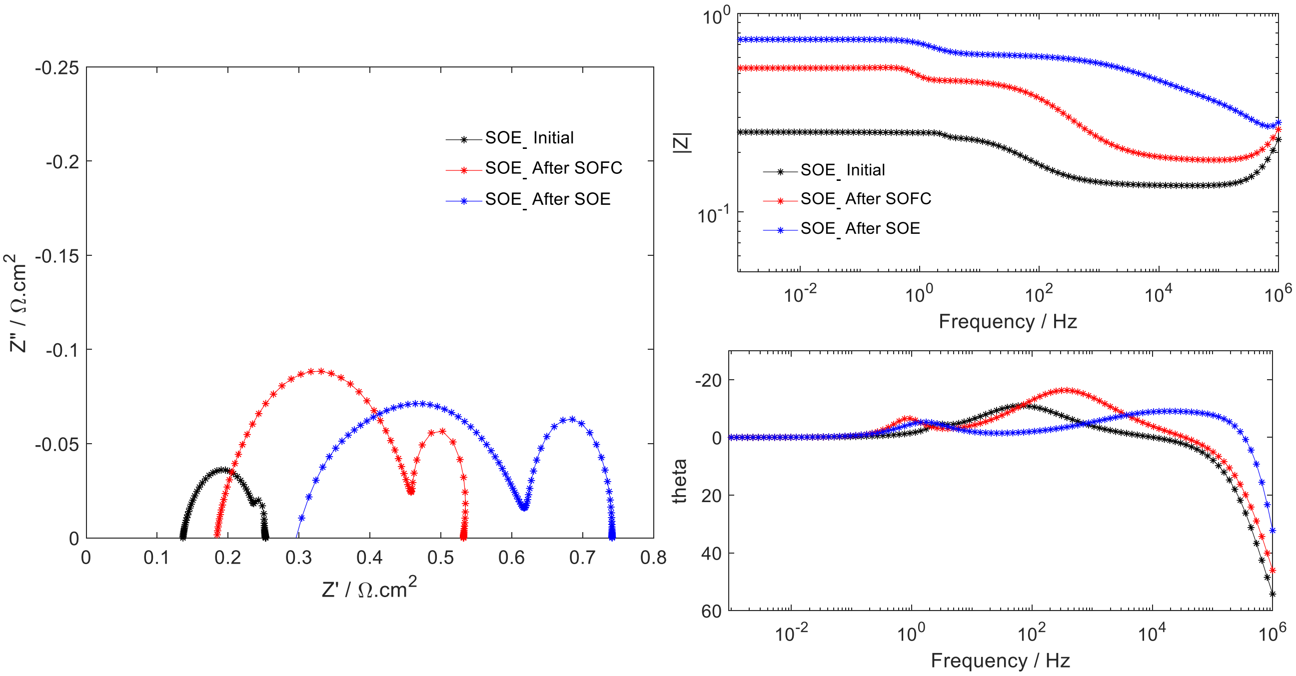

Figure 6-10: Nyquist and Bode impedance plots of CT2_0.5_750 before and after SOFC and SOE operation testing (captured under SOE conditions).

6.4 Test at 0.5 A/cm^2 Current Density (Cell ID: CT2_0.5_700)

This test (CT2_0.5_700) was conducted as the cell type 2 electrochemical equivalent of the CT1_0.5_700#1 test reported in Section 5.3. It was thus also carried out at a fuel utilisation of 52.3%, i.e., current density of 0.5 A/cm^2, with the following reactant flow rates:

1. During fuel cell operation, a dry mixture of 35.3 ml/min each of H_2 and N_2 was delivered to the fuel electrode, whilst 331.25 ml/min of air was delivered to the oxygen electrode;
2. During electrolysis operations, 1.3 g/hr of $H_2O_{(l)}$ (approximately 35.3 ml/min of $H_2O_{(g)}$) mixed with 8.8 ml/min H_2 was delivered to the fuel electrode, whilst 66.25 ml/min of air was delivered to the oxygen electrode.

The test temperature was 700°C. Even for solid oxide electrolyte cells which derive their relative high efficiency advantage due to high temperature operation, it is evident that adequate performance at temperatures relatively lower than the traditional 850°C would result in additional benefits such as wider choice of component materials (more cost-effective system manufacture). Therefore, tests at 750°C and 700°C with similar variables are being compared in order to better understand the relative impact of temperature differences and cell architectures on cell degradation, and hence cell performance.

Figure 6-11 shows the voltage evolution graph of cell CT2_0.5_700. Prior to the 120 hours of SOFC operation, the OCV was 1026.4 mV. Under the +0.5 A/cm^2 (SOFC operation) galvanostatic current density, the cell voltage dropped to 847 mV. Over the 120 hours of SOFC operation, the cell voltage dropped further to 839.8 mV with an overall cell degradation rate of 8.5 mV/1000 h (1.0% / 1000h). This degradation rate was significantly better than the degradation rate of the equivalent cell type 1 test CT1_0.5_700#1, which was 66 mV/1000 h (7.7% / 1000h). The OCV after the SOFC operation was 1039 mV, most likely as a result of further conditioning (e.g. nickel reduction) of the cell under the SOFC conditions. After the 120 hours of SOFC operation, the reactor was evacuated of the SOFC gases, and the SOE reactant gases introduced.

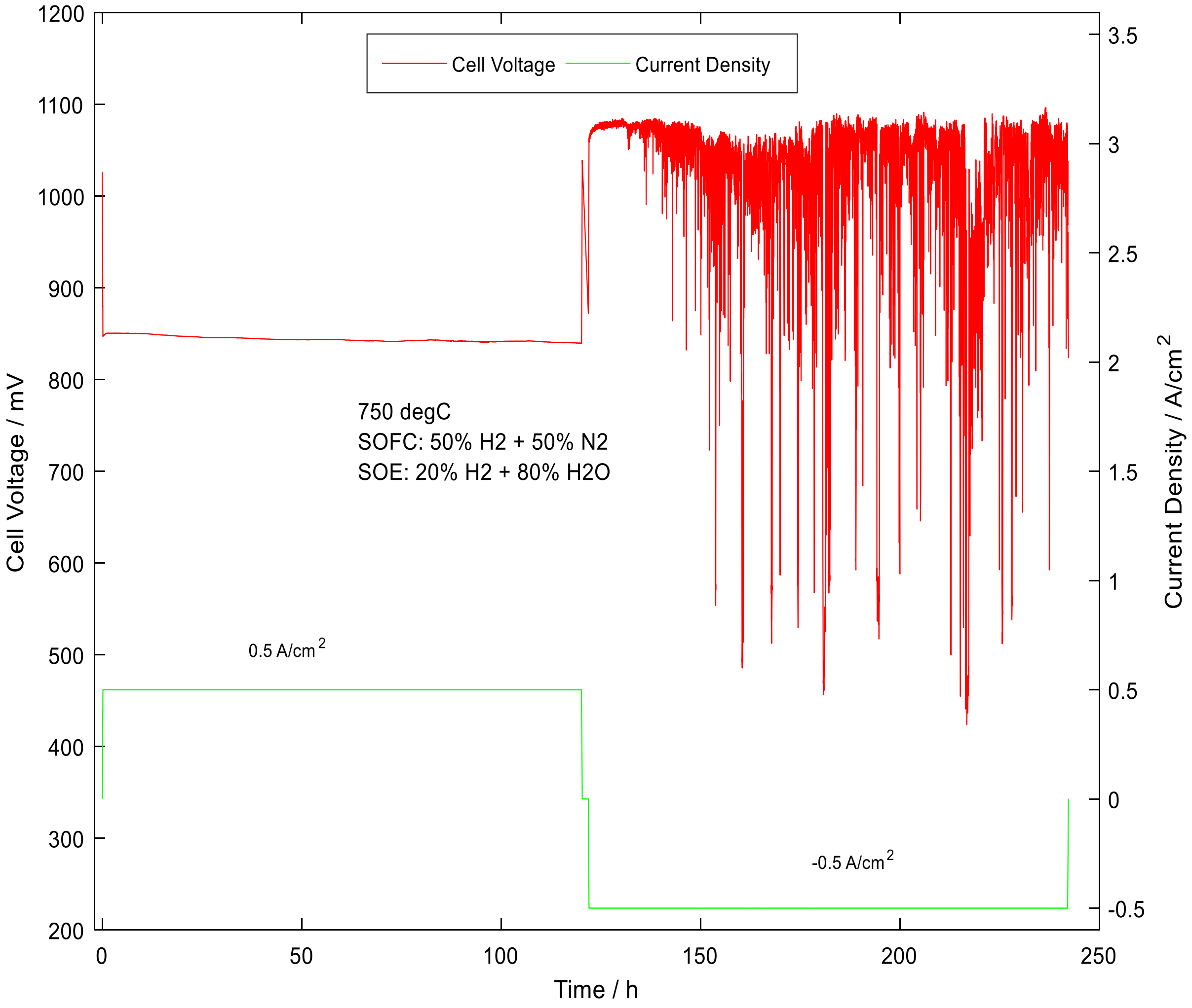

Figure 6-11: Voltage evolution characteristics of CT2_0.5_700 tested at 700°C and ±0.5 A/cm^2 current density.

The OCV prior to the 120 hours of SOE operation was 872.4 mV. The cell voltage increased to 1061 mV under the galvanostatic current density of -0.5 A/cm^2. Over the first 10 hours of SOE operation, the cell voltage increased further to 1081 mV. During the subsequent 110 hours of SOE operation, there were significant fluctuations in the cell voltage due to a suspected reactor leakage. The decision was thus made not to proceed to the rSOC testing regime. Upon demounting of the cell from the reactor, it was observed that the cell had cracked. The voltage fluctuations were therefore due to leakage / mass exchange of fuel and oxygen electrode compartment gases through the cracked cell. The degradation rate was approximately 205 mV/1000 h (19.3% / 1000h).

Figure 6-12 shows the j-V curves of the virgin cell, and of the cell after 120 hours of SOFC operation, as captured under SOFC (a) and SOE (b) conditions. The ASR of the virgin cell as captured in the SOFC conditions, *Figure 6-12*(a), was 0.33 Ω•cm^2. After the 120 hours of SOFC operation, the ASR increased to 0.39 Ω•cm^2. For the j-V curves captured under the SOE conditions, the ASR of the virgin cell was 0.35 Ω•cm^2. After the 120 hours of constant SOFC operation, the ASR had increased to 0.48 Ω•cm^2.

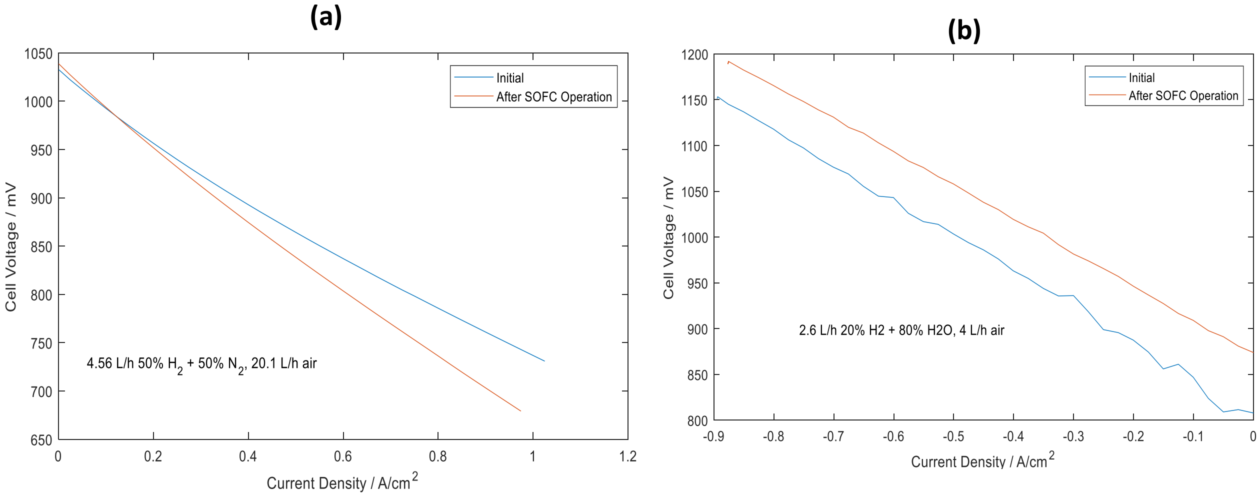

Figure 6-12: Comparison of j-V characteristic of CT2_0.5_700 before and after SOFC operation testing (captured under SOFC and SOE conditions).

Figure 6-13 shows the EIS information, captured under SOFC conditions, of the virgin cell and also of the cell after SOFC and SOE operations. Relative to the virgin cell, the Nyquist plot of the cell after the 120 hours SOFC operation only shows a marginal increase in the polarisation resistance. After the 120 hours SOE operation, very significant increases could be observed in the low and high frequency impedance components. It is particularly interesting to note the significant disparity between the cell durability (voltage evolution) information for the SOE operation in *Figure 6-11*, and the Nyquist plot in *Figure 6-13*.

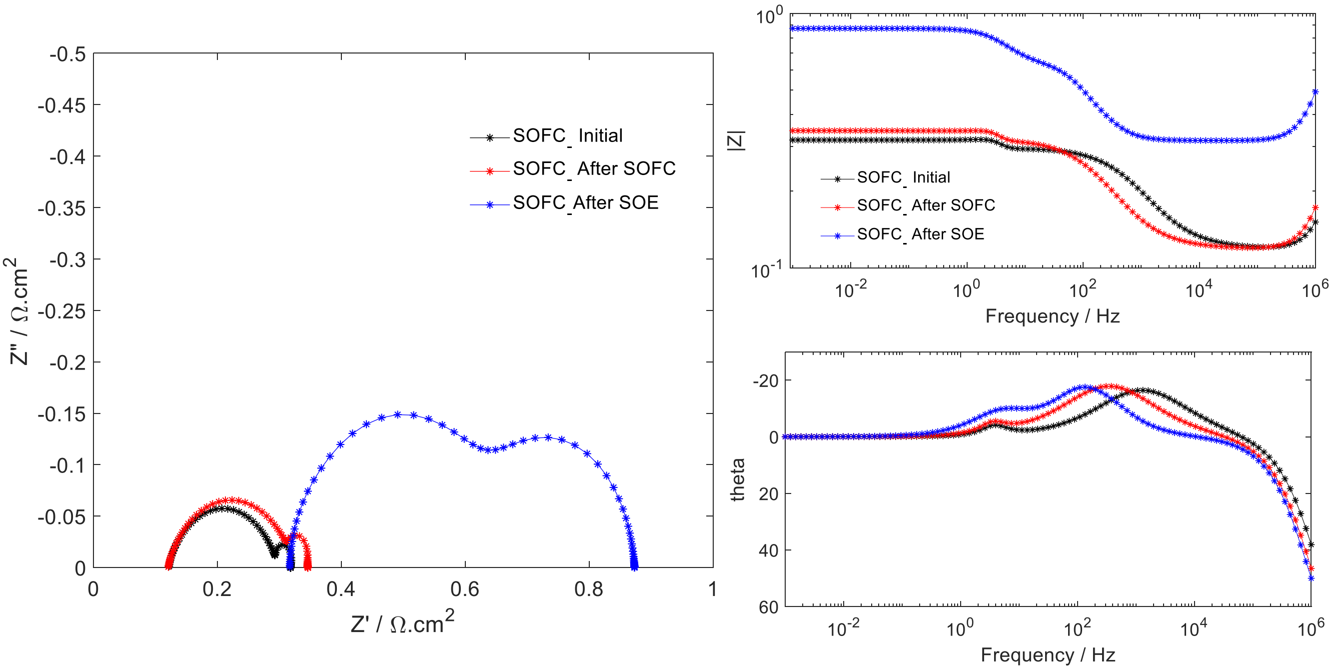

Figure 6-13: Nyquist and Bode impedance plots of CT2_0.5_700 before and after SOFC and SOE operation testing (captured under SOFC conditions).

Whereas the cell durability information suggested the cell performance was improving, the Nyquist plot clearly shows that the cell had undergone significant degradation (hence the significant increases in the impedance components). As mentioned earlier, the cell durability information was compromised by fuel and oxygen electrode compartments gas exchange due to cell cracking.

Figure 6-14 shows the EIS information, captured under SOE conditions, of the virgin cell and also of the cell after SOFC and SOE operations. Similar to the EIS information captured under SOFC conditions (*Figure 6-13*), there was a marginal increase in the polarisation resistance after the

120 hours of SOFC operation, as compared to the virgin cell. Significant increases in all the impedance components were observed after the 120 hours of SOE operation, indicating significant degradation in cell performance. It should be noted that the increases in cell resistance may be as a result of further induced stresses as a result of a dynamic fuel utilisation environment (due to gas leakages) under galvanostatic operation and also due to the cracks observed in the cell upon demounting.

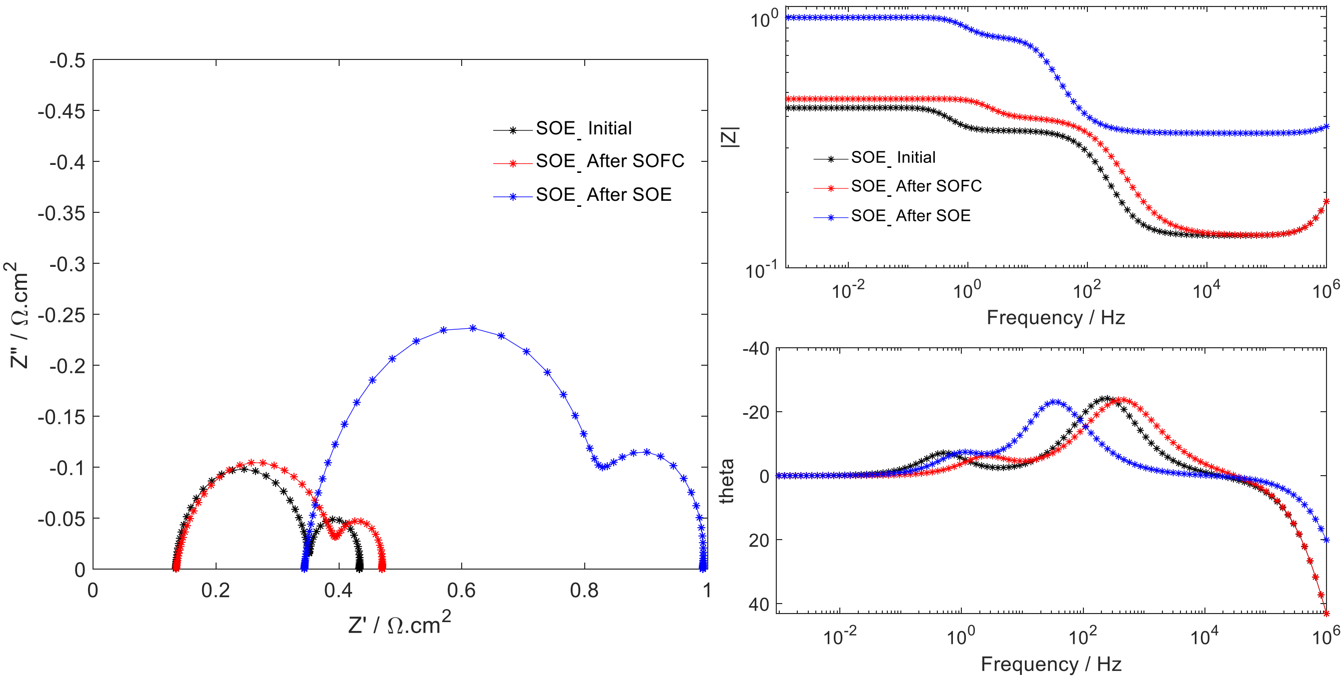

Figure 6-14: Nyquist and Bode impedance plots of CT2_0.5_700 before and after SOFC and SOE operation testing (captured under SOE conditions).

6.5 Summary of Cell Type 2 Results

Cell type 2 was tested at current densities of 0.5 A/cm^2 and 0.7 A/cm^2, and at temperatures of 700°C and 750°C, to enable effective comparison with the results of the cell type 1 tests. The cells were subjected to a test protocol which entailed 120 hours of constant SOFC operation followed by 120 hours of constant SOE operation and completed with rSOC cycling comprising 3 hours SOFC operation followed by 20 hours SOE operation. The rSOC cycling was designed to incorporate 33 cycles, however, the cells could not be subjected to the complete test protocol due to various factors such as damaged virgin cells, fuel starvation due to equipment malfunction and physical cell damage (cracking) during testing.

For all tests, cell performance, as measured by resistance changes and voltage durability, deteriorated under test. The rate of deterioration was higher for constant SOE operation relative to constant SOFC operation. During rSOC cycling, cell performance deteriorated continually under all SOE operation steps, whilst some performance recovery was observed under the subsequent SOFC operation steps.

An exhaustive discussion of the results is presented in chapter 7.

7 DISCUSSION

7.1 General Observations

In addition to the discussions presented in the following sections, the following general observations were made during testing and subsequent data analysis:

1. During rSOC operation, fuel cell OCVs generally increased with increasing cycle number, however the voltage-drop relative to applied current density increase were higher (see *Figure 7-1*, culled from CT1_0.5_750#1 results). This may indicate both progressive reduction of the nickel grains in the Ni-YSZ fuel electrode (hence the increasing OCVs) and deterioration of the cell internal structure, e.g. micro-fissuring and delamination, see *Figure 5-10*, (hence the higher voltage drops under load).

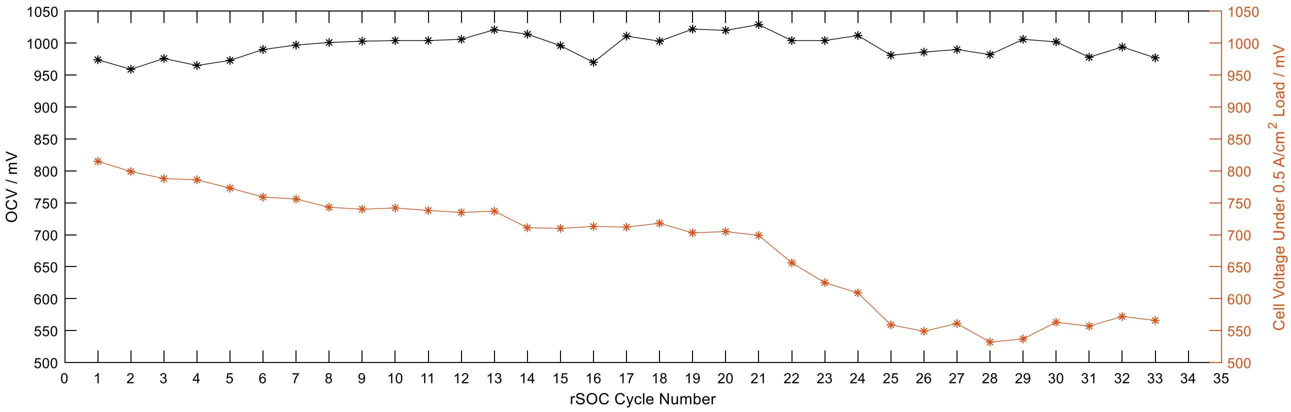

Figure 7-1: Characteristic changes in open circuit voltage and voltage under polarisation, relative to rSOC cycle number.

2. As already mentioned in Section 5.2, some voltage recovery occurred over the constant 3hrs of SOFC operation. However, this was not significant enough to offset the voltage losses observed during SOE operation.

3. Cell voltage tends to degrade appreciably (as measured via recorded voltage) during the current ramps to the required current densities for both SOFC and SOE operations, and then recovers somewhat at constant operation at the required current density. As mentioned in bullet point 2, further voltage recoveries were recorded all through the 3hrs of SOFC operation. Therefore, it seems that another contributor to overall cell degradation are the current ramps up or down to the required current density for SOFC/SOE. Thus, more degradation seems to be recorded during reversible cycling sessions (irrespective of the relative degradations in SOFC and SOE modes) due to the necessarily more frequent current ramping during rSOC cycling.

4. In SOE mode, the variance in cell voltage at a given current density is scattered around a mean (see all voltage durability results presented in Chapters 5 and 6, and also the SOE portions of *Figure 7-23* and *Figure 7-24*). This is related to the characteristics inherent in steam supply, i.e. intermittent starvation and oversupply on a microscale due to the small steam quantities required for 3 cm diameter unit cell testing. This voltage scatter was also observed during both the current density ramp ups and ramp downs.

5. After SOE operation, it takes a longer time (relative to reversible cycle number) to reach steady-state fuel cell OCV for the following SOFC operation (see Section 7.5). On average, it takes ≥30 minutes to recover from SOE operation, therefore switching straightaway from SOE to SOFC mode may not be conducive for efficient cell operation. If a mandatory minimum switching time is required, then on a system level, the fuel wastage during the switching time needs to be quantified relative to the benefits in SOFC operation from a steady state OCV. The ≥30 minutes taken to reach steady state SOFC OCV

after SOE operation is most likely the time required to evacuate the fuel electrode gas chamber of the SOE gas composition (mainly reactant steam) and establish the SOFC gas composition (no reactant steam) – also see *Figure 1-3*. A similar delay was not observed when switching from SOFC to SOE operation since the main difference was the addition of steam for SOE operation.

6. It seems that although low air flows to the oxygen electrode (relative to fuel flow to the hydrogen electrode) give higher SOFC OCVs, there is a rapid and significant voltage drop during constant SOFC operation. Therefore, although relatively higher OCVs may be recorded with a low air supply to the cathode in SOFC mode, the voltage drops significantly under current, and to a lower level than with a higher air supply to the cathode (e.g. from 1.1 to 0.76, compared to 1.00 to 0.88 V). This is related to cell cooling under high airflows, and oxygen starvation for low airflows under polarisation.

7.2 Effect of Temperature

Solid oxide cells promise high efficiencies due to the decreasing electric energy demand with increasing operating temperature (see *Figure 1-3*). Generally, the electrochemical processes are thermally activated, leading to lower overall cell resistances at high temperatures [39], [50], [34], [61], [108], [149] - [150] [151]. As an example, although ‘electrolysis’ at approximately 2500^{o}C is presently impractical mainly as a result of material limitations; at such temperatures, electrical input is unnecessary since water breaks down into oxygen and hydrogen by thermolysis.

At the more practical temperatures of interest, ≤850°C, the theoretically high efficiency of high temperature fuel cell / electrolysis is mainly a result of the following three factors (refer to Section 1.1.3 for further details):

1. Increased electrode catalytic activity at high temperatures (i.e. high electrode reaction kinetics leading to low activation over-potentials). The high operating temperatures of the technology result in typically small activation overpotentials.
2. The ionic conductivities of the electrolyte materials increase with increasing temperature.
3. Finally, the thermodynamics of reactant (i.e. water for electrolysis) decomposition is more favourable at higher temperatures. The contribution of the Gibbs free energy is lower at high temperatures, i.e. less electric energy input, more heat input use.

Nevertheless, at a system level, it may be more economic to operate at lower temperatures (<800°C) since that would permit a wider choice in materials of construction for the balance of plant components. Additionally, if adequate performance at lower operating temperatures can be demonstrated, then commercial operation at lower temperatures would be more desirable due to the associated decreased overall energy required and the possibility of utilising less expensive component materials.

A key criterion therefore should be to attain good performance of rSOC cells under operation at high current densities (≥0.5 A/cm^2) and relatively lower temperatures (≤ 750°C). Therefore, the tests reported under the scope of this thesis were performed at temperatures of 750°C and 700°C.

Figure 7-2 and *Figure 7-3* show the j-V comparisons of Cell types 1 and 2 operated at 750°C and 700°C. All four tests (two tests with cell type 1 and two tests with cell type 2) were carried out at a current density of 0.5 A/cm². The ASRs of the four tests represented in *Figure 7-2* and *Figure 7-3* are listed in *Table 7-1*.

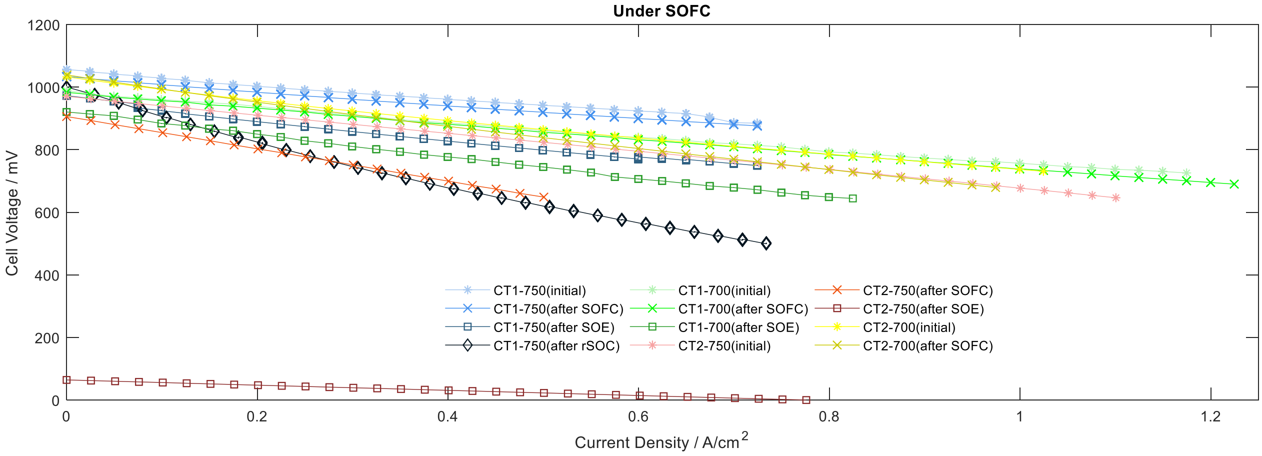

Figure 7-2: j-V Comparison of cell types 1 and 2 at temperatures of 750°C and 700°C (captured under SOFC conditions).

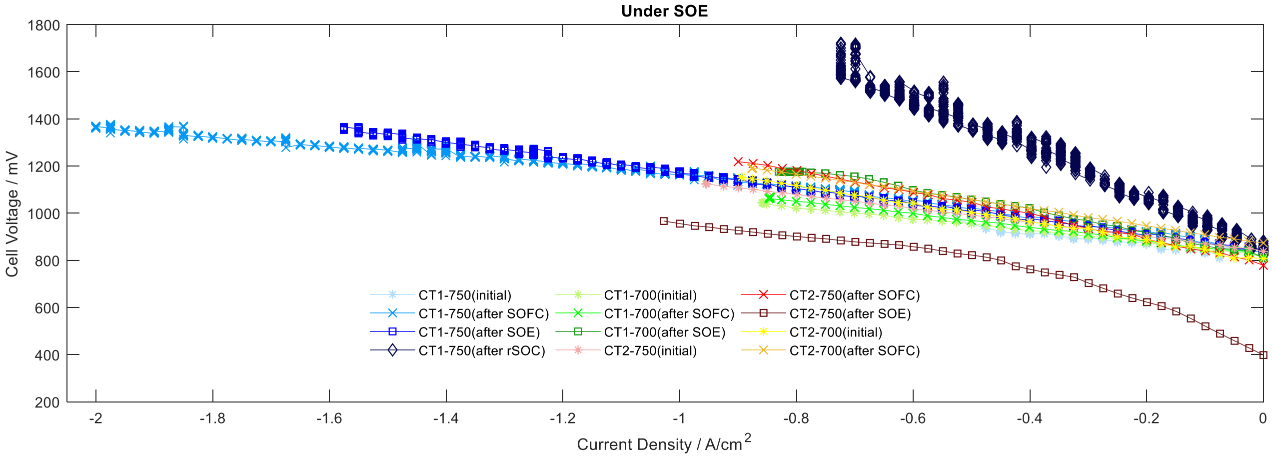

Figure 7-3: j-V Comparison of cell types 1 and 2 at temperatures of 750°C and 700°C (captured under SOE conditions).

As expected, for both cell types, performance at 750°C was better than performance at 700°C. In addition, according to the j-V characterisations, the performance of cell type 1 at both temperatures was better than the performance of cell type 2. Most importantly, the performance of cell type 1 at 700°C was better than the performance of cell type 2 at 750°C. It seems that LSC infiltration into a GDC backbone as an oxygen electrode, for cell type 2, which also included a pure GDC barrier layer between the YSZ electrolyte and the LSC infiltrated GDC backbone oxygen electrode, did not improve the catalytic activity of the oxygen electrode relative to cell type 1.

This reiterates the observation made in Chapter 3 that for rSOC operation, cell architecture and materials are very important variables.

Also clear from *Figure 7-2*, *Figure 7-3*, and *Figure 7-4* is that cell performance (based on increases in cell resistance and degradation rate) under SOFC conditions was better than cell performance under SOE conditions.

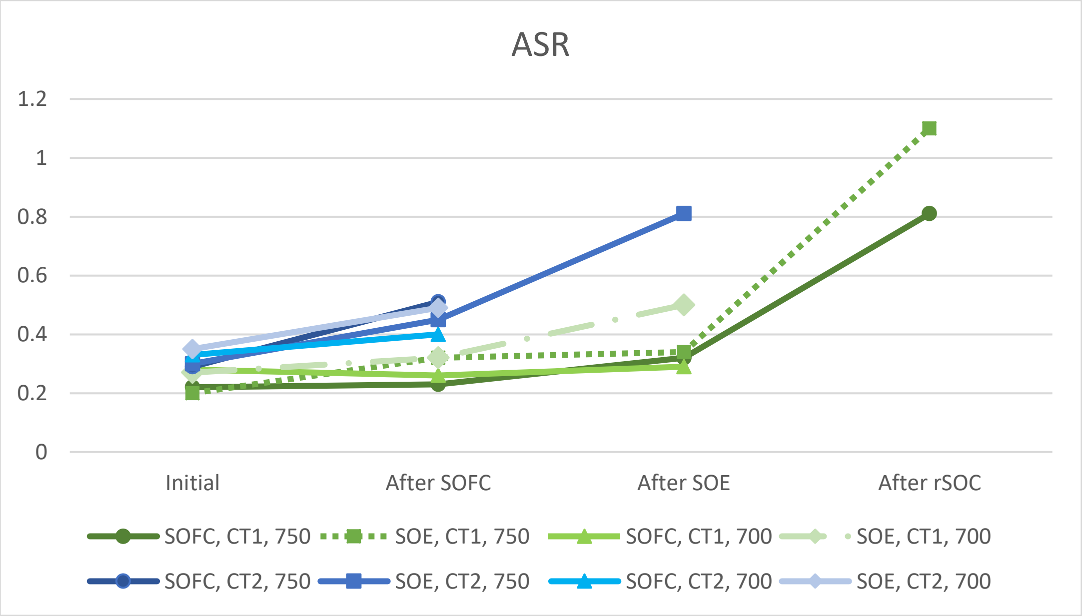

Figure 7-4: ASR comparison of cell types 1 and 2 at 700°C and 750°C (captured under SOFC and SOE conditions)

Table 7-1: ASR of cell types 1 and 2 tested at a current density of 0.5 A/cm^2 and temperatures of 750°C and 700°C

Parameter			Cell Type 1		Cell type 2	
			Under SOFC Conditions (Ω-cm^2)	Under SOE Conditions (Ω-cm^2)	Under SOFC Conditions (Ω-cm^2)	Under SOE Conditions (Ω-cm^2)
Cell Area Specific Resistance (ASR)	@750°C	Initial	0.22	0.2	0.29	0.3
		After SOFC	0.23	0.32	0.51	0.45
		After SOE	0.32	0.34	0.08[NOTE 1]	0.81
		After rSOC	0.81	1.1	-	-
	@700°C	Initial	0.28	0.27	0.33	0.35
		After SOFC	0.26	0.32	0.4	0.49
		After SOE	0.39	0.5	-	-
		After rSOC	-	-	-	-

1. The j-V characteristics of cell type 2, tested at 750 °C, could not be captured correctly under SOFC conditions due to hydrogen starvation (also see Section 6.3, *Figure 6-8* to *Figure 6-10*).

Figure 7-5 to *Figure 7-8* show the equivalent EIS information to the j-V comparisons detailed in *Figure 7-2* and *Figure 7-3*. *Figure 7-5* and *Figure 7-6* are the Nyquist and Bode plots, respectively, for the two cell type 1 and type 2 tests, carried out at 750°C and 700°C, captured under SOFC conditions.

Figure 7-7 and *Figure 7-8* are the Nyquist and Bode plots, respectively, for the two cell types, captured under SOE conditions.

The figures show that under both conditions, the overall performance of cell type 1 was better than cell type 2 at both temperatures. It was noted in Chapter 6 that the SOFC performance of cell type 2, as measured by the durability test, was significantly better than the SOFC performance of cell type 1, whilst the SOE performance was comparable. However, since the resistances in the virgin cell of cell type 2 were higher than for cell type 1 (see *Table 7-1*, *Figure 7-5* and *Figure 7-7*), it was evident that a premium in performance had to be accepted for the sake of improved durability.

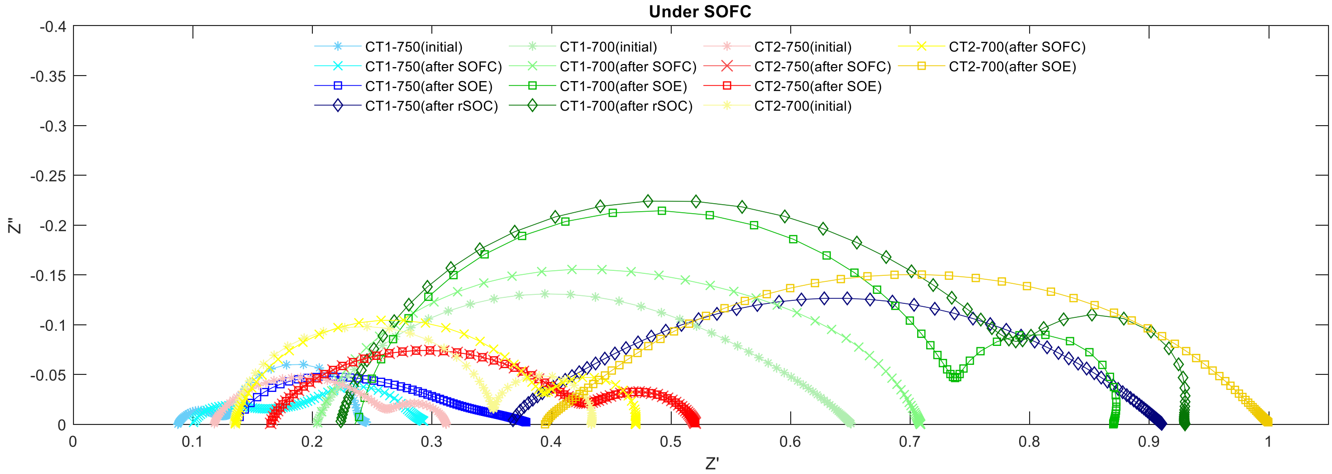

Figure 7-5:Nyquist comparison of cell types 1 and 2 at temperatures of 750°C and 700°C (captured under SOFC conditions).

Generally, *Figure 7-5* to *Figure 7-8* show that ohmic contributions increase with both time under test and operating mode, whilst electrode polarisation increases with decreasing operating temperature.

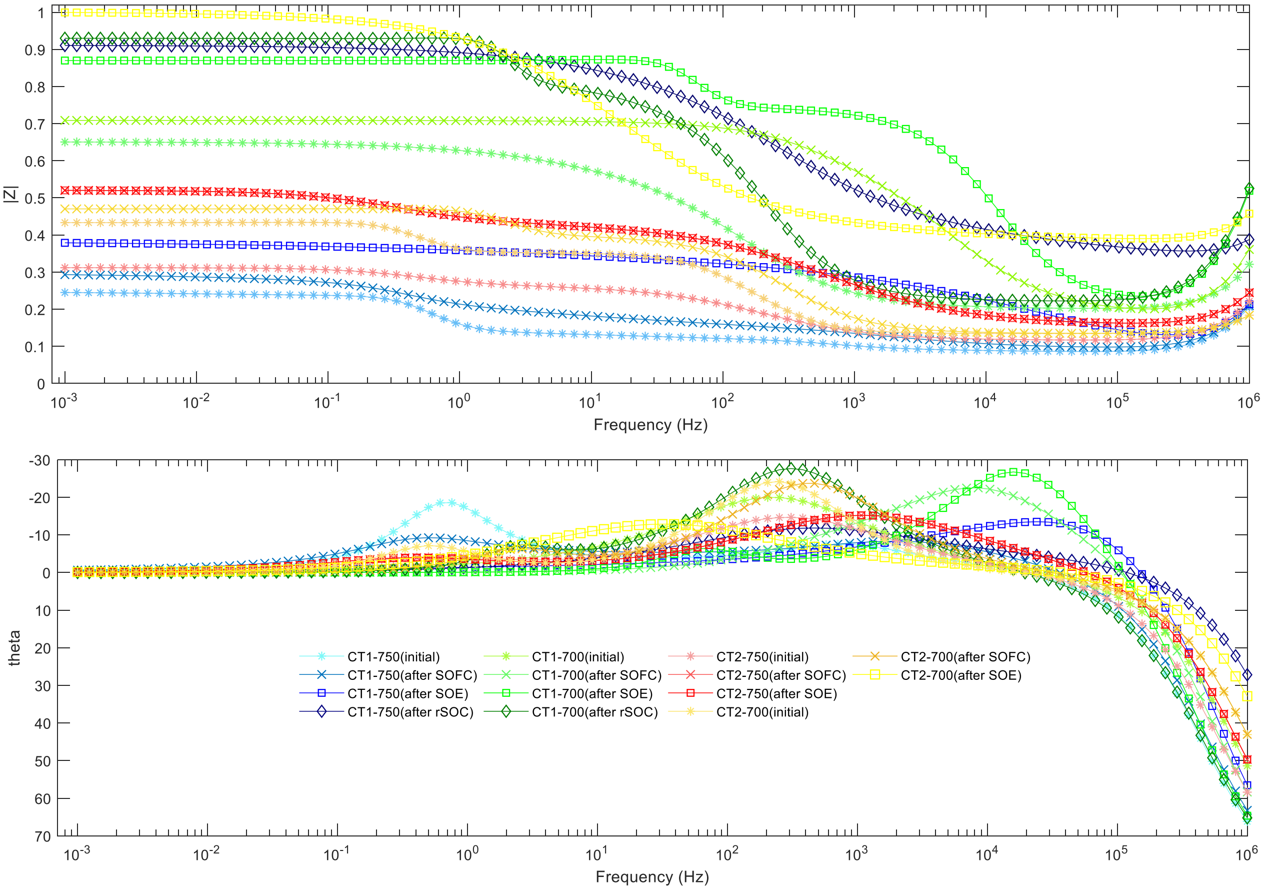

Figure 7-6: Bode comparison of cell types 1 and 2 at temperatures of 750°C and 700°C (captured under SOFC conditions).

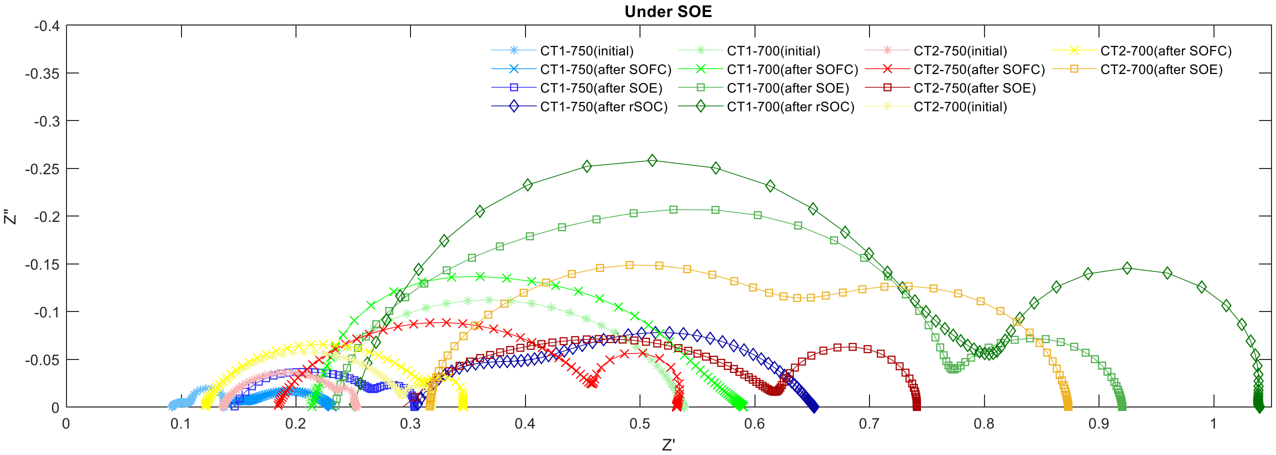

Figure 7-7: Nyquist comparison of cell types 1 and 2 at temperatures of 750°C and 700°C (captured under SOE conditions).

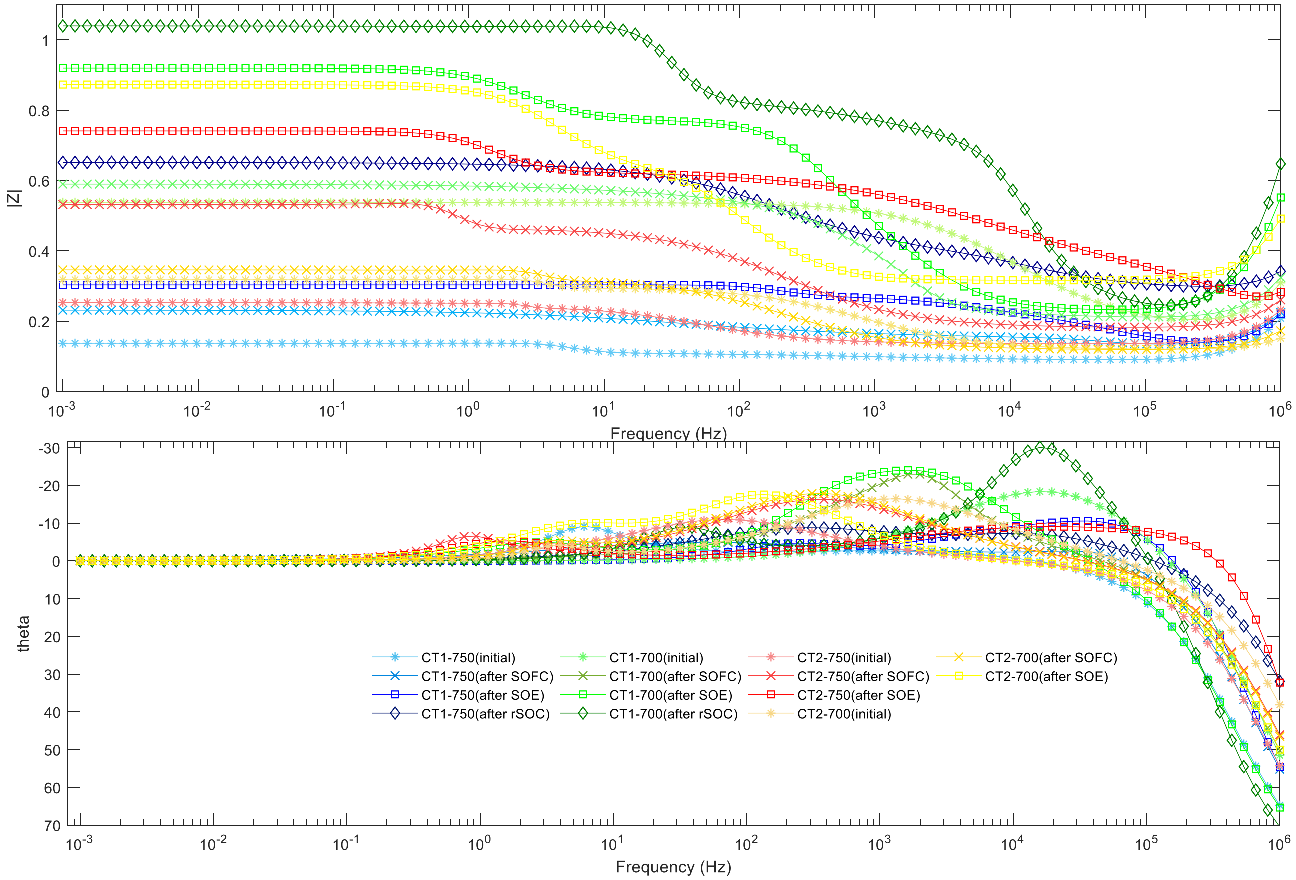

Figure 7-8: Bode comparison of cell types 1 and 2 at temperatures of 750°C and 700°C (captured under SOE conditions)

7.3 Effect of Current Density

As a result of the dominant mechanism reported for the degradation of SOE oxygen electrodes (i.e. oxygen pressure build-up at the oxygen electrode – electrolyte interface, see Section 3.2.2 for further details), it is expected that, under rSOC operation, the operating current density would have more of an impact on cell degradation during SOE operation relative to SOFC operation. This is because the magnitude of the oxygen flux responsible for the oxygen build-up at the electrode – electrolyte interface is a direct function of the operating current density, in accordance with the following equation (also see Section 1.1.4.3):

$$H_2O + ne^- \rightarrow \frac{n}{2}O^{2-} + \frac{n}{2}H_2 \qquad \textbf{Equation 7}-\textbf{1}$$

At low to intermediate current densities (i.e. up to ~ 0.5 A/cm^2), the overall cell degradation has mainly been attributed to oxygen electrode degradation [59], [68], [70], [73], [83]. This is especially the case for operation at intermediate current densities since cell degradation is minimal at low current densities. Cells operated for over 1000 hours at a low current density (<< 0.5 A/cm^2) exhibit negligible degradation or delamination, regardless of cycling conditions [72] [141]. rSOC systems can therefore sustain stable operation at low current densities (or possibly be operated at low current densities without any appreciable degradation). However, this may not be ideal due to the economics of fuel utilisation and heat energy input relative to the amount of useful product (hydrogen or power) since the cell may be significantly under-utilised at low current densities, albeit operating at high durability [72], [74]**.**

The mode of current supply also seems to affect cell degradation characteristics. The rate of degradation of the rSOC system is lower for variable current operation (potentiostatic) relative to constant current (galvanostatic) operation [72], [59], [73], [83]. This is to be expected due to the reported oxygen electrode delamination mechanism. Under potentiostatic SOE operation, since the current through the cell is a function of the electrode reactions and ion transport through the electrolyte, when oxygen ions begin to accumulate at the interface of the electrolyte and air electrode, the cell resistance increases whilst the current decreases in accordance with Ohms law (the voltage is constant). Therefore, the rate of electrode reactions and ion transport through the cell also decrease, thus mitigating the pressure build-up at the electrolyte – air electrode interface. Under galvanostatic SOE operation, the current through the cell is held constant and therefore the cell voltage and resistance could increase linearly until the interfacial pressure threshold for electrode delamination is reached. Nevertheless, for commercialisation, galvanostatic operation is desired due to the direct correlation between hydrogen production rate (and power density) and the operating current density.

Galvanostatic operation was thus employed for the tests reported in this thesis, and the tests were carried out at current densities ≥ 0.5 A/cm^2.

7.3.1 Comparison of Two different Cell Types Tested at 0.5 A/cm^2 and 0.7 A/cm^2

Figure 7-9 and *Figure 7-10* show the j-V comparisons of cell types 1 and 2 operated at 0.5 A/cm^2 and 0.7 A/cm^2. All four tests (two tests with cell type 1 and two tests with cell type 2) were carried out at a temperature of 750^{o}C. The ASRs of the four tests represented in Figure 7-9 and *Figure 7-10* are listed in *Table 7-2* and plotted as *Figure 7-11*.

As expected, for cell type 1, cell resistances were higher after operation at 0.7 A/cm^2 compared to 0.5 A/cm^2. However, for cell type 2, cell resistances for SOFC operation at 0.7 A/cm^2, were lower than cell resistances at 0.5 A/cm^2. This correlates very well with the theoretical observation that the operating current density would have more of an impact on cell degradation during SOE operation relative to SOFC operation because of the increased magnitude of oxygen flux responsible for the oxygen build-up at the electrode – electrolyte interface. Note that this oxygen flux is a direct function of the operating current density, in accordance with **Equation 7-1**.

Compared to the impact of operating temperature on the performance of the different cell types, see Section 7.2, cell type 2 seems to perform better at a current density of 0.7 A/cm^2 relative to the performance of cell type 1. Since the only difference between cell types 1 and 2 was the oxygen electrode architecture, it raises the possibility that cell type 1 had better oxygen electrode activation characteristics (electrode catalytic activity influenced by operating temperature) whilst cell type 2 had better oxygen electrode – electrolyte interfacial bonding characteristics (increasing its resistance interfacial fissuring/delamination at high operating current densities). This may be the case why cell type 1 performed better than cell type 2 at 0.5 A/cm^2 current density, whilst cell type 2 performed better than cell type 1 at 0.7 A/cm^2 current density (all four tests were conducted at 750^{o}C).

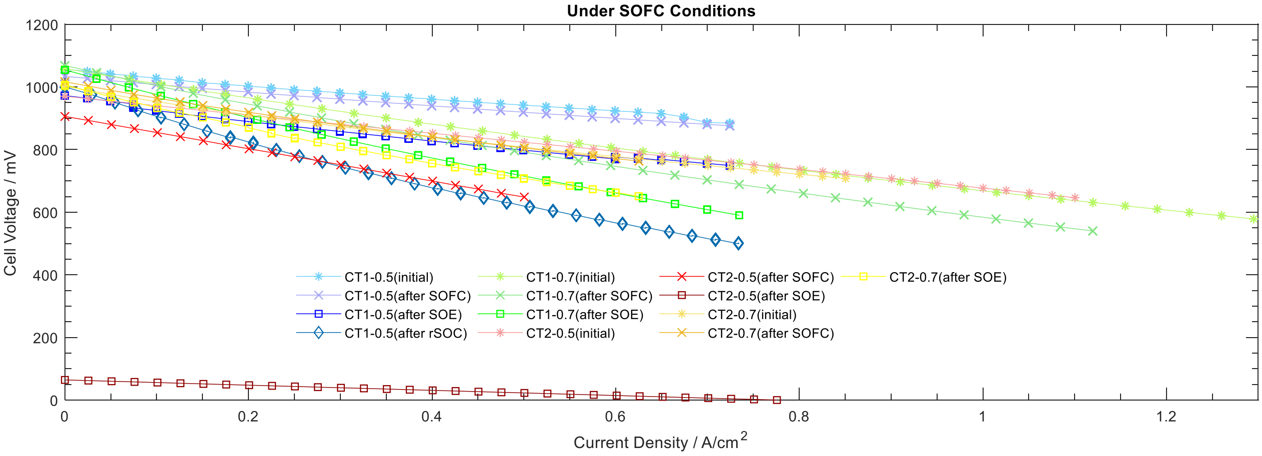

Figure 7-9: j-V comparison of cell types 1 and 2 at current densities of 0.5 A/cm^2 and 0.7 A/cm^2 (captured under SOFC conditions)

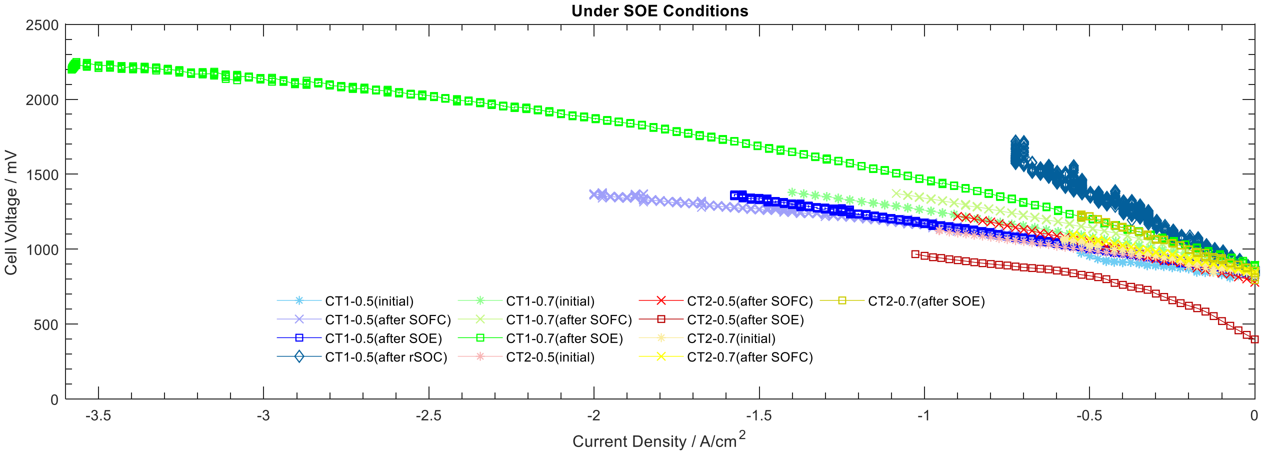

Figure 7-10: j-V Comparison of cell types 1 and 2 at current densities of 0.5 A/cm^2 and 0.7 A/cm^2 (captured under SOE conditions)

Table 7-2: ASR of cell types 1 and 2 tested at a temperature of 750°C and current densities of 0.5 A/cm^2 and 0.7 A/cm^2.

Parameter			Cell Type 1		Cell type 2	
			Under SOFC Conditions (Ω-cm^2)	Under SOE Conditions (Ω-cm^2)	Under SOFC Conditions (Ω-cm^2)	Under SOE Conditions (Ω-cm^2)
Cell Area Specific Resistance (ASR)	@0.5 A/cm^2	Initial	0.22	0.2	0.29	0.3
		After SOFC	0.23	0.32	0.51	0.45
		After SOE	0.32	0.34	0.08	0.81
		After rSOC	0.81	1.1	-	-
	@0.7 A/cm^2	Initial	0.43	0.45	0.34	0.38
		After SOFC	0.54	0.50	0.37	0.43
		After SOE	0.66	0.58	0.54	0.86
The lower change in ASR for CT2 documents its improved durability at the expense of (initially) lower performance (also see *Figure 7-11*).						

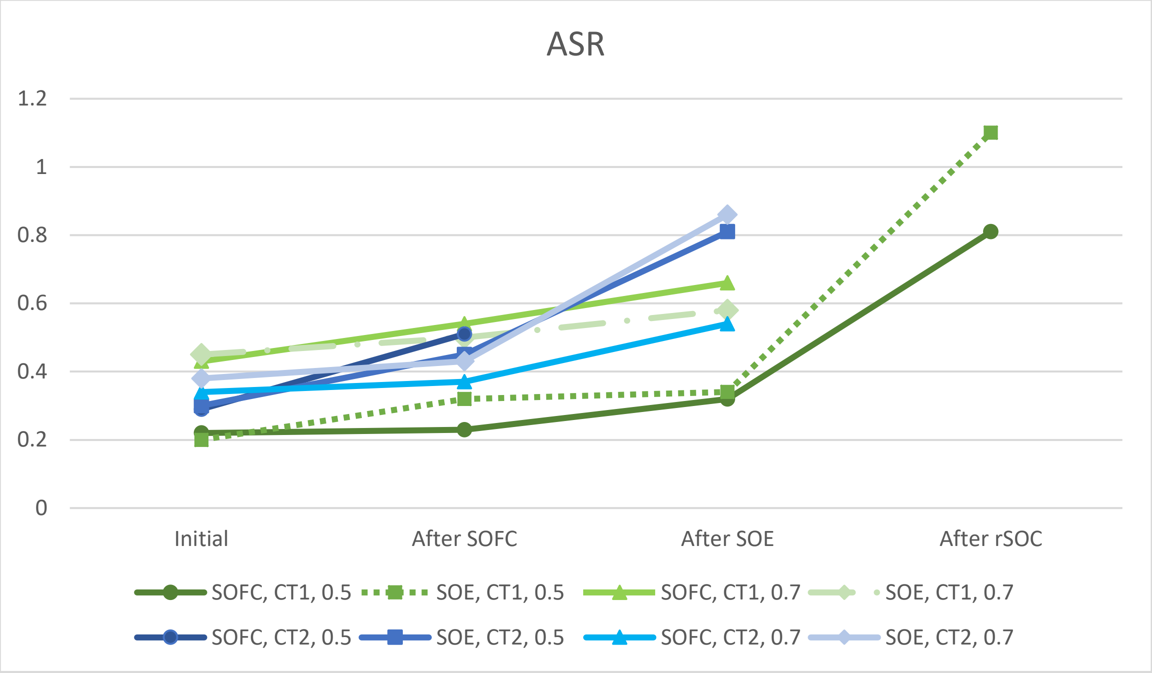

Figure 7-11: ASR comparison of cell types 1 and 2 at 0.5 A/cm^2 and 0.7 A/cm^2 (captured under SOFC and SOE conditions)

to Figure 7-15 show the equivalent EIS information to the j-V comparisons detailed in Figure 7-9 and Figure 7-10. and Figure 7-13 are the Nyquist and Bode plots, respectively, for the two cell type 1 cell type 2 tests (carried out at 0.5 A/cm^2 and 0.7 A/cm^2) captured under SOFC conditions.

Figure *7-14* and Figure 7-15 are the Nyquist and Bode plots, respectively, for the corresponding two cell type 1 and the two cell type 2 tests captured under SOE conditions.

The figures show that under both conditions, the overall performance of cell type 1 was better than cell type 2 at 0.5 A/cm^2, whilst the perfromance of cell type 2 was better than cell type 1 at 0.7 A/cm^2 operating current density. For the tests at 0.5 A/cm^2, both the ohmic contribution and the electrode polarisation were lower for cell type 1 relative for cell type 2. However, for the tests at 0.7 A/cm^2, whilst the ohmic contributions were similar, the electrode polarisation of cell type 2 was significantly lower.

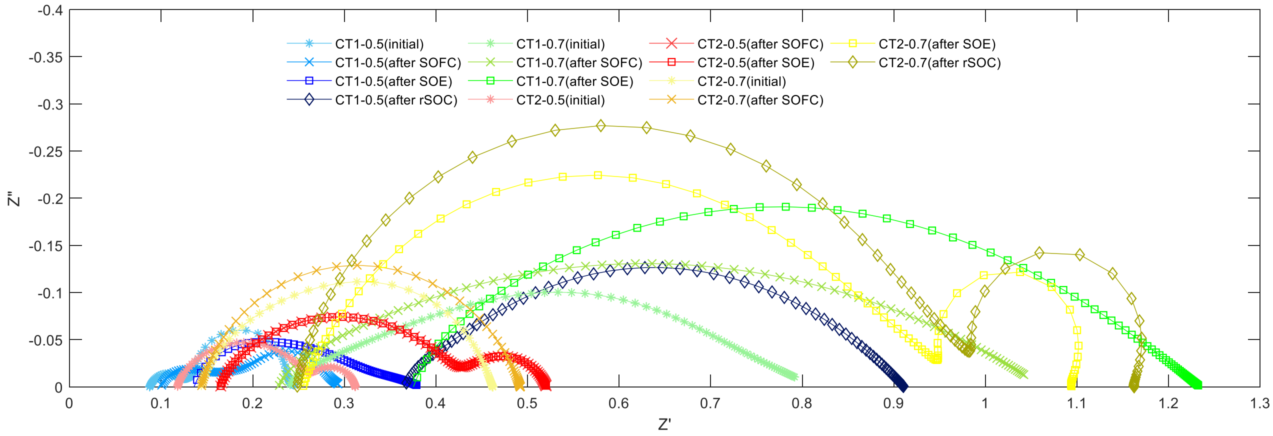

Figure 7-12: Nyquist comparison of cell types 1 and 2 at current densities of 0.5 A/cm2 and 0.7 A/cm2 (captured under SOFC conditions)

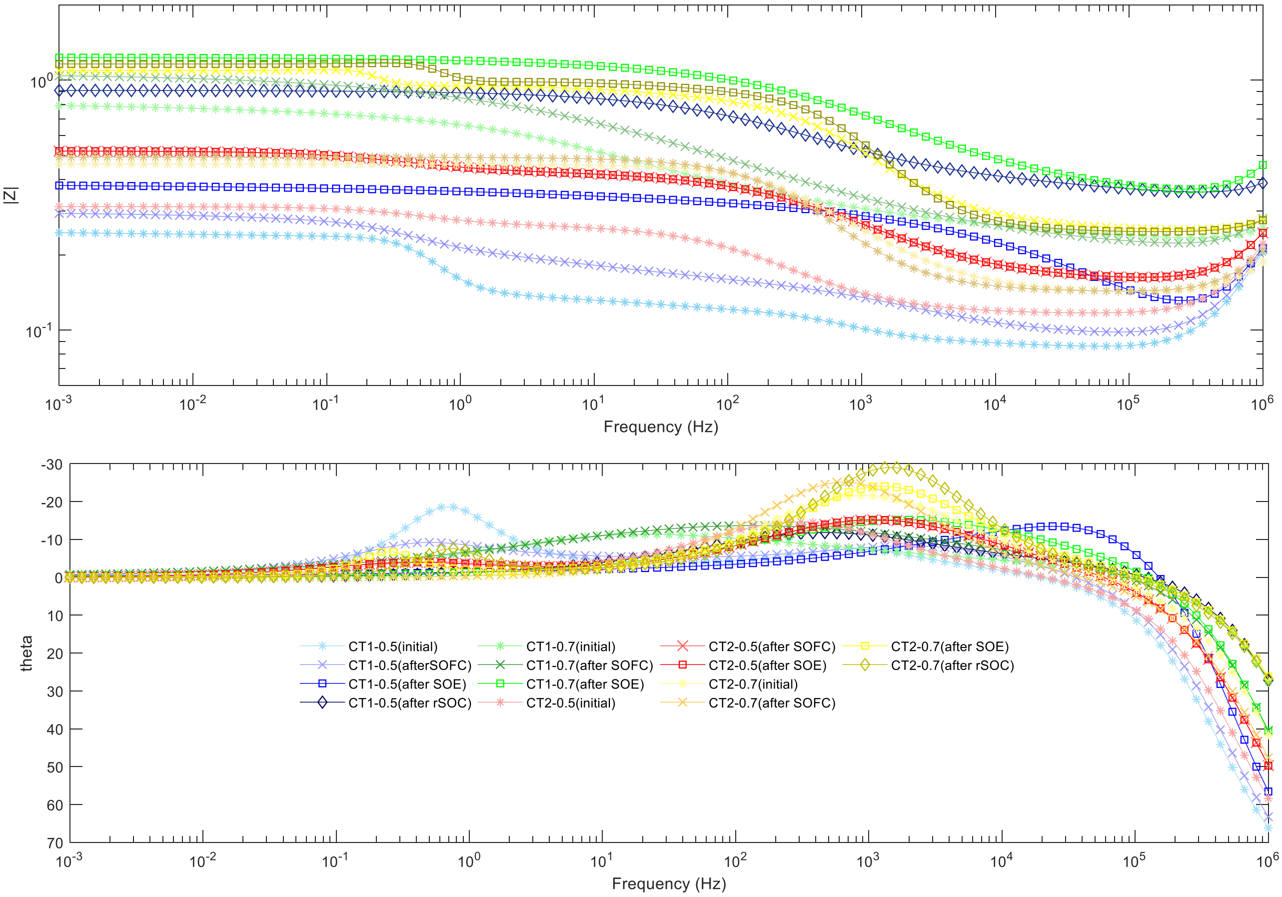

Figure 7-13: Bode comparison of cell types 1 and 2 at current densities of 0.5 A/cm^2 and 0.7 A/cm^2 (captured under SOFC conditions)

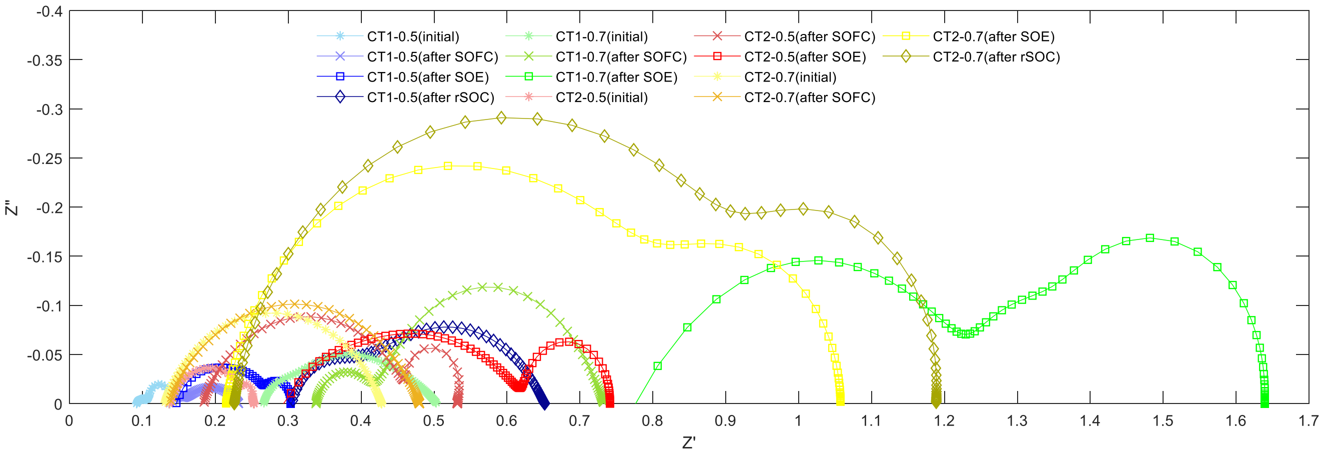

Figure 7-14: Nyquist comparison of cell types 1 and 2 at current densities of 0.5 A/cm2 and 0.7 A/cm2 (captured under SOE conditions)

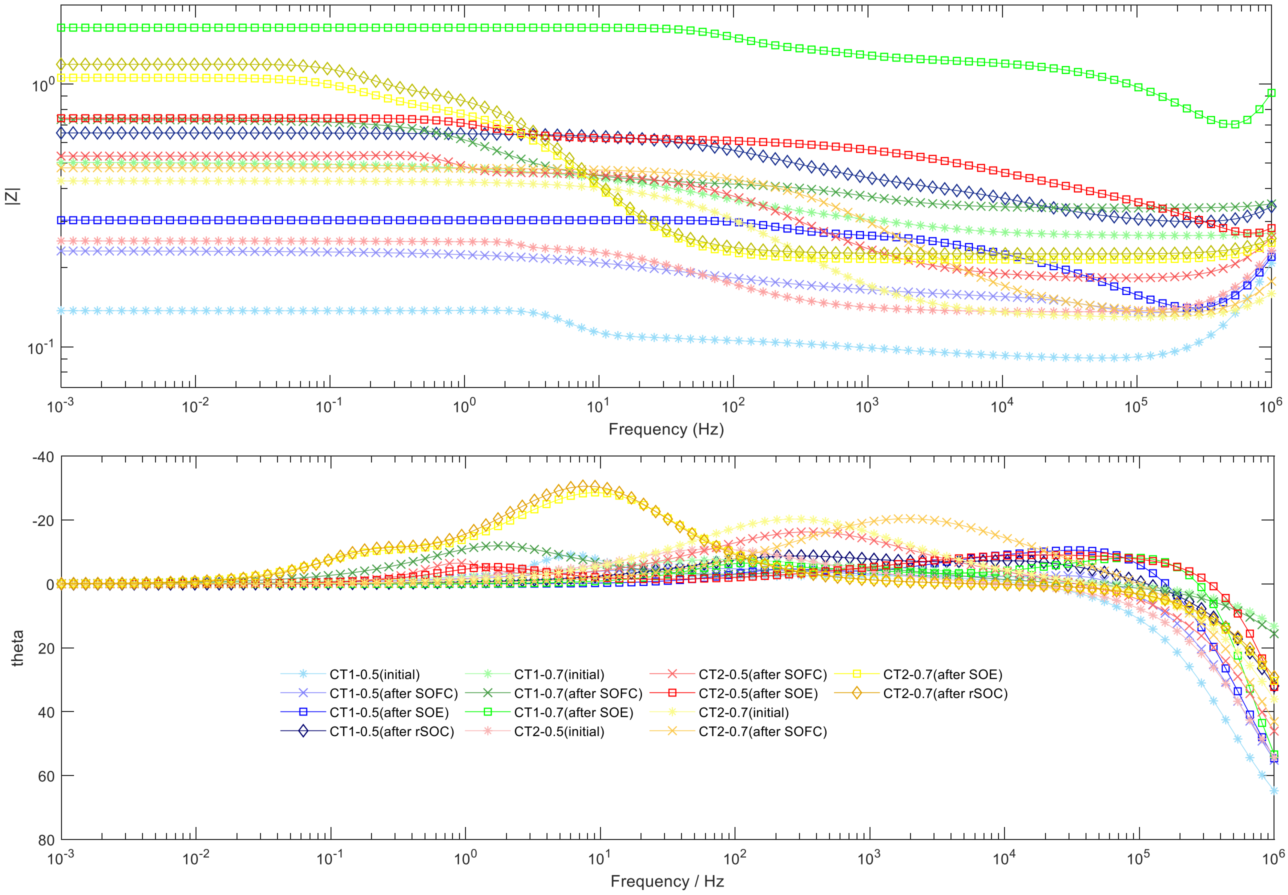

Figure 7-15: Bode comparison of cell types 1 and 2 at current densities of 0.5 A/cm^2 and 0.7 A/cm^2 (captured under SOE conditions)

7.3.2 Effect of Silver Paste Contacting on Overall Cell Resistance

This subsection compares the effect of silver paste contacting on the cell resistances at different current densities. Tests at 0.5 A/cm^2 and 0.7 A/cm^2 operating current density were performed without silver contacting, i.e. cell electrodes to current-collecters contacting relied on ‘dry thermal-bonding’ between the metallic connectors and cermet [Ni-YSZ] / ceramic[LSC-GDC] electrodes at 750°C operating temperature. For the tests at 1.25 A/cm^2, 1.39 A/cm^2 and 2.65 A/cm^2, silver paste was used to wet-bond the nickel and gold meshes to the fuel electrode and oxygen electrode, respectively.

Figure 7-16 and *Figure 7-17* show the j-V comparison of cell type 1 after operation at current densities of 0.5 A/cm^2 to 2.65 A/cm^2. Table 7-3 shows the ASR comparisons of the tests based on the j-V information shown in *Figure 7-16* and *Figure 7-17*. As already mentioned, the tests at 0.5 A/cm^2 and 0.7 A/cm^2 were performed without silver paste contacting. The tests at 1.25 A/cm^2 and 1.39 A/cm^2 and 2.65 A/cm^2 were perfomed with silver paste contacting. All the tests were conducted at an operating temperature of 750°C.

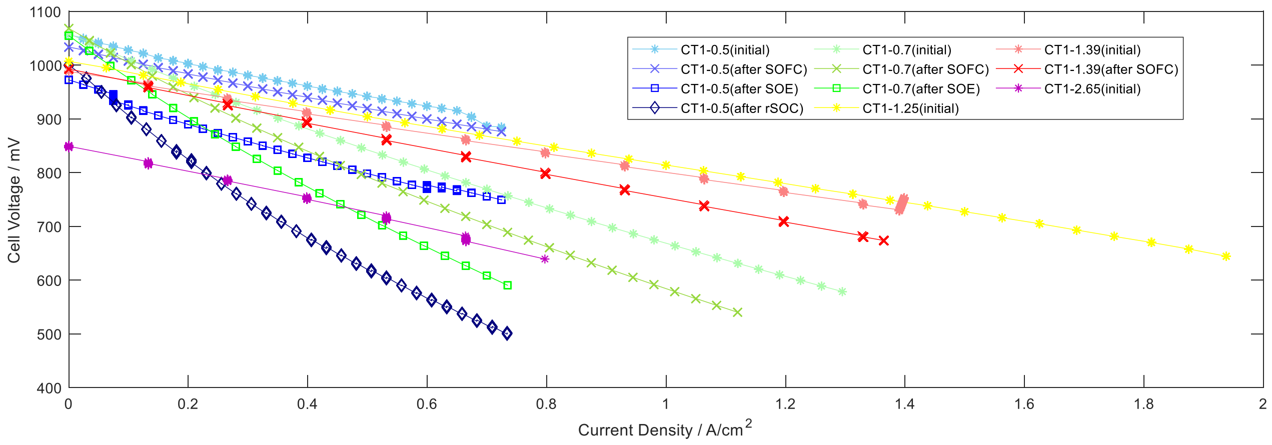

Figure 7-16: j-V comparison of cell type 1 at different current densities (captured under SOFC conditions)

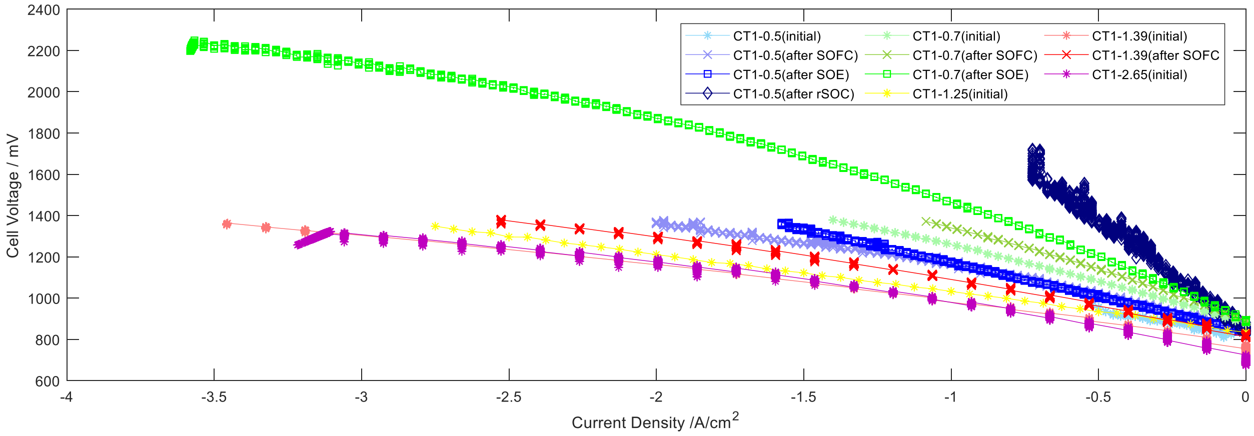

Figure 7-17: j-V comparison of cell type 1 at different current densities (captured under SOE conditions)

Compared to the tests carried out at 0.5 A/cm^2 and 0.7 A/cm^2 without silver contacting, the tests with silver contacting show significantly reduced cell resistances as represented by the ASR. This is even more pronounced when the tests at 1.25 A/cm^2, 1.39 A/cm^2 and 2.65 A/cm^2 are compared with the test carried out at 0.7 A/cm^2 without silver paste contacting. Due to Ohms law it was expected that the Ohmic component of the resistances across the cell would decrease with increasing current density since the test temperature is constant. However, the results presented in *Figure 7-16* to *Figure 7-22*, and *Table 7-3* indicate that this may apply only to Ohmic resistance contributions within the cell (with sound interfacial boundaries). The resistance contribution across the external boundary of the electrodes and mesh current collectors seem to increase with increasing current density (as can be seen from the 'initial' ASRs in *Table 7-3*). The Ohmic/series resistances (ionic and electronic) across the cell may be approximated as R1 (resistance across nickel current collecter and fuel electrode), R2 (resistance across fuel electrode to oxygen electrode), and R3 (resistance across oxygen electrode and gold current collector). R2 for the two types of tests reported in this subsection would be similar since they were done with similar cells from the same batch. However R1 and

R3 would be different for the tests without and with silver paste contacting. Therefore, since resistance is a function of both charge carrier density and time between collisions (basic Drude model), increasing the current density would cause electrons to “pile-up” at the electrode – current collector boundaries, hence decreasing the time between collisions and thereby increase R1 and R3. This would be more pronounced for tests with no silver paste bonding, as evidenced in *Figure 7-16* to *Figure 7-22*, and *Table 7-3* by the significant increase in resistance between tests at 0.5 A/cm^2 and 0.7 A/cm^2. This effect is less for cells with silver paste contacting.

Therefore, for long term rSOC operation, the type of bonding between the current collectors and electrodes have a significant effect on the overall cell performance. Overall resistances across the cell were lower, when silver paste was used to ‘wet-bond’ the current collectors to the electrodes. However, the long-term integrity of the bond was not verified.

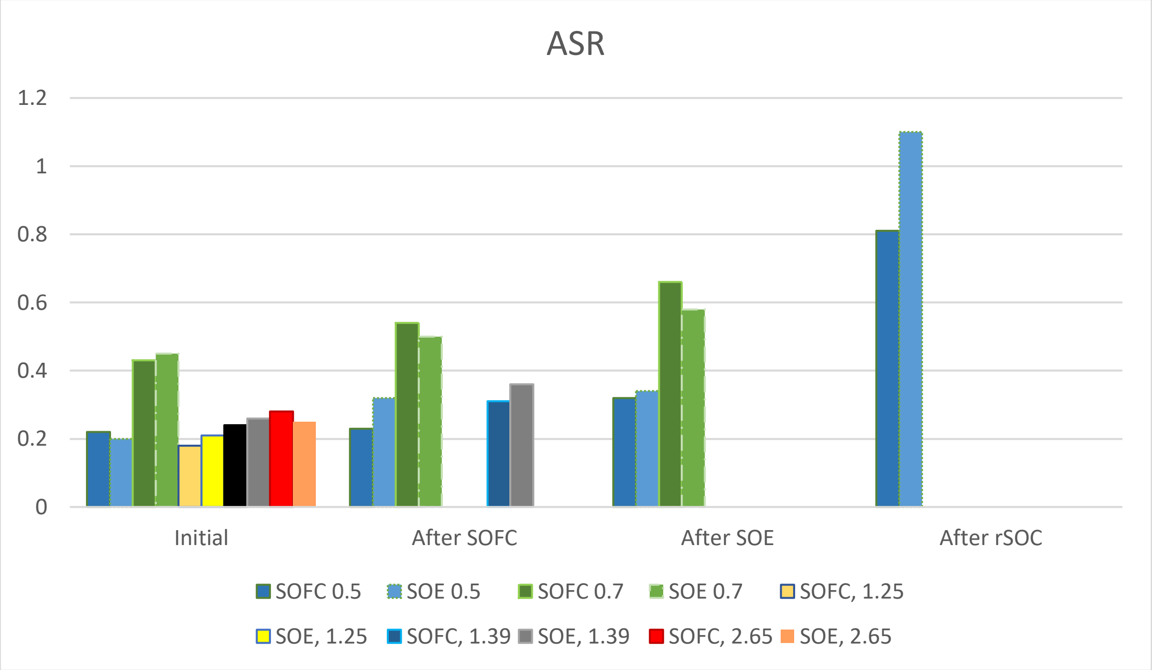

Figure 7-18: ASR comparison of cell types 1 and 2 at 750°C and 700°C (captured under SOFC and SOE conditions)

Table 7-3: ASR of cell type 1 tested at a temperature of 750°C and at different current densities

Parameter				Cell Type 1	
				Under SOFC Conditions (Ω-cm^2)	Under SOE Conditions (Ω-cm^2)
Cell Area Specific Resistance (ASR)	Without Silver Contacting (i.e. Dry-bonding)	@0.5 A/cm^2	Initial	0.22	0.2
			After SOFC	0.23	0.32
			After SOE	0.32	0.34
			After rSOC	0.81	1.1
		@0.7 A/cm^2	Initial	0.43	0.45
			After SOFC	0.54	0.50
			After SOE	0.66	0.58
			After rSOC	-	-
	With Silver Contacting	@1.25 A/cm^2	Initial	0.18	0.21
			After SOFC	-	-
			After SOE	-	-
			After rSOC	-	-
		@1.39 A/cm^2	Initial	0.24	0.26
			After SOFC	0.31	0.36
			After SOE	-	-
			After rSOC	-	-
		@2.65 A/cm^2	Initial	0.28	0.25
			After SOFC	-	-
			After SOE	-	-
			After rSOC	-	-
Dash (-) is used where the j-V characteristic of the cell could not be captured due to test failure.					

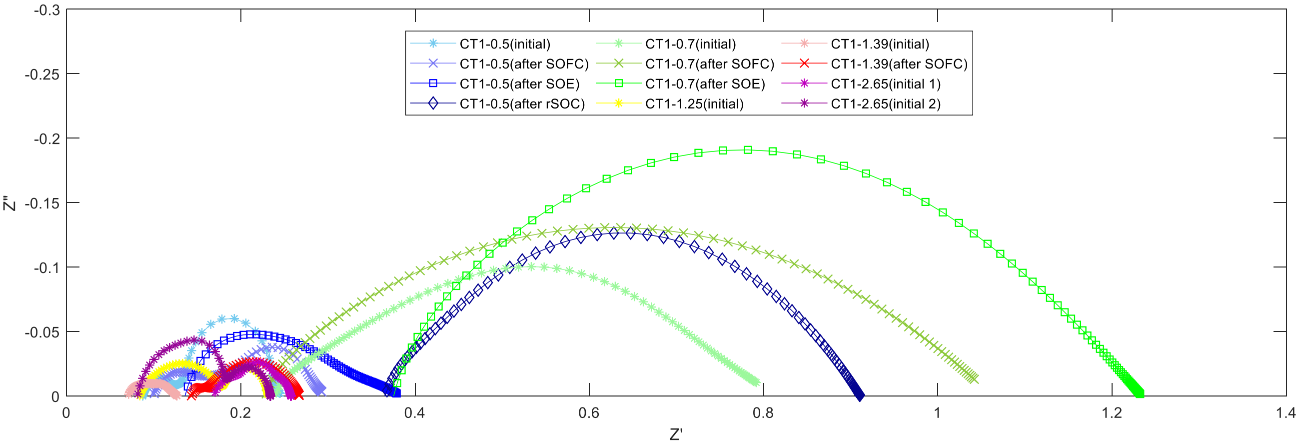

Figure 7-19: Nyquist comparison of cell type 1 at different current densities (captured under SOFC conditions)

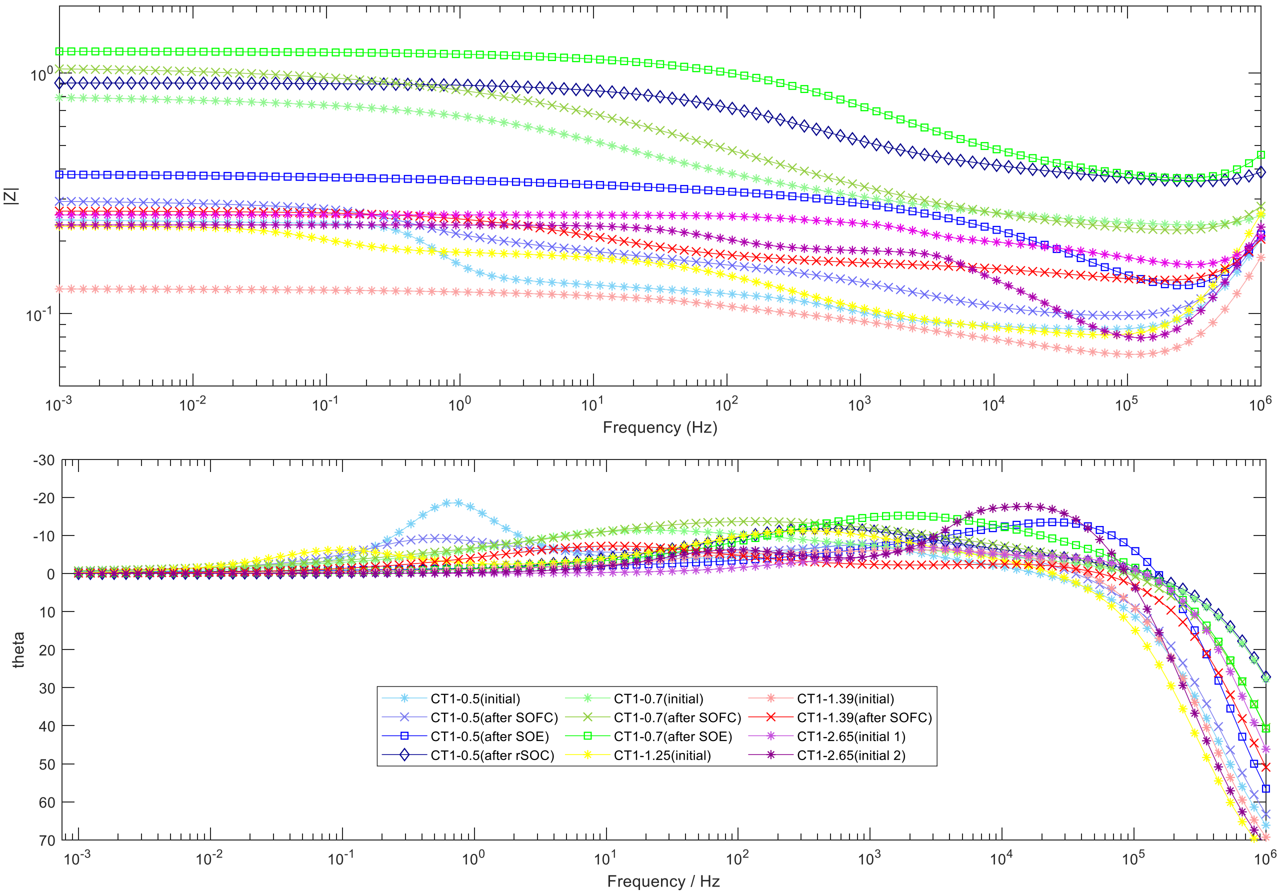

Figure 7-20: Bode comparison of cell type 1 at different current densities (captured under SOFC conditions)

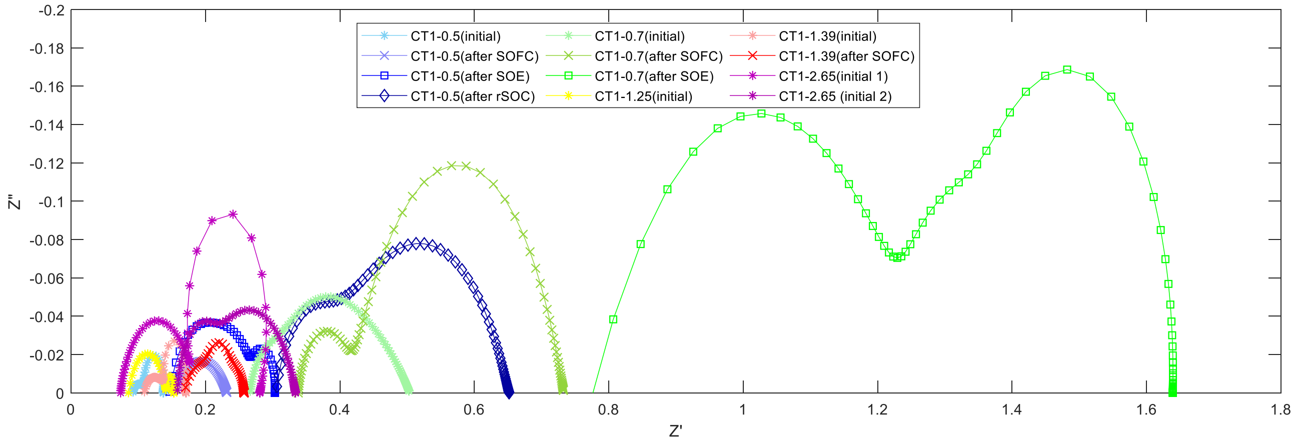

Figure 7-21: Nyquist comparison of cell type 1 at different current densities (captured under SOE conditions)

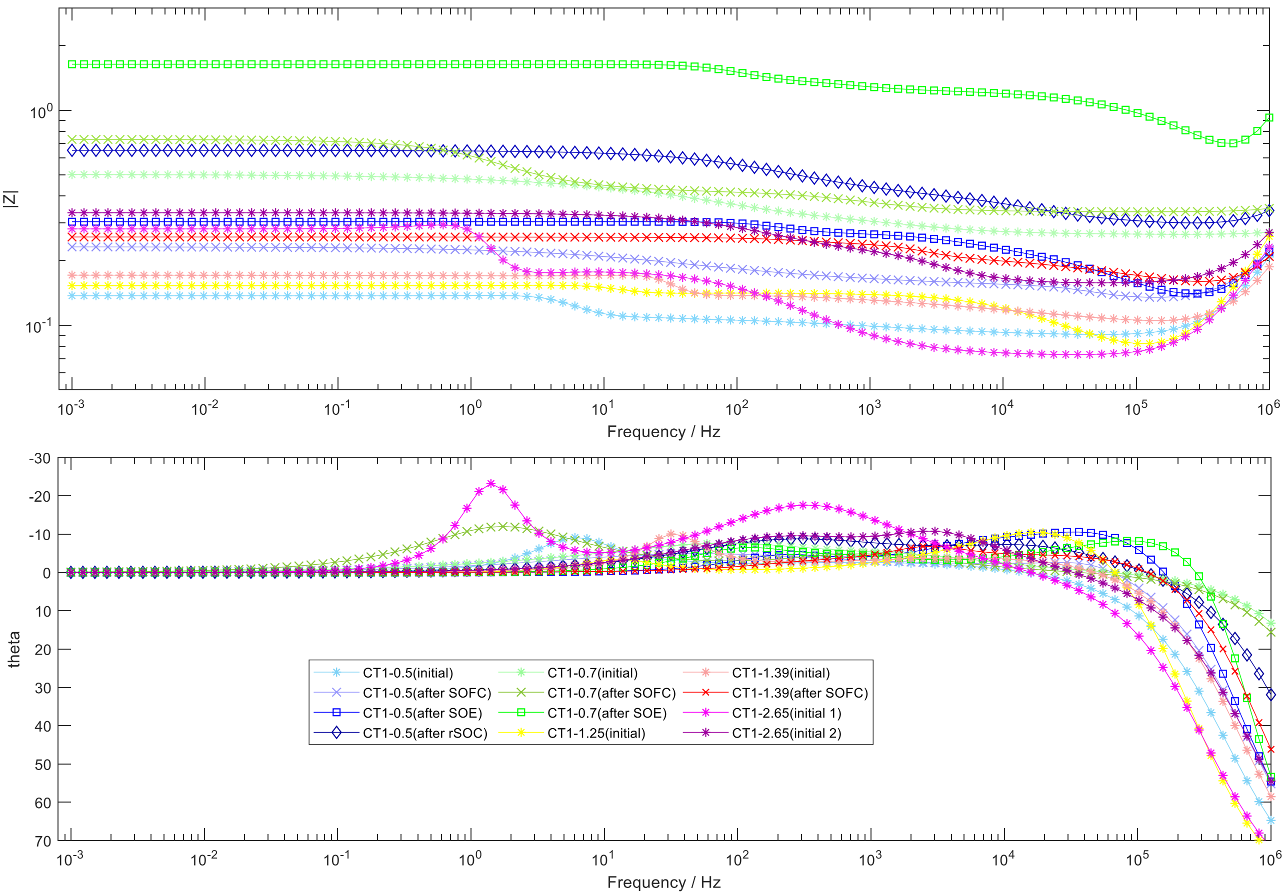

Figure 7-22: Bode comparison of cell type 1 at different current densities (captured under SOE conditions)

7.4 Effect of Fuel-Feed Parameters and Overall Fuel Utilisation

High peak power densities have been obtained by operating unit cells at low fuel electrode reactant utilisations [16]. However, operation at low fuel utilisations require an effective exhaust fuel reclamation system to prevent fuel waste and mitigate heat energy lossess [11]. Therefore, ideally, it is desirable to operate the rSOC system at high fuel utilisations. The fuel utilisation is defined as the ratio of the flow rate of electrons to the flow rate of hydrogen atoms (see Equations 3 – 1 to 3 – 3).

rSOCs may be operated at constant fuel utilisation by running the system under constant current density (galvanostatic) in both SOFC and SOE modes, and with defined fuel flow rates.

As explained in Section 3.3.3, fuel utilisation affects the mass transport of reactants and products, ionic transport of chemical species and electronic transport (see Equations 3 – 1 to 3 – 3). It was therefore hypothesised that at low fuel utilisations, the contributions of both electrode polarisation and electrolyte conduction to cell resistances would be low, and thus the overall cell degradation rate would be low. Conversely, at high fuel utilisations, due to the increased demands placed on both electrode mass transport and catalytic activity, and ionic transport through the electrolyte, as well as electron transfer rate through all relevant cell components, the cell degradation is more likely to be high due to the cell degradation mechanisms described in Section 3.2.

Therefore, fuel utilisations in accordance with were used in the work reported in this thesis. Since the fuel utilisation is the ratio of the molar flow of electrons over the molar flow of hydrogen atoms, it is significantly influenced by the operating current density. Therefore, similar to the discussion under Section 7.3, the cell degradation rate seems to increase with increasing magnitude of the fuel utilisation parameter (see *Table 7-2* and *Figure 7-11* for a comparison of the 52.3% and 73.2% fuel utilisations, equivalent to 0.5 A/cm^2 and 0.7 A/cm^2 operating current density and with a hydrogen flow of 35 ml/min in SOFC mode). This may be a result of the combined effect of both high atomic flux through the cell (higher induced pressure or stress at interphase and interface boundaries) and localised electrode fuel starvation (due to the higher electrode demand for fuel at high fuel utilisations).

7.5 Effect of Switching Time

During rSOC, after SOE operation, it took a significant time to establish steady-state fuel cell OCV for the subsequent SOFC operation. It took approximately ≥ 30 minutes to fully recover from SOE operation and establish a steady-state SOFC OCV (see *Figure 7-23*).

It is thus possible that switching straightaway from SOE to SOFC mode, without first establishing the steady-state SOFC OCV may negatively impact efficient cell operation. A preliminary investigation was therefore undertaken to study the effect of the switching time from SOE operation on cell performance during the subsequent SOFC operation (as indicated by cell voltages).

A similar delay was not observed when switching from SOFC to SOE operation (see *Figure 7-24*), which may be the case if the time taken to establish steady-state fuel cell OCV for the subsequent SOFC operation after SOE operation was a function of the time taken to establish a moisture-free SOFC test environment.

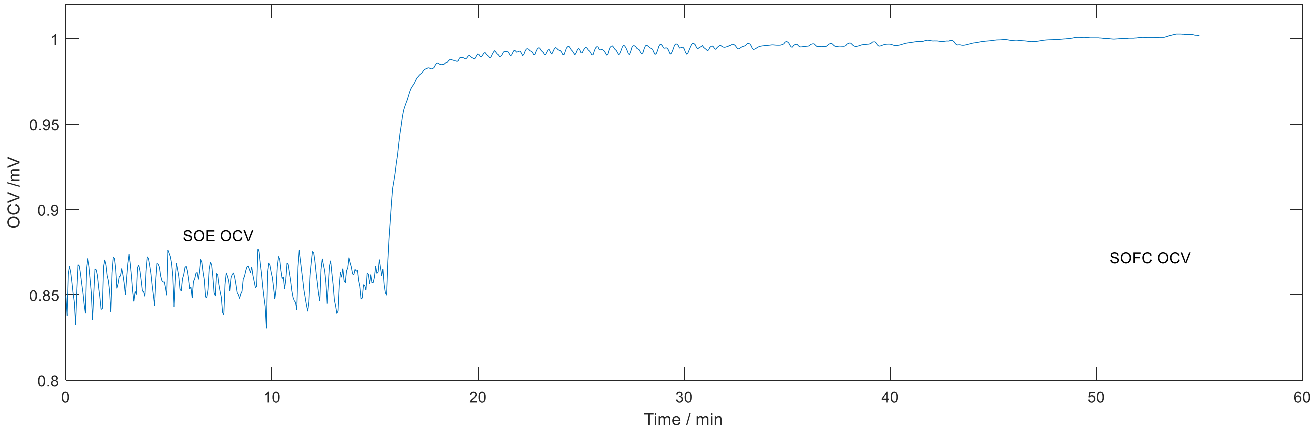

Figure 7-23: Time to establish steady state SOFC OCV after SOE operation

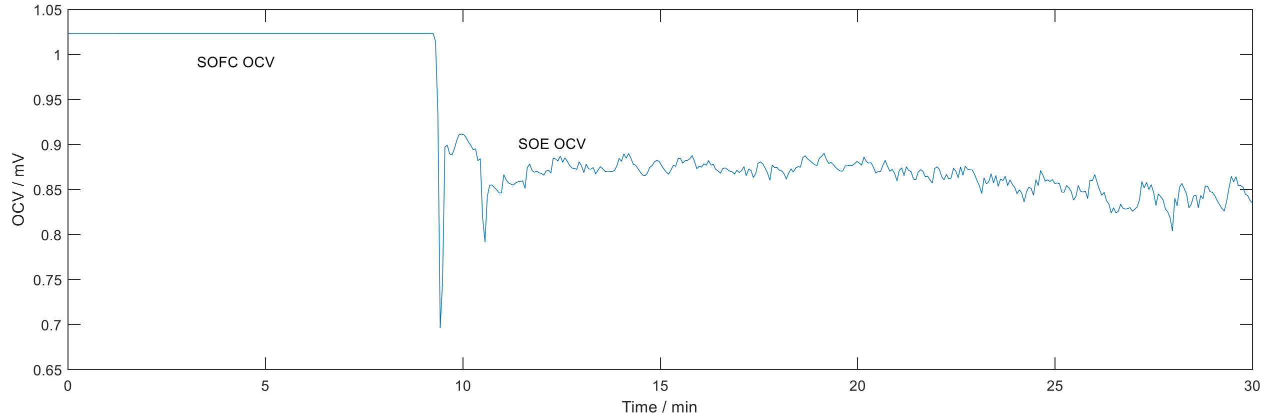

Figure 7-24: Time to establish steady state SOE OCV after SOFC operation

Ascertaining an optimum switching time from SOE to SOFC operation is important because:

1. It may potentially drive system-level design of rSOCs. If switching time influences cell performance, and the cells need to be idled for ≥30 mins under SOFC fuel flow in order to establish steady-state SOFC OCV, then rSOC systems need to be designed with a fuel reclamation/recycling system to mitigate fuel wastage.
2. It would be better to not have a mandatory delay between SOE operation to the start of SOFC operation, due to the obvious impact on system availability and flexibility.

3. If switching time influences cell performance, then the potential impacts of fuel wastage and system unavailability during the switching time needs to be quantified relative to the benefits of SOFC operation from a steady-state SOFC OCV.

For the purposes of this thesis, ‘steady-state SOFC OCV’ is defined as the OCV at the end of the previous SOFC cycle during rSOC. This is indicated as ‘OCV End’ in *Figure 7-25*. ‘OCV Start’ is the SOFC OCV after switching from SOE operation. Therefore ‘OCV Start’ of the next SOFC cycle equals ‘OCV End’ of the previous SOFC cycle at the minimum required switching time. *Figure 7-23* captures the switching time for cycle 30, and it may be noticed that the cell had still not reached its steady state OCV (i.e. ‘OCV End’ of cycle 29 which was 1020 mV) after 40 minutes. ‘CCV Start’ and ‘CCV End’ are the closed-circuit voltages, respectively, at the beginning and at the end of the SOFC operation. Therefore, the voltage sequence during operation is ‘OCV Start’ → ‘CCV Start’ → ‘CCV End’ → ‘OCV End’. The difference between ‘CCV End’ and ‘CCV Start’ is the cell performance recovery discussed under Section 5.2. The insert numbers in *Figure 7-25* are the switching times used prior to commencing the relevant SOFC operation after an SOE Operation.

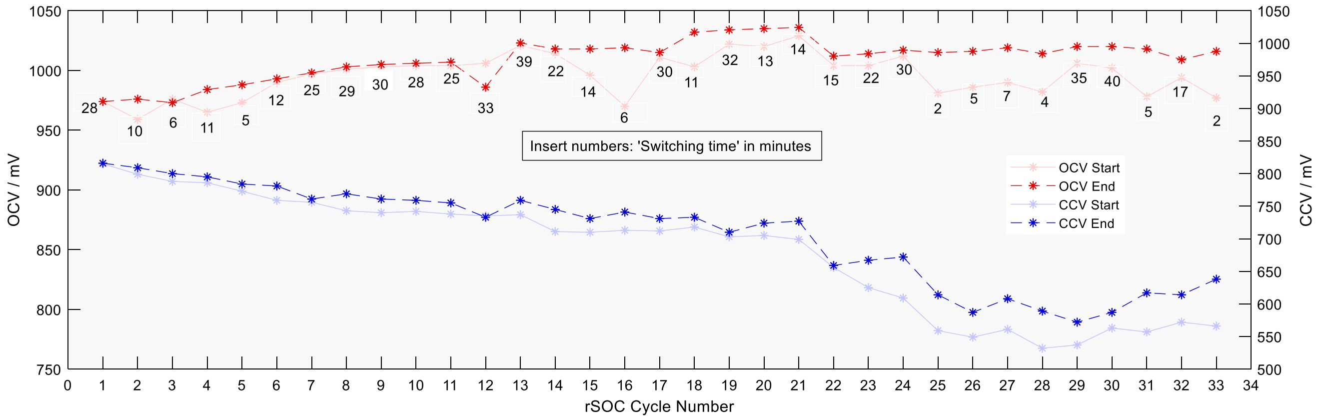

Figure 7-25: Effect of switching time from SOE operation to SOFC operation on SOFC voltages

It was expected that if switching time influences cell performance, then there would be significant decreases in both 'CCV Start' and 'CCV End' when SOFC operation is commenced prior to the cell reaching the steady-state OCV (i.e. the magnitude of 'CCV Start' would be lower relative to 'OCV End' of the previous cycle, whilst the magnitude of 'CCV End' would be lower relative to 'CCV Start'). However, a direct correlation could not be established (also see *Table 7-4* and *Figure 7-26*). Note that the significant drop in 'CCV Start' and 'CCV End' after cycle 21 was due to reactants starvation as mentioned in Section 5.2. In both *Figure 7-25* and *Table 7-4*, seemingly irrespective of switching time, the general trend was increasing voltage drop (difference between OCV and operating voltage) and voltage recovery (difference between operating voltage at the start and end of SOFC operation), with increasing cycle number. In any case, both the voltage drops, and voltage recoveries are more strongly linked to rSOC cycle number than any presently undiscernible link with switching time (if any).

The ≥30 minutes taken to reach steady-state SOFC OCV after SOE operation (see *Figure 7-25*) was most likely just the time required to evacuate the fuel electrode gas chamber of the SOE gas composition and establish the SOFC gas composition. Even though a direct correlation could not be established in this instance (*Figure 7-26*), it is still likely that switching time may have an effect on cell performance which a more exhaustive study may tease out.

Table 7-4: Effect of switching time on voltage drop and voltage recovery during SOFC operation

rSOC Cycle Number	Switching Time[1] (mins)	Difference between 'OCV Start' and 'CCV start' (ΔV)[2]	Difference between 'CCV End' and 'CCV Start' (ΔCCV)[3]
1	28	159	1
2	10	160	10
3	6	188	12
4	11	179	9

rSOC Cycle Number	Switching Time[1] (mins)	Difference between 'OCV Start' and 'CCV start' (ΔV)[2]	Difference between 'CCV End' and 'CCV Start' (ΔCCV)[3]
5	5	200	11
6	12	231	22
7	25	241	5
8	29	258	26
9	30	263	21
10	28	262	17
11	25	266	17
12	33	271	-2
13	39	284	22
14	22	303	34
15	14	286	21
16	6	257	28
17	30	299	19
18	11	285	15
19	32	319	7
20	3	315	19
21	4.4	330	28
22	5	348	3
23	22	379	42
24	30	403	63
25	2	422	55
26	5	437	38
27	7	429	47
28	4	450	57
29	35	469	35
30	40	439	24
31	5	421	60
32	17	422	42
33	2	411	72

rSOC Cycle Number	Switching Time[1] (mins)	Difference between 'OCV Start' and 'CCV start' (ΔV)[2]	Difference between 'CCV End' and 'CCV Start' (ΔCCV)[3]

1. Switching time is the amount of time allowed for the cell to idle under SOFC fluid flow at 0 current density. After SOE operation, ≥30 mins switching time was required for the cell to reach steady-state OCV. The switching times in red font are the times significantly below the observed 30 minutes minimum threshold.
2. ΔV is the voltage difference between the open cell voltage and the operating voltage at the required operating current density. Significant voltage drops indicate poor performance. Voltage drops in red font are significant increases (poorer performance) relative to the voltage drop of the preceding SOFC cycle. Voltage drops in green font are significant decreases (improved performance) relative to the voltage drop of the preceding SOFC cycle.
3. ΔCCV is the difference in operating voltage at the beginning and end of the SOFC operation. Positive values indicate performance recovery whilst negative values indicate performance degradation. Voltage recoveries in green font indicate significant performance recoveries. However, note that this generally correlated very well with significantly worse performance deterioration during the preceding SOE cycle as illustrated in Section 5.2.

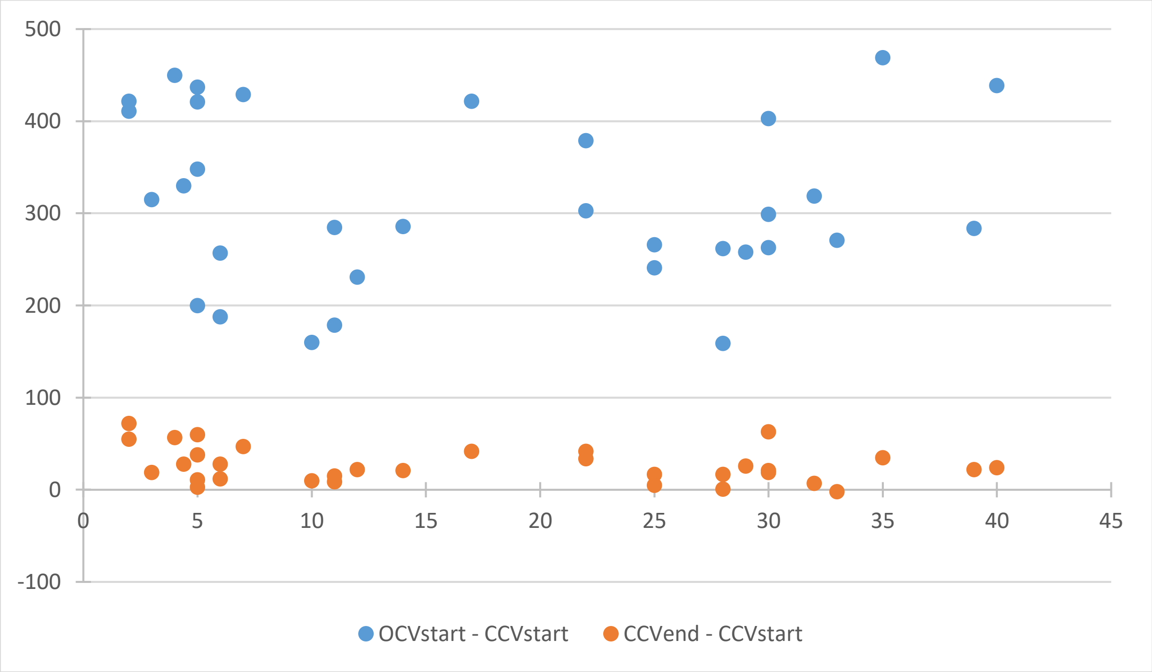

Figure 7-26: No discernible effect of switching time on voltage drop and voltage recovery during SOFC operation

8 SUMMARY AND OUTLOOK

8.1 Technology Relevance

The world is increasingly committing to a green energy future. However, to ensure transition of the energy landscape with relatively minimal disruptions, energy storage technologies are required. This is mainly because of the cyclical nature of the major and most promising green energy generators (solar and wind power generators). rSOC is an energy storage technology of significant promise. This device is able to operate in fuel cell mode (SOFC) to convert chemical energy to electrical energy, and operate in electrolyser mode (SOE) to convert electrical energy back to chemical energy. Generally, although SOFC and SOE are electrochemically reversible, this reversibility is not seamless. There seem to be appreciable differences in cell performance relative to the mode and parameters of operation.

8.2 Summary of Work

A rSOC test apparatus was designed and tests were performed in constant SOFC, constant SOE and cyclic rSOC mode. State of the art cells designed for rSOC operation, i.e. with oxygen electrode architectures fine-tuned for optimum reversibility, were tested at intermediate temperatures of 700^{o}C and 750^{o}C, and at current densities ranging from 0.5 A/cm^2 to 2.65 A/cm^2. The main highlights of the research work are as follows:

1. It was observed that cell performance losses increased with decreasing temperature and increasing current density. However, it seems that performance losses are more

strongly correlated with current density increases than with temperature decreases in all operating modes (SOFC, SOE and rSOC) within the range of parameters tested.

2. A comparison of two different types of cells tested at temperatures of 700°C and 750°C, as well as operating current densities of 0.5 A/cm^2 and 0.7 A/cm^2, was summarised in *Table 7-1* and *Figure 7-4*, and *Table 7-2* and *Figure 7-11*, respectively. It showed that for the virgin cell, the ASR increased from 0.22 Ω.cm^2 to 0.28 Ω.cm^2 with respect to temperature decrease (i.e. at 750°C and 700°C, respectively), but increased from 0.22 Ω.cm^2 to 0.43 Ω.cm^2 with respect to current density increase (i.e. at 0.5 A/cm^2 and 0.7 A/cm^2, respectively). Similar differences were noted for the cell after 120 hours of constant SOFC operation, 120 hours of constant SOE operation, and after rSOC operation with 33 cycles (3 hours SOFC followed by 20 hours SOE).
3. Similar to the operating current density, cell degradation also seemed to be strongly correlated with fuel utilisation (which is a function of both current density and reactant flow rates). The cell degradation rate increased with increasing magnitude of fuel utilisation. This may be as a result of the combined effect of both high atomic flux through the cell (higher induced pressure or stress at interphase boundaries and cell component interfaces) and localised electrode fuel starvation (due to the higher electrode demand for fuel at high fuel utilisations).
4. As already reported in the literature [5], [81], [134], [135], it was also observed in this study that cell degradation during SOE operation was generally more than double the degradation during SOFC mode.

5. It had also been reported in the literature [66] that degradation could be eliminated in solid oxide electrochemical cells by reversible operation. The present work confirmed this and observed some degradation recovery under the subsequent SOFC mode operation after SOE operation during reversible cycling (i.e. rSOC operation). Prior to the cell suffering extensive irreversible damage (noted as a delamination at the oxygen electrode / electrolyte interface in the present work), the magnitude of voltage recoveries were about 40% of the voltage losses during the preceding SOE mode operation. It is therefore proposed that although degradation could ultimately be eliminated in SOCs by reversible operation, the extent of the reversal seems to be subject to the relative duration of SOFC and SOE mode operation. When a rSOC cycling period of 1 hr SOE followed by 5 hrs SOFC was utilised [66], complete recovery was observed, whilst the work presented in this thesis utilised a rSOC cycling period of 20 hrs SOE followed by 3 hrs SOFC and noted 40% recovery. Since the significant promise of the rSOC technology lies in its great potential as an energy storage device, it is more desirable to use cycling periods which maximise its energy storage potential (i.e. longer operation in SOE mode relative to SOFC mode as done for this thesis). The cycling period used in this work, 20 hrs SOE followed by 3 hrs SOFC, is expected to be the most conservative rSOC operational scenario relative to the typical trend in electric energy output of the most promising renewable power generators (i.e. solar and wind power).
6. The effect of switching parameters (and associated transient processes during switching) on cell performance was also studied. It was observed that, during rSOC cycling, after SOE mode operation, the cell took about 30 minutes to recover to the SOFC cell voltage prior to the SOFC mode operation. During rSOC cycling, in order to study the

effects of switching time on cell performance, some SOFC mode operations were commenced without waiting for the cell to recover to SOFC OCV. No discernible effect of the switching time on subsequent cell performance was apparent.

8.3 Research Area Outlook

To fully optimise the rSOC technology, the effect of several other variables need to be ascertained:

1. The mode switching for the current work was carried out using a current density ramp rate of 10% of the operating current density per minute. Therefore, even without operating the cell under OCV conditions to fully recover during switching from fuel cell to electrolysis mode, and vice versa, a minimum of 20 minutes was required to fully switch over from one mode to the other. This is obviously not ideal if the technology would also be used for grid-balancing. For the grid-balancing scenario, instead of the technology seamlessly producing power based on instantaneous grid-demand, a time-lag of at least 20 minutes would need to be accommodated for in order not to incur unnecessary potential damage to the cell life. Therefore, more work should be done to understand the effects on the cell of instantaneous or near instantaneous switches to the operating current density without current density ramping via OCV.
2. Thermodynamic modelling of the entire process to understand the fundamental reaction mechanisms, operating regimes, energy requirements/dependencies, etc., would be required to optimise the rSOC operating parameters.

9 REFERENCES

[1] [Online]. Available: https://ec.europa.eu/energy/en/topics/energy-strategy-and-energy-union/2050-energy-strategy. [Accessed 8 July 2021].

[2] "Energy Roadmap 2050," April 2010. [Online]. Available: http://www.roadmap2050.eu/. [Accessed 15 February 2019].

[3] [Online]. Available: https://ec.europa.eu/research/participants/documents/. [Accessed 08 September 2021].

[4] "Climate Action," December 2015. [Online]. Available: http://www.cop21paris.org/. [Accessed 16 October 2020].

[5] M. C. H. F. C. G. J. H. K. H. A. H. T. J. S. J. T. S. a. X. S. M.B. Mogensen, "Reversible solid-oxide cells for clean and sustainable energy," *Clean energy,* vol. 3, no. 3, pp. 175 - 201, 2019.

[6] [Online]. Available: https://en.wikipedia.org/wiki/List_of_countries_by_proven_oil_reserves. [Accessed 20 April 2020].

[7] G. G. Botte, "Electrochemical Manufacturing in the Chemical Industry," *The Electrochemical Society Interface,* vol. 23, no. 3, pp. 49-55, 2014.

[8] [Online]. Available: https://en.wikipedia.org/wiki/Electrochemistry. [Accessed 22 June 2021].

[9] V. K. M. Paidar, "Membrane electrolysis—History, current status and perspective," *Electrochimica Acta,* vol. 209, pp. 737-756, 2016.

[10] S. D. E. M. M. K. S. L. Christopher Graves, "Sustainable hydrocarbon fuels by recycling CO2 and H2O with renewable or nuclear energy," *Renewable and Sustainable Energy Reviews,* vol. 15, no. 1, pp. 1 - 23, 2011.

[11] Y. S. K. Y. D. L. K. Y. A. Van-Tien Giap, "Waste heat utilization in reversible solid oxide fuel cell systems for electrical energy storage: Fuel recirculation design and feasibility analysis," *Journal of Energy Storage,* vol. 29, no. 101434, 2020.

[12] M. Mogensen, S. H. Jensen, S. D. Ebbesen, A. Hauch, C. Graves, J. V. T. Høgh, X. Sun, S. Das, P. V. Hendriksen, J. U. Nielsen, A. H. Pedersen, N. Christiansen and a. J. B. Hansen, "Natural Gas and Renewables," in *25th World Gas Conference*, Kuala Lumpur, Malaysia, 2012.

[13] S. Singhal, "Advances in solid oxide fuel cell technology," *Solid State Ionics,* vol. 135, pp. 305-313, 2000.

[14] [Online]. Available: https://www.j-lpgas.gr.jp/en/appliances/index.html#ENE-FARM. [Accessed 21 February 2021].

[15] H2FC SUPERGEN, "Opportunities for Hydrogen and Fuel Cell Technologies to Contribute to Clean Growth in the UK," The Hydrogen and Fuel Cell Research Hub, London, 2020.

[16] N. Q. Minh and M. B. Mogensen, “Reversible Solid Oxide Fuel Cell Technology for Green Fuel and Power Production,” *The Electrochemical Society,* vol. 22, no. 4, pp. 55-62, 2013.

[17] C. M. Stoots, J. E. O’Brien, K. G. Condie and J. J. Hartvigsen, “High-temperature electrolysis for large-scale hydrogen production from nuclear energy - Experimental investigations,” *International Journal of Hydrogen Energy,* vol. 35, no. 10, pp. 4861-4870, 2010.

[18] S. D. Ebbesen, J. Høgh, K. A. Nielsen, J. U. Nielsen and M. Mogensen, “Durable SOC stacks for production of hydrogen and synthesis gas by high temperature electrolysis,” *International Journal of Hydrogen Energy,* vol. 36, no. 13, pp. 7363-7373, 2011.

[19] F. Bidrawn, G. Kim, G. Corre, J. T. S. Irvine, J. M. Vohs and R. J. Gortea, “Efficient Reduction of CO2 in a Solid Oxide Electrolyzer,” *Electrochemical and Solid-State Letters,* vol. 11, no. 9, pp. B167-B170, 2008.

[20] S. D. Ebbesen and M. Mogensen, “Electrolysis of carbon dioxide in Solid Oxide Electrolysis Cells,” *Journal of Power Sources,* vol. 193, no. 1, pp. 349-358, 2009.

[21] C. Graves, S. D. Ebbesen and M. Mogensen, “Co-electrolysis of CO2 and H2O in solid oxide cells: Performance and durability,” *Solid State Ionics,* vol. 192, pp. 398-403, 2011.

[22] P. Kim-Lohsoontorn and J. Bae, “Electrochemical performance of solid oxide electrolysis cell electrodes under high-temperature coelectrolysis of steam and carbon dioxide,” *Journal of Power Sources,* vol. 196, pp. 7161-7168, 2011.

[23] M. C. H. L. F. C. G. J. B. H. K. V. H. A. H. T. J. S. H. J. T. L. S. X. S. M B Mogensen, “Reversible solid-oxide cells for clean and sustainable energy,” *Clean Energy,* vol. 3, no. 3, pp. 175 - 201, 2019.

[24] US Department of Energy, “Report on the Status of the Solid Oxide Fuel Cell Program,” Report to Congress, Washington, 2009.

[25] NELLHI, [Online]. Available: http://www.nellhi.eu/sofc. [Accessed 21 February 2021].

[26] K. Eguchi, T. Hatagishi and H. Arai, “Power generation and steam electrolysis characteristics of an electrochemical cell with zirconia- or ceria-based electrolyte,” *Solid State Ionics,* Vols. 86-88, no. Part 2, pp. 1245-1249, 1996.

[27] GE Global Research Center, “High Performance Flexible Reversible Solid Oxide Fuel Cell,” US Dept of Energy, Golden, CO, 2006.

[28] A. Hauch, S. D. Ebbesen, S. H. Jensen and M. Mogensen, “Solid Oxide Electrolysis Cells: Microstructure and Degradation of the Ni/Yttria-Stabilized Zirconia Electrode,” *Journal of the Electrochemical Society,* vol. 155, no. 11, pp. B1184-B1193, 2008.

[29] [Online]. Available: https://ec.europa.eu/energy/topics/technology-and-innovation/strategic-energy-technology-plan_en#documents. [Accessed 29 November 2020].

[30] [Online]. Available: https://www.ewea.org/wind-energy-basics/faq/. [Accessed 2 December 2020].

[31] M. B. Mogensen, “Materials for reversible solid oxide cells,” *Current Opinion in Electrochemistry,* vol. 21, pp. 265-273, 2020.

[32] M. Laguna-Bercero, “Recent advances in high temperature electrolysis using solid oxide fuel cells: A review,” *Journal of Power Sources,* vol. 203, pp. 4-16, 2012.

[33] Y. Tao, H. Nishino, S. Ashidate, H. Kokubo, M.Watanabe and H. Uchida, “Polarization properties of La0.6Sr0.4Co0.2Fe0.8O3-based double layer-type oxygen electrodes for reversible SOFCs,” *Electrochimica Acta,* vol. 54, no. 12, pp. 3309-3315, 2009.

[34] M. A. Laguna-Bercero, N. Kinadjan, R. Sayers, H. E. Shinawi, C. Greaves and S. J. Skinner, “Performance of La(2-x)Sr(x)Co(0.5)Ni(0.5)O(4+delta) as an Oxygen Electrode for Solid Oxide Reversible Cells,” *Fuel Cells,* vol. 11, no. 1, pp. 102-107, 2010.

[35] B. Molero-Sánchez, P. Addo, A. Buyukaksoy, S. Paulson and V. Birss, “Electrochemistry of La0.3Sr0.7Fe0.7Cr0.3O3-[small delta] as an oxygen and fuel electrode for RSOFCs,” *Faraday Discussions,* vol. 182, pp. 159-175, 2015.

[36] N. Ai, K. Chen, S. Liu and S. Jiang, “Performance and stability of nano-structured Pd and Pd0.95M0.05 (M = Mn, Co, Ce, and Gd) infiltrated Y2O3–ZrO2 oxygen electrodes of solid oxide electrolysis cells,” *International Journal of Hydrogen Energy,* vol. 38, no. 36, pp. 16569-16578, 2013.

[37] C. Bernuy-Lopez, R. Knibbe, Z. He, X. Mao, A. Hauch and K. Nielsen, “Electrochemical characterisation of solid oxide cell electrodes for hydrogen production,” *Journal of Power Sources,* vol. 196, no. 9, pp. 4396-4403, 2011.

[38] L. Bi, S. Boulfrad and E. Traversa, “Reversible solid oxide fuel cells (R-SOFCs) with chemically stable proton-conducting oxides,” *Solid State Ionics,* vol. 275, pp. 101-105, 2015.

[39] F. Chauveau, J. Mougin, J. M. Bassat, F. Mauvy and J. C. Grenier, “A new anode material for solid oxide electrolyser: The neodymium nickelate Nd2NiO(4+delta),” *Journal of Power Sources,* vol. 195, no. 3, pp. 744-749, 2010.

[40] K. Chen, N. Ai and S. Jiang, “Enhanced electrochemical performance and stability of (La,Sr)MnO3–(Gd,Ce)O2 oxygen electrodes of solid oxide electrolysis cells by palladium infiltration,” *International Journal of Hydrogen Energy,* vol. 37, no. 2, pp. 1301-1310, 2012.

[41] K. Chen, N. Ai and S. Jiang, “Performance and stability of (La,Sr)MnO3–Y2O3–ZrO2 composite oxygen electrodes under solid oxide electrolysis cell operation conditions,” *International Journal of Hydrogen Energy,* vol. 37, pp. 10517-10525, 2012.

[42] K. Chen, N. Ai and S. Jiang, “Reasons for the high stability of nano-structured (La,Sr)MnO3 infiltrated Y2O3–ZrO2 composite oxygen electrodes of solid oxide electrolysis cells,” *Electrochemistry Communications,* vol. 19, pp. 119-122, 2012.

[43] M. Chen, S. Paulson, V. Thangadurai and V. Birss, “Sr-rich chromium ferrites as symmetrical solid oxide fuel cell electrodes,” *Journal of Power Sources,* vol. 236, pp. 68-79, 2013.

[44] X. Z. J. C. L. P. Jia Xu, “Electrochemical performance of highly active ceramic symmetrical electrode La0.3Sr0.7Ti0.3Fe0.7O3-δ-CeO2 for reversible solid oxide cells,” *Electrochimica Acta,* vol. 257, pp. 64-72, 2017.

[45] Y. L. Q. W. C. S. X. Y. Z. W. Shaojing Yang, “Effects of porous support microstructure enabled by the carbon microsphere pore former on the performance of proton-conducting reversible solid oxide cells,” *International Journal of Hydrogen Energy,* vol. 43, no. 43, pp. 20050-20058, 2018.

[46] N. W. J. C. J. W. Jun Zhou, “Structural and electrochemical properties of B-site Ru-doped (La0.8Sr0.2)0.9Sc0.2Mn0.8O3-δ as symmetrical electrodes for reversible solid oxide cells,” *Journal of Alloys and Compounds,* vol. 792, pp. 1132-1140, 2019.

[47] C. L. S. L. Liuzhen Bian, “Highly stable La0.5Sr0.5Fe0.9Mo0.1O3-δ electrode for reversible symmetric solid oxide cells,” *International Journal of Hydrogen energy,* vol. 45, no. 38, pp. 19813-19822, 2020.

[48] S. Elangovan, J. Hartvigsen and L. Frost, “Intermediate temperature reversible fuel cells,” *International Journal of Applied Ceramic Technology,* vol. 4, no. 2, pp. 109-118, 2007.

[49] B. Ge, J. Ma, D. Ai, C. Deng, X. Lin and J. Xu, “Sr2FeNbO6 Applied in Solid Oxide Electrolysis Cell as the Hydrogen Electrode: Kinetic Studies by Comparison with Ni-YSZ,” *Electrochimica Acta,* vol. 151, pp. 437-446, 2015.

[50] F. He, D. Song, R. Peng, G. Meng and S. Yang, “Electrode performance and analysis of reversible solid oxide fuel cells with proton conducting electrolyte of BaCe(0.5)Zr(0.3)Y(0.2)O(3-delta),” *Journal of Power Sources,* vol. 195, no. 11, pp. 3359-3364, 2010.

[51] P. Kim-Lohsoontorn, D. Brett, N. Laosiripojana, Y. Kim and J. Bae, “Performance of solid oxide electrolysis cells based on composite La0.8Sr0.2MnO3-δ – yttria stabilized zirconia and Ba0.5Sr0.5Co0.8Fe0.2O3-δ oxygen electrodes,” *International Journal of Hydrogen Energy,* vol. 35, no. 9, pp. 3958-3966, 2010.

[52] Y. Z. Z. C. K. C. S. P. J. Na Ai, “Progress on direct assembly approach for in situ fabrication of electrodes of reversible solid oxide cells,” *Materials Reports: Energy,* vol. 1, no. 2, 2021.

[53] Q. Liu, C. Yang, X. Dong and F. Chen, “Perovskite Sr2Fe1.5Mo0.5O6-δ as electrode materials for symmetrical solid oxide electrolysis cells,” *Internal Journal of Hydrogen Energy,* vol. 35, no. 19, pp. 10039-10044, 2010.

[54] O. Marina, L. Pederson, M. Williams, G. Coffey, K. Meinhardt, C. Nguyen and E. Thomsen, “Electrode performance in reversible solid oxide fuel cells,” *Journal of the Electrochemical Society,* vol. 154, no. 5, pp. B452-B459, 2007.

[55] B. Molero-Sánchez, J. Prado-Gonjal, D. Ávila-Brande, M. Chen, E. Morán and V. Birss, “High performance La0.3Ca0.7Cr0.3Fe0.7O3−δ air electrode for reversible solid oxide fuel cell applications,” *International Journal of Hydrogen Energy,* vol. 40, no. 4, pp. 1902-1910, 2015.

[56] A. V. Virkar and G. Tao, “Reversible high temperature cells for power generation and hydrogen production using mixed ionic electronic conducting solid electrolytes,” *International Journal of Hydrogen Energy,* vol. 40, no. 16, pp. 5561-5577, 2015.

[57] B. Zhu, I. Albinsson, C. Andersson, K. Borsand, M. Nilsson and B. E. Mellander, “Electrolysis studies based on ceria-based composites,” *Electrochemistry Communications,* vol. 8, no. 3, pp. 497-498, 2006.

[58] S. C. Singhal and K. Kendall, High |Temperature Solid Oxide Fuel Cells: Fundamentals, Design, and Applicatons, Oxford: Elsevier Limited, 2003.

[59] A. V. Virkar, “Mechanism of oxygen electrode delamination in solid oxide electrolyzer cells,” *International Journal of Hydrogen Energy,* vol. 35, no. 18, pp. 9527-9543, 2010.

[60] O. Yamamoto, Y. Arati, Y. Takeda, N. Imanishi, Y. Mizutani, M. Kawai and Y. Nakamura, “Electrical conductivity of stabilized zirconia with ytterbia and scandia,” *Solid State Ionics,* vol. 79, pp. 137-142, 1995.

[61] M. Laguna-Bercero, S. Skinner and J. Kilner, “Performance of solid oxide electrolysis cells based on scandia stabilised zirconia,” *Journal of Power Sources,* vol. 192, pp. 126-131, 2009.

[62] G. Wu, K. Xie, Y. Wu, W. Yao and J. Zhou, “Electrochemical conversion of H2O/CO2 to fuel in a proton-conducting solid oxide electrolyser,” *Journal of Power Sources,* vol. 232, pp. 187-192, 2013.

[63] K. Rhu and S. Haile, “Chemical stability and proton conductivity of doped BaCeO3 –BaZrO3 solid solutions,” *Solid State Ionics,* vol. 125, no. 1-4, pp. 355-367, 1999.

[64] K. Katahira, Y. Kohchi, T. Shimura and H. Iwahara, “Protonic conduction in Zr-substituted BaCeO3,” *Solid State Ionics,* vol. 138, no. 1-2, pp. 91-98, 2000.

[65] P. Stuart, T. Unno, J. Kilner and S. Skinner, “Solid oxide proton conducting steam electrolysers,” *Solid State Ionics,* vol. 179, no. 21-26, pp. 1120-1124, 2008.

[66] S. E. S. J. S. s. M. M. C. Graves, “Eliminating degradation in solid oxide electrochemical cells by reversible operation,” *Nature Materials,* vol. 14, pp. 239-244, 2015.

[67] S. H. Jensen, X. F. Sun, S. D. Ebbesen, R. Knibbe and M. Mogensen, “Hydrogen and synthetic fuel production using pressurized solid oxide electrolysis cells,” *International Journal of Hydrogen Energy,* vol. 35, no. 18, pp. 9544-9549, 2010.

[68] Y. Zhang, K. Chen, C. Xia, S. Jiang and M. Ni, “A model for the delamination kinetics of La0.8Sr0.2MnO3 oxygen electrodes of solid oxide electrolysis cells,” *International Journal of Hydrogen Energy,* vol. 37, pp. 13914-13920, 2012.

[69] K. Chen, Z. Lü, X. Chen, N. Ai, X. Huang, X. Du and W. Su, “Development of LSM-based cathodes for solid oxide fuel cells based on YSZ films,” *Journal of Power Sources,* vol. 172, no. 2, pp. 742-748, 2007.

[70] J. Wang, Y. Zhang, T. Liang, C. Deng and J. Xu, “Effect of oxygen partial pressure on the electrochemical impedance of La0.8Sr0.2MnO3−δ/Zr0.92Y0.08O2 porous composite anodes in solid oxide electrolysis cell,” *Journal of Power Sources,* vol. 208, pp. 415-420, 2012.

[71] J. Mougin, A. Chatroux, K. Couturier, M. Petitjean, M. Reytier, G. Gousseau and F. Lefebvre-Joud, “High temperature steam electrolysis stack with enhanced performance and durability,” *Energy Procedia,* vol. 29, pp. 445-454, 2012.

[72] G. Hughes, . Yakal-Kremskia and . Barnett, “Life testing of LSM–YSZ composite electrodes under reversing-current operation,” *Physical Chemistry Chemical Physics,* vol. 15, no. 40, pp. 17257-17262 , 2013.

[73] M. Keane, M. Mahapatra, A. Verma and P. Singh, “LSM–YSZ interactions and anode delamination in solid oxide electrolysis cells,” *International Journal of Hydrogen Energy,* vol. 37, pp. 16776-16785, 2012.

[74] F. Tietz, D. Sebold, A. Brisse and J. Schefold, “Degradation phenomena in a solid oxide electrolysis cell after 9000 h of operation,” *Journal of Power Sources,* vol. 223, pp. 129-135, 2013.

[75] A. Hauch, S. Jensen, J. Bilde-Sørensen and M. Mogensen, “Silica segregation in the Ni/YSZ electrode,” *Electrochemical Society Journal,* vol. 154, no. 7, pp. A619-A626, 2007.

[76] D. Wiedenmann, A. Hauch, B. Grobety, M. Mogensen and U. Vogt, “Complementary techniques for solid oxide elec-trolysis cell characterisation at the micro- and nano-scale,” *International Journal of Hydrogen Energy,* vol. 35, no. 10, pp. 5053-5060, 2010.

[77] J. Mawdsley, J. Carter, A. Kropf, B. Yildiz and V. Maroni, “Post-test evaluation of oxygen electrodes from solid oxide electrolysis stacks,” *International Journal of Hydrogen Energy,* vol. 34, no. 9, pp. 4198-4207, 2009.

[78] V. Sharma and B. Yildiz, “Degradation mechanism in La(0.8)Sr(0.2)CoO(3) as contact layer on the solid oxide electrolysis cell anode,” *Journal of the Electrochemical Society,* vol. 157, no. 3, pp. B441-B448, 2010.

[79] X. Sun, M. Chen, P. Hjalmarsson, S. D. Ebbesen, S. H. Jensen, M. Mogensen and P. V. Hendriksen, “Performance and Durability of Solid Oxide Electrolysis Cells for Syngas Production,” *Journal of the Electrochemical Society,* vol. 41, no. 33, pp. 77-85, 2012.

[80] S. H. Jensen, P. H. Larsen and M. Mogensen, “Hydrogen and synthetic fuel production from renewable energy sources,” *International Journal of Hydrogen Energy,* vol. 32, no. 15, pp. 3253-3257, 2007.

[81] S. D. E. S. H. J. a. M. M. A. Hauch, “Solid Oxide Electrolysis Cells: Microstructure and Degradation of the Ni/Yttria-Stabilized Zirconia Electrode,” *The Electrochemical Society,* vol. 155, no. 11, pp. B1184-B1193, 2008.

[82] M. C. A. R. A. Nechache, “Solid Oxide Electrolysis Cell Analysis by means of Electrochemical Impedance Spectroscopy: A Review,” *Journal of power Sources,* vol. 258, pp. 164 - 181, 2014.

[83] K. Chen and S. Jiang, “Failure mechanism of (La,Sr)MnO3 oxygen electrodes of solid oxide electrolysis cells,” *International Journal of Hydrogen Energy,* vol. 36, pp. 10541-10549, 2011.

[84] C. Yang, C. Jin, A. Coffin and F. Chen, “Characterization of infiltrated (La0.75Sr0.25)0.95MnO3 as oxygen electrode for solid oxide electrolysis cells,” *International Journal of Hydrogen Energy,* vol. 35, no. 11, pp. 5187-5193, 2010.

[85] K. Chen, N. Ai and S. Jiang, “Performance and structural stability of Gd0.2Ce0.8O1.9 infiltrated La0.8Sr0.2MnO3 nano-structured oxygen electrodes of solid oxide electrolysis cells,” *International Journal of Hydrogen Energy,* vol. 39, no. 20, pp. 10349-10358, 2014.

[86] S. Jiang, “Nanoscale and nano-structured electrodes of solid oxide fuel cells by infiltration: Advances and challenges,” *International Journal of Hydrogen Energy,* vol. 37, no. 1, pp. 449-470, 2012.

[87] P. Patro, T. Delahaye and E. Bouyer, “Development of Pr0.58Sr0.4Fe0.8Co0.2O3 − δ–GDC composite cathode for solid oxide fuel cell (SOFC) application,” *Solid State Ionics,* vol. 181, no. 29-30, pp. 1378-1386, 2010.

[88] J. Schuler, Z. Wuillemin, A. Hessler-Wyser, C. Comminges, N. Steiner and J. V. herle, “Cr-poisoning in (La,Sr)(Co,Fe)O3 cathodes after 10,000 h SOFC stack testing,” *Journal of Power Sources,* vol. 211, pp. 177-183, 2012.

[89] V. Nguyen, Q. Fang, U. Packbier and L. Blum, “Long-term tests of a Julich planar short stack with reversible solid oxide cells in both fuel cell and electrolysis modes,” *International Journal of Hydrogen Energy,* vol. 38, pp. 4281-4290, 2013.

[90] J. Schefold, A. Brisse, M. Zahid, J. Ouweltjes and J. Nielsen, “Long Term Testing of Short Stacks with Solid Oxide Cells for Water Electrolysis,” *Journal of the Electrochemical Society,* vol. 35, no. 1, pp. 2915-2927, 2011.

[91] V. Singh, H. Muroyama, T. Matsui, S. Hashigami, T. Inagaki and K. Eguchi, “Feasibility of alternative electrode materials for high temperature CO2 reduction on solid oxide electrolysis cell,” *Journal of Power Sources,* vol. 293, pp. 642-648, 2015.

[92] S. Kim and G. Choi, “Stability of LSCF electrode with GDC interlayer in YSZ-based solid oxide electrolysis cell,” *Solid State Ionics,* vol. 262, pp. 303-306, 2014.

[93] S. Kim, K. Kim and G. Choi, “A novel solid oxide electrolysis cell (SOEr) to separate anodic from cathodic polarization under high electrolysis current,” *International Journal of Hydrogen Energy,* vol. 40, pp. 9032-9038, 2015.

[94] Y. Zheng, Q. Li, T. Chen, W. Wu, C. Xu and W. Wang, “Comparison of performance and degradation of large-scale solid oxide electrolysis cells in stack with different composite air electrodes,” *International Journal of Hydrogen Energy,* vol. 40, no. 6, pp. 2460-2472, 2015.

[95] P. Hjalmarsson, X. Sun, Y. Liu and M. Chen, “Durability of high performance Ni– yttria stabilized zirconia supported solid oxide electrolysis cells at high current density,” *Journal of Power Sources,* vol. 262, pp. 316-322, 2014.

[96] M. Chen, Y.-L. Liu, J. Bentzen, W. Zhang, X. Sun, A. Hauch, Y. Tao, J. Bowen and P. Hendriksen, “Microstructural degradation of Ni/YSZ electrodes in solid oxide electrolysis cells under high current,” *Journal of the Electrochemical Society,* vol. 160, no. 8, pp. F883-F891, 2013.

[97] M. A. Daroukh, F. Tietz, D. Sebold and H. P. Buchkremer, “Post-test analysis of electrode-supported solid oxide electrolyser cells,” *International Journal of Ionics,* vol. 21, no. 4, pp. 1039-1043, 2015.

[98] S. Kim, K. Kim and G. Choi, “Effect of Ce0.43Zr0.43Gd0.1Y0.04O2−δ contact layer on stability of interface between GDC interlayer and YSZ electrolyte in solid oxide electrolysis cell,” *Journal of Power Sources,* vol. 284, pp. 617-622, 2015.

[99] Z. Shao and S. Haile, “A high-performance cathode for the next generation of solid-oxide fuel cells,” *Nature,* vol. 431, pp. 170-173, 2004.

[100] K. Hansen and K. Hansen, “A-site deficient (La0.6Sr0.4)1−sFe0.8Co0.2O3−δ perovskites as SOFC cathodes,” *Solid State Ionics,* vol. 178, no. 23-24, pp. 1379-1384, 2007.

[101] X. Zhang, H. Zhang and X. Liu, “High performance La2NiO4þδ-infiltrated (La0.6Sr0.4)0.995Co0.2Fe0.8O3δ cathode for solid oxide fuel cells,” *Journal of Power Sources,* vol. 269, pp. 412-417, 2014.

[102] S. Gómez, J. Gurauskis, V. Øygarden, D. Hotza, T.Grande and K. Wiik, “Synthesis and oxygen transport properties of La2 − ySryNi1 − xMoxO4 + δ,” *Solid State Ionics,* vol. 292, pp. 38-44, 2016.

[103] S. Jeon, B. Singh, H. Im, K. Seong and S. Song, “Charge and mass transport properties of La2Ni0.95Al0.05O4.025+δ,” *Journal of Alloys and Compounds,* vol. 589, pp. 572-578, 2014.

[104] J. Dailly, S. Fourcade, A. Largeteau, F.Mauvy, J.C.Grenier and M. Marrony, “Perovskite and A2MO4-type oxides as new cathode materials for protonic solid oxide fuel cells,” *Electrochimica Acta,* vol. 55, no. 20, pp. 5847-5853, 2010.

[105] E. Boehm, J. Bassat, P. Dordor, F. Mauvy, J. Grenier and P. Stevens, “Oxygen diffusion and transport properties in non-stoichiometric Ln2 − xNiO4 + δ oxides,” *Solid State Ionics,* vol. 176, no. 37-38, pp. 2717-2725, 2005.

[106] R. Sayers, J. Liu, B. Rustumji and S. J. Skinner, “Novel K2NiF4-Type Materials for Solid Oxide Fuel Cells: Compatibility with Electrolytes in the Intermediate Temperature Range,” *Fuel Cells,* vol. 8, no. 5, pp. 338-343, 2008.

[107] A. Montenegro-Hernández, J. Vega-Castillo, L. Mogni and A. Caneiro, “Thermal stability of Ln2NiO4+δ (Ln: La, Pr, Nd) and their chemical compatibility with YSZ and CGO solid electrolytes,” *International Journal of Hydrogen Energy,* vol. 36, no. 24, pp. 15704-15714, 2011.

[108] M. Laguna-Bercero, A. Hanifi, H. Monzon, J. Cunningham, T. Etsell and P. Sarkar, “High performance of microtubular solid oxide fuel cells using Nd2NiO4þ[small delta]-based composite cathodes,” *Journal of Materials Chemistry,* vol. 2, no. 25, pp. 9764-9770, 2014.

[109] G. Amow, P. Whitfield, I. Davidson, R. Hammond, C. Munnings and S.J.Skinner, “Structural and sintering characteristics of the La2Ni1−xCoxO4+δ series,” *Ceramics International,* vol. 30, no. 7, pp. 1635-1639, 2004.

[110] A. Momma, Y. Kaga, K. Takano, K. Nozaki, A. Negishi, K. Kato, T. Kato, T. Inagaki, H. Yoshida, K. Hoshino, M. Yamada, T. Akbay and J. Akikusa, “Experimental investigation of anodic gaseous concentration of a practical seal-less solid oxide fuel cell,” *Journal of Power Sources,* vol. 145, no. 2, pp. 169-177, 2005.

[111] G. Schiller, A. Ansar, M. Lang and O. Patz, “High temperature water electrolysis using metal supported solid oxide electrolyser cells (SOEr),” *Journal of Applied Electrochemistry,* vol. 39, no. 2, pp. 293-301, 2009.

[112] N.H. Menzler, F. Tietz, S. Uhlenbruck, H.P. Buchkremer and D. Stöver, “Materials and manufacturing technologies for solid oxide fuel cells,” *Journal of Materials Science,* vol. 45, no. 12, pp. 3109-3135, 2010.

[113] M. Sohal, J. O’Brien, C. Stoots, V. Sharma, B. Yildiz and A. Virkar, “Degradation Issues in Solid Oxide Cells During High Temperature Electrolysis,” *Fuel Cell Science and Technology,* vol. 9, no. 1, pp. 377-387, 2012.

[114] S. Lee, J.-M. Kim, H. Hong and S.-K. Woo, “Fabrication and characterization of Cu/YSZ cermet high temperature electrolysis cathode material prepared by high-energy ball-milling method: II. 700 °C-sintered,” *Journal of Alloys and Compounds,* vol. 467, no. 1-2, pp. 614-621, 2009.

[115] J. Ruiz-Moralez, J. Canales-Vazquez, D. Marrero-Lopez and P. Nunez, “Is YSZ stable in the presence of Cu?,” *Journal of Materials Chemistry,* vol. 18, no. 42, pp. 5072-5077, 2008.

[116] A. Atkinson, S. Barnett, R. J. Gorte, J. Irvine, A. McEvoy, M. Mogensen, S. Singhal and J. Vohs, “Advanced anodes for high-temperature fuel cells,” *Nature Materials,* vol. 3, no. 1, pp. 17-27, 2004.

[117] M. Gong, X. Liu, J. Trembly and C. Johnson, “Sulfur-tolerant anode materials for solid oxide fuel cell application,” *Journal of Power Sources,* vol. 168, no. 2, pp. 289-298, 2007.

[118] L. Yang, S. Wang, K. Blinn, M. Liu, Z. Liu, Z. Cheng and M. Liu, “Enhanced sulfur and coking tolerance of a mixed ion conductor for SOFCs: BaZr0.1Ce0.7Y0.2–xYbxO3– δ,” *Science,* vol. 326, no. 5949, pp. 126-129, 2009.

[119] Y.-H. Huang, R. Dass, Z.-L. Xing and J. Goodenough, “Double perovskites as anode materials for solid-oxide fuel cells,” *Science,* vol. 312, no. 5771, pp. 254-257, 2006.

[120] S. K. J. B. Youngjin Kwon, “Development of a PrBaMn2O5+δ-La0.8Sr0.2Ga0.85Mg0.15O3-δ composite electrode by scaffold infiltration for reversible solid oxide fuel cell applications,” *International Journal of Hydrogen Energy,* vol. 45, no. 3, pp. 1748 - 1758, 2020.

[121] P. Addo, B. Molero-Sanchez, A. Buyukaksoy, S. Paulson and V. Birss, “Sulfur Tolerance of La0.3M0.7Fe0.7Cr0.3O3-δ (M=Sr, Ca) Solid Oxide Fuel Cell Anodes,” *ECS Transactions,* vol. 66, no. 2, pp. 219-228, 2015.

[122] S. Lee, G. Kim, J. Vohs and R. Gorte, “SOFC Anodes Based on Infiltration of La0.3Sr0.7TiO3,” 22 9 2008. [Online]. Available: http://repository.upenn.edu/cbe_papers/143. [Accessed 20 10 2017].

[123] G. Kim, G. Corre, J. Irvine, J. Vohs and R. Gorte, “Engineering Composite Oxide SOFC Anodes for Efficient Oxidation of Methane,” 02 2008. [Online]. Available: http://repository.upenn.edu/cbe_papers/103. [Accessed 20 10 2017].

[124] J.-S. Park, I. Hasson, M. Gross, C. Chen, J. Vohs and R. Gorte, “A high-performance solid oxide fuel cell anode based on lanthanum strontium vanadate,” *Journal of Power Sources,* vol. 196, no. 18, pp. 7488-7494, 2011.

[125] J. Haag, D. Bierschenk, S. Barnett and K. Poeppelmeier, “Structural, chemical, and electrochemical characteristics of LaSr2Fe2CrO9-δ-based solid oxide fuel cell anodes,” *Solid State Ionics,* vol. 212, pp. 1-5, 2012.

[126] S. Jiang, L. Zhang and Y. Zhang, “Lanthanum strontium manganese chromite cathode and anode synthesized by gel-casting for solid oxide fuel cells,” *Journal of Materials Chemistry,* vol. 17, no. 25, pp. 2627-2635, 2007.

[127] J. Ruiz-Morales, J. Canales-Vázquez, J. Peña-Martínez, D. López and P. Núñez, “On the simultaneous use of La0.75Sr0.25Cr0.5Mn0.5O3−δ as both anode and cathode material with improved microstructure in solid oxide fuel cells,” *Electrochimica Acta,* vol. 52, no. 1, pp. 278-284, 2006.

[128] D. Bastidas, S. Tao and J. Irvine, “A symmetrical solid oxide fuel cell demonstrating redox stable perovskite electrodes,” *Journal of Materials Chemistry,* vol. 16, pp. 1603-1605, 2006.

[129] S. Tao and J. Irvine, “A redox-stable efficient anode for solid-oxide fuel cells,” *Nature Materials,* vol. 2, pp. 320-323, 2003.

[130] A. Reyes-Rojas, J. .Alvarado-Flores, H. Esparza-Ponce, M. Esneider-Alcala, I. Espitia-Cabrera and E. Torres-Moye, “Symmetry breaking and electrical conductivity of La0.7Sr0.3Cr0.4Mn0.6O3−δ perovskite as SOFC anode material,” *Materials Chemistry and Physics,* vol. 126, no. 3, pp. 773-779, 2011.

[131] Y. Li, Y. Gana, Y. Wang, k. Xie and Y. Wu, “Composite cathode based on Ni-loaded La0.75Sr0.25Cr0.5Mn0.5O3−δ for direct steam electrolysis in an oxide-ion-conducting solid oxide electrolyzer,” *International Journal of Hydrogen Energy,* vol. 38, no. 25, pp. 10196-10207, 2013.

[132] S.-E. Yoon, J.-Y. Ahn, B.-K. Kim and J.-S. Park, “Improvements in co-electrolysis performance and long-term stability of solid oxide electrolysis cells based on ceramic composite cathodes,” *International Journal of Hydrogen Energy,* vol. 40, no. 39, pp. 13558-13565, 2015.

[133] P. Addo, B. Molero-Sanchez, M. Chen, S. Paulson and V. Birss, “CO/CO2 study of high performance La0.3Sr0.7Fe0.7Cr0.3O3-δ reversible SOFC electrodes,” *Fuel Cells,* vol. 15, no. 5, pp. 689-696, 2015.

[134] A. Brisse, J. Schefold and M. Zahid, “High temperature water electrolysis in solid oxide cells,” *International Journal of Hydrogen Energy,* vol. 33, no. 20, pp. 5375-5382, 2008.

[135] A. L. A. W. E. I.-T. D. Klotz, “Electrochemical model for SOFC and SOEC mode predicting performance and efficiency,” *Internal Journal of Hydrogen Energy,* vol. 39, no. 35, pp. 20844-20849, 2014.

[136] A. B. Philippe Mocoteguy, “A review and comprehensive analysis of degradation mechansims of solid oxide electrolysis cells,” *International Journal of Hydrogen Energy,* vol. 38, pp. 15887 - 15902, 2013.

[137] S. H. J. A. H. I. C. a. T. J. Mogens Mogensen, “Performance of reversible solid oxide cells: A review,” in *Proceedings of the sixth European Solid Oxide Fuel Cell Forum*, Lucerne, 2006.

[138] X. Sun, M. Chen, Y.-L. Liu, P. Hjalmarsson, S. Ebbesen, S. Jensen, M. Mogensen and P. Hendriksen, “Durability of solid oxide electrolysis cells for syngas production,” *Journal of The Electrochemical Society,* vol. 160, no. 9, pp. F1074-F1080, 2013.

[139] M. C. M. L. J. Y. Chaoyang Wang, “Dynamic modeling and parameter analysis study on reversible solid oxide cells during mode switching transient processes,” *Applied Energy,* vol. 263, no. 114601, 2020.

[140] Y. Zheng, Y. Luo, Y. Shi and a. N. Cai, “Dynamic Processes of Mode Switching in Reversible Solid Oxide Fuel Cells,” *Journal of Energy Engineering,* vol. 143, no. 6, 2018.

[141] S. Gómez and D. Hotza, “Current developments in reversible solid oxide fuel cells,” *Renewable and Sustainable Energy Reviews,* vol. 61, pp. 155-174, 2016.

[142] W. Wang, Y. Huang, S. Jung, J. Vohs and R. Gorte, “A Comparison of LSM, LSF, and LSCo for Solid Oxide Electrolyzer Anodes,” *The Electrochemical Society,* vol. 153, no. 11, pp. 2066-2070, 2006.

[143] K. P. P. H. S. S. E. K. N. Perdikaris, “Design and exergetic analysis of a novel carbon free tri-generation system for hydrogen, power and heat production from natural gas, based on combined solid oxide fuel and electrolyser cells,” *International Journal of Hydrogen Energy,* vol. 25, pp. 2446 - 2456, 2010.

[144] A. M. M. V. A. K. E. I.-T. H. Schichlein, “Deconvolution of electrochemical impedance spectra for the identification of electrode reaction mechanisms is solid oxide fuel cells,” *Journal of Applied Electrochemistry,* vol. 32, pp. 875 - 882, 2002.

[145] B. K. Đ. J. M. K. H. S. C. H. P. B. Vanja Subotić, “Detailed insight into processes of reversible solid oxide cells and stacks using DRT analysis,” *Energy Conversion and Management,* vol. 226, no. 113509, 2020.

[146] S. M. A. R. S. U. Shuab Khan, “Equivalent Circuit Modelling using Electrochemical Impedance Spectroscopy for Different Materials of SOFC,” *Institute of Electrical and Electronics Engineers,* vol. 978, no. 9, pp. 3805 - 4421, 2016.

[147] Struers, “struers.com,” struers, [Online]. Available: www.struers.com/en/Knowledge/Mounting/Cold-mounting. [Accessed 15 January 2018].

[148] J. E. O. R. C. O. G. K. H. Xiaoyu Zhang, “Durability evaluation of reversible solid oxide cells,” *Journal of Power Sources,* vol. 242, pp. 566 - 574, 2013.

[149] Z. W. Wang, M. Mori and T. Araki, “Steam electrolysis performance of intermediate-temperature solid oxide electrolysis cell and efficiency of hydrogen production system at 300 nm3/ h,” *International Journal of Hydrogen Energy,* vol. 35, no. 10, pp. 4451-4458, 2010.

[150] M. Liang, B. Yu, M. Wen, J. Chen, J. Xu and Y. Zhai, “Preparation of LSM–YSZ composite powder for anode of solid oxide electrolysis cell and its activation mechanism,” *Journal of Power Sources,* vol. 190, no. 2, pp. 341-345, 2009.

[151] M. Ni, M. Leung and D. Leung, “A modeling study on concentration overpotentials of a reversible solid oxide fuel cell,” *Journal of Power Sources,* vol. 163, no. 1, pp. 460-466, 2006.

[152] M. Mori, T. Abe, H. Itoh, O. Yamamoto, Y. Takeda and T. Kawahara, “Cubic-stabilized zirconia and alumina composites as electrolytes in planar type solid oxide fuel cells,” *Solid State Ionics,* vol. 74, no. 3-4, pp. 157-164, 1994.

[153] B. Yu, W. Zhang, J. Xu and J. Chen, “Microstructural characterization and electrochemical properties of Ba0.5Sr0.5Co0.8Fe0.2O(3-delta) and its application for anode of SOEC,” *International Journal of Hydrogen Energy,* vol. 33, no. 23, pp. 6873-6877, 2008.

[154] M. Ni, M. Leung and D. Leung, “Electrochemical modeling of hydrogen production by proton-conducting solid oxide steam electrolyzer,” *International Journal of Hydrogen Energy,* vol. 33, no. 15, pp. 4040-4047, 2008.

[155] A. Mielewczyk-Gryn, K. Gdula, S. Molin, P. Jasinki, B. Kusz and M. Gazda, “Structure and electrical properties of ceramic proton conductors obtained with molten-salt and solid-state synthesis methods,” *Journal of Non-Crystalline Solids,* vol. 356, no. 37-40, pp. 1976-1979, 2010.

[156] J. Dailly, S. Fourcade, A. Largeteau, F. Mauvy, J. Grenier and M. Marrony, “Perovskite and A2MO4-type oxides as new cathode materials for protonic solid oxide fuel cells,” *Electrochimica Acta,* vol. 55, pp. 5847-5853, 2010.

[157] H. E. Shinawi and C. Greaves, “Synthesis and characterization of La1.5þxSr0.5x Co0.5Ni0.5O4þ/- [small delta] (x¼0, 0.2),” in *Synthesis and Characterization of Cobalt-containing Perovskite-type Oxides: A thesis Submitted to the University of Birmingham For the Degree of Doctor of Philosophy*, Birmingham, University of Birmingham, 2010, pp. 108-130.

[158] M. Rieu, R. Sayers, M. Laguna-Bercero and F. Ansart, “Investigation of Graded La2NiO4 + δ Cathodes to Improve SOFC Electrochemical Performance,” *Journal of The Electrochemical Society,* vol. 157, no. 4, pp. B477-B480, 2010.

[159] N. Pujare, K. Semkow and A. Sammells, “A Direct H2S/Air Solid Oxide Fuel Cell,” *Journal of The Electrochemical Society,* vol. 134, no. 10, pp. 2639-2640, 1987.

[160] K. Blinn and M. Liu, “BaZr0.9Yb0.1O3−δ-modified bi-electrode supported solid oxide fuel cells with enhanced coking and sulfur tolerance,” *Journal of Power Sources,* vol. 243, pp. 24-28, 2013.

[161] S. Yoon, J. Han, S. Nam, T.-H. Lim and S.-A. Hong, “Improvement of anode performance by surface modification for solid oxide fuel cell running on hydrocarbon fuel,” *Journal of Power Sources,* vol. 136, no. 1, pp. 30-36, 2004.

[162] I. Jung, D. Lee, S. Lee, D. Kim, J. Kim, S.-H. Hyun and J. Moon, “LSCM–YSZ nanocomposites for a high performance SOFC anode,” *Ceramics International,* vol. 39, no. 8, pp. 9753-9758, 2013.

[163] N. Q. Minh, “Solid Oxide Fuel Cell Technologies - Features and Applications,” *Solid State Ionics,* vol. 174, pp. 271-277, 2004.

APPENDIX A SUPPLEMENTARY RESULTS

A.1 Test at 1.5 A/cm^2 Current Density (Cell ID: CT1_1.5_750#1)

This test was also conducted with a fuel utilisation of 83.5% (similar to test CT1_1.25_750 as reported in Section 5.8) but at a current density of 1.5 A/cm^2.

Figure A- *1* shows the cell durability information. The open cell voltage of the virgin cell prior to the start of the 120 hours of constant SOFC operation was 998 mV. Under the 1.5 A/cm^2 SOFC current density load, the cell voltage dropped to -450 mV. This indicated either a damaged virgin cell, cell damage due to the high current density load (similar to test CT1_2.65_750 reported in Section 5.9), or a lack of electronic contacting at the fuel electrode. Nevertheless, the test was continued for two main reasons:

1. It may give important information to enable possible understanding of how damaged cells may behave in an rSOC stack or system.
2. The initial reading indicating cell damage or inadequate anodic contacting may be due to equipment malfunction. All equipment was therefore checked during the residual testing period and were found to be operating correctly.

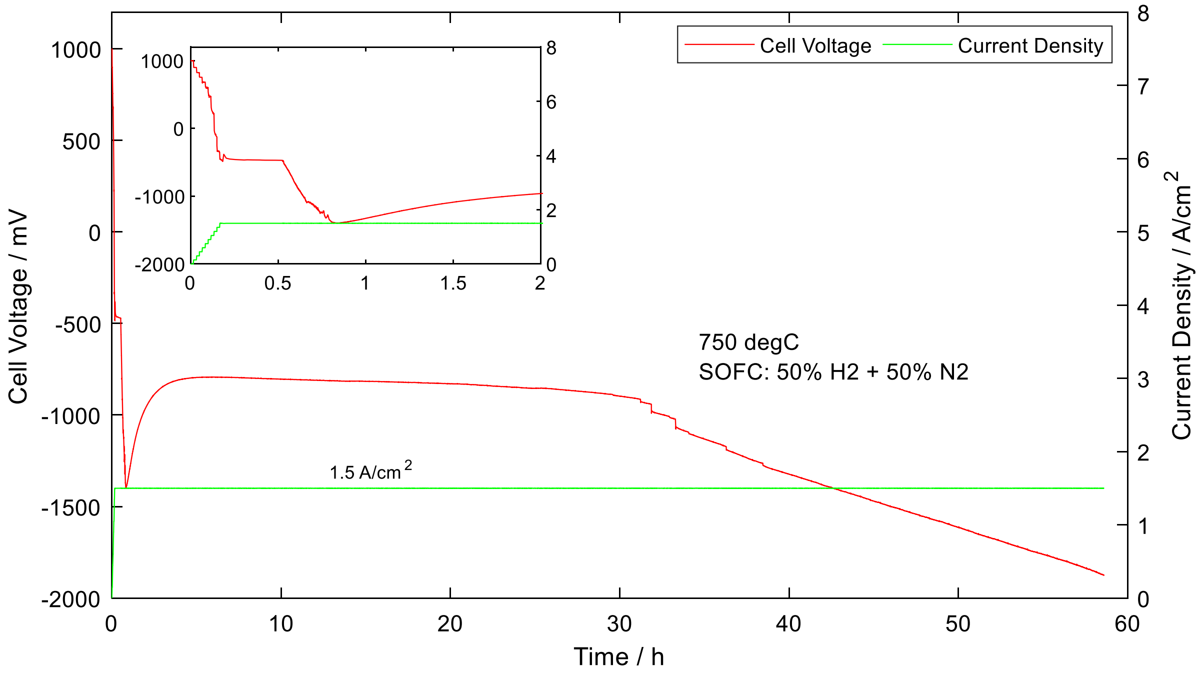

Figure A- 1: Voltage evolution characteristics of CT1_1.5_750#1 tested at 750oC and ±1.5 A/cm2 current density.

After the initial drop to -450 mV, the cell voltage continued dropping to -1396 mV over a one-hour period before recovering and stabilising at approximately -795 mV over the following 30 hours.

The j-V characteristics of the virgin cell, Figure A- 2, indicate that the cell was not primarily damaged due to high current density exposure, as may also be seen from the crack-like features observed on the virgin cell electrode surfaces under SEM, **Figure A- 3**. Figure A- 2 shows large voltage drops relative to negligible current density exposure. Therefore, the virgin cell was damaged prior to the galvanostatic exposure to the 1.5 A/cm^2 SOFC current density.

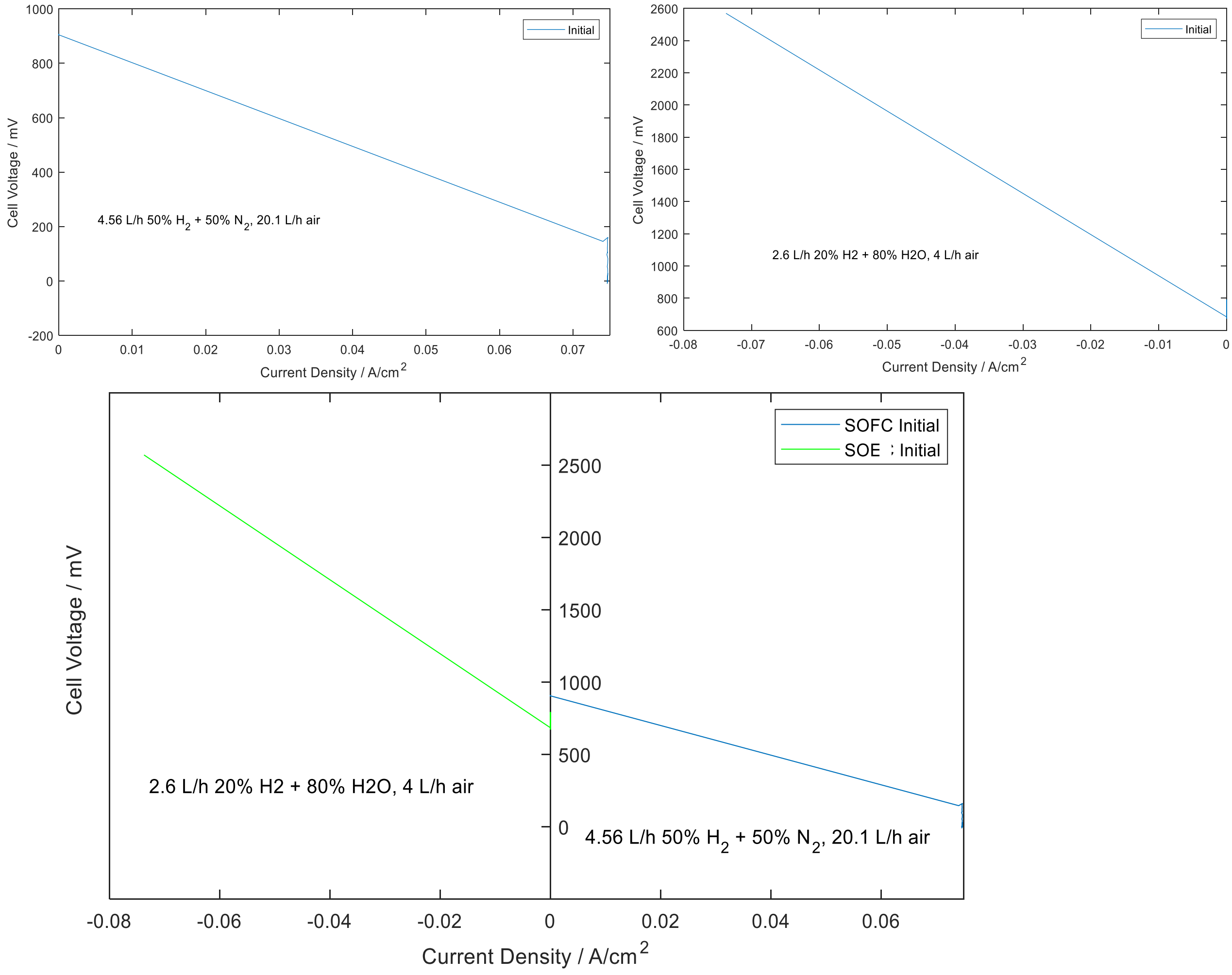

Figure A- 2: Initial j-V characteristics of CT1_1.5_750#1.

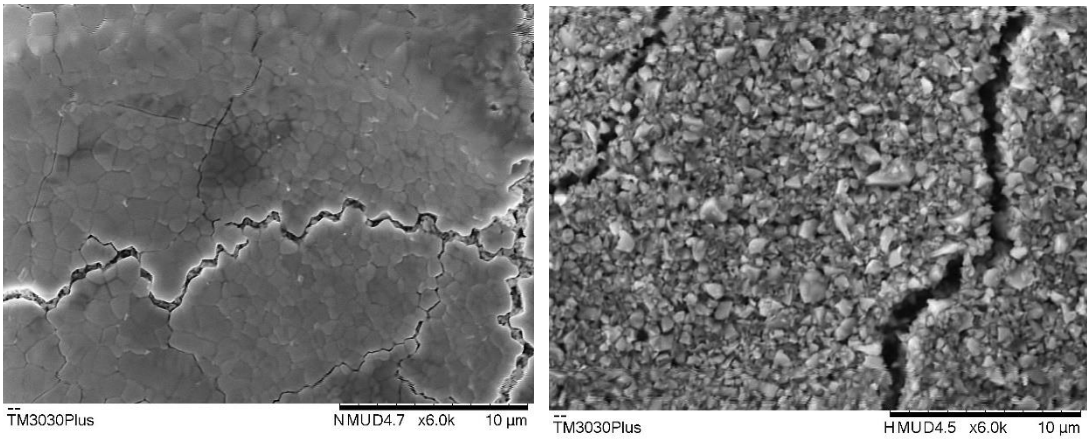

Figure A- 3: Virgin CT1_1.5_750#1 SEM image showing crack-like features

A.2 Test at 1.5 (1.05) A/cm^2 Current Density (Cell ID: CT1_1.5_750#2)

This test was meant to replicate the test reported in Appendix A.1 (CT1_1.5_750#1) due to the failure of that test as a result of a damaged virgin cell. Therefore, this test was also conducted at 1.5 A/cm^2 current density, with a fuel utilisation of 83.5%.

The OCV prior to the commencement of the 120 hours of constant SOFC operation was 836 mV, which was the first indication that this cell was also probably damaged. The attempt to then step the test current density from 0 to 1.5 A/cm^2 (0.15 A/cm^2 per step with a 1 minute hold time per step, see Section 4.2.2 for further details) was not succesful. The current density steps were succesfully ramped up to 0.9 A/cm^2 (with a corresponding cell voltage of -335 mV), at 1 minute holdtime per step, after which it took approximately 2 hours to ramp up to the next current density step (1.05 A/cm^2), see Figure A- *4*. After reaching 1.05 A/cm^2, the current density could not be ramped up to the next step, 1.2 A/cm^2. The current density remained at approximately 1.05 A/cm^2 for up to 12 hours with some voltage recovery, after which the test was discontinued at a cell voltage of -111 mV.

This indicated that the cell was not capable of producing the required 1.5 A/cm^2 galvanostatic current density, indicating that the virgin cell was damaged. The negative voltages, under galvanostatic operation, indicate zero electrochemical activity under the galvanostatic current.

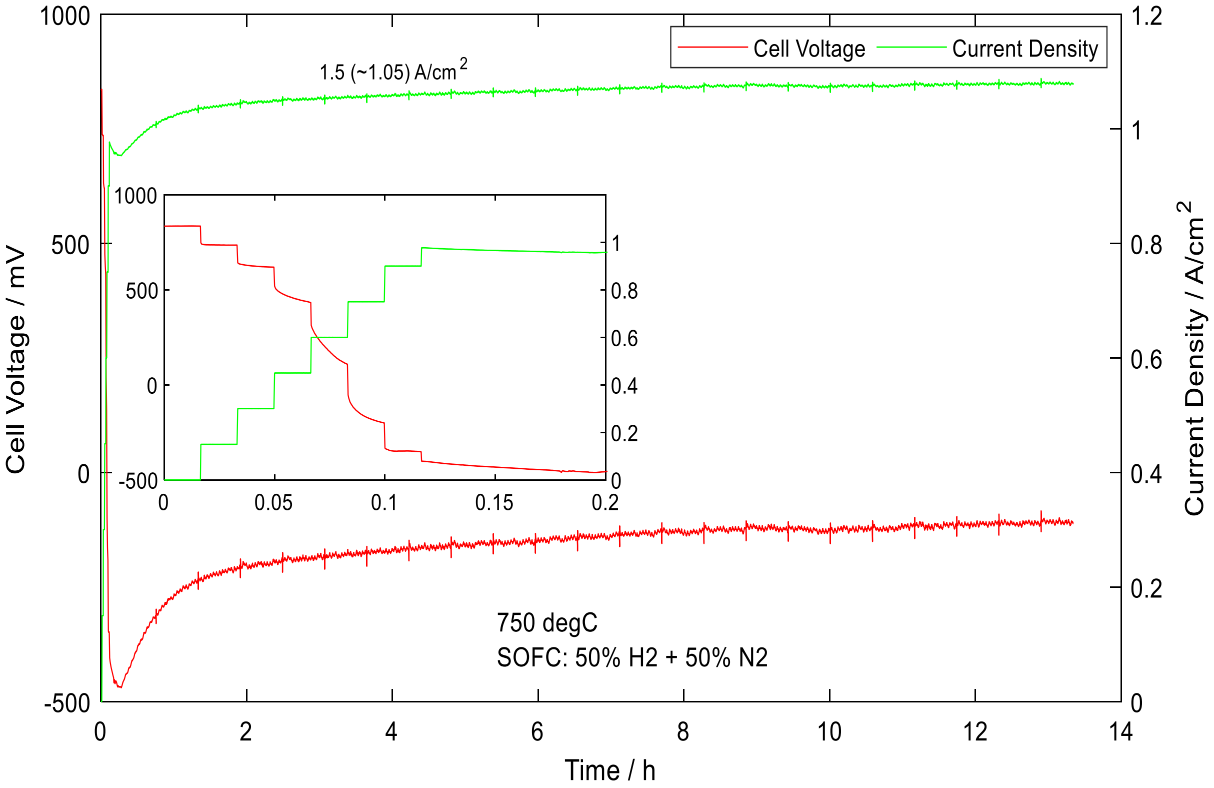

Figure A- 4: Voltage evolution characteristics of CT1_1.5_750#2 tested at 750oC and 1.5 (1.05) A/cm2 current density.

The j-V characteristics of the virgin cell, Figure A- 5, also indicate that the cell was damaged prior to testing due to the observed large voltage drops relative to very small current density exposure.

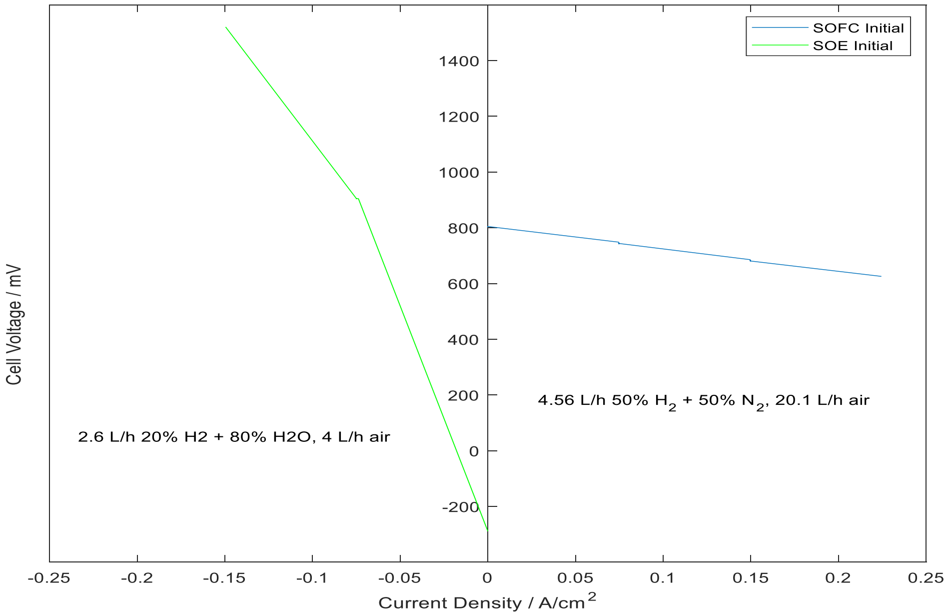

Figure A- 5: j-V characteristics of virgin CT1_1.5_750#2

Quality control and assurance (QA/QC) procedures during manufacturing, transport and storage of rSOC cells are therefore very essential variables in system performance, since even microscopic damages to the cell have potentially debilitating effects on cell performance. Figure A- *6* for instance shows some micro crack-like features at the oxygen electrode side of the cell which may be possibly linked to the observed poor performance, if the crack-like features extend through the electrolyte.

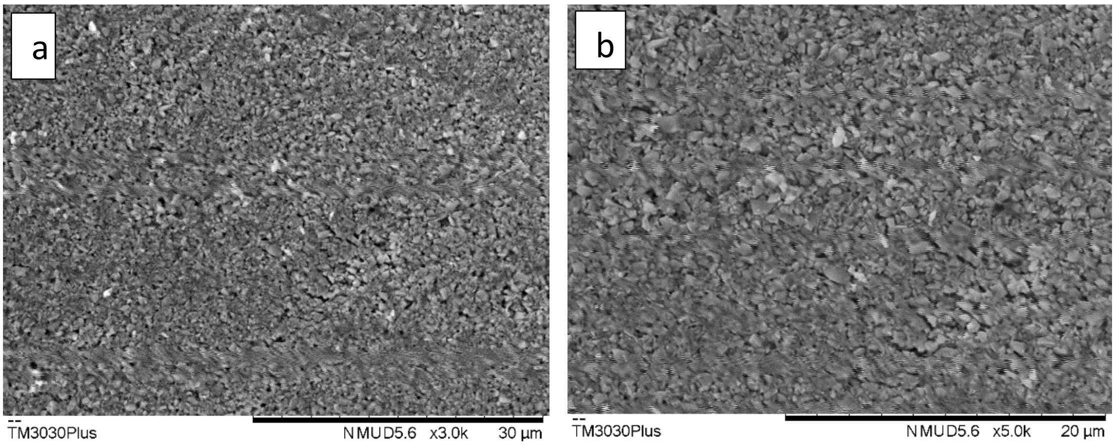

Figure A- 6: Virgin CT1_1.5_750#2 SEM images showing crack-like features in cathode possibly linked to the observed poor performance